UNIVERSITY OF HERTFORDSHIRE

Submillimetre Observations of Clusters of Galaxies

Author:
Ryan CHEALE

Supervised by:
Dr. James Geach

Centre for Astrophysics Research
School of Physics, Astronomy and Mathematics
University of Hertfordshire

Submitted to the University of Hertfordshire in partial fulfilment of the requirements of the degree of Doctor of Philosophy.

June 2019

Abstract

Advances in submillimetre astronomy has opened the doors to carrying out surveys and high-resolution imaging of intense star forming galaxies out to and beyond the cosmic star-formation peak ($z \approx 1$ - 4). The Submillimetre Galaxy (SMG) population may well be the progenitors to the massive elliptical galaxies seen today, but the detailed nature of their assembly is still not clear. Gravitational lensing provides a route to highly resolved and detailed studies, but the current sample of lensed SMGs is relatively small. Capitalising on the lensing potential of a galaxy cluster observed were 202 massive clusters at $850\mu m$ in relatively poor submillimetre observing conditions ($\tau_{225\mathrm{GHz}} > 0.1$) with the SCUBA-2 instrument mounted on the JCMT. The SCUBA-2 Cluster Snapshot Survey (S2CSS) aim was to identify rare examples of bright (tens of mJy) gravitationally lensed submillimeter galaxies. The S2CSS covered over 0.33 deg^2 to an average depth of $\sigma_{850} \approx 12\,\mathrm{mJy\,beam^{-1}}$. In this thesis a sample of 97 bright 850μm point sources selected from the S2CSS which are potentially gravitationally lensed and, eight sources where the strong submillimetre emission is co-located with the central Brightest Cluster Galaxy (BCG) are presented. Constructed are far-infrared spectral energy distributions for each that have additional Herschel SPIRE coverage; used in conjunction to estimate the redshifts and luminosities of the sources. The bright submillimetre flux density of the sources make them excellent targets for detailed follow-up work that will allow for detection of spectral features in the submillimetre/millimetre that would otherwise be too faint to detect. Already an extension of the original S2CSS aimed at confirming a number of potentially lensed galaxies which fell beneath a coarse selection criterion but formally were $> 4\sigma$ or sources exceeding 80% completeness in the central deep regions of the SCUBA-2 maps has been successfully been observed. Higher signal-to-noise maps will confirm or rule out candidates as a spurious detection. The additional observations will allow for the lensed source counts to be refined sufficiently that they can be directly compared with lensed sources found with ALMA in clusters.

It is well known that BCGs harbour AGN, possibly reserves of cold gas and some on-going star formation. All of these might cause (directly or indirectly) submillimeter emission. This has yet to have been well-explored in a large sample like the one presented in this thesis. The individual maps are too shallow in general to detect a lot of this sub-mm emission, but since we observed a large number, and know where the BCG is, we can stack - average the maps together, co-aligned on the BCG - to detect statistical (average) emission. Matching sources from the SCUBA-2 Cluster Snapshot Survey with radio observations from the NRAO Very Large Array and the TGSS Alternative Data Release we constructed SEDs comprised of radio-binned clusters stacked on their Brightest Cluster Galaxy (BCG) location. In doing so we found that the radio and $850\mu m$ emissions correlate and suggest that in the strongest radio sources AGN are dominating the submillimeter excess whereas for galaxies with weak radio emission, star formation is the driving mechanism. Furthermore, measurements of the Sunyaev Zel'dovich effect (due to the Compton scattering of CMB photos by the hot intracluster medium) is contaminated

from the sub-mm emission present in clusters which may well detriment mass measurements, this work finds an average contribution from BCGs $S_{850\mu m} = 2.16 \pm 0.58$ mJy

Finally, the serendipitous detection of a bright 3-mm continuum source in the brightest galaxy cluster in Abell 0851 ($z = 0.4$). Collating decades of multi-frequency observations across 21cm–100μm including new Arcminute Microkelvin Imager 15 GHz observations, evidence for a relatively flat, variable (Mean of 53% increase in flux density between 1.9 to 21 cm) core source associated with the BCG. The radio power and amplitude of variability observed in this galaxy is consistent with the cores in lower redshift BCGs in X-ray–selected clusters, and the flat mm–cm spectrum is suggestive of the BCG being a low luminosity AGN archetype due to the relatively low X-ray and Optical flux compared to the radio flux. The discovery of this system could provide a basis for a long-term study of the role of low luminosity radio mode 'regulatory' feedback in massive clusters.

Declaration

I declare that no part of this work is being submitted concurrently for another award of the University or any other awarding body or institution. This thesis contains a substantial body of work that has not previously been submitted successfully for an award of the University or any other awarding body or institution.

The following parts of this submission have been published previously and/or undertaken as part of a previous degree or research programme:

1. Chapter 2 & 3: have been published as Cheale et al. 2019 The SCUBA-2 Cluster Snapshot Survey - I. Catalogue of lensed galaxies and submillimetre-bright central galaxies. *Monthly Notices of the Royal Astronomical Society* 484:2757

2. Chapter 4: this has been published as Cheale et al., 2018 The nature of the variable millimetre-selected AGN in the brightest cluster galaxy of Abell 851. *Monthly Notices of the Royal Astronomical Society* 481:L54

3. Chapter 5.1: has been granted 11.0 hours in Semester 18B. Proposal ID: M18BP056 PI: Ryan Cheale

Except where indicated otherwise in the submission, the submission is my own work and has not previously been submitted successfully for any award.

Acknowledgements

Dr. James Geach and Dr. Alastair Edge for their infallible patience,

David Pike for his persistent encouragement to pursue my goals,

Rob Mayes and Dr Nicholas Murray for all of their support and advice,

Matt and Noelle Stallard for keeping me focused and driven,

Alex Swinnerton, Erin Charles and Owen Hinton for keeping me upright,

Rob, Lindsey, Matt, Nathan and Luke Day, for giving me purpose.

Without these, and many others, I would have lost direction.

For my grandparents,

Norman and Millicent Cheale

Contents

Chapter 1

Introduction

1.1 A brief overview of Cosmic History and Galaxy Formation

Until the early 20th century, the Universe was thought to be in a static state. However, this view was empirically challenged in the 1920s with two key discoveries. Edwin Hubble applied Henrietta Swan Leavitt's period-luminosity law [Leavitt, 1908, Leavitt and Pickering, 1912] for Cepheid Variables (and used other standard candles) and combined this with Vesto Slipher's spectroscopy [Slipher, 1915] of a sample of 'spiral nebulae' to show that there are galaxies external to our own, and that these galaxies are generally receding from us. The recession velocities (v) cause a Doppler shift in the observed wavelength of light emitted by distant galaxies, giving us the term 'redshift', z

$$z = \frac{\lambda_{\rm o} - \lambda_{\rm e}}{\lambda_{\rm e}} = \frac{v}{c}, \tag{1.1}$$

where c is the speed of light in a vacuum and $\lambda_{\rm o,e}$ are the observed and emitted wavelengths of light.

Hubble measured a linear relationship between the recession velocity of a galaxy and its distance (d) from us, now known as the Hubble-Lemaître Law [Hubble, 1929],

$$v = {\rm H}_0 d, \tag{1.2}$$

where $\rm H_0$ is the Hubble constant describing the rate of expansion of the Universe, with current constraints indicating ${\rm H}_0 = 67.66 \pm 0.42\,{\rm km\,s^{-1}\,Mpc^{-1}}$ [Planck Collaboration et al., 2018] determined by measurements of Cosmic Microwave Background (CMB) anisotropies [Planck

Collaboration et al., 2016]. However, alternative measurements of the Hubble constant find differing values e.g., Chen et al., 2019 make use of three strongly lensed systems to calculate a value of $H_0 = 76.8 \pm 2.6\,\mathrm{km\,s^{-1}\,Mpc^{-1}}$. Numerous other methods (e.g., quasars, red giant stars, supernovae, etc.) produce alternative values, it is this discrepancy between values that has created tension in the exact value of the Hubble Constant to this day [e.g.; Freedman, 2017].

After the discovery of the expanding Universe in the 1920s, the following few decades saw the emergence of two theories to attempt to explain the observations: a Steady State theory championed by Thomas Gold, Hermann Bondi and Fred Hoyle, and what became known as the 'Big Bang' theory, that can find its roots in the 'Primeval Atom' theory proposed by Georges Lemaître.

The Steady State theory argued that new matter appears in the spaces between galaxies as they recede from one another, and the Universe has no beginning. However, the discovery of a relic background radiation – predicted to exist by proponents of what was to become known as the Big Bang theory by Ralph Alpher, Robert Herman and George Gamow [Alpher et al., 1948] – by Robert Wilson and Arno Penzias in 1964 [Penzias and Wilson, 1965] made the Steady State model untenable. In the Big Bang model, the Universe was smaller, denser and hotter in the past, originating in a infinitely dense 'singularity'. At some point in the past this singularity 'exploded' (although that is a misleading term), creating space and time, matter and energy. In the very early Universe, matter was in a fundamental state; existing only as quarks and leptons in a 'quark soup', mixed with radiation (photons). Cooling resulted in a quark-hadron transition phase whereby quarks combined to form pions and nucleons. Electron-positron pairs annihilated, and as their number densities dropped, the reduction in the number density of electrons caused neutron-proton reactions to slow to the point where they no longer have a significant effect on the neutron-proton ratio, i.e.'freezing' out. This freeze-out determined the abundance of elements which would consequently form from the elementary particles through nucleosynthesis. Once the temperature approached $T \sim 10^9\,K$ – primordial nucleosynthesis could begin, building the most stable of elemental nuclei: Hydrogen (H), Helium (He) (H makes up 73% by mass and 25% He) and trace amounts of Lithium (Li) and Beryllium (Be) [Schramm and Turner, 1998, Burles et al., 2001].

Prior to 380,000 years after the Big Bang, the Universe had a temperature $T \gg 3000\,K$. Preceding this point electrons were not locked into atoms, and were in thermal equilibrium. As a result photons and electrons were constantly interacting through Thomson scattering, with

a short mean free path. But at 380,000 years the temperature was low enough ($T \approx 3000\,K$) for electrons to become bound to protons forming (mostly) atomic hydrogen. Once scattering ceased in the photon-baryon fluid, radiation that was 'trapped' could free-stream across the Universe. The distribution of photon energies is a nearly perfect blackbody, and we observe this redshifted ($z = 1100$) blackbody as the cosmic microwave background today, with a temperature of $T_{CMB} = 2.7260 \pm 0.00013\,K$.

Following Recombination the Universe was in a neutral state – pervaded by a relatively smooth distribution of dark matter and atomic hydrogen. Although the matter distribution was quite smooth, the density field did contain fluctuations. These density fluctuations trace back to the Big Bang itself, where random, quantum-level perturbations arose as the Universe was born. Amplified during a period of inflation [Guth, 1981], and through gravitational collapse, these perturbations grew, forming deeper gravitational wells. These are the regions of the Universe where the formation of galaxies is more biased – i.e. there is a preference for galaxies to form in the high-density peaks. We can observe the distribution of the density fluctuations at $z \approx 1100$ in the power spectrum of temperature anisotropies of the CMB, which arise because the photons were coupled to the baryons prior to recombination, and had a slightly higher(lower) energy in higher(lower) density regions; a signature that was encoded into the CMB spectrum at the time of recombination. Atomic hydrogen (HI) cooled in the growing potential wells, eventually igniting into the first generation of (Population III) stars, and the first galaxies were formed, at a redshift of $z \approx 20$, a few hundred million years after the Big Bang. The ignition of star formation in the Universe resulted in a source of ultraviolet radiation, streaming out of protogalaxies and illuminating the neutral intergalactic medium (IGM). Photons with energies in excess of 13.6 eV are capable of ionising HI in the IGM, and so this epoch is known as the Epoch of Reionisation, when the neutral Universe transitioned back to a state that is nearly entirely ionised.

Aside from the CMB, the galaxies born at the Epoch of Reionisation, and since, make up most of the directly observable Universe. They are assembled within a large scale web-like structure of filaments and nodes (the evolution of the density fluctuations imprinted at the start of the Universe). The largest, most over-dense nodes contain 'clusters' of galaxies, typically numbering 100s or 1000s of galaxies within a volume just a few million light years across. Galaxies themselves reside in dark matter 'halos' – roughly spherically symmetric distributions of dark matter particles that only interact gravitationally. Evidence of a dark matter dominated Universe started to emerge early in the mid-20th century with measurements of velocities of galaxies within the Coma Cluster by Fritz Zwicky [Zwicky, 1937]. Surprisingly it was found that the

mass required for the Coma Cluster to remain bound was 400 times greater than the luminous observable matter. Later, in the 1980s, galaxy rotation curves measured by Vera Rubin and Kent Ford provided further evidence for the presence of a dominant dark matter component in galaxies. In the late 20th century the cold dark matter (CDM) paradigm emerged as a solution to the collisionless nature and hierarchical growth of dark matter halos and became established as the theoretical framework to explain the origin of large-scale structure in the Universe [Blumenthal et al., 1984]. Dark matter aside, galaxies themselves generally comprise of bound populations of stars in a rotationally-supported disk (like our Milky Way) or dispersion-dominated elliptical distribution around a central super massive black hole (SMBH). Between the stars is the interstellar medium (ISM) made up of ionized, atomic and molecular gas and dust – grains of carbonaceous and silicate material formed during stellar evolution and in supernovae. The varying distribution of stellar populations (characterised by stellar masses and ages) and their total mass, morphologies, and gas and dust content give rise to a complex 'zoo' of galaxies in the observable Universe. Understanding the processes that gave rise to this zoo is the goal of galaxy formation studies.

The discovery that every massive galaxy contains a SMBH, and that the masses of the stellar bulge and SMBH are correlated [Magorrian et al., 1998, Silk and Rees, 1998] demonstrates that the growth of the central black hole and its host galaxy are inexorably linked. Black hole accretion releases large amounts of feedback energy into the ISM and IGM via collimated jets and fast winds driven from the hot accretion disc, and is thought to be a driving feature in the regulation of stellar mass growth [Bower et al., 2006, Croton et al., 2006]. Active Galactic Nucleus (AGN) feedback is now an established feature of galaxy formation models that aim to correctly reproduce the key observable features of the galaxy population [e.g., Sijacki et al., 2007, Booth and Schaye, 2009, Fabian, 2012, Ishibashi and Fabian, 2012].

We observe a wide range of nuclear activity in galaxies; from low luminosity or quiescent systems such as Sgr A* at the center of the Milky Way, up to powerful radio galaxies and quasars where AGN feedback can completely expel large fractions of the gas reservoir and pump energy into the circumgalactic and intergalactic medium [Gaspari et al., 2011, Dubois et al., 2013, Schaye et al., 2015]. This feedback regulates stellar mass growth by stifling the cooling of interstellar and intracluster gas (which is plentiful as revealed by X-ray observations [see; Fabian, 2012]). Energy input into the surroundings must be sustained for many Gyr to suppress the stellar mass growth of the host galaxy [Dunn and Fabian, 2008] and it is likely that a self-regulating process also affects the growth of the central SMBH, as shown in numerical simulations [e.g.,

Springel et al., 2005] and predicted in galaxy formation theories [Silk and Rees, 1998, Benson, 2010].

From the birth of the first stars during the 'Cosmic Dawn', the volume-averaged star formation rate (SFR) density in the Universe grew rapidly from $z \sim 20$; peaking at $z \approx 2$, marking the epoch when galaxies were assembling the bulk of their stellar mass [Connolly et al., 1997, Madau et al., 1998, Blain et al., 2002, Arnouts et al., 2005, Seymour et al., 2008, Shim et al., 2009]. Half of observed stellar mass in the Universe today was formed prior to $z = 1.4$ [Madau and Dickinson, 2014]. In general, galaxies appear to follow a tight correlation between their SFR and stellar mass [Daddi et al., 2007, Elbaz et al., 2007, Whitaker et al., 2014], forming a so-called 'Main Sequence' of star-forming galaxies. Galaxies forming stars at a rate much higher than the MS for a given stellar mass are said to be 'starbursts'. The normalisation of the MS increases towards the peak epoch of galaxy formation, with the SFRs of all galaxies elevated compared to those of a similar mass today. This is likely driven largely by an increase in the mass of the cold gas reservoirs of galaxies at high redshift [Tacconi et al., 2010] – supporting overall higher levels of star formation. However, in some galaxies in the early Universe, star formation appears to be significantly elevated, with SFRs exceeding 1000 times that of the Milky Way. A key question is whether the fundamental astrophysics governing star formation is the same or different for galaxies in the early Universe compared to today: e.g., changes in gas accretion, AGN feedback processes, gas component relative to mass in high-z galaxies is greater, do earlier galaxies have greater instabilities and does an increase in merger rate effect the star formation processes. However, understanding the astrophysics governing the star formation in a range of galaxies requires detailed studies of individual systems [Tanvir et al., 2012, Schinnerer et al., 2016], where the focus is the properties of the dense ISM from which the stars are forming.

1.2 Basic picture of galaxy formation

Galaxies are distributed across the entire Universe, mostly existing within clusters along filaments which span great distances, acting as cosmological laboratories which continuously challenge our understanding of our cosmological model. Within the first moments of the Universe, random density fluctuations at the quantum level were amplified in phase of inflation, seeding some of the sites of galaxy formation.

After electrons became bound to protons – the epoch of recombination – fluctuations in a relatively smooth distribution of dark matter and baryonic matter resulted in regions of over density, and hence gravitational potential, relative to the background. Dark and baryonic matter accelerated towards potential wells, with the collisionless dark matter eventually forming dark matter 'halos' of different sizes; regions where the particles reach the virial equilibrium. Baryonic matter accreted on the halos was either shock heated to the virial temperature, subsequently cooling onto the proto-galaxy, or streamed in via 'cold flows' [Benson, 2010, e.g.,]

Rotationally supported discs of gas formed due to the presence of large scale angular momentum in the large scale environment of the accreting material. Within these discs, local gravitational collapse of gas clouds that could cool sufficiently formed the first generation of stars. Their subsequent evolution polluted the galaxy and later the intergalactic medium with metals, the presence of which dramatically affected the cooling properties of gas by offering a much wider range of cooling channels than was available in the very early, metal-free Universe.

Energy and momentum return into the interstellar medium from stars, and as a result of the accretion onto a central supermassive black hole, heats and transports the gas in and around galaxies [Heger et al., 2003, e.g.,]. This is now known to have a profound influence of galaxy evolution, since it regulates (and perhaps in some circumstances triggers) star formation [Ostriker and Shetty, 2011, e.g.,]. However, the details of feedback, in particularly how it operates over many scales and gas phases in and around galaxies, is still uncertain.

As galaxies grew and evolved, assembling within a range of environments, from regions of relatively low local density, through groups, filaments and clusters of galaxies that make up the 'cosmic web', they also experienced mergers and interactions with other systems. Violent mergers between gas rich disc galaxies trigger bursts of new star formation, and also morphologically transform galaxies - for example by dispersing stellar orbits onto random radial paths and consuming gas, such that two spiral discs can merge and coalesce into a 'passive' elliptical galaxy.

The complex interplay of gravitational collapse, feedback and environmental processing has, over nearly 14 billion years of cosmic history, shaped the galaxy population into a diverse 'zoo'. Disentangling those processes, and assessing their contributing influences in producing that zoo is the goal of galaxy evolution studies.

1.3 The Diffuse and Dense Interstellar Medium

Cool dust (T$<$ 30 K) emits between $30-50\%$ of the total galactic luminosity infrared continuum ($3-1000\mu m$) [Bernstein et al., 2002]. Though first reported to exist in the ISM in 1930 by Trumpler, 1930 dust was initially considered to be a nuisance for the studies of stars, as it absorbs and scatters their ultraviolet and visible light. However the ultraviolet (UV) light (largely coming from from young O/B stars) is reprocessed by intervening dust: dust grains heat up and re-emit the radiation in the infrared. For galaxies that are actively forming stars, but contain a large amount of dust (or at least have star-forming regions blanketed by dust), the total amount of star formation activity will be missed through UV/optical surveys alone [Casey et al., 2014]. Indeed, a large fraction of the extragalactic background light (EBL) is the Cosmic Infrared Background (CIB), representing the integrated emission of dust-observed star formation in the Universe, indicating that one of every two photons produced through star formation has been re-processed by dust [Dwek and Krennrich, 2013].

Resolving the CIB is, of course, important to understand the galaxies that contribute to the CIB, but this is no easy challenge as the majority of these galaxies are highly obscured (therefore, faint or undetected in the optical) and fall below the confusion limit of current sub-mm survey facilities. At wavelengths longer than $250\mu m$ only $\sim$15% of the background has been resolved [Coppin et al., 2006, Clements et al., 2010]. At $450\mu m$ and $850\mu m$ this is higher at $\sim$60% [Chen et al., 2013], determined through direct detection and stacking studies. Despite much progress in recent years, we still require more detailed observations of single dust-obscured galaxies to understand the properties of these systems that contribute a large fraction of the stellar mass in the Universe today.

In individual galaxies, the integrated spectral energy distribution (SED) of interstellar dust thermally heated in the stellar radiation field is close to a blackbody, since the dust grains generally reach thermal equilibrium with the radiation field [Dwek, 2005]. The peak of the SED is determined by the dust temperature, which is typically a few 10s of Kelvin and thus peaks in the rest-frame far-IR at a few 100μm. The exact shape of the SED is determined by the dust composition, density, and the intensity of the interstellar radiation field (ISRF). Stochastic heating of small dust grains (of radius, a$\lessapprox 200\mu m$) by the ISRF or an active galactic nuclei (AGN) give rise to a warm/hot dust component at wavelength $\lambda \leq 50\,\mu m$. Large grains radiatively heated by young O/B stars to characteristic temperatures of 30–50 K are those which dominate the $\lambda \geq 50\mu$m component of the SED. Thus, we can fit the shape of a dusty star forming galaxay

(DSFG) with a simple model described by few parameters: α the power law slope, β the dust emissivity index and T_d, the average dust temperature [Casey et al., 2014].

The cycle of matter through the ISM [Compiégne, 2010] (see Figure 1.1) is fundamental to the evolution of galaxies [Riechers et al., 2016] and dust plays a vital role in this. Dust grains are dispersed into the ISM via: supernovae explosions (SNe), Wolf-Rayet and Asymptotic Giant Branch (AGB) stars, and a complex chemistry underlies dust physics and indeed the overall chemical evolution of the ISM: species dependent (C, Si) destruction processes occur, ice mantles of H_2O will form on dust grains and vaporise through photodesorption; SNe shocks can sputter dust, lifting atoms off of grain surfaces; and dust can catalyse the formation of molecular hydrogen [Jones, 2004], most of which is contained within giant molecular clouds (GMCs). In local GMCs we can indirectly trace the H_2 through the abundant carbon monoxide (CO) rotational emission lines [Burton et al., 1990, Kaufman et al., 1999, Bolatto et al., 2013, Carilli and Walter, 2013]. This has been the 'workhorse' observable for measuring the abundance of cold, dense molecular gas in local and distant galaxies, although it is not without disadvantages as it is not necessarily the best tracer of the very dense fuel in the actively star-forming regions of starburst galaxies [Papadopoulos, 2007, Bisbas et al., 2015]. So-called 'heavy-rotor' molecules like HCN, might be better tracers for these environments [Gao and Solomon, 2004, Gao et al., 2007].

Whether studying the thermal dust continuum emission, or the key emission lines originating from the cold/cool diffuse/dense ISM, it is the submillimetre (submm) and millimetre (mm) windows that provide the most insight for galaxies at the peak epoch of galaxy formation, as the rest-frame far-IR and submm emission is redshifted further into the submm and mm windows.

1.4 Submillimetre Galaxies

The Infrared Astronomical Satellite [IRAS; Neugebauer et al., 1984] launched in 1983 was the first dedicated IR space observatory. Operating at wavelengths of 12, 25, 60 and 100μm IRAS catalogued $\sim$350,000 luminous infrared sources (IRAS bright galaxy sample [BGS; Soifer et al., 1989]); revealing for the first time that the combined infrared luminosity density of the Universe (30% between $\lambda = 8 - 1000\mu$m) is comparable to that of the total luminosity density in the optical [e.g.; Soifer et al., 1991, Puget et al., 1996, Fixsen et al., 1998]. One of IRAS's major achievements was the discovery of galaxies with infrared luminosities of order $10^{12} < L_{IR} <$

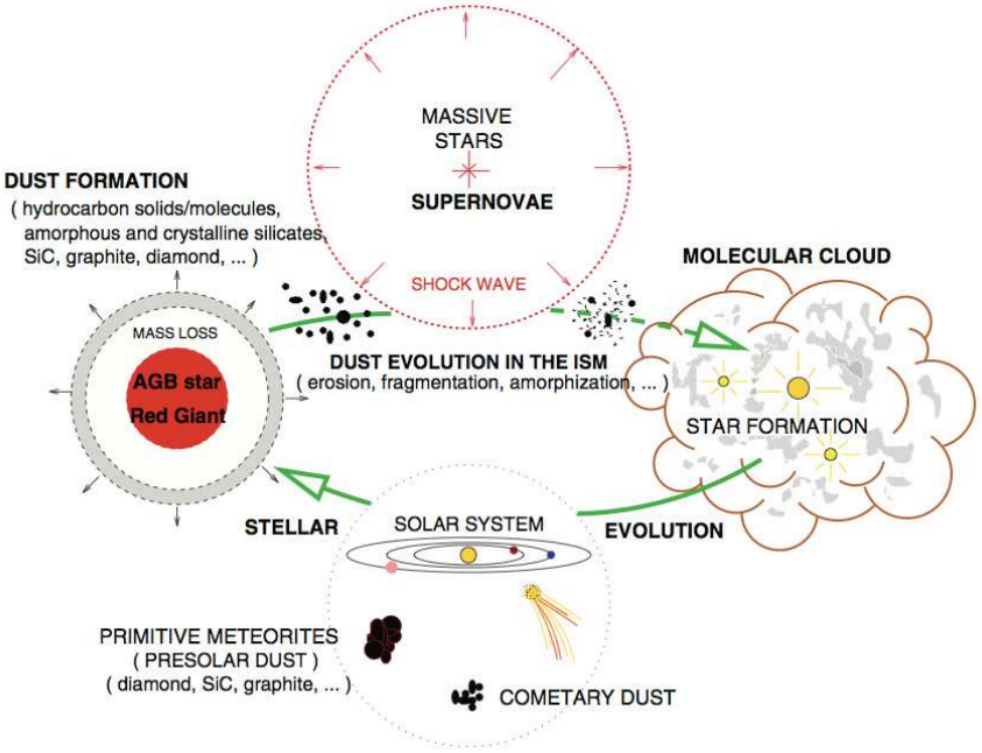

Figure 1.1 The cartoon describes the cycle of interstellar dust from molecular clouds condensing into stars, evolving into complex systems of gas and rocky bodies, the eventual destruction and birth of dust through supernovae, supernovae shocks and mass loss shell ejection during a stars lifetime. Figure obtained from [Jones, 2004]

$10^{13}L_{\odot}$, termed 'ultra luminous' infrared galaxies [ULIRGs; Soifer et al., 1984, 1987, Sanders and Mirabel, 1996].

Studies of the morphological structure of these rare objects [0.1% of local galaxies; Blain et al., 2002] indicated that ULIRGs in the local Universe are exclusively the result of major mergers [Moorwood, 1996], a process that can drive intense, efficient star formation with rates of hundreds of times that of the Milky Way [Lonsdale et al., 1984, Sanders et al., 1988, Sanders and Mirabel, 1996, Genzel et al., 1998]. ULIRGs are the power-houses of star formation in the local Universe, dominating other galactic types by orders of magnitude [$\approx 50 M_{\odot} yr^{-1}$; Wang and Heckman, 1996, Martin et al., 2005, Bothwell et al., 2011, Casey et al., 2014,]. Local ULIRGs are thought to represent a stage of a larger evolutionary process whereby gas-rich disks collide and ignite star-formation once again from the rapid compression and cooling of gas, eventually forming passively evolving spheroids [Sanders et al., 1988, Bolatto et al., 2013, Casey et al., 2014].

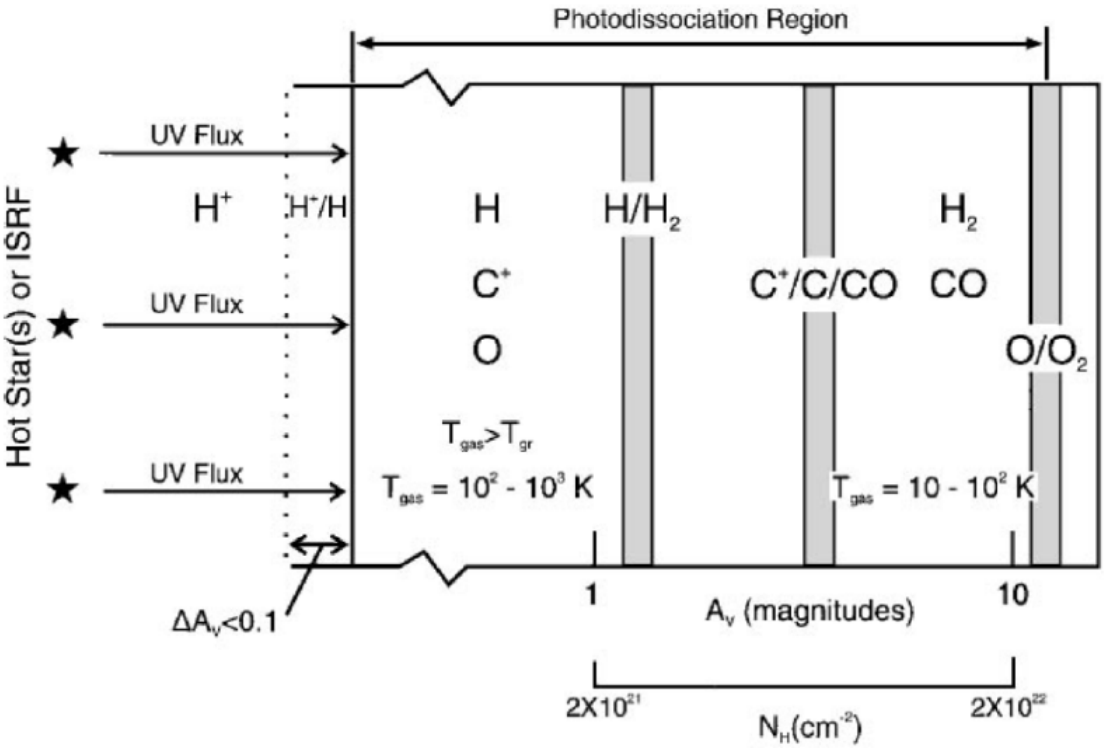

Figure 1.2 A basic cartoon of a classic PDR from [Hollenbach and Tielens, 1997]. Birthing stars heats H which absorbs a large proportion of the radiation energy. A layer of C is present which has a lower energy transition so excites due to the star UV emissions which, as C is abundant, acts as a tracer to the layer of molecular Hydrogen.

In the post-IRAS era, our eyes have now been opened to the obscured and active galaxy population of the early Universe. The Submillimeter Common User Bolometer Array [SCUBA; Holland et al., 1999] was mounted on the James Clerk Maxwell Telescope (JCMT), a 15 m diameter single dish telescope atop Mauna Kea, Hawaii; operating in submillimetre wavebands. SCUBA operated from 1997 to 2005 with a 91 pixel array for $450\mu m$ and a 37 pixel array for $850\mu m$ observations coupled with a 2.3 arcmin field of view (FOV). SCUBA was designed primarily for the detection of the thermal dust emission signature of the ISM (T$\approx 3-30$ K) and to measure synchrotron emission from AGN [SCUBA; Holland et al., 1999]. One of SCUBA's main achievements was the detection of a population of high redshift star forming 'submillimetre galaxies' (SMGs) [Smail et al., 1997, Hughes and Dunlop, 1998, Hughes et al., 1998, Barger et al., 1998, Swinbank et al., 2004]. With a characteristic redshift of $z \approx 2$ (corresponding to peak cosmic SFRD), SMGs have ULIRG-levels of total infrared luminosity [Chapman et al., 2005, Simpson et al., 2014, Narayanan et al., 2015], with the bulk of their output emerging in the dust-reprocessed UV/optical light of young stars (see Burigana et al., 1997, Blain et al., 1999, Chapman et al., 2005, Coppin et al., 2006, Aretxaga et al., 2007, Ivison et al., 2007, Dye et al., 2008). As such, their SEDs are characterised by a modified blackbody as described above.

The Rayleigh-Jeans tail of the SED gives rise to a strong negative K-correction [Barger et al., 1998, Blain et al., 1999], such that cosmological dimming is cancelled out by the fact that the fixed observed band pass will 'climb up' the redshifted tail of thermal dust emission [Blain et al., 2002]. This is extraordinarily useful, because the negative K-correction keeps flux densities constant over a redshift range for a given luminosity $z \approx 1 - 10$ (see, Figure 1.4). Observations of SMGs are important probes of star formation in the high redshift Universe since these systems may well be the progenitors of the most massive passive galaxies seen at low redshift [Stevens et al., 2003, Daddi et al., 2007, Cimatti et al., 2008, Daddi et al., 2009a].

In 2005 SCUBA was decommissioned and later replaced by an upgraded version, SCUBA-2. SCUBA-2 is currently at the forefront of single dish submillimeter observations of the high redshift Universe, capable of both wide field mapping and imaging compact sources with an efficiency 100–150 times that of SCUBA; again, simultaneously detecting 450 and 850μm photons with two bolometer arrays [Holland et al., 2013]. Detection of submm light is achieved by exploiting the temperature-dependent nature of a superconducting molybdenum/copper bilayer in transition edge sensors measuring resistance change from an incident photon [Irwin, 1995, TES]. Interferometry with its small field of view has limitations to searching wide-fields for SMGs, SCUBA-2 with its large field of view has been performing new surveys of the SMG population. The SCUBA Half-Degree Extragalactic Survey [Coppin et al., 2006, SHADES] covered 720 arcmin^2 finding > 100 sources of flux density < 22 mJy at redshift $< z >= 2.8$ [Ivison et al., 2007, Aretxaga et al., 2007] other surveys cover a wide-field, SCUBA-2 Cosmology Legacy Survey [Dye et al., 2008, Geach et al., 2013, Koprowski et al., 2016, Geach et al., 2017, S2CLS], The LABOCA ECDFS Submm Survey [Greve et al., 2010, LESS] have revealed huge populations of SMGs which importantly have a large contribution to the EBL and therefore important cosmological probes. However, due to the confusion limit of SCUBA-2 at < 2 mJy, fainter SMGs are harder to detect and therefore follow-up and the direct observations of SMGs cannot reveal information about their substructure which means that the properties of un-lensed SMGs are inferred from ULIRGs. However, by exploiting the gravitational lensing [Schneider, Ehlers & Falco 1992, Smail et al. 1997] effect of clusters (which contribute little to the submm continuum due to ellipitcals dominating their members), the magnification of background galaxies allows detailed, resolved studies of SMGs that would otherwise be impossible [Ivison et al., 1998, Valtchanov et al., 2011, Combes et al., 2012, Decarli et al., 2012, Omont et al., 2013]. However, if the lens models is not sufficient (requiring very high-res observations). Without this, it is very difficult to interpret the observations due to the distortion, possible differential

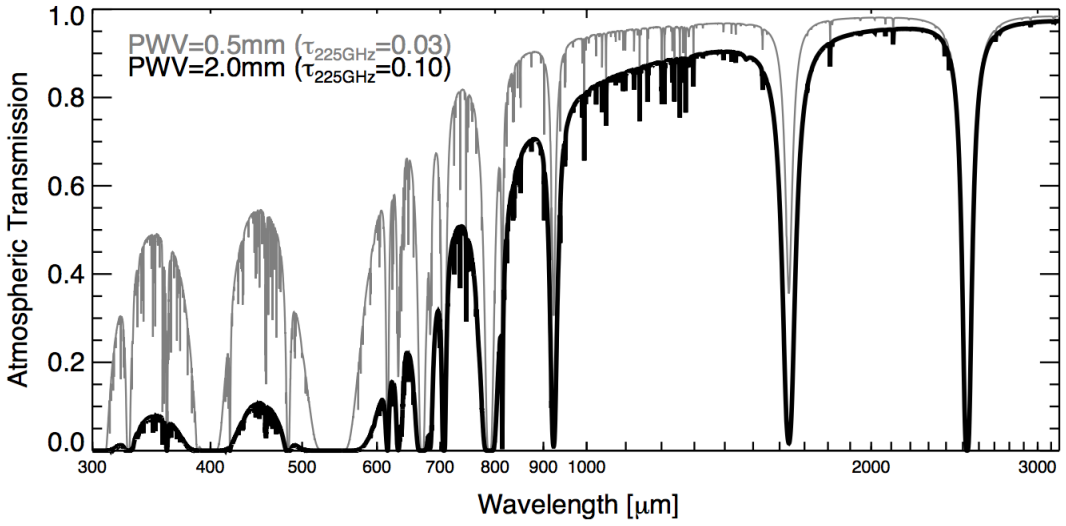

Figure 1.3 An example of the atmospheric transmission windows achievable up-top Mauna Kea. The Dark line represents a precipitable water vapour (PWV) of 2.0mm and the faint line, 0.5mm. The majority of attenuation caused by the atmosphere is clearly shown at shorter wavelengths $\approx \lambda < 1000\mu m$ and has a noticeable effect for the, $850\mu m$ and $450\mu m$ bands. Figure obtained from [Casey et al., 2014].

magnification, etc. Furthermore, lenses are intrinsically rare, and you will always be biased towards the brighter systems, so there is the worry that although you may get an exquisite view, it is a biased representation of the wider population. One of the most famous examples is the 'Cosmic Eyelash' at $z = 2.3$ [Swinbank et al., 2010]. It is a highly lensed SMG with a magnification of 32 times, boosting the 870μm flux density to over 100 mJy (compared to typical unlensed SMGs which have flux densities below 10 mJy. The Eyelash has provided a treasure trove of information, including insights into the properties of the cold and dense ISM [see; Danielson et al., 2011, 2013], probing star-forming cloud complexes [Thomson et al., 2015] and molecular outflows [George et al., 2014].

.

1.5 Thesis Motivation and Outline

The Cosmic Eyelash was first identified with the LABOCA $870\mu m$ camera [Swinbank et al., 2010] when observing the cluster MACS J2135-010217 ($z = 0.325$). Lensed galaxies like the Eyelash are scarce due to the requirement of alignment between an SMG (or generally DSFG)

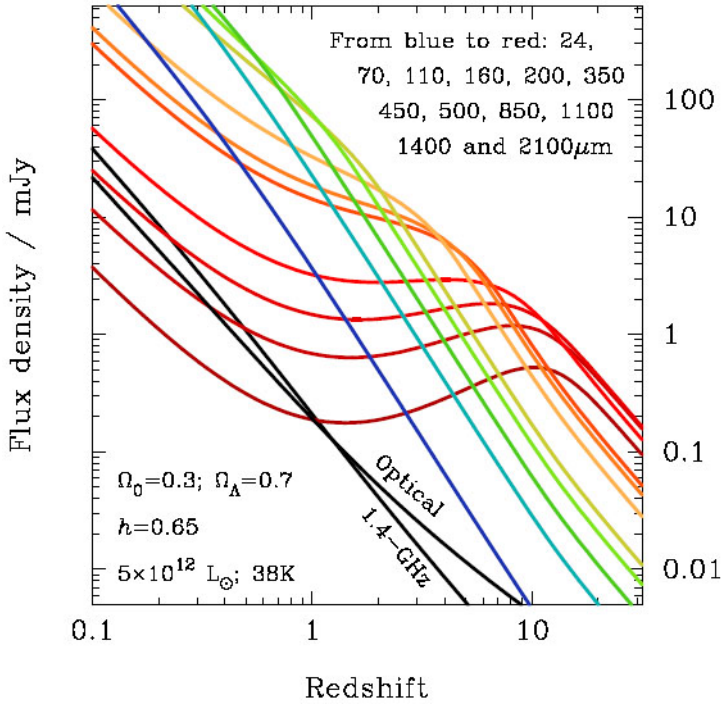

Figure 1.4 The flux density as function of the wavelengths for a broad range of redshifts is shown. Optical and radio are quickly diminished when observing out to higher redshifts. The colored lined are based off the SED from [Blain et al., 1999] and clearly show at longer emission wavelengths there is not a drop in the observable flux density of these rest-frame bands. Figure obtained from [Blain et al., 2002].

and foreground deflector. Clusters themselves are rare cosmic objects. But the wealth of information that can be gleaned from objects like the Cosmic Eyelash has sparked the hunt for more comparable systems; i.e., those who have amplified 850 μm flux densities exceeding 100mJy. By providing access to spatial scales not available in the unlensed case, and amplifying fainter exotic molecular and atomic tracers of the dense ISM, it is possible to study the astrophysics of star formation in systems close to the peak epoch of galaxy formation at a level rivalling resolved studies of star formation in local galaxies.

The key motivation for this project is to conduct a systematic survey for more examples of 'Eyelash'-like targets through a submm survey of rich clusters of galaxies. In Chapter 2 we present the SCUBA-2 Cluster Snapshot Survey, designed to identify a larger sample of Eyelash-like SMGs for detailed follow-up. Having a large number of submm maps of the cores of rich clusters is not just useful for the detection of lensed galaxies. The data can be used for further analysis of the properties of the clusters themselves. Powerful AGN in central ellipticals play a pivitol role in regulating star formation in the most massive galaxies: submm observations can reveal insights into the nature of radio-loud AGN and also potentially detect hidden star

formation. The submm properties of Brightest Cluster Galaxies (BCGs) are presented in Chapter 3.

In Chapter 4 we report the serendipitous detection of a strong submm/mm excess in the relatively flat, variable core radio source associated with the BCG of Abell 851. The radio power and amplitude of variability observed in this galaxy is consistent with the cores in lower redshift BCGs in X-ray–selected clusters, and the flat mm–cm spectrum is suggestive of the BCG being a low luminosity AGN archetype. The discovery of this system could provide a basis for a long-term study of the role of low luminosity radio mode regulatory feedback in massive clusters.

Chapter 5 lays out the conclusions of each of the chapters and, finally Chapter 6 details future work as a result of the thesis; a follow-up to the the Scuba-2 Cluster Snapshot Survey aiming to confirm a number of potentially lensed systems which did not meet the original selection but may well yield a positive identification by obtaining, and analysing, deeper observations.

Throughout, a ΛCDM cosmology is assumed with $H_0 = 67.3\,\mathrm{km\ s^{-1}\,Mpc^{-1}}$, $\Omega_\mathrm{M} = 0.315$, and $\Omega_\Lambda = 0.685$ Planck Collaboration et al., 2014.

Chapter 2

SCUBA-2 Cluster Snapshot Survey: A population of lensed Galaxies

2.1 Introduction

Twenty years ago 'SubMillimeter Galaxies' (SMGs) were discovered [Smail et al., 1997, Hughes et al., 1998, Barger et al., 1998] with the Submillimetre Common User Bolometer Array [SCUBA; Gear and Cunningham, 1990, Holland et al., 1999]. Optically faint [Hughes et al., 1998, Smail et al., 1999] SMGs lie out at $z \approx 1-4$ [see; Chapman et al., 2005, Coppin et al., 2006, Aretxaga et al., 2007, Ivison et al., 2007, Dye et al., 2008, Serjeant et al., 2008, Simpson et al., 2014, Danielson et al., 2017] near the peak in cosmic star formation rate density (SFRD) [Hopkins and Beacom, 2006, Madau and Dickinson, 2014]. SMGs have infrared luminosities and intrinsic properties similar to local Ultra Luminous Infrared Galaxies (ULIRGs) with SMGs having $\mathrm{L} \approx 10^{12}\mathrm{L}_{\odot}$ [Houck et al., 1985, Dey et al., 1999, Chapman et al., 2005], intense star formation rates $10^{2}-10^{3}\mathrm{M}_{\odot}\mathrm{yr}^{-1}$ [Tacconi et al., 2010, Magnelli et al., 2012] and stellar masses of order $10^{10-11}M_{\odot}$ [Hainline et al., 2011] however, the picture of the SMG-ULIRG link is still not fully clear given the size distributions of ULIRGs [e.g., Simpson et al., 2015, Spilker et al., 2016]. SMGs are excellent candidates for being the progenitor population of the massive elliptical galaxies seen today [see; Lilly et al., 1999, Eales et al., 2000, Daddi et al., 2009b, Simpson et al., 2014, Toft et al., 2014] and, serve as a useful tool for probing the interstellar medium (ISM) and the crucial mechanisms at play in the evolution of dusty star-forming galaxies [Valtchanov et al., 2011, Danielson et al., 2011, 2013, Bothwell et al., 2013].

In the $850\mu m$ band, a flux limited survey will return a near constant infrared luminosity selection between redshifts of 1 and 7, owing to the well known negative *k*-correction; where cosmological dimming is cancelled out by the fact that a fixed observed bandpass will climb up the redshifted Rayleigh-Jeans tail of thermal dust emission [Blain et al., 2002]. Though the redshift distribution is strongly influenced by selection effects as the dust temperature plays a significant role [e.g. Béthermin et al., 2015] but the bias can be quantified by broadening the number of SMGs detected at various redshifts. Negative *k*-correction makes submillimetre observations very efficient at detecting actively growing galaxies across most of cosmic history. However, the bright confusion limit [e.g., Blain and Longair, 1996] (the difficulty in distinguishing individual sources from fluctuations of extragalactic origin which are present in the background of a typical observation) of ground-based submillimetre surveys typically limits SMG surveys to a few mJy [e.g., Karim et al., 2013]. At these limits, detailed follow-up work with submillimetre/millimetre-band interferometry is challenging, but with instruments like the Atacama Large Millimeter/Submillimeter Array (ALMA) targeting bright sources high-resolution data can be obtained but, this requires targets. Indeed, the ALMA era has already discovered spectacular examples of high-redshift SMGs out to redshift 7, e.g., SPT0311-58 [Marrone et al., 2018], A1697-zD1 [Knudsen et al., 2017].

Gravitational lensing [Schneider et al., 1992] allows one to overcome the low flux limit by boosting the intrinsic flux density of distant galaxies that are fortuitously aligned with foreground masses such as other galaxies or clusters [Smail et al., 1997]. The observation of galaxies via a gravitational lens will increase the spatial resolution and as lensing is a achromatic process and nor does it trigger any known absorption/emission processes, surface brightness is conserved. As galaxies will not be perfectly aligned the lensing effect will magnify sources regions to different degrees, and therefore their line ratios, differently. This differential lensing bias should be aimed to be minimised to disentangle lensed features back with in increased reliability. By preferentially selecting cluster-galaxy systems as target lenses we can minimise the differential lensing bias [Serjeant, 2012]. The magnification of background galaxies allows for detailed studies that would otherwise be impossible; yielding new insights into the properties of early galaxies [Ivison et al., 1998, 2010, Valtchanov et al., 2011, Combes et al., 2012, Decarli et al., 2012, Omont et al., 2013]. Arguably, the most famous example of an extremely lensed galaxy is the 'Cosmic Eyelash' [Swinbank et al., 2010, $z = 2.3259$, $S_{870} \approx 100\,\mathrm{mJy}$], a highly lensed SMG with a magnification of $32\times$, boosting the 870μm flux density to 103 mJy. The Eyelash has provided a treasure trove of information, including insight into the properties of the cold

and dense interstellar medium [see; Danielson et al., 2011, 2013, George et al., 2014], probing 100 pc giant molecular cloud complexes [Thomson et al., 2015], molecular outflows [George et al., 2014] and evidence arguing against the SMG-ULIRG scaling [Ivison et al., 2010].

Galaxies like the Eyelash are exceptionally rare. Gathering a larger sample of similarly bright lensed SMGs would be of immense value as target sources for detailed follow-up observations, especially with powerful interferometric facilities such as NOEMA and ALMA. This motivates the SCUBA-2 Cluster Snapshot Survey (S2CSS), described in this work, the survey has been conducted with the SCUBA-2 submillimetre camera mounted on the 15 m James Clerk Maxwell Telescope [Holland et al., 2013].

This paper is organised as follows: In section 2.2 we describe the target selection, observations and data reduction. section 2.3 discusses the process of determining the nature of the sources. section 2.4 discusses the sources detected. Finally, section 2.5 will summarize the results and detail future work.

2.2 Survey strategy, observations and data reduction

Here we describe our survey targets, selection criteria and how we reduced the data.

2.2.1 Target selection

Our targets are rich clusters of galaxies visible by the JCMT. These are the most massive targets that we could choose and we thereby maximize the probability of detecting lensed background sources because the SCUBA-2 FOV (45 arcmin^2) exceeds the Einstein radius ($r_E \approx 20''$) for a typical cluster-lens system (properties of order: $M_{cluster} \approx 10^{14} M_\odot$, $z_{cluster} \approx 0.5$, $z_{source} \approx 2.5$). Specifically, we target clusters with the highest X-ray luminosities ($L_X \geqslant 4 \times 10^{44}$ erg s^{-1}, 0.1-2.4 keV). The clusters were selected from the from the ROSAT All-Sky Survey [Voges et al., 1999, RASS], ROSAT Bright Cluster Survey [Ebeling et al., 1998, BCS], extended-BCS [Ebeling et al., 2000, eBCS], ROSAT-ESO Flux-Limited X-ray [Böhringer et al., 2004, REFLEX] and the Massive Cluster Survey [MACS; Ebeling et al., 2001, 2013] samples, which constitute the most X-ray luminous, and therefore the most massive, clusters in the local universe ($z \approx 0.5$). The majority of the sample have matching *Herschel* SPIRE data from the *Herschel* Lensing

Survey Snapshot-1 sample (HLS; Egami et al. 2010; Egami et al., in preparation). In particular, many of the S2CSS-targeted clusters were observed in the HLS-Snapshot I Survey, which obtained shallow but nearly confusion-limited SPIRE images for 279 X-ray-luminous clusters from the X-ray samples that had not been already been scheduled for *Herschel* in the first two cycles. Of these clusters, 216 are visible from the JCMT observatory atop Mauna Kea ($\delta \geqslant -30^{\circ}$) and 202 were successfully observed in the S2CSS. Of the 72 remaining X-ray-selected clusters, a total of 48 have *Herschel* data from a combination of projects: *Herschel* Lensing Survey Deep-1, LoCUSS and the Cooling Flow Open Time Key Project [Edge et al., 2010, Egami et al., 2010, Smith et al., 2010, Rawle et al., 2012]. An extra nine clusters with lower X-ray luminosity and particularly radio bright central galaxies were also included, the results for these are summarised in Hogan et al. [H15]

2.2.2 Observations and data reduction

Observations were conducted in JCMT weather bands 4 and 5 over the period from August 2012 - July 2013 (formally a scheduling limit of $\tau_{225\mathrm{GHz}} > 0.12$), corresponding to a precipitable water vapor column of over 2.6 mm. The top panel of Figure 2.1 shows the distribution of $\tau_{225\mathrm{GHz}}$for the observations; the average opacity is $\langle \tau_{225\mathrm{GHz}} \rangle = 0.19 \pm 0.08$. A small number of maps were taken in better conditions than requested, but overall a longer tail of higher $\tau_{225\mathrm{GHz}}$values were recorded. We adopted the '`CV_ DAISY`' mapping pattern to maximise the exposure time on cluster centers [Thomas and Currie, 2014], with a beam size of 13–arcsec. The camera is slewed in a Lissajous-like pattern at constant velocity, ensuring the target remained on the SCUBA-2 array throughout the 30 minute observation [e.g.; Geach et al., 2013, G13]. $450\,\mu m$ data were recorded simultaneously, but the conditions were too poor for the data to be scientifically useful in all cases.

Data were reduced using the dynamic iterative map maker (DIMM) of the SubMillimetre User Reduction Facility [`SMURF`; Chapin et al., 2013]. We follow the same data reduction procedure as described in G13, which accounts for flat-fielding, common mode subtraction, extinction correction and aggressive spatial filtering (because we are only interested in point sources). The maps were all match-filtered to maximise the sensitivity to the detection of point sources. We applied a constant flux conversion factor $\mathrm{FCF}_{850} = 556 \pm 65\,\mathrm{Jy\,beam^{-1}\,pW^{-1}}$, with an additional 10% correction to account for flux lost during the filtering process (determined by

[1] http //cso.caltech.edu/tau_data/

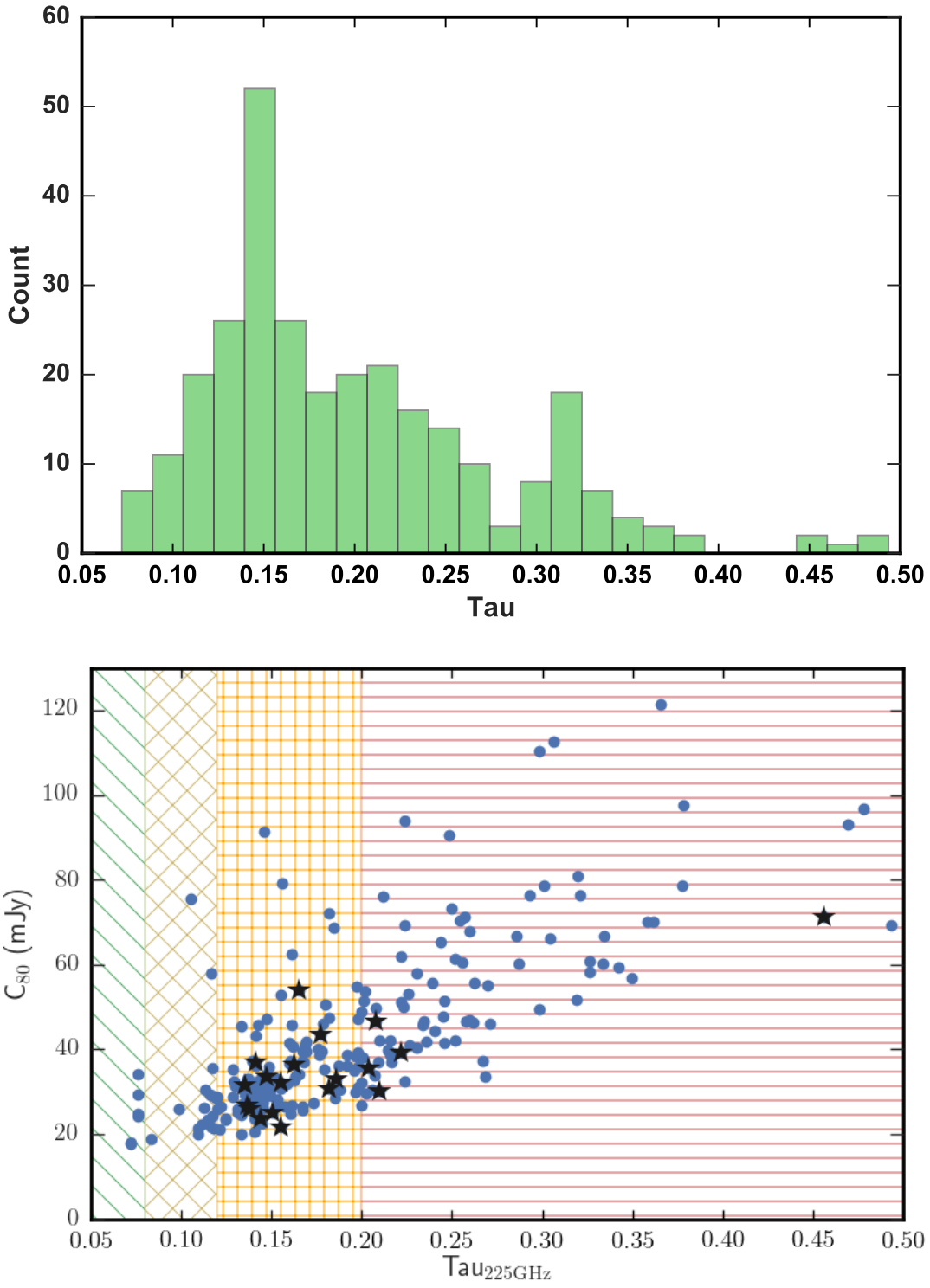

Figure 2.1 Panel 1: The S2CSS $\tau_{225\mathrm{GHz}}$distributions for all observations. The observations were primarily conducted in JCMT band 4 weather conditions ($\tau_{225\mathrm{GHz}}$= 0.19 ± 0.8), corresponding to a 53% extinction[1]. Panel 2: $\tau_{225\mathrm{GHz}}$vs C_{80} of the sample shows a clear relation between the observing weather conditions and the completeness of each map. Black stars indicated SPIRE counter-parted sources, the different hatched regions refer to the JCMT weather bands in increasing ranges of PWV.

inserting a bright Gaussian point source into the time stream of each individual observation to measure the model response to the filtering, as in G13). The total survey area is approximately a third of a square degree with a range of map depths.

2.2.3 $850\mu m$ source detection and selection

To detect point sources we simply used a peak-finding algorithm, with a signal-to-noise (SNR) threshold, on each observation; the local noise is determined from the instrumental noise map produced as part of the reduction process (the depth of the maps is far from confused, so we ignore confusion noise). Following this method we detect 1016 sources with SNR $3.5 \leq \sigma < 4$, 312 with $4 \leq \sigma < 5$ and 39 with $\geq 5\sigma$ across all observations. We opted to use the $351 > 4\sigma$ detections as our initial candidate source list, as the contamination rate from false positives is non-negligible [e.g., Geach et al., 2017, G17]. Completeness simulations provide an independent check of the significance of the detection. We injected multiple point sources into a map and re-ran the detection algorithm to re-extract our fake sources. By repeating this numerous times over a number of flux intervals initiated at 100 mJy, we built completeness statistics for each map. We refer to the 80% completeness for each map using the descriptor 'C_{80}' as a proxy for a 5σ detection, as discussed, as a map dependent measurement takes into account the error properties unique to each map and indicates its depth; that is, a low C_{80} corresponds to a deeper and therefore more sensitive map. The bottom panel in Figure 2.1 compares the calculated C_{80} value for each observation with the atmospheric opacity ($\tau_{225\mathrm{GHz}}$) and provides an indicator of map sensitivity averaged over the full area covered. Sources with significant SPIRE counterparts are denoted as black stars, with all except one observed in reasonable conditions. The top panel of Figure 2.2 shows the distribution of the S_{850} vs C_{80} for all our detected peaks (we do also show sources of $> 3.5\sigma$ to illustrate the sheer number of low σ detections compared with the 351 sources $> 4\sigma$); the black stars represent sources having bright ($> 3\sigma$) SPIRE counterparts. It is clear that sources detected with a low S_{850} flux density correspond to maps with a low C_{80} value for sources detected at $> 3.5\sigma$.

We compared the median depth of all maps to the median 80% completeness confirming that a 5σ limit corresponds to approximately the C_{80} value [e.g.; Saha, 1995] in each map, allowing us to slightly tailor our selection criteria by jointly using the 1σ instrumental noise and the completeness curve. We opted for this method over simply using the 5σ map depth because the majority of the data were taken in poor JCMT weather bands and a map dependent descriptor of the sensitivity is a better measure than using a sweeping 5σ limit. We also found the noise in each map sharply increases at larger radii when taking annular rings from the centre. Given the noise profile of the SCUBA-2 maps we applied an additional radial component to our selection to take this into account. For selection, we employ a hand-crafted selection criterion for the S2CSS

catalog that uses SCUBA-2 photometry, the radius (R) from map pointing center (usually the position of the BCG), and the ratio of the detection flux to the C_{80} value, S_{850}/C_{80}, for each observation. By combining all the factors discussed we insist the nature of a selected source exceeds:

$$\frac{S_{850}}{C_{80}} \geq 0.6 + 0.05R^2, \tag{2.1}$$

which is illustrated in the middle panel of Figure 2.2, as a solid black line. We used a hard radial cut-off at 3.5 arcmin from the pointing center, which covers the deepest region of the SCUBA-2 `DAISY` mapping pattern. With our layout we determined 106 lens candidates across the survey with a mean flux density of $\langle S_{850} \rangle = 43$mJy. They are listed in Table A.1. The expected surface density of sources of similar flux density in blank fields is $N(S_{850\,\mu m} > 15\,\mathrm{mJy})(\mathrm{deg}^{-2}) \approx 2$ (see, G17) whereas this work finds $N(S_{850\,\mu m} > 15\,\mathrm{mJy})(\mathrm{deg}^{-2}) \approx 300$. Hence, by biasing observations towards massive clusters we have successfully detected sources well beyond the limitations of a blank-field survey. Sources with a formal $\geq 5\sigma$ detection at the pointing center will of course be preferentially detected: these are cases where the submillimetre emission originates from the BCG itself, or a strongly lensed background source along the same line of sight.

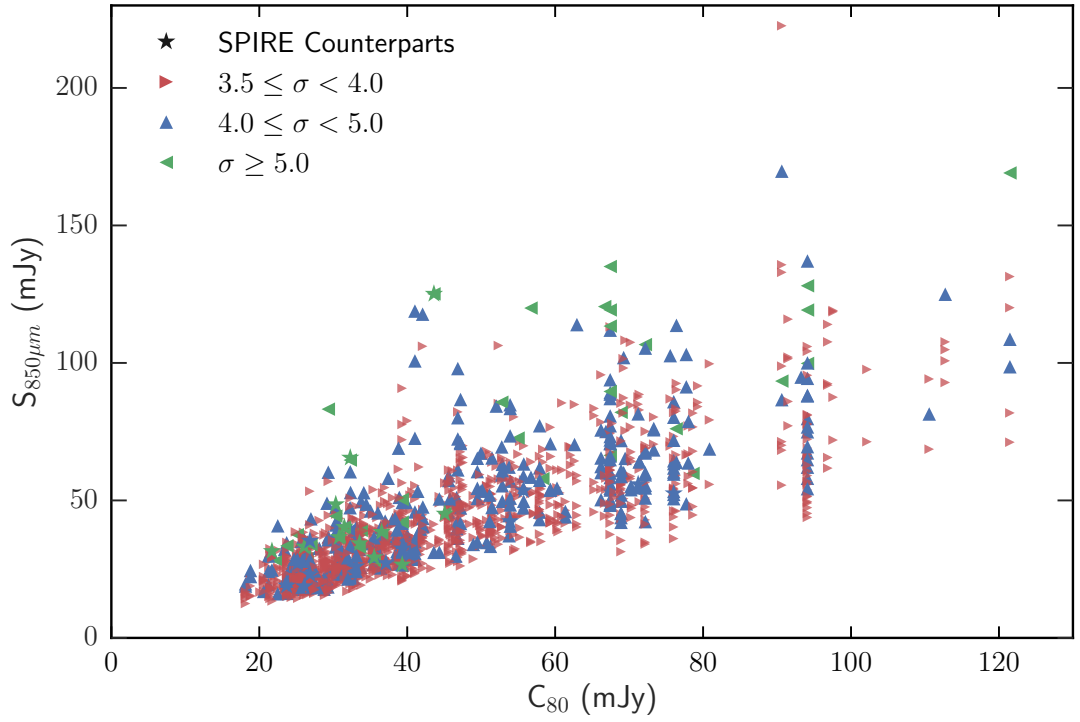
SPIRE Counterparts
$3.5 \leq \sigma < 4.0$
$4.0 \leq \sigma < 5.0$
$\sigma \geq 5.0$
$S_{850\mu m}$ (mJy)
C_{80} (mJy)
0
50
100
150
200
0
20
40
60
80
100
120

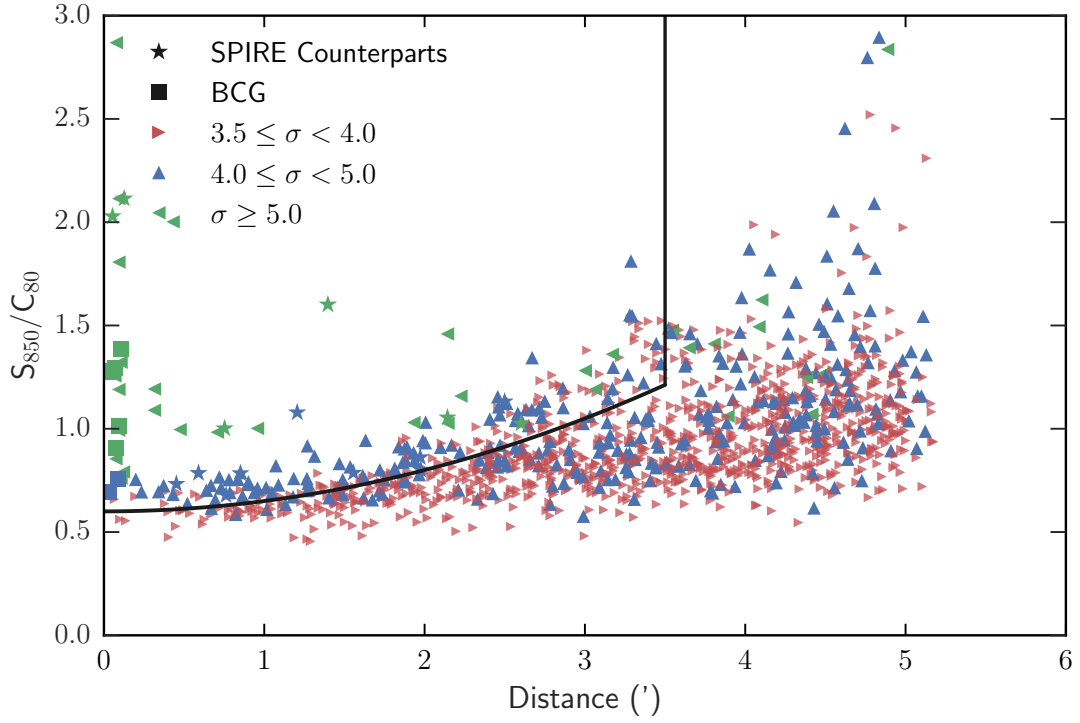
SPIRE Counterparts
BCG
$3.5 \leq \sigma < 4.0$
$4.0 \leq \sigma < 5.0$
$\sigma \geq 5.0$
S_{850}/C_{80}
Distance (')
0.0
0.5
1.0
1.5
2.0
2.5
3.0
0
1
2
3
4
5
6

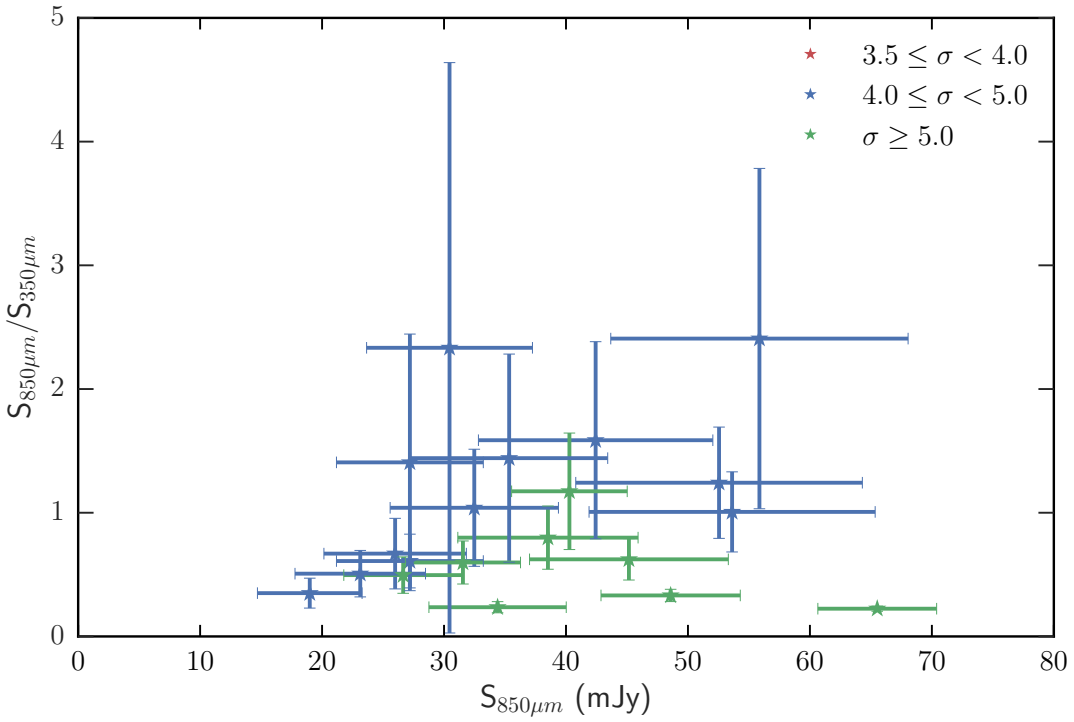

Figure 2.2 Top Panel: The peak flux density of the detection against the 80% completeness of the map, it is evident a large number of sources correlate with a low flux density and a corresponding low C_{80}. The seemingly vertical columns are a result of a single map showing considerable number of detections. The SPIRE counterparts are stars which are colour coded respective to σ. Middle Panel: The ratio S850/C80 is plotted as a function of radial distance from the SCUBA-2 field centre. The ratio of S850/C80 is related to the Signal-to-noise ratio, and provides a clear metric for false positives in our sample and we truncate our search at 3.5' to cover the deepest region of the SCUBA-2 `DAISY` mapping pattern. The SPIRE counterparts are stars and the BCG squares which are both colour coded respective to σ. Bottom Panel: We show high confidence sample of our cross matched HLS sources as $850\,\mu m/350\,\mu m$ to $850\,\mu m$ colour-magnitude plot.

2.2.4 *Herschel* Lensing Survey Data Products

The *Herschel* Lensing Survey (HLS) consists of two types of surveys: HLS-Deep, which conducted deep PACS (100/160 μm) and SPIRE (250/350/500 μm) imaging for 54 clusters, and the HLS-Snapshot, which carried out shallower SPIRE-only imaging for 527 clusters (E. Egami et al. in preparation). Many of the S2CSS target clusters were selected from the latter sample, whose SPIRE images are nearly confusion-limited despite their short integration times. For all clusters, images were produced via the standard reduction pipeline in HIPE [Ott, 2010] v12 (v12.2 calibration product), with median baseline removal and using the destriper. All the observations target the nominal cluster center and have a beam size of 18, 25, 36 arcsec respectively. The S2CSS and HLS complement one another, and in cases where there are joint SCUBA-2/SPIRE detections the data sets provide greater confidence in the nature of detections and allow us to roughly estimate redshifts through FIR colours: a 850 μm/350 μm to 850 μm colour-magnitude plot in the bottom panel of Figure 2.2.

2.3 Analysis

In the following, we examine the 108 sources to determine whether they are lensed background sources, or cases where strong submillimetre emission originates from the BCG. We find that eight are co-located with the BCG, 78 $>$ 0.1-arcmin SCUBA-2 only detections, 19 are joint SCUBA-2 and SPIRE sources, and three that were targeted in order to follow up a known SPIRE source.

2.3.1 Nature of the SCUBA-2 submillimetre sources

From the pool of 108 SCUBA-2 sources that fit the criteria described above, we found that 78 (non-starred in Table A.1) have no significant ($< 3\sigma$) SPIRE counterpart or are $< 0.1'$ from the cluster BCG, 19 have SPIRE counterparts, and three were targeted in order to follow up known SPIRE sources (See Appendix D). The cluster BCG was taken as the brightest cluster galaxy member nearest the X-ray peak [see; Sanderson et al., 2009]. In Appendix C we show the S2CSS detections overlaid as contours onto Pan-STARRS *i*-band optical imaging [see; Flewelling et al., 2016] to show the location of the submillimetre source relative to the cluster centers/BCGs.

Table 2.1. Brightest Cluster Galaxy sources with SCUBA-2 and GISMO, CARMA and AMI data from Hogan et al. [H15]. Observations closest in time to SCUBA-2 snapshots quoted. Column 1: ID; Column 2: Cluster Name; Column 3: SCUBA-2 850 μm Peak Flux; Column 4: GISMO 150GHz Peak Flux; Column 5: CARMA 90GHz Peak Flux; Column 6: AMI 16GHz Peak Flux.

ID	Cluster	$S_{850\,\mu m}$ (mJy)	S_{150GHz} (mJy)	S_{90GHz} (mJy)	S_{16GHz} (mJy)
MACSJ0242.5−2132	MACS0242-21	34 ± 8	35.6 ± 6.0	–	–
MACSJ0834.9+5534	4C+55.16	29 ± 7	81.7 ± 13.2	–	1317.7 ± 66.0
MACSJ0918.0−1205	Hydra-A	76 ± 9	273.8 ± 43.8	–	–
MACSJ1407.5−2701	A3581	59 ± 9	62.1 ± 10.1	82.5 ± 9.1	–
MACSJ1558.3−1410	RXJ1558-14	40 ± 4	39.2 ± 6.4	44.8 ± 4.9	–
MACSJ1727.3+5510−B	A2270	34 ± 4	70.8 ± 4.1	164.7 ± 17.2	226.9 ± 11.6
MACSJ1744.2+3359	Z8276	37 ± 5	12.5 ± 2.7	35.4 ± 6.0	87.6 ± 4.6
MACSJ2341.1+0018−A	RXJ2341+00	33 ± 3	41.8 ± 6.9	72.8 ± 8.0	209.2 ± 11.8

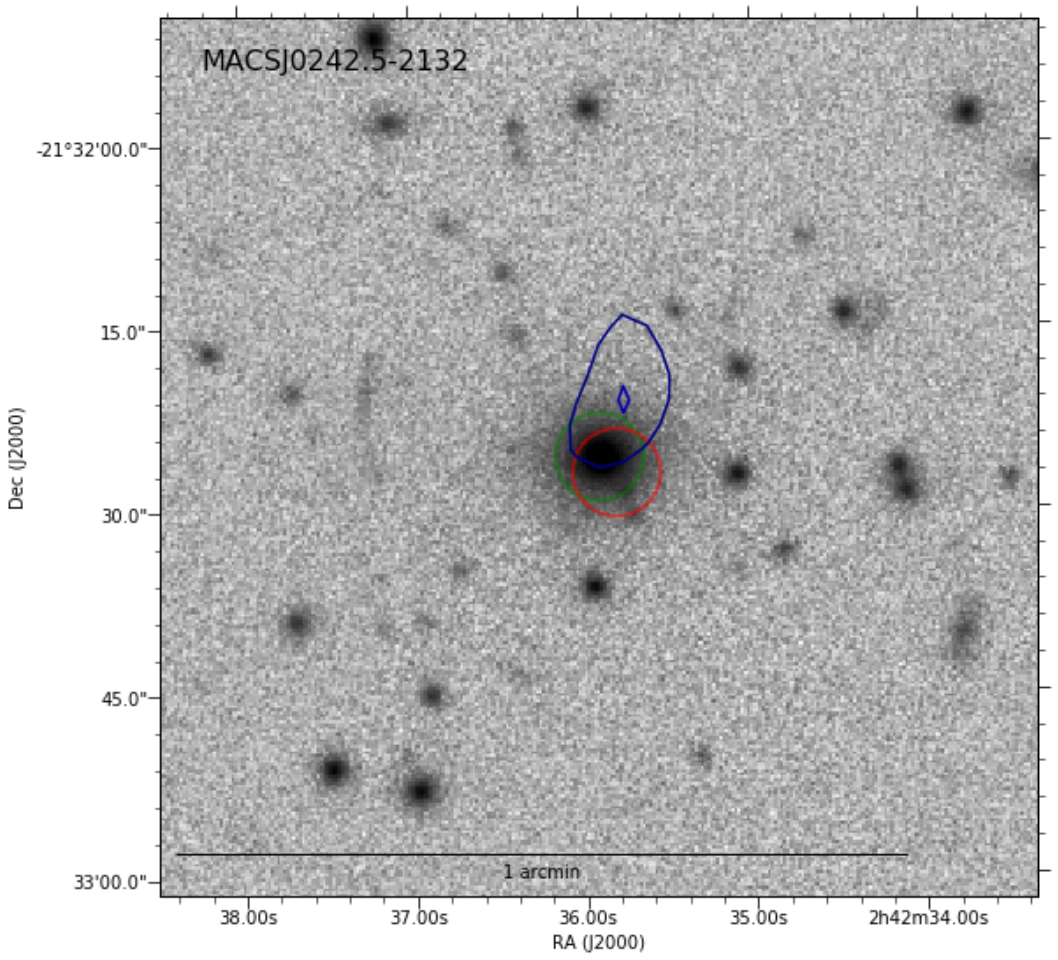
MACSJ0242.5-2132
-21°32'00.0"
15.0"
30.0"
45.0"
33'00.0"
Dec (J2000)
1 arcmin
38.00s
37.00s
36.00s
35.00s
2h42m34.00s
RA (J2000)

Figure 2.3

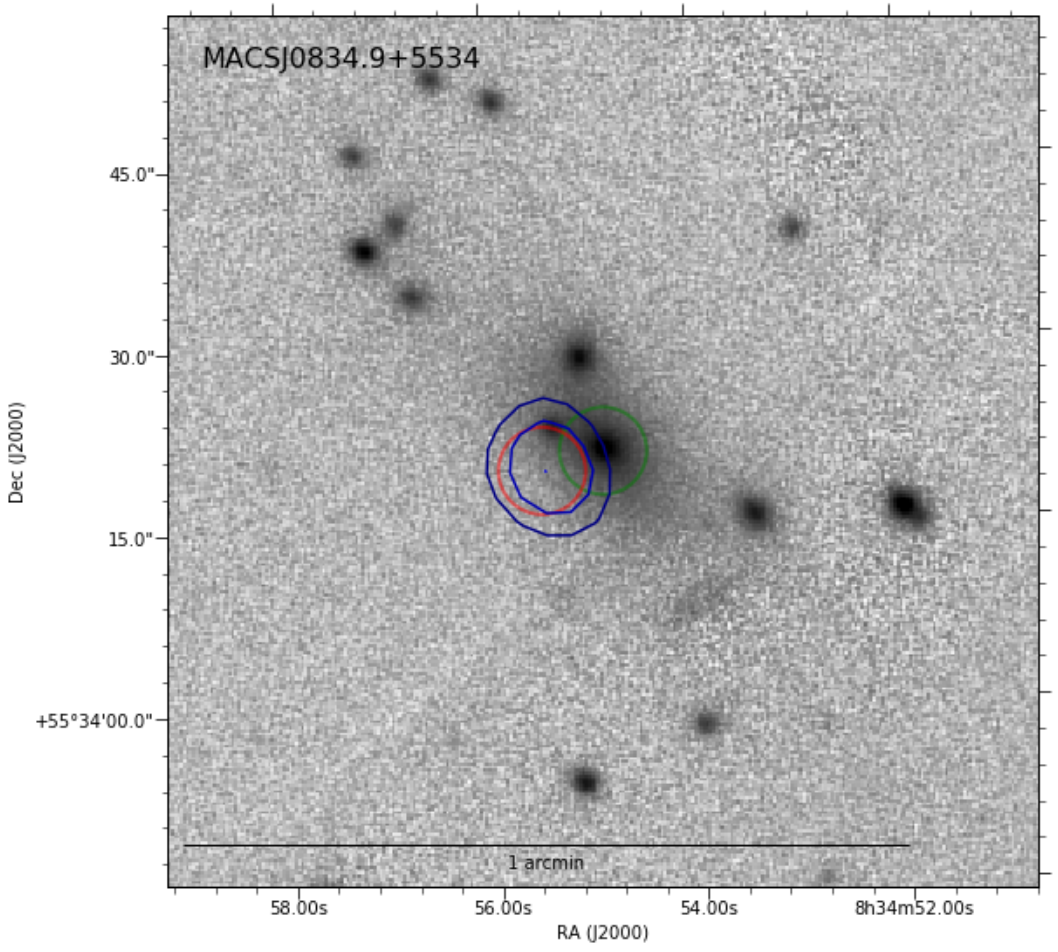
MACSJ0834.9+5534
45.0"
30.0"
15.0"
+55°34'00.0"
Dec (J2000)
1 arcmin
58.00s
56.00s
54.00s
8h34m52.00s
RA (J2000)

Figure 2.3

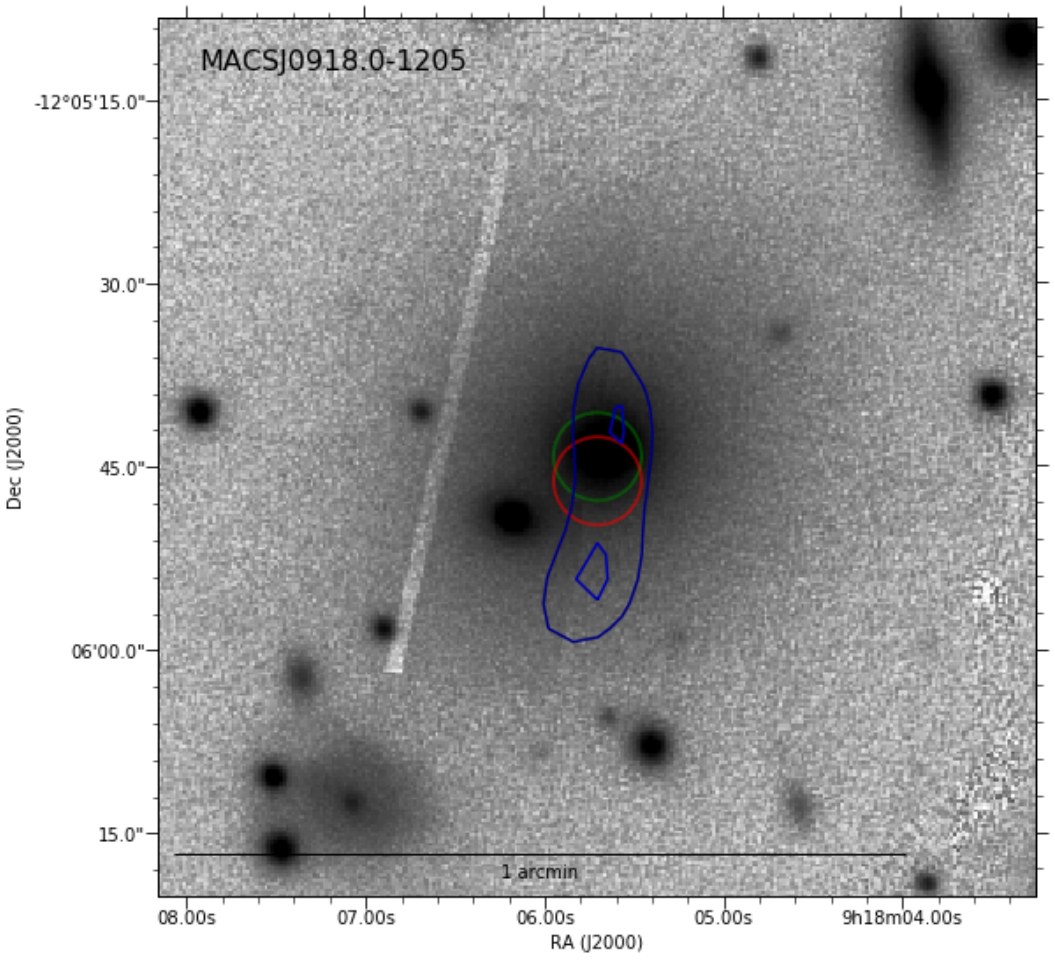
MACSJ0918.0-1205
-12°05'15.0"
30.0"
45.0"
06'00.0"
15.0"
Dec (J2000)
1 arcmin
08.00s
07.00s
06.00s
05.00s
9h18m04.00s
RA (J2000)

Figure 2.3

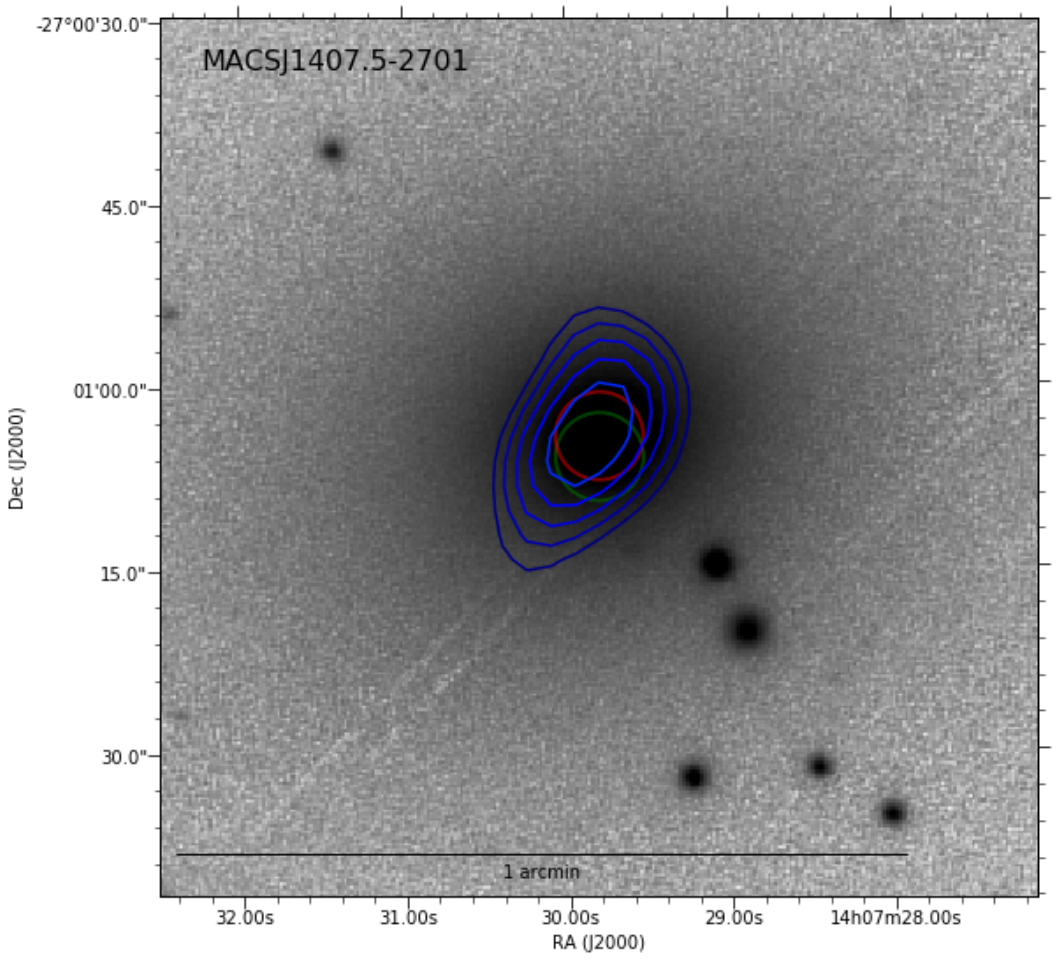
MACSJ1407.5-2701
-27°00'30.0"
45.0"
01'00.0"
15.0"
30.0"
Dec (J2000)
1 arcmin
32.00s
31.00s
30.00s
29.00s
14h07m28.00s
RA (J2000)

Figure 2.3

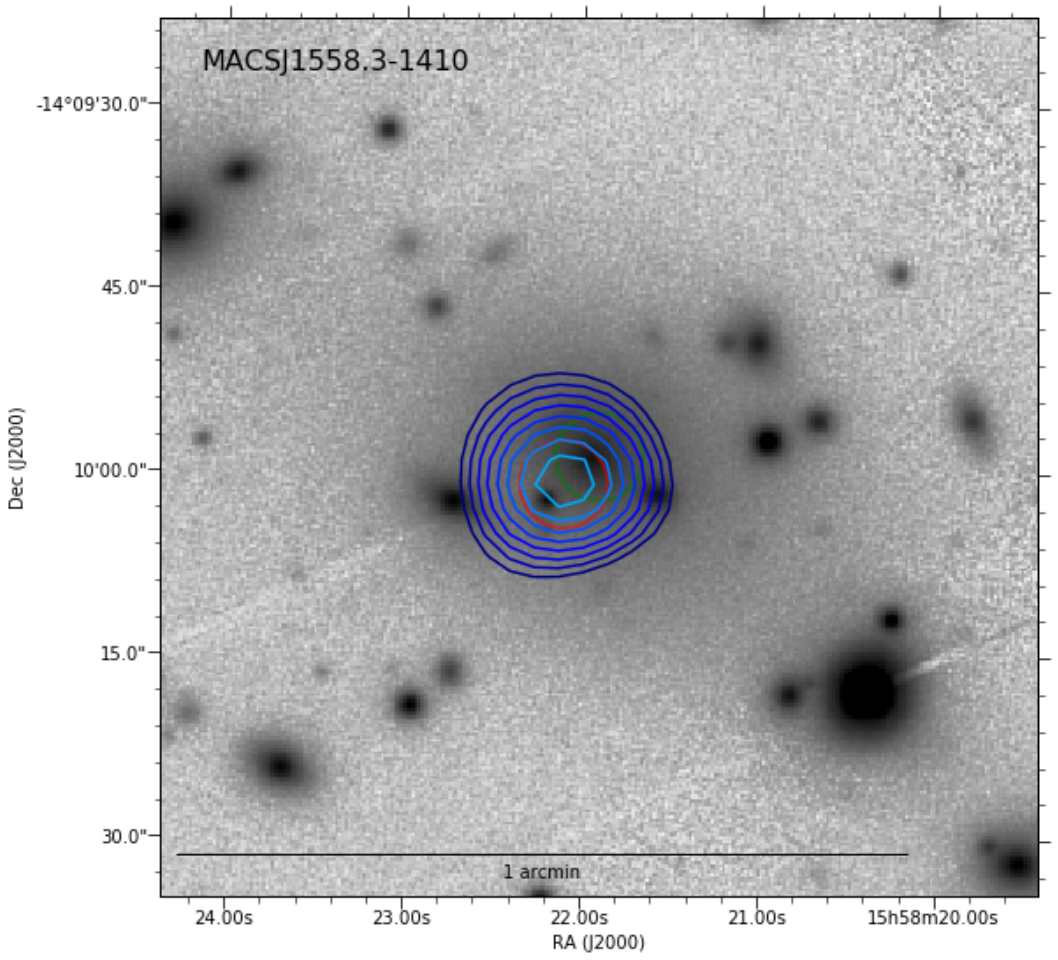
MACSJ1558.3-1410
-14°09'30.0"
45.0"
10'00.0"
15.0"
30.0"
Dec (J2000)
1 arcmin
24.00s
23.00s
22.00s
21.00s
15h58m20.00s
RA (J2000)

Figure 2.3

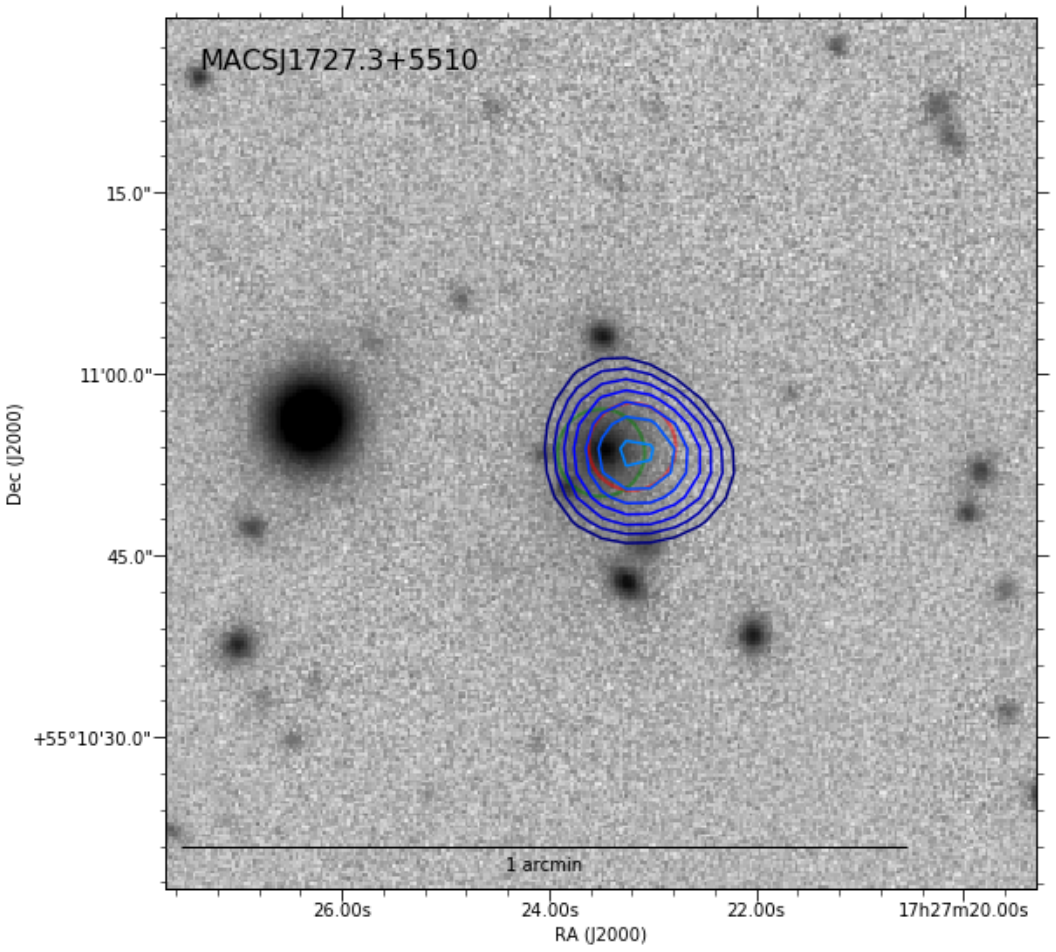
MACSJ1727.3+5510
15.0"
11'00.0"
45.0"
+55°10'30.0"
Dec (J2000)
1 arcmin
26.00s
24.00s
22.00s
17h27m20.00s
RA (J2000)

Figure 2.3

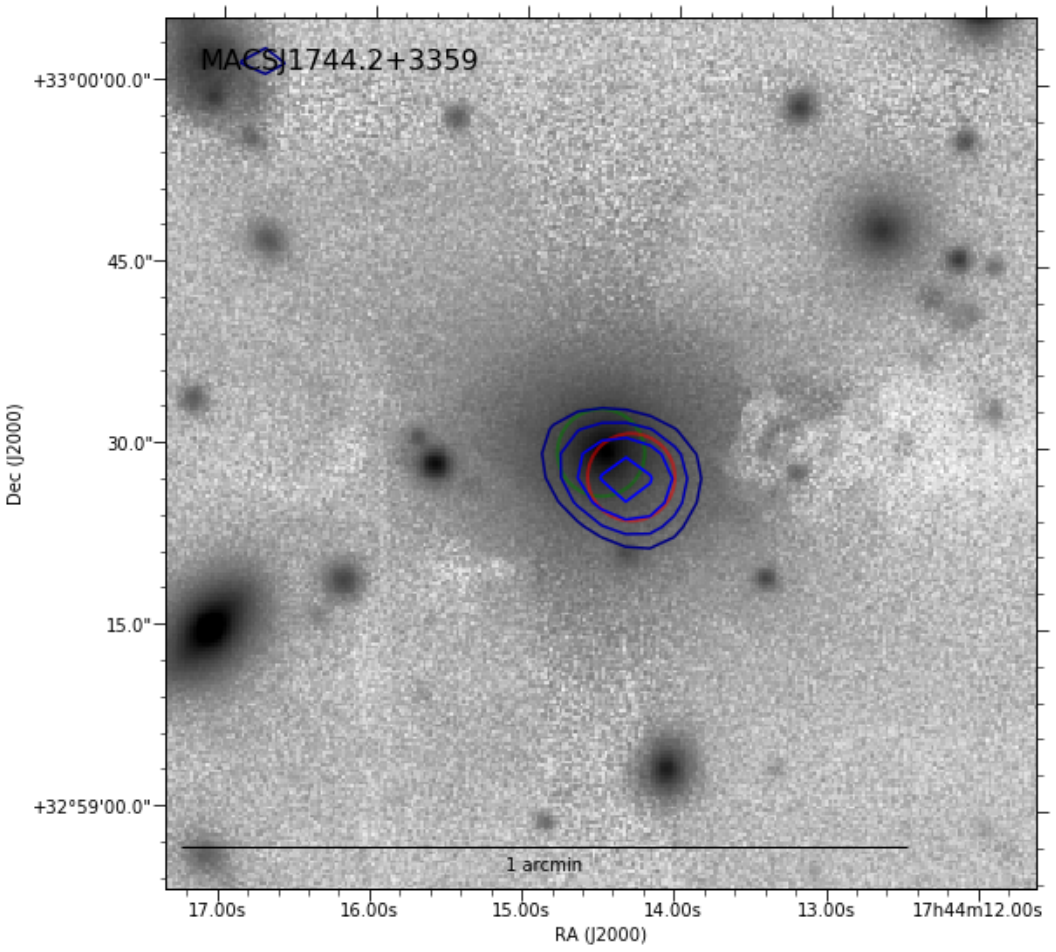
MACSJ1744.2+3359
+33°00'00.0"
45.0"
30.0"
15.0"
+32°59'00.0"
Dec (J2000)
1 arcmin
17.00s
16.00s
15.00s
14.00s
13.00s
17h44m12.00s
RA (J2000)

Figure 2.3

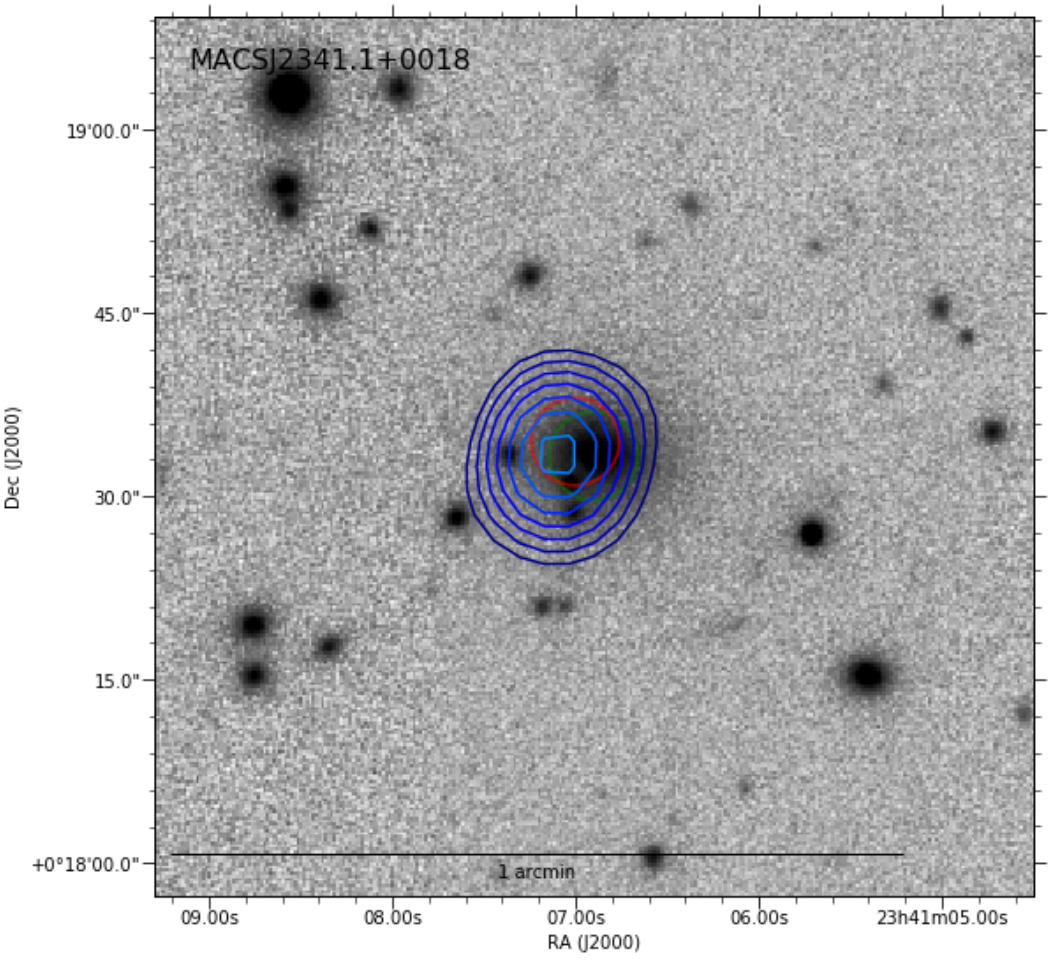

Figure 2.3 Pan-STARRS i-band imaging with SCUBA-2 850μm contours overlaid (3σ in 0.5σ increments) of the eight BCG sources found in the S2CSS and H15, red circle: BCG, green circle: Detection. Left to Right: MACSJ0242.5−2132, MACSJ0834.9+5534, MACSJ0918.0−1205, MACSJ1407.5−2701, MACSJ1558.3−1410, MACSJ1727.3+5510−B, MACSJ1744.2+3259 and MACSJ2341.1+0018−A fields.

Pan-STARRS i-band imaging (Figure 2.3) of the eight sources listed in Table 2.1 shows that the submillimeter contours are co-located with the position of the BCG. Indeed our precursor work Hogan et al., 2015a, (H15) showed that these fields contain BCGs with strong radio cores. In Table 2.1 we also include multiband data spanning from $850\,\mu m$ to 16GHz. In a recent ACT-POL survey Datta et al., 2018 observed MACSJ2341+0018-A, reporting a 148GHz flux density of $S_{148\mathrm{GHz}} = 45.8 \pm 7$mJy, which agrees with our 150GHz observation reported in H15. We also reported, in H15, that there is $850\,\mu m$ emission co-located with the BCG in MACSJ0439.0+0520. Because the point source is $< 4\sigma$ we do not include it in our sample; however, we do find a $> 4\sigma$ source $2'$ from the BCG in the cluster (reported in Table A.1). H15 reported no SCUBA-2 flux for either MACSJ2153.6 + 1741 (A2390) and MACSJ2325.3–1207 (A2597). We find SCUBA-2 fluxes of 20.9 ± 6.4 and 25.4 ± 7.2 co-located at the BCG respectively, although we too do not formally accept these as sources for the S2CSS as they are $< 4\sigma$. Their fluxes do constrain the GPS model of Orienti and Dallacasa [2014] further though, and MACSJ2325.3-1207 (A2597) is also reported Tremblay et al., [2018]. Five of the detected BCGs are in clusters with a lower X-ray luminosity than our main sample selection, so the fraction of submillimetre-bright BCGs in any mass-selected sample is particularly low, with only three found in over 200 observed clusters. Interestingly, in MACSJ1348.8+2635 (A1795), another BCG emitter, we find a bright (≈ 30 mJy, 4.5σ) submillimeter source $0.5'$ away from the position reported in H15. Either it is co-located with the BCG and is a coordinate error or it is a significantly bright lensed source located very close to the BCG. MACSJ0918.0-1205 (Hydra-A/3C218) is the only detection (of all 108 sources) showing a double-lobe submillimeter morphology (Figure 2.3). This is a well studied powerful radio galaxy, and its radio properties are discussed in detail in H15. The 78 non-SPIRE detections (i.e. SCUBA-2 only) are significantly offset (> 0.1') from their cluster BCG, have bright submillimetre flux densities that argue against them being cluster members (since their corresponding far-infrared luminosities would be unfeasibly high), and lack strong radio emission. They are therefore more likely to be background galaxies that have been lensed by a combination of the overall cluster potential plus a foreground cluster member rather than a radio-bright AGN or single cluster member. Indeed, one of our detections is the Cosmic Eyelash (MACSJ2135.2−01012) with $S_{850\,\mu m} = 120 \pm 9$mJy (in agreement with Swinbank et al., 2010), which was included in the sample to ensure we recovered the well-known source. We can further classify and investigate the properties of these bright submillimetre sources by examining additional data across the radio and submillimetre bands, where they are available. The 19 sources that also have SPIRE detections are convincing examples of lensed cases having significant detections in all three SPIRE bands and no reported 1-100GHz data (H15 targets the

same clusters). All 97, non-targetd, detections from our catalogue of lensed sources are reported in Table A.1, in which the SPIRE sources are marked by a superscript 'H'; their SPIRE fluxes are reported in Table 2.2.

2.3.2 *Herschel* SPIRE imaging: far-infrared spectral energy distribution

In cases where we have joint SCUBA-2/SPIRE detections, we can construct far-infrared spectral energy distributions (SEDs). We extracted SPIRE photometry from the position of the SCUBA-2 source, estimating uncertainties (including confusion noise [e.g.; Nguyen et al., 2010, Hardcastle et al., 2013]) by randomly sampling a large number of pixels around the source positions and evaluating the standard deviation of the flux distribution for the 22 sources (including the three targeted sources listed in Appendix D) and their host fields listed in Table D. Of these sources, 18 are offset from the BCG target, one is the Cosmic Eyelash and the final three are targeted (discussed in Appendix D).

We then performed a FIR photometric redshift fit to the photometery at 250–850 μm. We assumed that the SED can be described by a greybody with emissivity term $\beta = 1.5$ [Hildebrand, 1983, Rawle et al., 2012]

$$S(\nu) \propto [1 - e^{-\tau(\nu)}] B_\nu(T) = \frac{[1 - e^{-\tau(\nu)}]\nu^3}{e^{h\nu/kT} - 1}, \tag{2.2}$$

$\tau(\nu)$ accounts for the optical depth where $\tau(\nu) = (\nu/\nu_0)^\beta$, ν_0 is the frequency where the optical depth tends to unity [i.e. $\sim$3 THz; Draine, 2006, Conley et al., 2011]. We fitted the photometry with the redshift as a free parameter using least squares fitting SciPy packages, restricting the temperatures to values between 30–50 K. We also evaluated the redshift for a fixed standard 40 K dust temperature. Table 2.2 gives the redshift estimates for the full temperature range and the fixed 40K fit, Appendix B shows the best fitting SEDs and an example is shown in Figure 2.4. We find that the FIR colours are consistent with high-z sources behind the clusters, with redshifts in the range $z \approx$ 2–4.

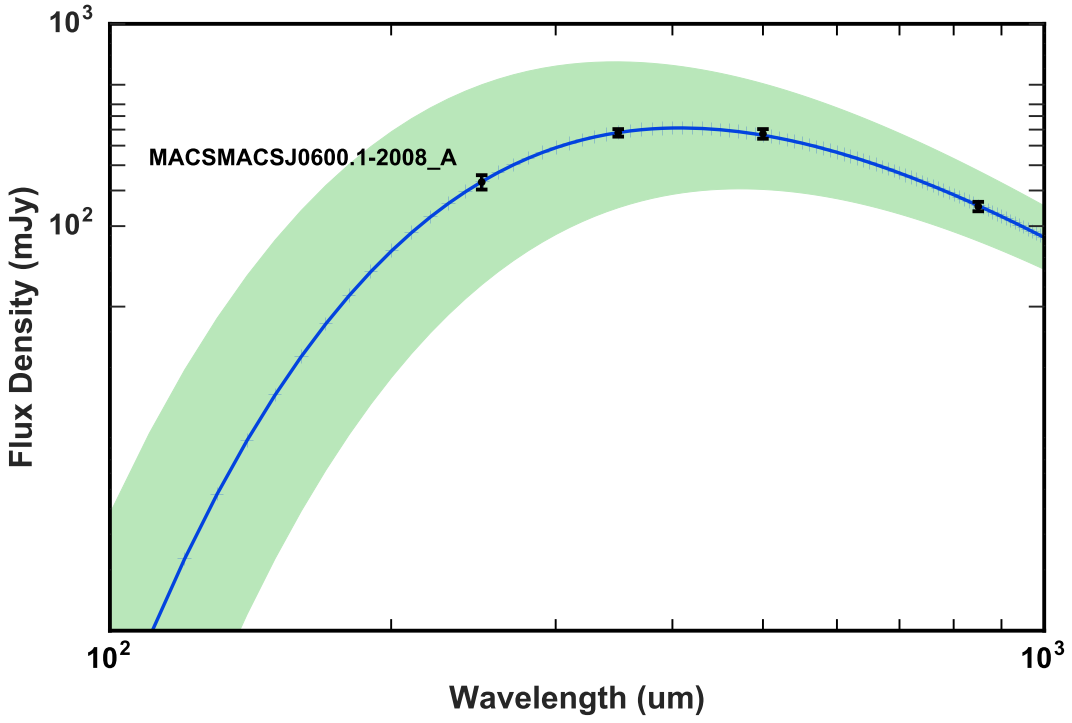

Figure 2.4 Greybody fits for the SPIRE 250 μm, 350 μm, 500 μm and SCUBA-2 850 μm photometry for a fixed dust temperature of 40 K. The filled region represent the range of redshift fits for T = 30–50 K as in column 8 of Table 2.2. We show an exemplar plot here and the remaining plots can be found in Appendix B.

Table 2.2. SPIRE photometry for the S2CSS sources and far-infrared photometric redshift estimates based on greybody fits to the SPIRE+SCUBA-2 photometry. The penultimate column indicates the range of acceptable redshifts for a range of dust temperatures 30–50 K, and the final column for a fixed temperature of 40 K. $^{i}>$ MACSJ2135.2-0102 S_{500} flux density value obtained from [Ivison et al., 2010], $^{T}>$ refers to the targeted sources in Appendix D and, $^{CE}>$ the cosmic eyelash.

ID	SCUBA-2 Detection Position J2000	C_{80} (mJy)	S_{850} (mJy)	S_{500} (mJy)	S_{350} (mJy)	S_{250} (mJy)	Photometric Redshift	T=40K Redshift
MACSJ0417.5−1154	04:17:33.4 −11:55:02.0	33	25 ± 5	62 ± 15	38 ± 14	54 ± 13	$2.3-3.8$	3.1 ± 0.3
MACSJ0429.6−0253	04:29:33.3 −02:52:35.5	71	55 ± 12	32 ± 15	23 ± 12	32 ± 12	$4.5-7.1$	5.8 ± 0.8
MACSJ0958.3−1103-B	09:58:14.5 −11:03:08.0	26	23 ± 5	27 ± 17	45 ± 13	35 ± 13	$2.4-3.9$	3.2 ± 0.4
MACSJ0958.3−1103-C	09:58:10.1 −11:02:10.0	26	35 ± 8	14 ± 17	24 ± 13	23 ± 13	$4.0-6.4$	5.3 ± 0.9
MACSJ1022.4+5006	10:22:26.6 +50:05:38.5	45	45 ± 8	76 ± 17	72 ± 14	57 ± 14	$2.6-4.2$	3.4 ± 0.3
MACSJ1023.8−2715	10:23:57.1 −27:16:53.0	36	38 ± 7	55 ± 18	48 ± 12	23 ± 13	$3.1-5.0$	4.1 ± 0.4
MACSJ1200.3+0320	12:00:15.2 +03:23:17.5	21	31 ± 4	79 ± 17	52 ± 13	47 ± 13	$2.5-4.2$	3.4 ± 0.3
MACSJ1229.0+4737	12:29:09.1 +47:36:50.3	25	27 ± 6	43 ± 15	44 ± 12	39 ± 12	$2.5-4.1$	3.3 ± 0.4
MACSJ1314.3−2515	13:14:21.2 −25:15:47.5	33	34 ± 5	106 ± 17	145 ± 14	136 ± 14	$1.6-2.8$	2.3 ± 0.2
MACSJ1325.1−2013−B	13:24:59.6 −20:13:32.5	53	42 ± 9	45 ± 16	26 ± 11	33 ± 13	$3.6-5.8$	4.8 ± 0.6
MACSJ1722.4+3207-A	17:22:30.2 +32:07:32.0	39	26 ± 4	36 ± 15	53 ± 12	50 ± 13	$2.2-3.7$	3.0 ± 0.3
MACSJ1731.6+2252-A	17:31:40.5 +22:50:35.0	30	48 ± 5	153 ± 16	146 ± 13	130 ± 13	$1.9-3.2$	2.5 ± 0.1
MACSJ1910.4+6741	19:10:26.2 +67:41:51.2	37	27 ± 6	34 ± 15	19 ± 13	15 ± 13	$3.6-5.8$	4.7 ± 0.8
MACSJ2043.2−2144	20:43:14.5 −21:44:39.0	32	65 ± 4	234 ± 21	292 ± 15	197 ± 14	$1.8-3.1$	2.5 ± 0.1

Table 2.2 (cont'd)

ID	SCUBA-2 Detection Position J2000	C_{80} (mJy)	S_{850} (mJy)	S_{500} (mJy)	S_{350} (mJy)	S_{250} (mJy)	Photometric Redshift	T=40K Redshift
MACSJ2050.7+0123-A	20:50:37.9 +01:24:58.5	23	18 ± 4	55 ± 16	54 ± 14	55 ± 14	$1.9 - 3.3$	2.6 ± 0.3
MACSJ2104.8+1401	21:05:03.1 +14:00:43.9	47	53 ± 12	51 ± 17	47 ± 14	49 ± 13	$2.7 - 4.5$	3.7 ± 0.5
MACSJ2341.1+0018-A	23:41:07.0 +00:18:34.5	26	33 ± 3	49 ± 15	57 ± 12	81 ± 13	$2.2 - 3.6$	2.9 ± 0.2
MACSJ2341.1+0018-B	23:41:07.3 +00:19:34.5	26	18 ± 4	38 ± 15	25 ± 12	26 ± 13	$2.7 - 4.4$	3.6 ± 0.5
MACSJ0326.8−0043^{T}	03:26:57.8 −00:45:17.0	35	29 ± 5	73 ± 15	72 ± 13	61 ± 13	$2.1 - 3.6$	2.9 ± 0.3
MACSJ0455.2+0657^{T}	04:55:18.1 +07:01:01.0	30	36 ± 5	98 ± 15	123 ± 12	188 ± 13	$1.3 - 2.3$	1.8 ± 0.2
MACSJ0600.1−2008^{T}	06:00:24.0 −20:06:40.0	43	125 ± 6	286 ± 15	289 ± 12	165 ± 13	$2.4 - 4.0$	3.3 ± 0.1
MACSJ2135.2−0102^{CE}	21:35:11.7 −01:02:54.0	57	120 ± 9	366 ± 55^{i}	325 ± 49	429 ± 64	$1.9 - 3.2$	2.6 ± 0.2

2.3.3 AzTEC and RSR follow-up

In a precursor paper, Zavala et al., 2015, (Z15) presented Large Millimeter Telescope (LMT) follow-up of four of the S2CSS sources reported here. Z15 reported on follow-up observations with AzTEC and RSR on the LMT of MACSJ0455.2+0657, MACSJ1022.4+5006, MACSJ1731.6+2252 and MACSJ2043.2-2144. The analysis in Z15 found CO line detections in MACSJ0455, MACSJ1731 and MACSJ2043, reporting redshifts of $z = 2.927$ and 2.712 and a blended source of $z = 2.04, 3.25, 4.68$ respectively. In comparison, we found photometric redshifts for MACSJ0455 of $z = 1.3 - 2.3$, MACSJ1022 of $z = 2.6 - 4.2$, MACSJ1731 of $z = 1.9 - 3.2$ and MACSJ2043 of $z = 1.8 - 3.1$. Thus, our photometric redshift estimates are at least reliable enough to determine that the remaining detections lie at high redshift, behind the clusters.

Z15 used a conservative threshold for the singal-to-noise ratio of S/N$\geq$ 3.5 to determine a CO line detection. They reported new 1.1 mm fluxes for three sources, which are also observed in this work: MACSJ1022 $S_{1.1\,mm} = 11 \pm 2$ mJy, MACSJ0455 $S_{1.1\,mm} = 23 \pm 3$ mJy and MACSJ2043 $S_{1.1\,mm} = 29 \pm 3$ mJy. RSR observations found no detections for MACSJ1022, but this galaxy is one of the faintest in both Z15 and this work, so it is likely that longer integration times are required. Photometric redshift-fitting in this work yields $2.6 < z < 4.2$, which is the typical expected range for a lensed submillimeter galaxy. MACSJ0455 has a single line detection, namely $\nu = 88.051$ GHz with S/N = 7.3, and therefore can provide a tentative redshift. Z15 suggests that the line is associated with the CO(2-1) transition, implying $z = 1.618$; however, one would expect redshifts typically in the range $z = 2 - 3$ for a lensed galaxy. Z15 deduced that the CO(3-2) transition is a more likely candidate at $z = 2.927$, and this is in agreement with the redshift range found here of $1.8 < z < 3.0$. Multiple lines are detected in MACSJ2043, and this coincides with the image having the brightest 1.1 mm detection. This work finds a wide range of redshift photometric fits of $1.8 < z < 3.1$; however, this does not account for the RSR detections of multiple lines, which has the interesting case that they may originate from multiple sources. Four lines were detected at $\nu = 75.827$, 81.178, 101.459, and 108.428 GHz with S/N $\geqslant$ 3.5. Z15 concluded that the lines represent a multisource component with redshifts $z = 2.04$, 3.25, and 4.68. MACSJ1731 has a single line detection at $\nu = 93.163$GHz, and Z15 deduced with follow-up observations that the line corresponds to CO(3-2), $z = 2.712$. In all three cases where lines were detected, we find that the redshifts determined by Z15 fall within the photometric ranges deduced in this work. Furthermore the Cosmic Eyelash redshift of $z = 2.3259$

also lies within the range quoted in Table 2.2. Following our AzTEC/RSR-S2CSS analysis, we have confidence that our redshift ranges are reliable for our other multiband detections in the survey.

2.4 Discussion

From the sample, we identified a total of 108 sources with a bright submillimeter component in the field that are $> 4\sigma$, within $3.5'$ of the pointing, and exceed the ratio in Equation 2.1 with positional uncertainty of 1.7 for $> 4\sigma$ and decreasing to 1.0 for $> 5\sigma$ (assuming $\theta_{\rm FWHM} \propto (2 \times {\rm S/N})$. Of these 108, eight are co-located with the BCG (confirmed by H15) and 18 have significant *Herschel* counterparts with four bands of IR (250–850 μm) that are unlikely to belong to a cluster member. The catalog of sources comprise of three targeted sources and the remainder are candidate lenses as they have exceedingly bright corresponding IR luminosities which would not be expected from blank fields because N($S_{850\,\mu m} > 15\,$mJy)(deg^{-2})≈ 2 (see, G17).

Using these detections and our estimates of the sensitivity of each of the SCUBA-2 observations, we can determine the number of detections brighter than a certain 850 μm flux expected per cluster surveyed to that depth. This calculation was made out to two different radii. The first to within $1'$ of the BCG, where the maps are most sensitive (see Figure 2.2), and we assume that the maps reach a depth of $S_{850\,\mu m}/C_{80} > 0.6$. The second was to within $3'$ of the BCG where the map sensitivity is significantly lower and we can assume a depth of only $S_{850\,\mu m}/C_{80} > 1.0$ over this full area in each cluster. Any very bright sources will be selected in any of our maps out to the $3'$ limit used, but for the faintest sources a significant contamination from spurious sources would be expected.

Figure 2.5 shows the number counts derived for the S2CSS survey, split on whether a significant *Herschel* SPIRE counterpart to the SCUBA-2 source was found or not. The results show a significantly flatter slope to the counts for the central $1'$, as would be expected for the strongly lensed sources detected in the core. It is also clear that there are very few $> 5\sigma$ sources without a SPIRE counterpart, particularly within $1'$. The higher fraction of sources between $4 < \sigma < 5$ sources in this exclusively 850 μm detected sample compared with those with a SPIRE counterpart suggests that more spurious sources are present. However, the possibility that at least some of these sources are at high redshift ($z > 4$) means this sample deserves careful follow-up.

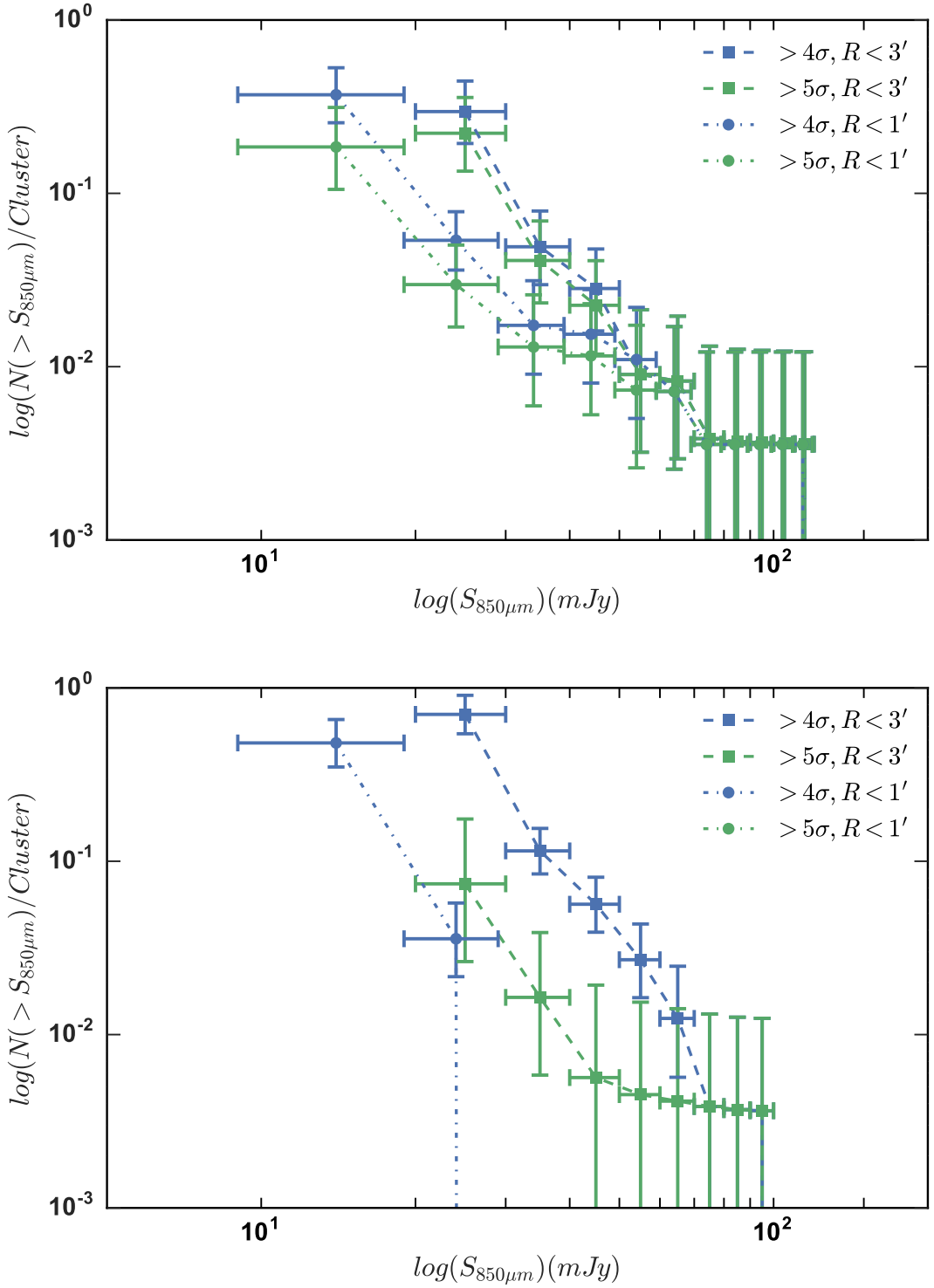

Figure 2.5 Top Panel: Number counts for the S2CSS sources, excluding BCGs, with a significant SPIRE counterparts within $1'$ or $3'$ (dashed-dot-dash or dashed lines) and on detection significance ($>5\sigma$ green, $>4\sigma$ blue). Bottom Panel: Number counts for SCUBA-2 only sources in the S2CSS catalog. R$<1'$ bins are center offset by -1 to disentangle the overlaps. Uncertainties in 850 μm bins refer to the bin width (5 mJy in all cases) and, the number counts are a 1σ confidence range assuming Poisson statistics [Gehrels, 1986]. No $>5\sigma$ sources were found within $1'$ not having a bright SPIRE counterpart.

We found that eight of the target clusters have a bright submillimeter component ($S_{850} > 29$ mJy) co-located with their BCG. The most likely origin for the submillimetre emission in these massive, passive galaxies is from a central AGN. The submillimetre emission could arise from a synchrotron component, or alternatively an Advection-Dominated Accretion Flow [ADAF; Mahadevan, 1997], which contributes excess millimetre/submillimetre emission in addition to the synchrotron component; we note, however, that if there is strong synchrotron self-absorption then this could mimic millimetre excess emission. There could also be an alternative emission process, namely from remnant dust in the BCG heated by the stellar population; there may even be residual star formation present [Doi et al., 2005]. Our BCG sample is discussed in H15 with follow-up AMI, CARMA and GISMO detections.

The brightest detection by far from this survey is MACSJ0600: with $S_{850\,\mu m} = 125 \pm 7$ mJy and detected $\approx 4'$ away from the BCG, it is a convincing candidate cluster–galaxy lensed SMG. MACSJ0600 was one of three selected targets having extreme SPIRE fluxes, and we further added to the observed bands for this source with our SCUBA-2 data. Comparing MACSJ0600 with the S2CSS observations indicates that there are $< 1\%$ of clusters acting as strong lenses for bright SMGs ($S_{850} > 100$ mJy). Of the non-selected targets (excluding the Cosmic Eyelash), the brightest SCUBA-2 source is found in MACSJ1452.9+5802, with $S_{850\,\mu m} = 98 \pm 18$ mJy and the brightest non-selected SCUBA-2 + SPIRE source was identified in MACSJ2043.2-2144 having, $S_{850\,\mu m} = 66 \pm 5$ mJy.

The bright $850\,\mu m$ sources in the cluster fields MACSJ2043.2-2144, MACSJ2104.8+1401 (65 ± 5, 52 ± 12 mJy) have been followed up with ALMA observations (PI Egami et al. in prep) and; MACSJ0455,2+0657, MACSJ0600.1-2008, MACJ1115.8+0129 and MACSJ1314.3-2515 (37 ± 5, 125 ± 7, 20 ± 4, 34 ± 5 mJy) are scheduled for Cycle 5 (PI: E.Egami) for observations.

2.5 Summary

We have presented the first results from the SCUBA-2 Cluster Snapshot Survey, targeting a large number of massive clusters of galaxies in the poorest of submillimetre observing conditions in order to detect the brightest submillimetre sources. Our main findings can be summarized as follows.

1. The SCUBA-2 Cluster Snapshot Survey took snapshots of 202 massive clusters, and we identified a total of 108 850μm bright sources.

2. We identified 78 SCUBA-2 candidate lensed sources - these have no significant SPIRE detections and their IR luminosity is too high to be local. We identified eight sources which appear co-located with the BCG [these have been reported previously by Hogan et al., 2015a.]

3. We identified 19 sources that were not only bright in the SCUBA-2 field but also have exceptionally bright SPIRE counterparts (reported in Table 2.2, including the Cosmic Eyelash [Swinbank et al., 2010].

4. We constructed basic photometric SEDs for 22 sources that have both SPIRE and SCUBA-2 counterparts (including the Cosmic Eyelash and three targeted sources). Encouragingly, in a precursor paper Zavala et al., 2015 undertook a spectroscopic analysis of four of these sources which lay within our photometric redshifts. Based off an agreement we are confident that the photometric redshift ranges quoted for each source in this chapter are reliable.

The S2CSS has produced a large number of lensed submillimeter bright sources by looking at X-ray luminous clusters. This survey assists a broader goal of hunting for more submillimeter bright sources with the SCUBA-2 instrument. Further work will aim towards making use of ALMA for high resolution CO measurements of our potentially high redshift sources and SCUBA-2 follow-up observations.

Chapter 3

SCUBA-2 Cluster Snapshot Survey: Properties of Brightest Cluster Galaxies

3.1 Introduction

The SCUBA-2 Cluster Snapshot Survey (S2CSS; Chapter 2) detected a number of Brightest Cluter Galaxies (BCGs) with bright 850μm emission within 2-arcmin of observations pointed at a host cluster BCG; the radio nature of these sources was discussed in Hogan et al., [H15]However, few cluster members can actually be detected at 850μm through their strong dust continuum or Synchrotron emission, both of which dominate the cluster emission in the short and millimeter wavelength regime [Edge et al., 1999, Hogan et al., 2015a]. Shorter wavelength surveys with *Herschel* [e.g., Coppin et al., 2011] do show a statistical excess of bright FIR dusty cluster members. Considering we have observed a large number of clusters, each containing a BCG, we can examine statistical 850μm excess emission from BCGs by means of stacking numerous SCUBA-2 maps at their confirmed optical positions [see; Ebeling et al., 2001] which will allow emission detection below the formal limit of any one individual map. The presence of an active galactic nucleus (AGN) is an obvious contributor to the submillimetre emission of BCGs. This has not been well-explored in a large sample like ours - we would like to know about the properties of AGN in central cluster galaxies from the point of view of their feedback affects the

surrounding cluster gas (radio maintenance feedback), and to know more about their star formation history (traditional view being that BCGs are big red and dead ellipticals that ceased SF long ago). Therefore, as an experiment, we split the sample into groups according to the radio properties of the BCG as AGN should dominate the radio contributions. By excluding the catalog of sources from the S2CSS (as lensed galaxies that are bright in the submillimetre and found close to the BCG of the foreground cluster $< 0.1'$ would bias this analysis) we can split our data set into discrete radio bins allowing us to quantify the average radio and submillimetre BCG properties without contribution from potentially bright lenses $S_{850\,\mu m} > 20$ mJy. The inverse Compton scattering interactions between CMB photons, free-streaming from the early Universe, and the dense electron regions of clusters of galaxies is known as the Sunyaev-Zel'dovich effect [SZE; Sunyaev and Zeldovich, 1972]. The SZE increment peak is at $\approx 850\mu m$, redshift independent and can be used to measure the mass of clusters [Carlstrom et al., 2002]. However the SZe may well contaminate the central regions of clusters [see; Zemcov et al., 2010] effecting wide field surveys in the mm-sub-mm regime. Fortunately, as the S2CSS is a collection of filtered point sources, and the fact that the SZE is an extended emission component, we can obtain a SZE free thermal contribution at 350 GHz by conducting an analysis on a complete stack of all our observations.

This chapter is organised as follows: In Section 3.2 we describe the target selection, observations and data reduction.Section 3.3 provides an analysis on the BCG properties over multiple wavebands. Section 3.4 discusses the nature of the BCG stacking analysis. Finally, Section 3.5 will summarize the results and detail future work.

3.2 Radio Data

The NRAO Very Large Array (VLA) Sky Survey [NVSS; Condon et al., 1998] is a 1.4 GHz (21.4 cm) continuum survey at declinations greater than -40°, with an angular resolution of $45''$ and depth 2.5mJy [Jones et al., 2015]. The TGSS Alternative Data Release [TGSS-ADR; Intema et al., 2017] is a recent addition to the TIFR Giant Meterwave Radio Telescope (GMRT) Sky Survey (TGSS). The TGSS-ADR is a 147.5 MHz (200 cm) radio survey covering a declination range of -55° to +90° to a median depth of 3 mJy with a $25''$resolution.

We matched the BCGs in each cluster to the NVSS and TGSS-ADR to detect radio bright BCGs, identifying the radio sources within $30''$ of the optical position of the BCG. We found 105 matches for clusters targeted by the S2CSS.

3.3 Stacking

In order to stack sources, we binned the data by the NVSS 1.4 GHz radio flux (because some BCGs will be radio-bright, containing an AGN, whereas others will be quiescent). Bins are distributed by splitting the matched data into Interquartile Ranged (IQR) bins. The result is four bins that we classify as Radio Faint (RF), Radio Intermediate I (R-I), Radio Intermediate II (R-II), and Radio Bright (RB) as described in Table 3.3. To evaluate the average 850μm flux density of the bins below the limit possible from our individual observations, we extract thumbnail images from each SCUBA-2 map around the optical BCG location and evaluate the average flux density with inverse variance weighting, with the weights derived from an identical map extracted from the instrumental noise maps. We detected significant stacked 850μm emission in the R-II and R-B bin with $S_{850} = 3.3 \pm 1.1$ and $S_{850} = 4.4 \pm 0.9$ respectively (See Figure **??**, whereas the remaining bins are $< 3\sigma$. We constructed rest-frame SEDs for each of the four bins using the binned 1.4 GHz NVSS sources with their 140 MHz TGSS counterparts and the respective stacked 850 μm flux values. They are presented in Figure 3.3.

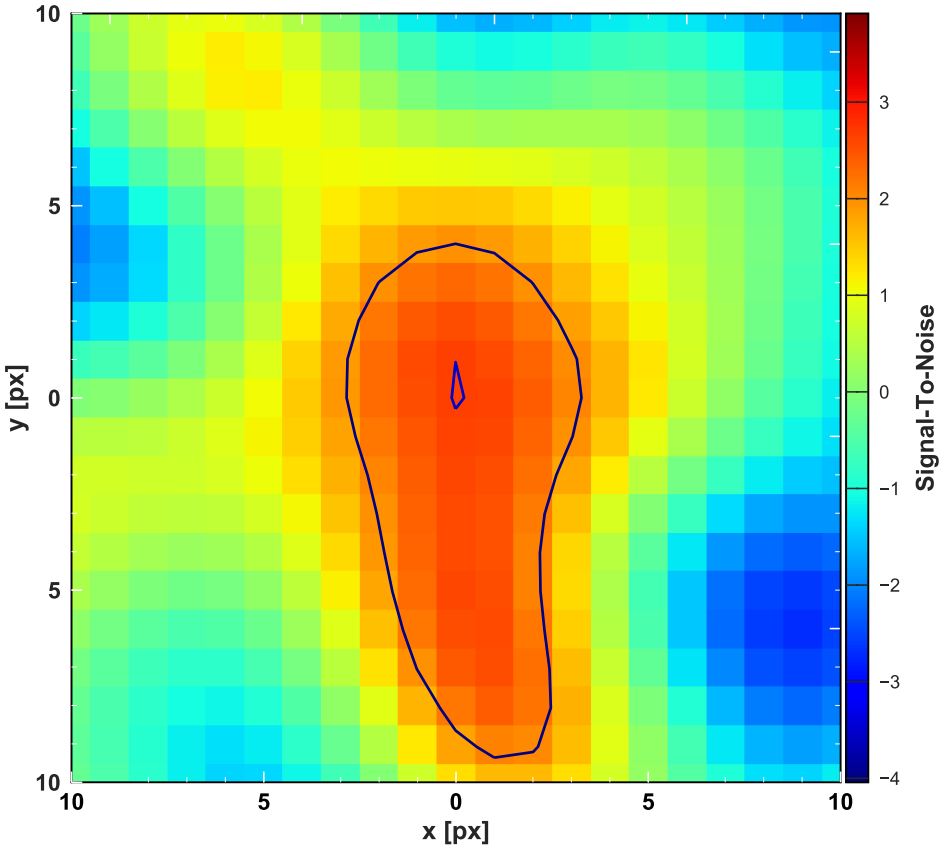

(a) Intermediate Sample (R-II): $41 \leq S_{1.4\,GHz} \leq 111$mJy

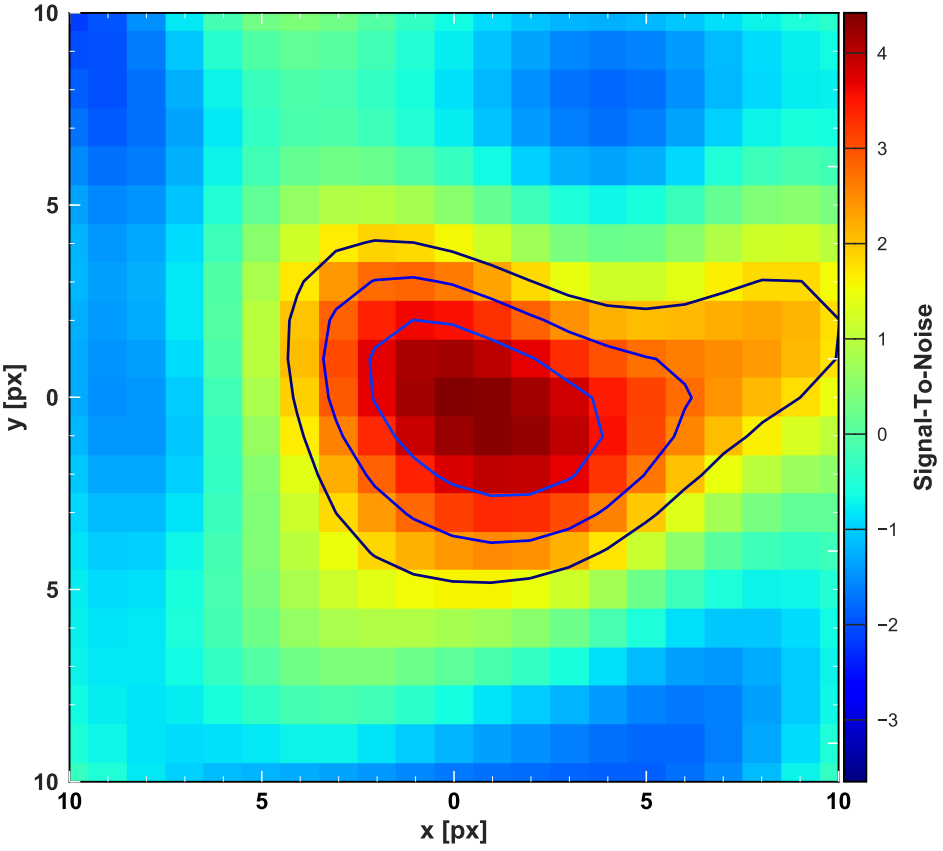

(b) Bright Sample (R-B): $S_{1.4\,GHz} > 111$mJy

Figure 3.1 The flux density maps for the R-II and R-B IQR binned data, contours represent $\sigma > 2$ in intervals of 1.

Table 3.1. Each bin has been determined via interquartile sets from the 1.4 GHz data, the peak flux and error from each bin stack is presented here. We find that the radio bright bin stack is also the bin with the highest significance (3.3σ) in the $850\mu m$ band. we show two different spectral indexes, a fitted value based on fitting to the data and a median of set value calculated by taking the median of the set of spectral indexes pooled from each of clusters in the stack. Column 1: Label; RF: Radio Faint, I & II: Intermediate Sample 1 and 2, RB: Radio Bright; column 2: Bin width; column 3: Number of Entries; column 4: Mean 1.4 GHz with standard deviation error; column 5: Peak stacked flux densities; column 6: fitted spectral index order; column 7: median set spectral index.

Label	Bin	No. Entries	$\langle S_{1.4GHz} \rangle$ (mJy)	Peak $S_{850\mu m}$ (mJy)	Spectral Index	Median set Spectral Index
R-F	$S_{1.4GHz} \leq 18$mJy	26	11 ± 4	2.7±1.1	-0.99±0.01	-0.91±0.05
R-I	$18 < S_{1.4GHz} \leq 41$mJy	26	27 ± 6	2.1±1.0	-0.94±0.01	-0.71±0.06
R-II	$41 < S_{1.4GHz} \leq 111$mJy	26	67 ± 21	3.3±1.1	-0.50±0.01	-0.36±0.05
R-B	$S_{1.4GHz} > 111$mJy	27	1981 ± 468	4.4±0.9	-0.71±0.01	-0.85±0.04

The individual 1.4 GHz and 150 MHz sources were K-corrected using their respective spectroscopic cluster redshift. The SCUBA-2 stacks were K-corrected to the median redshift of the bin. In Figure 3.3 we show a fitted power law of the form $S = A\nu^{\alpha}$ (solid line) using the least squares algorithm in SciPy Python package simultaneously for the TGSS and NVSS data for each bin, the power law describes an expected Synchrotron emission component of the cluster stack. We also show the power law calculated by the median of each individual spectral index within a bin (dot-dash, median of set) for a comparison of methods. For an AGN, synchrotron emission would be the dominate feature. If star formation were to be the major contributor we would expect to see an excess in the 850 μm stacks compared with our extrapolated Synchrotron power laws. This is only likely in the R-B bin as the stack result falls above the fitted power law.

In the two faintest bins we find only upper limits for our 850μm stacks. The R-II bin 850μm stack result falls below the fitted and median of set Synchrotron power laws. The R-B bin displays a large variance; this is due to the nature of a bin which contains extreme radio flux values with no upper constraint. The spectral indicies (α) approach a flatter state ($\alpha \to 0$) in the first three bins, but due to the large variance in the brightest bin the trend turns over. However, in spite of the fact that the turn over is associated with lack of constraints, there may well be a different mechanism involved, i.e., that more powerful AGN or star formation are causing a spectrum shift.

3.4 Discussion

BCGs tend to have gone through a number of mergers early in their evolution and already formed the bulk of their stars. Despite this, BCGs often still contain huge reservoirs of molecular gas, which should lead to easily observable star formation e.g., Vantyghem et al., 2016. However, BCGs appear relatively passive and generally considered to regions of star formation regions. There is growing evidence that this is not entirely true for a number of BCGs however, it may be that there are isolated star forming pockets driven and controlled though both AGN feedback and the 'cooling flow' mechanism [see; Fabian, 1994]. Cooke et al., 2016 (C16) provide evidence of low star formation rates in BCGs for the redshift range $0.2 < z < 0.7$. They found that the star formation does not contribute significantly to stellar mass growth, but that the radio emissions in their sample is higher than that expected from just star formation alone. It is likely BCGs are dominated by AGN at this waveband. McDonald et al., 2016 (M16) also looked at BCGs in the range $0.25 < z < 1.25$ and their average properties. In the low redshift range $0.25 < z < 0.45$ the

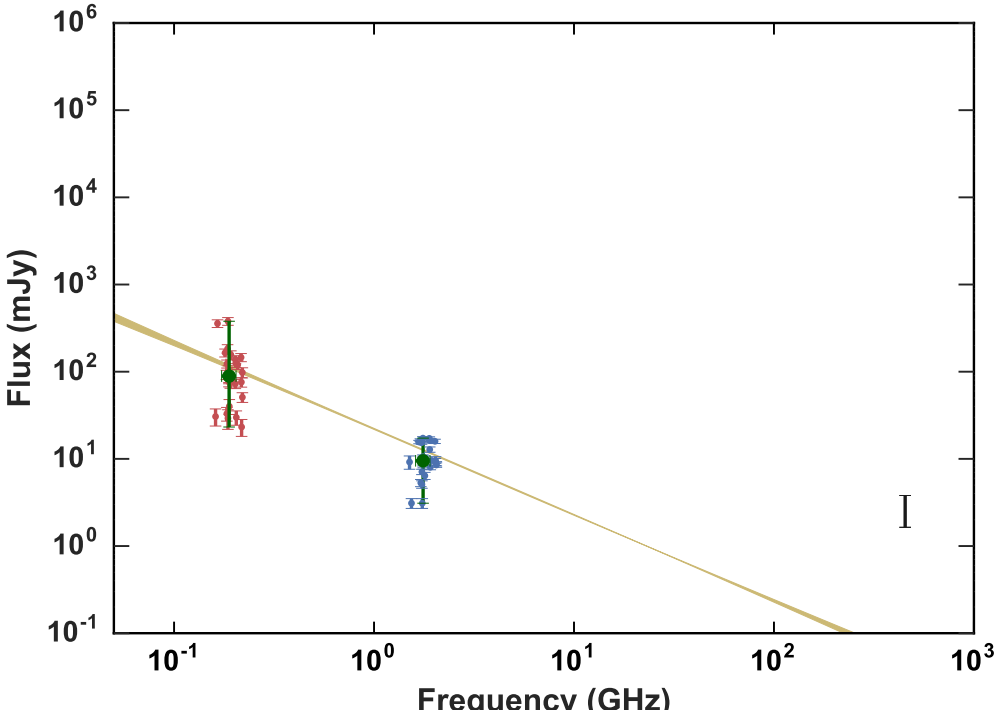

(c) Faint Sample (R-F): $S_{1.4GHz} \leq 18$mJy

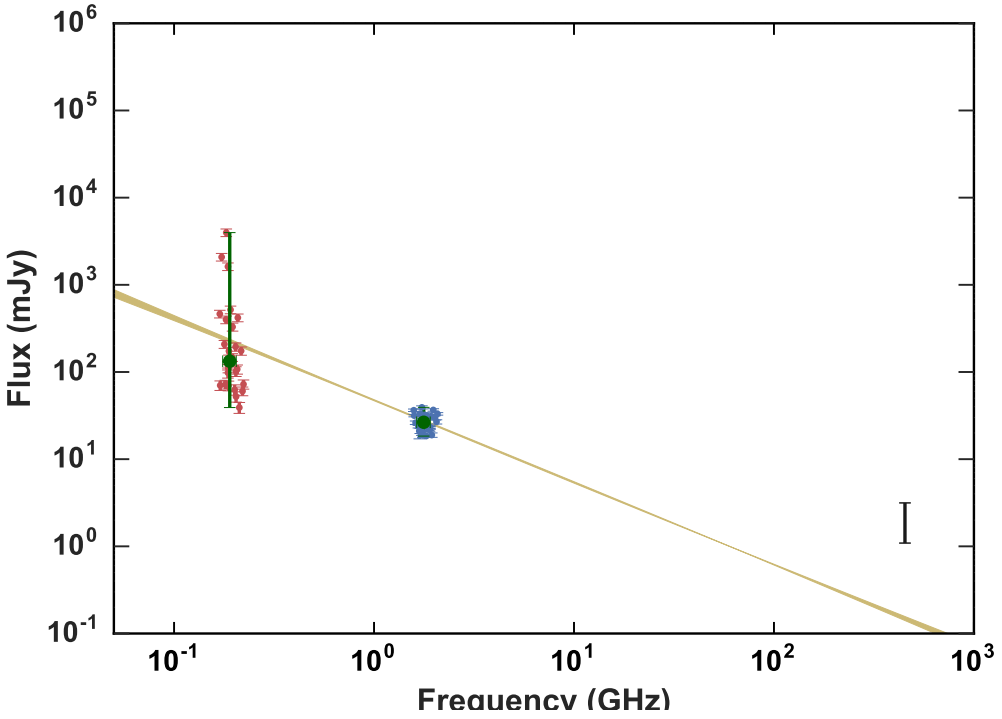

(d) Intermediate Sample (R-I): $18 \leq S_{1.4GHz} \leq 41$mJy

Figure 3.2

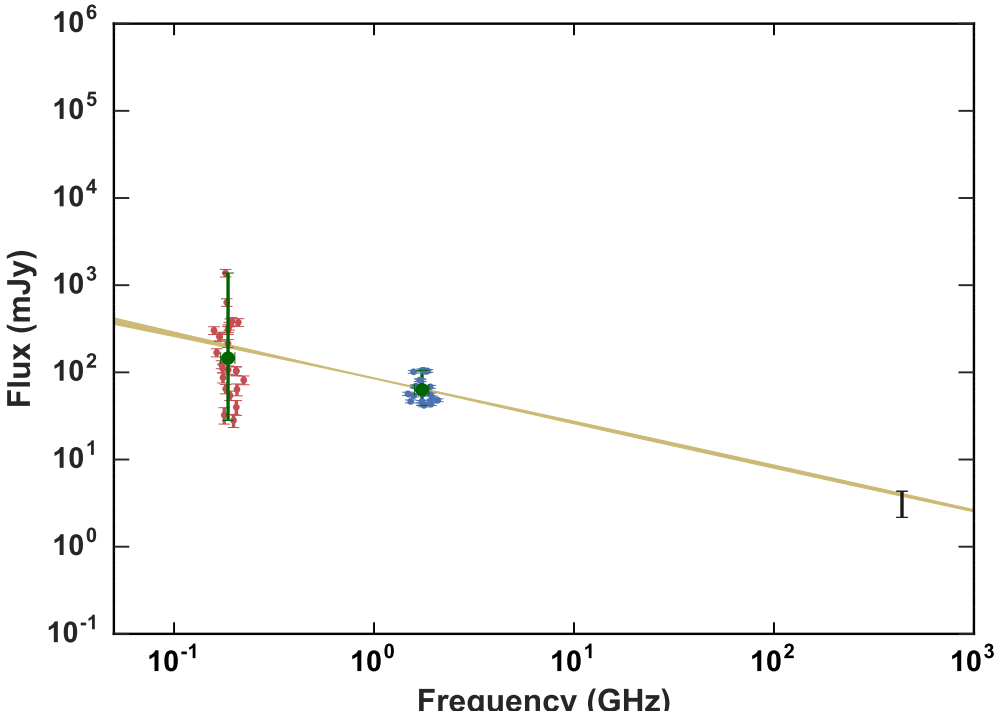

(a) Intermediate Sample (R-II): $41 \leq S_{1.4\,GHz} \leq 111$mJy

Figure 3.2

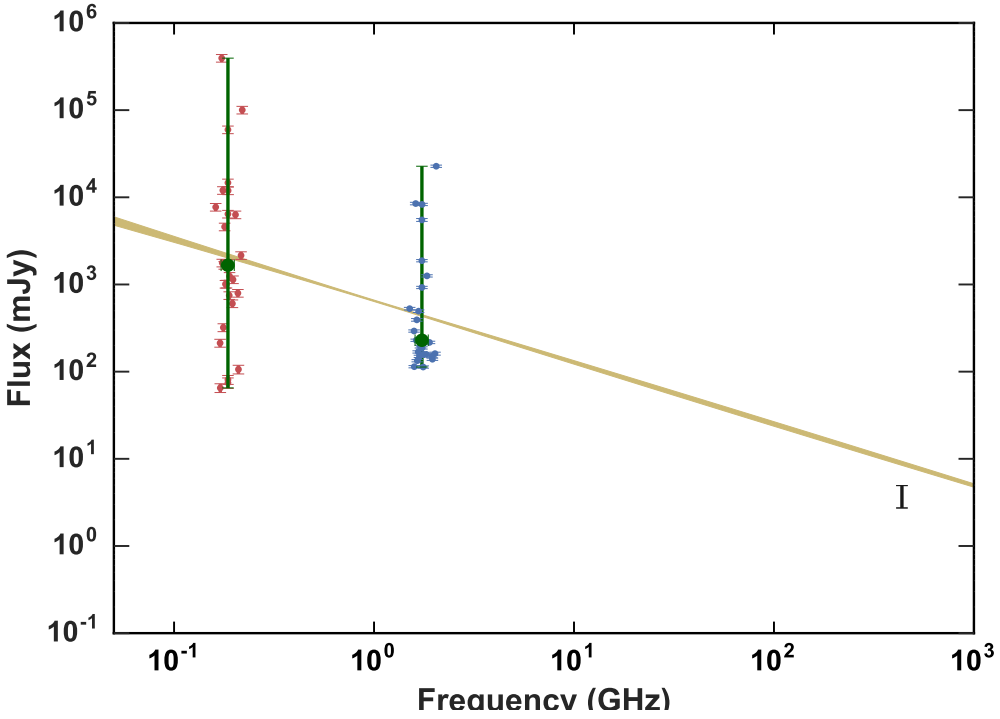

(b) Bright Sample (R-B): $S_{1.4\,GHz} > 111$mJy

Figure 3.3 Red: TGSS-ADR, blue: NVSS, black: SCUBA-2, yellow: the expected Synchrotron emissions with 1σ errors. (a) is the radio faint sample; (b) & (c)the intermediate selection I & II, (d) the 'radio bright' sample. The overlaid bars show the median with range in the flux values and, the mean with standard deviation in frequency. The stacks are binned by their 1.4 GHz data via interquartile ranging. The four stacks clearly show the change in the observed stacked $850\mu m$ flux compared to the predicted where in the R-II and R-B stacks the predicted takes over. This trend is suggestive of a greater power-output from the AGN compared to those fainter bins where it is likely star-formation is the main contributor.

SFR is found to be $4-15\,M_{\odot}yr^{-1}$, increasing with redshift as one would expect approaching the cosmic peak. Within clusters of galaxies, peak X-ray emissions coincides with the BCG [Lin and Mohr, 2004] which may be indicative of cooling flows. These flows may be responsible for the observed star formation, but in the cases of more powerful AGN in some BCGs, the star formation will not be as prominent in the radio and will be hidden by a dominant synchrotron component.

Our individual maps are too shallow in general to detect a lot of this sub-mm emission, but since we observed a large number, and know where the BCG is, we can stack - average the maps together, co-aligned on the BCG - to detect statistical (average) emission. We split our data into 1.4GHz bins and found that in increasing flux intensity radio bins the average $850\mu m$ signal also increases, both in intensity and in the signal-to-noise ratio. In the fainter bins, we see the upper limits of $850\mu m$ emissions above the predicted emission based on the 1.4GHz and 140MHz observations, but as the average radio emission increases, so does the $850\mu m$ emission. We calculated the spectral index values in two ways: fitting and a median of the set. In three faintest bins both methods provide similar results; in the brightest bin the spectral index order deviates significantly and occupy regions above and below the stack value, but this is likely due to the lack of an upper constraint to the bin. Furthermore, Figure 3.4 shows the calculated excess in the $850\mu m$ flux density, the flux density excess increases as the radio power increases. We conclude from our stacking analysis that the emission is primarily synchrotron, produced via an AGN in the central region, similar to the findings in C16 and M16. We note that this does not preclude ongoing active star formation in BCGs, but star formation may well be suppressed by a powerful AGN.

3.4.1 Sunyaev-Zel'dovich Effect Contribution

The Planck Survey satellite [Tauber et al., 2004] builds on the IRAS infrared coverage by obtaining SEDs of the emissions in clusters of galaxies. This sampling complements the IRAS spectral coverage it however does not improve upon the angular resolution; subjecting the submillimeter detections to confusion limitations [Thompson et al., 2007]. Despite Plancks total sky coverage over all wavebands and the high sensitivity of the instrument, the low angular resolution limits Planck's ability to fully subtract the galactic foreground and any secondary anisotropies from the Cosmic Microwave Background (CMB) with respect to submillimeter emitters. Identifying

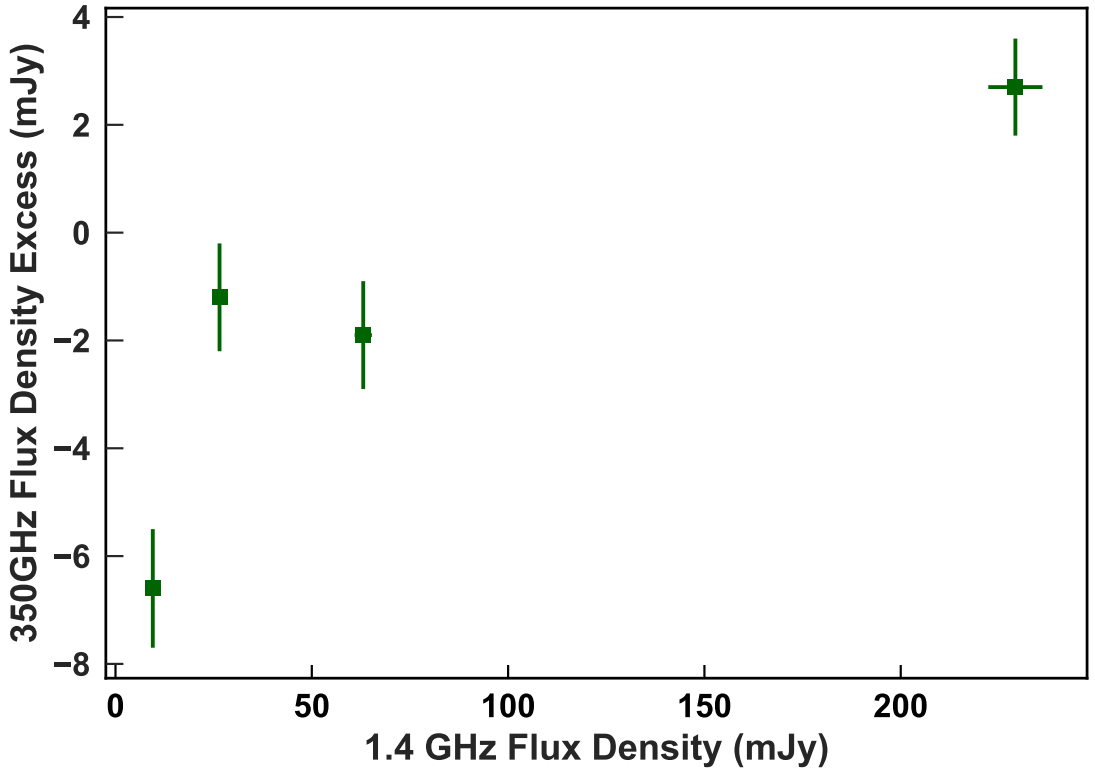

Figure 3.4 The 850μm excess for each IQR bin showing the difference between observed and predicted. The median of each 1.4 GHz IQR bin has been used.

the origin of 850*micron* emission at low redshift ($z < 1$) is an important step for removing contamination from other large scale mm-sub-mm surveys, for example when analysing properties of the Sunyaev-Zel'dovich Effect [SZE; Sunyaev and Zeldovich, 1972]. The SZE arises when dense regions of electrons undergo inverse Compton scattering within clusters of galaxies on the cosmic microwave background causing a redshift independent shift in the observed spectra. The SZE makes a strong contribution at 350GHz, especially when observing clusters and the ICM. Wide field surveys seek to remove the SZE contribution by removal of a contaminate map [i.e., Planck Collaboration et al., 2016]. The advantage of the individual S2CSS maps is each have been filtered as point source maps in the reduction stage. As the SZE is prominent on extended sources, filtering removes any potential SZE excess at 850μm. To confirm this, we calculate an expected SZE contribution at 850μm for an average size cluster ($M_C \approx 10^{14}$) to be $S_{SZe} = 0.03$mJy [see; Sunyaev and Zeldovich, 1980]. Stacking all of the S2CSS maps provides a inverse variance average 850μm flux density, $S_{850\mu m} = 2.16 \pm 0.58$mJy. Two orders of magnitude greater than the predicted SZE contribution thus the SZE has been filtered out.

3.5 Conclusions

Through a stacking analysis of our cross-matched sources from the S2CSS with, both, NVSS and TGSS-ADR the following conclusions have been reached:

1. We obtained radio fluxes for our sources from NVSS and TGSS-ADR, and constructed radio SEDs for various radio bins where we found a match (136 cases). Within four inter-quartile range bins, we stacked the corresponding SCUBA-2 imaging and found that the radio and 850-μm emissions correlate with the radio luminosity, becoming increasingly more intense compared with the 850-μm stacks. It is most probable that we are seeing intense AGN activity in the form of synchrotron emission, which may well be dominating low star formation in the brightest radio sources. However, as the radio intensity decreases we see low significant levels of a submillimetre excess, suggestive of ongoing star formation.

2. By stacking all of the observed clusters we were able to investigate the $850\mu m$ excess without contamination of bright lensed sources. We compare with a calculated expected SZ contribution, for a standard cluster of $M_C \approx 10^{14} M_{\odot}$ the SZ flux desnity contribution would be of order $S_{SZE} \approx 0.03$ mJy, whereas from our stacking analysis a contribution $S_{850\mu m} = 2.16 \pm 0.58$ mJy was found, which is two orders of magnitude greater than expected. We conclude that the emissions in this waveband are dominated by thermal contributions and should be taken into careful consideration in future millimetre/submillimetre surveys when considering the SZ effect in wide field surveys of X-ray bright clusters.

   Our stacking analysis has allowed us to take a further look at the radii-submillimetre properties of a handful of BCGs. The data obtained in this work can be used as reliable indicator of $850\mu m$ emission when observing BCG members in the radio, across two bands by extrapolating from the synchrotron component of a SED.

Chapter 4

AGN Variability in Abell 851

4.1 Introduction

The discovery that every massive galaxy contains a super-massive black hole (SMBH), and that the masses of the stellar bulge and SMBH are correlated [Magorrian et al., 1998, Silk and Rees, 1998] demonstrates that the growth of the central black hole and its host galaxy are inexorably linked. Black hole accretion releases large amounts of feedback energy and momentum into the interstellar medium (and beyond) via collimated jets and fast winds driven from the hot accretion disc, and is thought to be a driving feature in the regulation of stellar mass growth [Bower et al., 2006, Croton et al., 2006]. Active Galactic Nucleus (AGN) feedback is now an established feature of galaxy formation models that are required to correctly reproduce the key observable features of the local galaxy population [e.g., Sijacki et al., 2007, Booth and Schaye, 2009, Fabian, 2012, Ishibashi and Fabian, 2012]

We observe a wide range of nuclear activity in galaxies; from low luminosity or quiescent systems such as Sgr A* at the center of the Milky Way, up to powerful radio galaxies and quasars where AGN feedback can expel large fractions of the gas reservoir and pump energy into the circumgalactic and intergalactic medium [Gaspari et al., 2011, Dubois et al., 2013, Schaye et al., 2015]. This substantial energy input into the local environment is necessary for regulating stellar mass growth on galaxy scales by stifling the cooling of intracluster gas [see; Fabian, 2012], but this must be sustained for many Gyr to maintain the suppression of stellar mass growth in the host galaxy [Dunn and Fabian, 2008]. It is likely that a self-regulating process affects the growth

of the central black hole, as exhibited in numerical simulations [e.g., Springel et al., 2005] and galaxy formation theories [Silk and Rees, 1998, Benson, 2010].

Variability is associated with all AGN from high luminosity quasars to Seyfert galaxies [McHardy et al., 2006]. Low-luminosity AGN (LLAGN), like Sgr A*, M81 [Sakamoto et al., 2001, Schodel et al., 2007], Centaurus A [Israel et al., 2008] and, NGC7469 [Baldi et al., 2015] have relatively low Eddington rates ($L \approx 0.1\,L_{\rm Edd}$) and often exhibit bright inverted/flat cm-mm spectra likely originating from a compact core [e.g. Behar et al., 2018]. Recent advances in mm-interferometry in resolution and sensitivity make the detection of such LLAGN more probable. Indeed, work by Doi et al., 2011 supports the view that many large passive galaxies have compact millimetre cores with significant variable radio activity at their cores, but few systematic searches for such LLAGN have yet been made, and in general the detection and monitoring of AGN variability requires multiple observations over weeks to decades.

Here we present evidence of a variable AGN in the well known cluster Abell 851 (also known as CL 0939+4713), a rich [Seitz et al., 1996] cluster ($M \sim 10^{14} M_\odot$ at $z = 0.411$ containing several hundred spectroscopically classified members [Dressler and Gunn, 1992]. The galaxy in question is a possible Sa/S0 transition object close to the cluster centre, catalogued by Dressler & Gunn (1992) as object 311 and hence referred to in this paper as dg92_311. dg92_311 is optically classified as an early-type disc (Sa/S0) with post-starburst spectral features; namely weak nebular emission but relatively strong Balmer absorption [k+a spectral type having Balmer absorption but little-to-no emission spectra Belloni et al., 1995, Dressler et al., 1999, Oemler Jr et al., 2009]. In this Letter we present the observational evidence for a variable AGN across the radio-far-infrared spectral energy distribution of dg92_311, including new 3 mm IRAM Plateau de Bure interferometer and new 1.9 cm Arcminute Microkelvin Imager observations.

4.2 Data Collection and Analysis

We make use of a number of archival observations of dg92_311 including *WISE* $3.4-22\mu m$, *Hershel* PACS and SPIRE 100–500μm, James Clerk Maxwell Telescope (JCMT) SCUBA 850μm (project M00BH05), NOEMA 3 mm, BIMA 1.05 cm, AMI 1.9 cm and, VLA/FIRST $6.2-21$ cm band archives. The *HST*/ACS F814W filter optical imaging is shown in Figure 4.1 (data retrieved from the MAST archive HST, project 10418). We report the various flux density measurements of dg92_311 in Table 4.1.

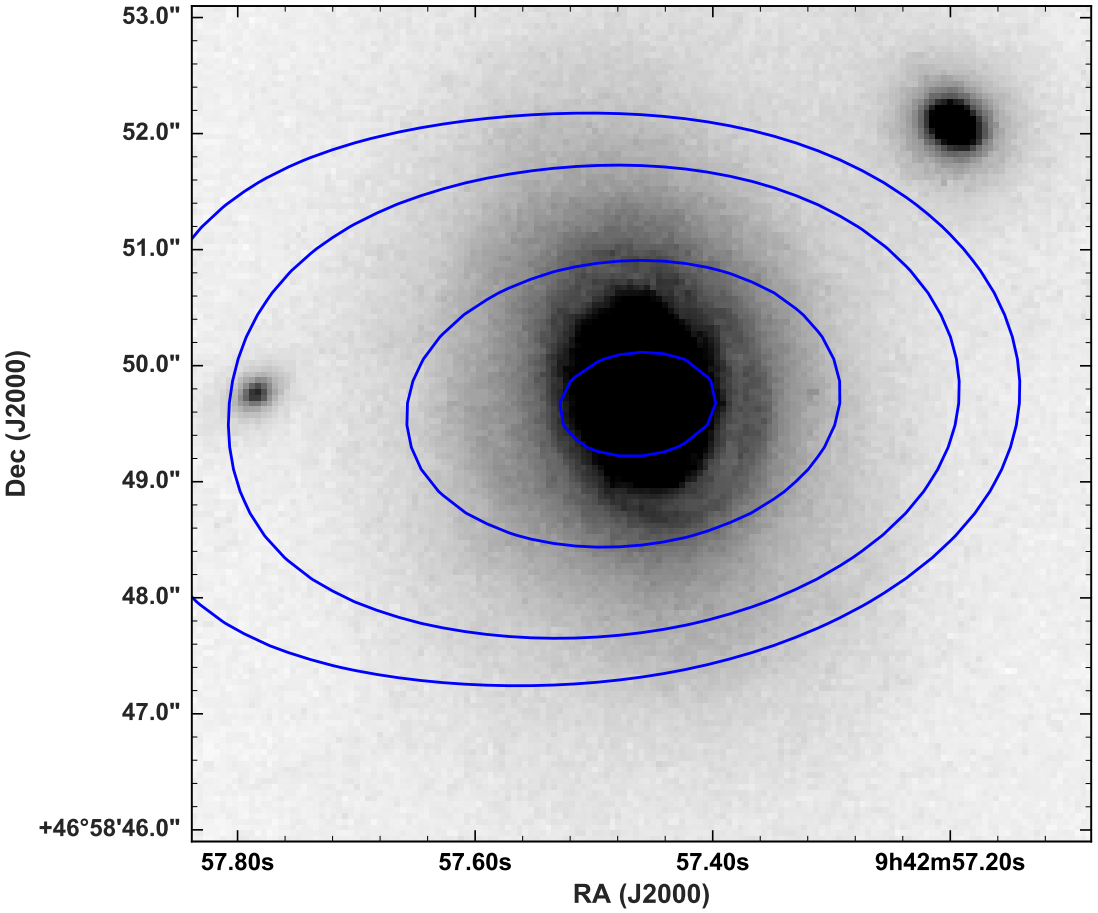

Figure 4.1 The archival *HST*/ACS F814W filter optical imaging. dg92_311 is optically classified as a k+a spectral type having Balmer absorption but little-to-no emission spectra, morphologically dg92_311 is a Sa/S0 late-type post-star-burst spiral galaxy. dg92_311 is located α; $09^{h}\,42^{m}\,57.50^{s}$, δ; $46^{d}\,48^{m}\,50.00^{s}$. The NOEMA primary beam corrected significance contours are overlayed, initiated at 1.05 mJy (3σ) and increase in 1σ intervals. We find a corrected (see Section 4.2.2 peak flux density of $S_{3.6mm}1.59 \pm 0.15$ mJy.

4.2.1 Archival Data

4.2.1.1 JCMT/SCUBA

Observations of dg92_311 with the JCMT equipped with the SCUBA detection array at 850 μm were conducted on the 27th November 2000. The target was observed in the 'jiggle' map mode used for observing sources smaller than the SCUBA-2 bolometer array [Jenness et al., 2000]. The target is formally undetected in the archival map, and so we determine an upper limit by sampling a large number of random pixels around the source position and fit a Gaussian to the resulting pixel distribution. We take the standard deviation of the Gaussian as a measure the 1σ noise, and determine a 3σ upper limit of $S_{850\mu m} < 4.6$ mJy for dg92_311.

4.2.1.2 Herschel Lensing Survey

The *Herschel* Lensing Survey [HLS Egami et al., 2010] observed Abell 851 with the PACS (100 and 160 μm) and SPIRE (250, 350 and 500 μm) instruments. These far-IR/sub-mm bands are useful to constrain the peak of the thermal dust emission. Rawle et al. [2012] analyse a number of BCGs from the HLS including A851. Photometry in the SPIRE bands was reduced by using the `IRAF` package `ALLSTAR` [Tody, 1993] by fitting the Point Spread Function to source locations. In the PACS bands flux densities were measured by using aperture photometry with the use of `SEXTRACTOR` [Bertin and Arnouts, 1996]; methods are described in detail in Rawle et al.. dg92_311 was detected in all but the 500 μm band, and we report the measurements in Table 4.1.

4.2.2 NOEMA observations

In project S14BV (PI: Geach), we observed dg92_311 as part of a larger 3 mm mosaic of Abell 851 to search for CO J(1–0) emission associated with cluster members (e.g. Geach et al. 2009). Abell 851 was observed in configuration D (baseline separations up to 150 m) for maximum sensitivity. We adopted a similar set up to Geach et al. (2009), where the 3 mm receiver was set to the frequency of the redshifted CO(1–0) line at the redshift of the cluster, and the correlator was set up with 2.5-MHz spacing (2×64 channels, 320-MHz bandwidth). The data were reduced using the standard Grenoble Image and Line Data Analysis Software (GILDAS[1]) and converted to a UVFITS data table for imaging in the CASA environment [McMullin et al., 2007]. The 3 mm continuum detection became obvious in a channel-by-channel inspection of the data cube. We note the source lies close to the edge of the 50″ primary beam, and we apply an appropriate primary beam correction to measure a flux density $S_{3.6\,\mathrm{mm}} = 2.6 \pm 0.4\,\mathrm{mJy}$. The 3 mm contours are overlaid on *HST*/ACS optical imaging in Figure 4.1.

4.2.3 The Arcminute Microkelvin Imager

The Arcminute Microkelvin Imager [AMI; Zwart et al., 2008, Hickish et al., 2018] is a dual aperture-synthesis array that operates between $13.9 - 18.2$GHz with 2048 channels. The principle use of the AMI detector is for imaging the Sunyaev-Zel'dovich effect by observing galaxy clusters. However, we make use of the instrument for its favourable bandwidth for observations

[1] http://www.iram.fr/IRAMFR/GILDAS

pointed at A851. dg92_311 was observed by AMI on the 4$^{\text{th}}$ October 2017 with an integration time of 7200 s, we make use of AMI-LA with angular resolution of $30''$ using seven of the eight 12.8 m diameter dishes.

The AMI-LA data were calibrated and imaged in CASA. Primary calibration was performed using a nearby observation of 3C 286, using the Perley and Butler, 2013a flux density scale along with a correction for the fact that AMI measures I+Q, using the polarization fraction and angle fits from Perley and Butler, 2013b; this is an $\approx 4.5\%$ correction for 3C 286 over the AMI band. The primary calibration observation supplied an instrumental bandpass in both phase and amplitude. This was applied to the target data, as well as a correction for atmospheric amplitude variations produced by the 'rain gauge', which is a noise injection system used to measure the atmospheric noise contribution [see; Zwart et al., 2008]. The nearby bright point source 5C 5.175 was observed throughout the observation in an interleaved manner and was used to correct for atmospheric and/or instrumental phase drift. After narrow-band RFI flagging, the data were binned down to 64 channels to reduce processing time and imaged at the central frequency, 15.5 GHz. We used the 'clean' task, using multi-frequency synthesis with nterms=2 which allows for a frequency dependence of the sky brightness. We used the CASA graphical Gaussian fitting task on the resulting image to confirm that the source was unresolved and measure a peak flux density of signal of $S_{1.9\,\text{cm}} = 3.46 \pm 0.09\,\text{mJy}$ including thermal noise and a 5% systematic error estimate at 15.5GHz (1.9cm). Hurley-Walker et al., 2012 (HW12) also observed cluster A851 in 2012 with AMI-LA reporting $S_{\text{LA}} = 2.2 \pm 0.1$ at the position of dg92_311 (Table 12, ID B in HW12) we include both results in Table 4.1.

Table 4.1. Observed bands for dg92_311 Abell 851, the flux density (S) and uncertainty (ΔS) for each wavelength is provided in column 3 and 4.

Instrument	Angular Resolution	Wavelength	S (mJy)	ΔS mJy)	Reference	Observation Date (YYYY-MM-DD)
WISE	6.1”	$3.4\mu m$	0.48	0.02	Wright et al., 2010	2010-2013
WISE	6..4”	$4.6\mu m$	0.31	0.02	Wright et al., 2010	2010-2013
WISE	6.5”	$12\mu m$	0.60	0.17	Wright et al., 2010	2010-2013
WISE	12”	$22\mu m$	< 3.0	—	Wright et al., 2010	2010-2013
PACS	8”	$100\mu m$	23.7	0.3	Rawle et al., 2012	2003-07-01
PACS	13”	$160\mu m$	25.3	0.7	Rawle et al., 2012	2003-07-01
SPIRE	18”	$250\mu m$	20.5	5.5	Rawle et al., 2012	2003-07-01
SPIRE	25”	$350\mu m$	12.3	6.2	Rawle et al., 2012	2003-07-01
SPIRE	36”	$500\mu m$	$<$11.0	—	Rawle et al., 2012	2003-07-01
SCUBA	14”	$850\mu m$	< 4.6	—	Smail et al., 2002	2000-11-27
IRAM PdBI	0.5”	3.6 mm	2.59	0.40	This work	2014-06-07
BIMA	23”	1.05 cm	1.06	0.15	Coble et al., 2007	1997-07-15
AMI-LA	30 ”	1.9cm	2.2	0.1	Hurley-Walker et al., 2012	2008-2009
AMI-LA	30”	1.9cm	3.46	0.09	This work	2017-10-04

Table 4.1 (cont'd)

Instrument	Angular Resolution	Wavelength	S (mJy)	ΔS mJy)	Reference	Observation Date (YYYY-MM-DD)
VLA	4"	6.2 cm	3.01	0.14	Archive[3]	1990-12-01
VLA	4"	6.2 cm	2.79	0.03	Archive[3]	1993-08-28
VLA	4"	21 cm	1.6	0.16	Morrison, 1999	1996-01-06
VLA/FIRST	4"	21 cm	2.13	0.31	White et al., 1997	1997-03-25
VLA	4"	21 cm	3.1	0.2	Condon et al., 1990	1987-05-23

[3]https://science.nrao.edu/facilities/vla/archive/index

4.3 Analysis and discussion

4.3.1 Spectral energy distribution

In Figure 4.2 we construct the spectral energy distribution using the data in Table 4.1 and fit three components spanning the radio, sub-mm and far-IR bands. Note that, despite the data spanning a range of angular resolutions, all observations are unresolved for dg92_311 and a comparison of the beam sizes to the optical imaging of dg92_311 shows that we are in all cases measuring galaxy-integrated flux densities with negligible contamination from neighbouring or background sources.

The *Herschel* $100-350\mu m$ flux density measurements allow for a simple least squares fit of an isothermal modified blackbody, where we employ a standard emissivity term, $\beta = 1.5$ [Hildebrand, 1983, Casey, 2012], allowing dust temperature as the free parameter. We find a best-fit dust temperature of $T_D = 24$ K, consistent with the S0 morphological–temperature results found by Bendo et al., 2003. We consider a two-component temperature fit, but as the single temperature is only barely constrained by the detections and the two-component fit is considered tenuous we suggest following up with higher resolution observations. We also make use of the well known FIR/sub-mm templates described by Dale and Helou, 2002 to fit the $100-350\mu m$ data. We normalise to the $160\mu m$ PACS detection as it lies near the peak of the thermal emission and we overlay the template which is best suited to the *Herschel* data (corresponding to a power law index of $\alpha = 1.875$), as a solid black curve (We show three other example fits in AppendixE).

In the radio bands the spectral index of the synchrotron power law component is estimated from the ratio of the most recent NOEMA 3 mm and the average AMI 1.9 cm observations, giving $\alpha \approx -0.1$ for $S \propto \nu^{\alpha}$. We overlay a grey hashed region onto Figure 4.2 to represent the range of flux density normalisations that fit the full range of radio observations up to the Rayleigh-Jeans tail of the thermal dust emission. While it is very likely that the synchrotron component will have some spectral curvature over the three orders of magnitude in frequency plotted Hogan et al., 2015a, as we lack simultaneous observations over the full spectral range then we must interpret any variability assuming a single power law index, as we discuss in the next section.

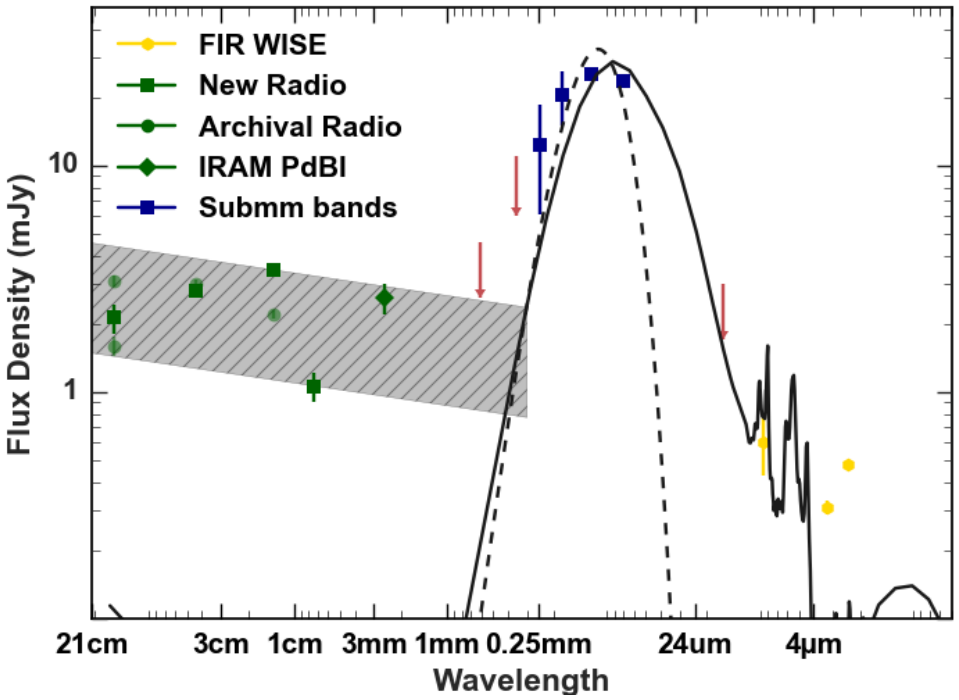

Figure 4.2 The rest-frame spectral energy distribution for dg92_311. The blue squares cover the sub-mm wavebands: 100, 160, 250, 350, 500, 850μm, the green diamond is the imaged IRAM PdBI 3.6mm detection, the gold hexagons are the FIR WISE bands, green squares are the most recent radio observations whereas the fainter green circles are historic observations (listed in Table 4.1). The shaded region shows the synchrotron emission amplitude range of a source with $\alpha \approx -0.1$ over two decades, the black dashed line is thermal blackbody component fit with a characteristic temperature of T$=$ 24 K and, finally, the black solid line is a PACS 160μm normalised template from Dale and Helou, 2002

4.3.2 Variability

The radio light curves with observations from VLA, BIMA, AMI and NOEMA spanning near two decades in time is shown in Figure 4.3. The source exhibits a flat spectrum over 1.4–82 GHz range and is unlikely to be extended on the >few arcsecond scales of the resolution of the majority of observations (Table 1). Although none of these data were taken simultaneously, it is clear that over the 1.4–82 GHz frequency range covered there has been a significant change in the normalisation of the power-law synchrotron component over the past 20–30 years. The source varies at the same frequency and resolution in data from both the VLA at 1.4 GHz and AMI-LA at 15 GHz; furthermore, the NOEMA data has better angular resolution than the BIMA and AMI-LA data but is brighter than all but the most recent AMI-LA point. If flux density were being missed on larger scales, then one would expect the 3 mm point to be fainter. The source appears to have been at a minimum around the year 2000 and has gradually increased in

brightness by a factor of more than three in the past 18 years. We argue that the observed radio variability is intrinsic to the source.

This magnitude and timescale for radio variability is observed in local BCGs such as NGC1275 in the Perseus cluster [Dutson et al., 2014] and a sample of bright, flat spectrum cores monitored with the OVRO 40m [Hogan et al., 2015a]. All of these variable BCGs are found in dusty BCGs with luminous optical lines in cool core clusters [Hogan et al., 2015a] with no evidence for jet contribution. As can be seen from the *HST* optical imaging in Figure 4.1, dg92_311 does exhibit dust lanes and the bright sub-mm detections across the *Herschel* bands indicate the presence of dust in the interstellar medium. dg92_311 does not exhibit any significant Hα line emission [Koyama et al., 2011] and, although there is no *Chandra* observation of A851 and dg92_311 falls on a chip-gap of the EPIC camera in the only on-axis pointing with *XMM-Newton*, the wider structure of the cluster in the X-ray from ROSAT [Schindler et al., 1998] suggests that any cool core in A851 is weak. On this basis dg92_311 is atypical of BCGs with a strong radio core. The observed radio power of dg92_311 of $\approx 10^{24}$ W Hz^{-1} implies that it falls in the upper quartile of core radio power of all X-ray luminous clusters [Hogan et al., 2015b] with a cool core or in the uppermost 3% of core radio power for BCGs without a surrounding cool core. Work by Torniainen et al., 2005 and **?** present results on the variability of GPS and flat spectrum sources. These imply that the BCG in dg92_311 shares the properties of radio sources and so could be considered a BL Lacertae object, however it would be an unusual case as it has a relatively low and optical and X-ray flux compared to the radio flux. While the observed radio variability could be due to a jet, the similarity in its amplitude and time-scale implies a similar origin for the core emission in other BCGs. Therefore dg92_311 is an important system that may have an unusual X-ray environment, and therefore more detailed X-ray follow-up is required to determine the properties of the intracluster gas on scales of tens of kpc around the BCG.

4.4 Conclusion

Optically, dg92_311 appears to be a relatively unremarkable, dusty early-type disc galaxy (Sa/S0) but when observed in the radio–submillimetre this optically inactive galaxy appears to contain a relatively powerful, variable LLAGN in what is the Brightest Cluster Galaxy in a rich cluster. While the variability of a factor of three on decade timescales is consistent with other BCGs, the lack of a prominent cool core in the host cluster is surprising and highlights the need to assess the temporal behaviour of all massive galaxies in cluster cores, particularly in the millimetre

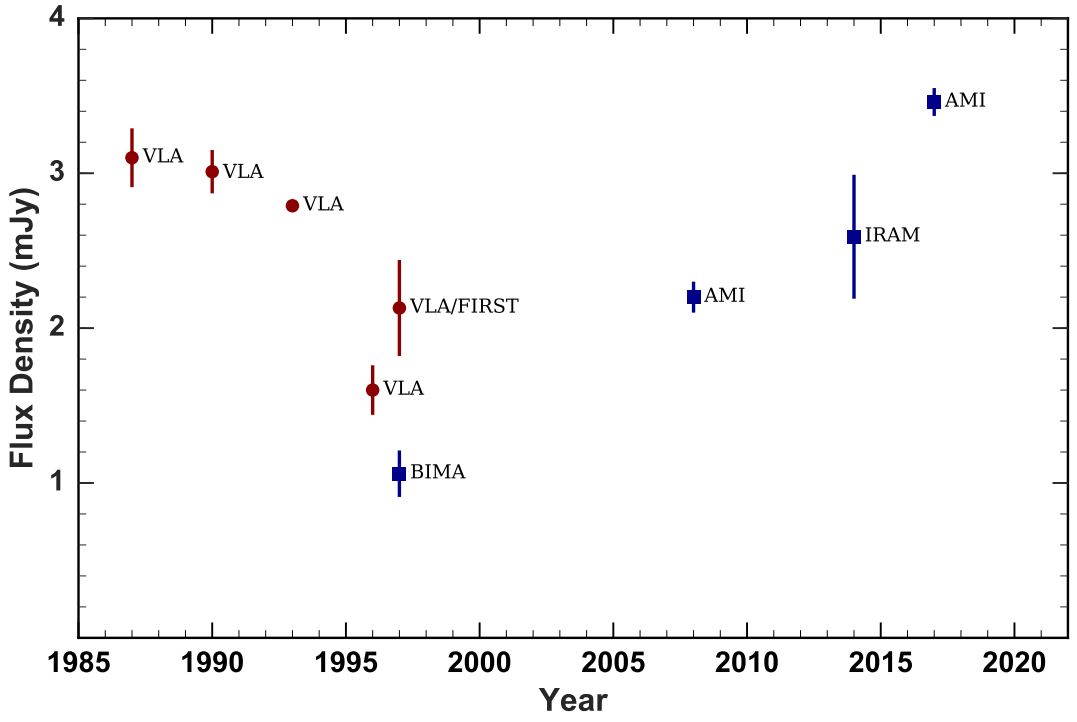

Figure 4.3 Two decades of radio data from VLA, BIMA, AMI and IRAM reveals an up-turn in the BCG light curve. We derive out spectral index from the most recent observations by AMI and IRAM-PdBI. Red squares indicate data $<$ 10 GHz and, blue circles $\geq$ 10 GHz. It is clear from the figure that at $<$ 10 GHz there has been a gradual decline in luminosity but in bands $\geq$ 10 GHz there is evidence of an increase.

wavelengths, to ascertain the underlying level radio mode regulatory feedback in massive clusters.

Chapter 5

Conclusions

Understanding how our Universe has evolved is an important question for astronomy. Submillimeter galaxies are a key cosmological probe; selected at long wavelengths that observe the thermal dust emission and allowing a large cosmic column to be probed, as at a fixed luminosity a SMG has the near equal observable flux density across a range of redshifts [$z \approx 0.5 - 10$ Blain et al., 2002]. SMGs when observed directly are of a low luminosity (few mJy) but gravitationally lensing of galaxies offers an opportunity to observe these massive gas-rich star forming systems with magnification 10-30$\times$. However, gravitationally lensed galaxies are exceptionally rare, even more so are those which are highly magnified bright systems. By observing the most massive gravitationally bound systems, clusters of galaxies, allows for a chance of hunting examples of brightly lensed galaxies. The S2CSS successfully observed 202 X-ray luminous MACs clusters exposed for 30-min observations with the SCUBA-2 instrument mounted on the JCMT in weather bands 4 and 5 over the period August 2012 - July 2013; an effort to hunt for these exceptionally bright lensed SMGs. 78 sources have been identified with a SCUBA-2 only sub-mm component with IR luminosity too high to be of local origin, and 19 with both SCUBA-2 and SPIRE band photometry co-located, forming a catalogue of 97 lensed candidates. A further three sources were purposefully targeted (MACSJ0600.1-2008, MACSJ0455.2+0657 and MACSJ0326.8-0043) as they have previously been identified in the HLS as bright SPIRE band sources. One other source, the Cosmic Eyelash (MACSJ2135.2-0102), was also targeted to assess our chosen method of data extraction. These sources are important candidates for follow up to investigate further the contributions of the EBL, the nature of the high redshift SMG population. Indeed, follows up of the Cosmic Eyelash, considerable amounts of information has been extracted: insights into the properties of the cold and dense ISM [see; Danielson et al.,

2011, 2013], probing star-forming cloud complexes [Thomson et al., 2015] and molecular outflows [George et al., 2014]. In the Cosmic Eyelash, the molecular ISM has been resolved into large, 100 pc scale clumps that may be overlapping molecular cloud regions where the volume averaged efficiency of star formation might be higher than in local galaxies due to the greater density of the gas reservoirs (e.g. Swinbank et al. 2011). If the S2CSS catalogue provides additional lensed systems for follow up, the access to spatial scales will facilitate the amplification of fainter of exotic molecular and atomic tracers of the dense ISM, it will be possible to study the astrophysics of star formation in systems close to the peak epoch of galaxy formation at a level rivalling resolved studies of star formation in local galaxies. A proposal to follow up a number of dim $> 4\sigma$ sources was accepted for follow up observations by the JCMT for Semester 18B (ID: M18BP056, PI: Ryan Cheale). A total of 37 targets will be observed in 30-min integrations using the standard CV DAISY pattern in at least JCMT band 3 weather ($225-$ GHz opacity $0.08 < \tau < 0.12$) aiming to achieve $> 6\sigma$ confirmation of our low luminosity sample, in doing so there is the exciting possibility for a number to be revealed as high redshift SMGs.

Clusters exhibit the Sunyaev-Zel'dovich effect, a well studied phenomenon of CMB photons inversely Compton scattered by the hot intra-cluster gas visible as an extended source and serving as a useful probe of cluster properties [Carlstrom et al., 2002]. However, the SZE increment peaks at ≈ 350 GHz, coincident with the SCUBA-2 band pass which means that the S2CSS having 202 30-min exposures of high-mass clusters centers at $850\mu m$ is the ideal data set to investigate the average 350 GHz properties of BCGs. The observations are point sources and as the SZE is an extended feature it is filtered out by design of the survey. But, by stacking all of the maps on each BCG (determined from their optical position) it is possible to obtain the average thermal emission power of high-mass clusters which can then be subtracted out of a SZE analysis. Using standard cluster mass, $M_{\odot} \approx 10^{14}$ the SZE contribution is of order $S_{SZE} = 0.03$ mJy; stacking all cluster maps at $850\mu m$ gives a thermal contribution of $S_{850\mu m} = 2.16 \pm 0.58$ mJy, thus when constructing a SZE analysis of any high-mass cluster the thermal component must be taken into account. We know that BCGs harbour AGN, possibly reserves of cold gas and some on-going star formation. All of these might cause (directly or indirectly) submm emission. This hasn't been well-explored in a large sample like ours - we'd like to know about the properties of AGN in central cluster galaxies from the point of view of their feedback affects the surrounding cluster gas (radio maintenance feedback), and to know more about their star formation history (traditional view being that BCGs are big red and dead ellipticals that ceased SF long ago). Our individual maps are too shallow in general to detect a lot of this sub-mm emission, but since we

observed a large number, and know where the BCG is, we can stack - average the maps together, co-aligned on the BCG - to detect statistical (average) emission. We construct SEDs using data from the NVSS and TGSS-ADR (which have a large number of co-located observations) and combine it with 1.4 GHZ binned stacked SCUBA-2 maps. From the S2CSS there were 105 co-located observations with the NVSS and TGSS-ADR and data was split equally into four bins by their 1.4 GHz luminosity and labelled as Radio Faint (RF) , Radio - I/II (RI/RII) and Radio Bright (RB). The S2CSS maps were stacked in their respective bins with the two faintest bins simply having upper limits and, the brighter bins a 3σ and a $> 3.5\sigma$ peak at $850\mu m$ Two spectral index analyses were conducted, a) the median spectral index of each individual spectral index and, b) a least squares fitted spectral index for each bin. The spectral indicies (α) approach a flatter state ($\alpha \rightarrow 0$) in the first three bins, but due to the large variance in the brightest bin the trend turns over. However, in spite of the fact that the turn over is associated with lack of constraints, there may well be a different mechanism involved, i.e., that more powerful AGN or star formation are causing a spectrum shift.

The most luninious member of a cluster within 3-arcsec of the X-ray peak is known as the Brightest Cluster Galaxy (BCG) and traditionally features powerful radio jets/lobes or intense star formation regions. In a recent IRAM PdBI project (S14BV), intended to perform a blind search for CO(1–0) in galaxies within the cluster Abell 851, a serendipitous detection of an extremely bright 3-mm point source co-located with the relatively unremarkable, dusty early-type disc galaxy (Sa/S0) BCG was identified. Using over 18 years of archival data from the VLA, BIMA, AMI and NOEMA and recent AMI observations a multi-band SED, with data ranging from 1.4 GHz to $4\mu m$, revealed the BCG to contain a relatively powerful, variable (factor of three on decade time-scales) Low Luminosity AGN (LLAGN). The data was not taking simultaneously but combining the dataset showed clear signs that there has been a significant shift in the Synchrotron component produced by the AGN over the last three decades. The variability of the BCG is not atypical, but unlike typical LLAGN it lacks a prominent cool core. Other local BCGs (e.g. NGC1275 [Dutson et al., 2014]) have too displayed variability whilst being in a dusty environment with luminious optical lines. Abell-851 lacks any significant Hα emission [Koyama et al., 2011] and though there is no X-ray observation with Chandra nor the EPIC camera on board XMM-Newton as the BCG fell on the chip gap, the only on-axis pointing with ROSAT found no significant X-ray emission suggesting a weak cool core. The observed radio power of Abell-851 of $\approx 10^{24}$ W Hz^{-1} implies that it falls in the upper quartile of core radio power of all X-ray luminous clusters [Hogan et al., 2015b] with a cool core or in the uppermost

3% of core radio power for BCGs without a surrounding cool core. While the observed radio variability could be due to a jet, the similarity in its amplitude and time-scale implies a similar origin for the core emission in other BCGs. The implication of the BCG being variable but seemingly lacking a cool core requires more detailed radio and X-ray observations to probe the properties of the intra-cluster gas and reveal the BCG's environment.

The combined datasets from the S2CSS-I and the re-observed sources are well suited for further follow up observations with high-resolution instruments such as ALMA or NOEMA. Observations with additional instruments will allow for joint analyses with simulations, as the catalogue contains potentially brightly lensed objects at high signal-to-noise. High signal-to-noise of these objects could not be achieved by direct observation; utilising the catalogue effectively, will allow for galaxy integrated properties to be compared with simulation outputs. There is potential for detecting rare isotopologues (e.g. $HC^{18}O^{+}$, $H^{13}CO^{+}$, $^{13}CO(5\text{-}4)$) in the densest molecular regions within high-redshift SMGs and although the lines will be faint, even in lensed systems, could yield insights into chemical abundances in the galaxy through isotopic ratio analysis. Many of these lines will be associated with the densest nodes of the molecular reservoir (e.g. Papadopoulos 2007) and cannot be detected in non-lensed galxies. Furthermore, the detection of these rare isotopologues would allow further study into the the average conditions of the actively star-forming gas (average density, thermal properties, radiation field, cosmic ray irradiation). Radiative transfer work will become more realistic with a broader range of line transfers included and excitingly may reveal the preceding star-forming physical conditions of the ISM. Furthermore, as with the Cosmic Eyelash, many of the objects detected may allow for resolving ISM structure which would otherwise be fraught with challenges without the strong lensing effect of clusters. The data produced by this thesis will deliver a large sample of eyelash-like systems to provide a more comprehensive empirical foundation for co-investigation of many interesting features of the nature of high-z cold gas reservoirs.

Chapter 6

Future Work

The SCUBA-2 Cluster Snapshot Survey (S2CSS, Chapter 2) aimed to hunt for the brightest lensed galaxies by exploiting the highest mass clusters in the local Universe. The success of the program has led to two follow up project; the first, an extension of the original S2CSS aimed at confirming a number of potentially lensed galaxies which fell beneath a coarse selection criterion but formally were $> 4\sigma$ or sources exceeding 80% completeness in the central deep regions of the SCUBA-2 maps. In either case following up the sources is of great interest to improve on the uncertainty at the faint end of the derived number counts.

6.1 SCUBA-2 Cluster Snapshot Survey II - confirming a sample of lensed submillimeter galaxies

6.1.1 Scientific Context

Gravitational lensing by clusters [Blain, 1997] opened the doors to high resolution observations of the SubMillimetre Galaxy (SMG) population, offering insight into the actual astrophysics of high redshift galaxies at an unprecedented level of detail that would be otherwise impossible [Casey et al., 2014]. Lenses are particularly advantageous for submillimetre observations as the sensitivity of submillimetre instrumentation struggles to resolve high redshift faint, un-lensed SMGs thus hindering our ability to probe their structure and properties in detail. Perhaps the most famous example of a lensed SMG is the 'Cosmic Eyelash', at $z = 2.3$ and boasting a $32\times$ magnification with $S_{870} \approx 100$mJy [Swinbank et al., 2010]. This source alone has turned out

to be a treasure trove of information to astronomers, providing insight into the cold ISM mass, density structure, kinematics and chemistry [Danielson et al., 2011, 2013].

Systems such as the Eyelash are notoriously rare – indeed, $< 1\%$ of the clusters in the MAC survey revealed a bright, potentially, lensed system – but, by focusing efforts on observing high mass clusters we can increase the probability of detecting them [e.g. Smail et al., 1997]. Highly lensed SMGs open up the exciting possibility to follow up bright sources with instruments such as ALMA and actually resolve the structure of the ISM at scales which would be near-impossible in non-lensed SMGs. The greater the number of confirmed lensed SMGs the better our understanding of the high redshift Universe becomes [e.g.; Danielson et al., 2011, 2013].

The SCUBA-2 Cluster Snapshot Survey (S2CSS) main targets are high-mass X-ray selected clusters of galaxies visible by the JCMT; these are the most massive targets currently available to maximize the probability of detecting lensed background sources. Specifically, we targeted clusters with the highest X-ray luminosities ($L_X \geqslant 4 \times 10^{44}$ erg s^{-1}, 0.1-2.4 keV) from the ROSAT All-Sky Survey. The clusters were selected from the BCS [Ebeling et al., 1998], eBCS [Ebeling et al., 2000], REFLEX [Böhringer et al., 2004] and MACS [MACS; Ebeling et al., 2001, 2013] samples, which constitute the most X-ray luminous, and therefore most massive, clusters in the local universe ($z \approx 0.5$). The majority of this sample matched the cluster selection for the Herschel Lensing Survey Snapshot-I sample which comprises of 279 clusters from the X-ray samples that had not already been scheduled on Herschel in the first two cycles [HLS; Egami et al., 2010]. Of these clusters, 216 are visible from Mauna Kea ($\delta >$-30°) and 202 were successfully observed in the S2CSS-I.

In semesters 14A and 14B a total of 145.5 hours were awarded in bands 4 and 5 as a bad weather filler project. As such it was very successful and all submitted targets were observed. While the very broad range of conditions that Bands 4 and 5 cover returns maps of quite different sensitivity, the depth of all maps were such that we could detect sources as bright as the Eyelash in our maps. The S2CSS resulted in 106 significant ($> 4\sigma$) detections at 850μm following a coarse selection procedure (See; [Cheale et al., 2019] for criteria). Eight were co-located with the target cluster BCG (also confirmed by Hogan et al., 2015a), 20 had bright SPIRE counterparts (matched to the HLS) and 78 were bright, $S_{850} > 15$ mJy, SCUBA-2 only detections. The original S2CSS was undertaken in JCMT weather Band 4–5 conditions with mean opacity $\tau_{225\mathrm{GHz}} = 0.19 \pm 0.08$. Doing so had the benefit of seeing all of the brightest sources so a statistically meaningful number count of sources brighter than $20 - 40$ mJy can be determined for

this sample of clusters (see Chapter 2, Figure2.5).

However, the derived number counts are uncertain at the fainter fluxes where dimmer sources will have been missed out of the catalog by the selection criteria and there is potential for spurious sources to have made their way in. By re-observing the most significant ($> 4\sigma$) in the central deep region of the SCUBA-2 mapping we will obtain higher signal-to-noise detection or rule out the candidate as a spurious detection. Either way these additional observations will allow for the lensed source counts to be refined sufficiently that they can be directly compared with lensed sources found with ALMA in clusters [e.g. Swinbank et al., 2012, Nagao et al., 2012, Simpson et al., 2014, 2015, ALMA Partnership et al., 2015, Danielson et al., 2017].

The number counts derived for the S2CSS survey split for the SCUBA-2 only and SCUBA2/SPIRE detections are shown in Figure 2.5. The results show a significantly flatter slope to the counts for the central $1'$ as would be expected for the strongly lensed sources detected in the core. The number counts show that there are very few $> 5\sigma$ sources without a SPIRE counterpart, particularly within the central $1'$ region. The higher fraction of $4 < \sigma < 5$ sources in this exclusively 850μm detected sample compared to those with a SPIRE counterpart suggests that more spurious sources are present. However, the possibility that at least some of these sources are at high redshift ($z > 4$) means this sample deserves careful follow-up.

The proposal submitted was such that the observations of 37 sources are to be conducted in JCMT weather band 3 conditions or better ($225-$GHz opacity $0.08 < \tau < 0.12$) making use of the CV Daisy pattern which will aid in confirming their nature. With 15 sources having flux densities $>$ 20mJy, at a radius R$< 1'$ from the center of each map and 22 $>$ 40mJy, R$< 3'$ to observe, there is the exciting possibility of detecting a number of potentially $z > 4$, $> 6\sigma$ lensed SMGs. Achieving this follow-up will increase the number of known lensed objects, an absolute necessity for improving current RT modelling [e.g. Narayanan et al., 2010, Krumholz, 2014] by comparing real resolved interferometric observations to synthetic observations.

Large Velocity Gradient (LVG) modeling is used to investigate galaxy integrated SLED for various properties (e.g. gas temperature, molecular abundances etc.) which are intrinsically linked to the CO transitions and therefore the galaxy environment which drives star-formation [Narayanan and Krumholz, 2014]. Successful observations of the Cosmic Eyelash's SLED has shown that star formation may potentially be dominated by high mass stars. LVG modelling has been suggestive of a hot (T$>$ 100 K) ISM at high-z, implying that Cosmic rays may well play a more important role in the heating of the ISM than UV heating (Typically T$\approx$ 30 K) and

may lend it-self to favour the formation of high mass stars, explaining CO abundances. These high-mass star dominated IMF galaxies have the potential to be the progenitors to the massive elliptical galaxies seen locally [Danielson et al., 2013]. Expanding the number of known lensed SMGs which will rapidly improve our understanding of the resolved star formation law in early galaxies and the density structure of the cold ISM of high redshift ($z > 2$) galaxies [Narayanan et al., 2010].

Appendix A

S2CSS Survey Selection Results

Table A.1. The 44 submillimeter sources detected based on the criteria prescribed in Chapter 2. C_{80} gives the 80% completeness limit of the SCUBA-2 map and uncertainties on flux densities are the 1σ instrumental noise at the position of each detection peak. Column 1: Map ID, *H* indicates SPIRE counterparts, suffixes indicate multiple sources in the field, *CE* the Cosmic Eyelash and, *BCG* the bright cluster galaxy sources; column 2: Peak location; column 3: Angular Separation between candidate and cluster BCG; column 4: 80% completeness; column 5: Peak $850\mu m$ flux density; column 6: Signal-to-noise ratio

ID	SCUBA-2 Detection Position (J2000)	Angular Separation (arcmin)	C_{80} (mJy)	Peak $S_{850\mu m}$ (mJy)	SNR
MACSJ0033.8−0751	00:34:00.5 −07:49:36.5	2.5	52	62±14	4.2
MACSJ0144.7−2213	01:44:41.6 −22:14:53.0	1.3	30	23±5	4.6
MACSJ0145.9+2134	01:46:00.1 +21:34:11.5	0.9	31	24±5	4.3
MACSJ0159.8−0849	01:59:54.4 −08:47:59.0	2.1	59	57±13	4.4
MACSJ0207.2+0536	02:07:15.6 +05:35:45.5	1.0	26	19±4	4.2
MACSJ0242.5−2132^{BCG}	02:42:35.8 −21:31:27.0	0.2	48	34±7	4.5
MACSJ0301.6+0155	03:01:54.5 +01:57:17.0	1.9	39	34±8	4.1
MACSJ0303.2−2735−A	03:03:20.3 −27:34:44.5	1.1	53	37±8	4.2
MACSJ0303.2−2735−B	03:03:25.7 −27:33:54.5	2.5	53	67±14	4.6
MACSJ0312.9+0822	03:13:01.4 +08:22:12.1	1.2	66	51±11	4.3
MACSJ0417.5−1154^{H}	04:17:33.4 −11:55:02.0	0.9	33	25±5	4.5
MACSJ0429.6−0253^{H}	04:29:33.3 −02:52:35.5	0.7	71	55±12	4.6
MACSJ0439.0+0520	04:38:54.4 +05:20:08.5	2.0	23	31±6	4.5
MACSJ0454.1+0255	04:54:16.1 +02:54:24.0	2.0	73	68±16	4.2

Table A.1 (cont'd)

ID	SCUBA-2 Detection Position (J2000)	Angular Separation (arcmin)	C_{80} (mJy)	Peak $S_{850\mu m}$ (mJy)	SNR
MACSJ0510.4+0220	05:10:33.6 +02:19:49.0	1.6	31	30±6	4.7
MACSJ0834.9+5534^{BCG}	08:34:55.5 +55:34:19.5	0.2	38	28±6	4.4
MACSJ0845.4+0327	08:45:30.4 +03:27:57.0	0.9	32	25±5	4.6
MACSJ0913.7+4056	09:13:48.5 +40:56:58.5	0.8	40	30±6	4.5
MACSJ0918.0−1205^{BCG}	09:18:05.7 −12:05:46.2	0.1	54	76±8	8.9
MACSJ0949.8+1708	09:49:49.6 +17:08:01.0	0.9	25	18±4	4.3
MACSJ0958.3−1103−A	09:58:19.9 −11:04:14.0	0.7	26	20±4	4.4
MACSJ0958.3−1103−B^{H}	09:58:14.5 −11:03:08.0	1.8	26	23±5	4.3
MACSJ0958.3−1103−C^{H}	09:58:10.1 −11:02:10.0	3.2	26	35±8	4.4
MACSJ0959.8+2223	09:59:53.8 +22:23:27.0	1.1	20	16±3	4.6
MACSJ1022.4+5006^{H}	10:22:26.6 +50:05:38.5	1.0	45	45±8	5.5
MACSJ1023.6+0411	10:23:42.1 +04:11:04.0	0.7	27	18±4	4.2
MACSJ1023.6+4908	10:23:41.7 +49:08:42.0	0.3	41	28±7	4.1
MACSJ1023.8−2715^{H}	10:23:57.1 −27:16:53.0	2.2	36	38±7	5.2

Table A.1 (cont'd)

ID	SCUBA-2 Detection Position (J2000)	Angular Separation (arcmin)	C_{80} (mJy)	Peak $S_{850\mu m}$ (mJy)	SNR
MACSJ1105.7−1014−A	11:05:49.0 −10:11:58.2	2.6	30	32±7	4.5
MACSJ1105.7−1014−B	11:05:51.8 −10:12:21.0	2.6	30	34±8	4.2
MACSJ1108.8+0906−A	11:08:58.9 +09:03:34.0	2.9	25	30±7	4.2
MACSJ1108.8+0906−B	11:09:04.6 +09:06:48.0	2.8	25	28±6	4.3
MACSJ1114.3+5823	11:14:10.4 +58:20:58.5	2.9	36	41±8	4.6
MACSJ1115.8+0129	11:15:56.0 +01:29:25.0	0.8	27	20±4	4.6
MACSJ1123.9+2129	11:23:49.7 +21:29:56.5	1.9	30	28±6	4.5
MACSJ1124.5+4351−A	11:24:23.3 +43:51:43.5	1.3	24	18±4	4.1
MACSJ1124.5+4351−B	11:24:35.3 +43:53:53.5	2.5	24	24±5	4.7
MACSJ1130.3−1434	11:30:29.3 −14:33:24.8	2.0	42	44±9	4.8
MACSJ1141.4−1216	11:41:19.9 −12:14:19.7	2.5	45	50±12	4.1
MACSJ1157.3+3336	11:57:11.4 +33:37:33.3	1.5	25	19±4	4.4
MACSJ1200.3+0320^{H}	12:00:15.2 +03:23:17.5	0.1	21	31±4	6.7
MACSJ1203.2−2131	12:03:20.8 −21:32:22.5	1.8	28	21±5	4.1

Table A.1 (cont'd)

ID	SCUBA-2 Detection Position (J2000)	Angular Separation (arcmin)	C_{80} (mJy)	Peak $S_{850\mu m}$ (mJy)	SNR
MACSJ1206.2−0847	12:06:18.7 −08:50:29.0	3.1	37	42±10	4.1
MACSJ1218.4+4012	12:18:30.9 +40:11:08.5	1.8	38	35±7	4.7
MACSJ1229.0+4737^{H}	12:29:09.1 +47:36:50.3	1.3	25	27±6	4.5
MACSJ1236.9+6311	12:37:05.9 +63:07:51.0	3.5	26	35±7	4.5
MACSJ1258.0+4702	12:58:02.0 +47:04:31.5	1.9	27	23±5	4.1
MACSJ1259.3−0411	12:59:28.3 −04:10:03.0	2.2	33	40±7	5.2
MACSJ1303.7−2415−A	13:03:51.1 −24:16:44.5	2.4	52	55±12	4.4
MACSJ1303.7−2415−B	13:03:29.6 −24:14:50.5	3.2	52	63±13	4.9
MACSJ1306.8+4633−A	13:06:53.5 +46:30:13.0	3.0	26	28±6	4.1
MACSJ1314.3−2515^{H}	13:14:21.2 −25:15:47.5	0.7	33	34±5	6.1
MACSJ1314.4+6434	13:14:17.2 +64:33:46.5	1.2	31	21±5	4.1
MACSJ1325.1−2013−A	13:25:18.6 −20:15:14.5	3.3	53	83±18	4.5
MACSJ1325.1−2013−B^{H}	13:24:59.6 −20:13:32.5	1.5	53	42±9	4.4
MACSJ1348.8+2635−A	13:48:51.1 +26:35:07.6	0.5	46	30±7	4.1

Table A.1 (cont'd)

ID	SCUBA-2 Detection Position (J2000)	Angular Separation (arcmin)	C_{80} (mJy)	Peak $S_{850\mu m}$ (mJy)	SNR
MACSJ1348.8+2635−B	13:48:46.7 +26:34:15.6	1.8	57	45±10	4.4
MACSJ1354.6+7715	13:54:41.9 +77:16:41.5	1.5	77	63±15	4.2
MACSJ1359.1−1929	13:59:08.1 −19:26:23.5	2.7	55	58±14	4.2
MACSJ1407.5−2701^{BCG}	14:07:29.8 −27:01:04.2	0.1	58	59±9	6.5
MACSJ1411.3+5212−A	14:11:28.2 +52:11:18.0	1.9	36	32±7	4.4
MACSJ1411.3+5212−B	14:11:27.1 +52:09:44.0	3.3	36	45±11	4.0
MACSJ1447.4+0827	14:47:28.6 +08:27:27.0	0.8	38	27±6	4.3
MACSJ1452.9+5802	14:52:44.4 +58:01:35.5	1.9	90	97±17	5.5
MACSJ1500.3+2122	15:00:12.3 +21:21:09.5	2.2	51	50±9	5.1
MACSJ1516.7+0701−A	15:16:57.9 +07:01:48.1	3.4	49	60±14	4.0
MACSJ1516.7+0701−B	15:16:40.6 +07:02:10.1	1.3	49	34±8	4.3
MACSJ1516.7+0701−C	15:16:55.4 +07:01:36.1	2.7	49	54±12	4.4
MACSJ1522.4+2742	15:22:27.7 +27:45:38.5	3.1	68	82±16	5.1
MACSJ1532.8+3021	15:32:39.2 +30:20:17.5	3.2	94	128±24	5.2

Table A.1 (cont'd)

ID	SCUBA-2 Detection Position (J2000)	Angular Separation (arcmin)	C_{80} (mJy)	Peak $S_{850\mu m}$ (mJy)	SNR
MACSJ1539.7+3424	15:39:53.1 +34:25:45.2	2.7	51	51±11	4.4
MACSJ1551.9−0207	15:51:54.3 −02:07:40.5	0.6	44	31±7	4.3
MACSJ1558.3−1410^{BCG-H}	15:58:22.1 −14:10:01.0	0.1	31	40±4	8.5
MACSJ1615.7−0608	16:15:48.4 −06:08:47.5	0.4	23	16±3	4.3
MACSJ1635.8+6612	16:36:03.7 +66:13:27.0	1.6	35	27±6	4.2
MACSJ1640.3+4642	16:40:30.3 +46:42:25.5	1.9	35	32±6	5.2
MACSJ1644.9+0139	16:45:00.3 +01:40:51.5	1.9	29	21±4	4.3
MACSJ1651.1+0459	16:51:15.2 +05:00:02.0	1.9	33	32±6	4.8
MACSJ1722.4+3207−A^{H}	17:22:30.2 +32:07:32.0	1.0	39	26±5	4.9
MACSJ1722.4+3207−B	17:22:12.4 +32:08:00.0	3.0	39	50±9	5.3
MACSJ1723.3+2350	17:23:17.2 +23:52:03.0	1.3	69	60±12	4.8
MACSJ1727.3+5510−A	17:27:35.0 +55:12:23.8	2.2	26	23±5	4.4
MACSJ1727.3+5510−B^{BCG}	17:27:23.2 +55:10:54.0	0.1	26	34±4	7.4
MACSJ1727.3+5510−C	17:27:13.0 +55:11:00.0	1.5	26	22±5	4.3

Table A.1 (cont'd)

ID	SCUBA-2 Detection Position (J2000)	Angular Separation (arcmin)	C_{80} (mJy)	Peak $S_{850\mu m}$ (mJy)	SNR
MACSJ1731.6+2252−A^{H}	17:31:40.5 +22:50:35.0	2.2	30	48±5	8.5
MACSJ1731.6+2252−B	17:31:28.4 +22:52:45.0	2.7	30	35±8	4.2
MACSJ1744.2+3259^{BCG}	17:44:14.3 +32:59:27.4	0.1	30	27±5	5.5
MACSJ1910.4+6741^{H}	19:10:26.2 +67:41:51.2	0.4	37	27±6	4.5
MACSJ2043.2−2144^{H}	20:43:14.5 −21:44:37.0	0.4	32	65±4	13.5
MACSJ2050.7+0123−A^{H}	20:50:38.0 +01:24:58.5	1.7	23	18±4	4.4
MACSJ2050.7+0123−B	20:50:45.5 +01:24:54.5	1.3	23	21±4	4.8
MACSJ2104.8+1401^{H}	21:05:03.1 +14:00:43.9	2.6	46	52±12	4.3
MACSJ2134.6−2706	21:34:24.4 −27:03:49.5	3.3	37	58±13	4.5
MACSJ2135.2−0102^{CE}	21:35:11.7 −01:02:54.0	0.1	56	119±9	13.1
MACSJ2153.6+1741	21:53:39.0 +17:39:28.8	2.4	39	36±7	4.7
MACSJ2211.7−0349−A	22:11:43.1 −03:50:39.0	1.0	22	16±3	4.2
MACSJ2211.7−0349−B	22:11:56.6 −03:48:29.0	3.3	22	40±9	4.2
MACSJ2214.9−1359	22:14:57.8 −14:02:24.0	2.6	18	19±3	4.8

Table A.1 (cont'd)

ID	SCUBA-2 Detection Position (J2000)	Angular Separation (arcmin)	C_{80} (mJy)	Peak $S_{850\mu m}$ (mJy)	SNR
MACSJ2258.6+2745−A	22:58:38.3 +27:42:49.5	2.7	49	68±15	4.4
MACSJ2258.6+2745−B	22:58:32.7 +27:43:05.5	2.5	49	53±12	4.4
MACSJ2325.3−1207	23:25:17.2 −12:08:56.6	1.6	46	36±8	4.5
MACSJ2341.1+0018−A^{BCG-H}	23:41:07.0 +00:18:34.5	0.3	26	33±3	8.4
MACSJ2341.1+0018−B	23:41:07.3 +00:19:34.5	1.0	26	18±4	4.4

Appendix B

S2CSS Spectral Energy Distributions

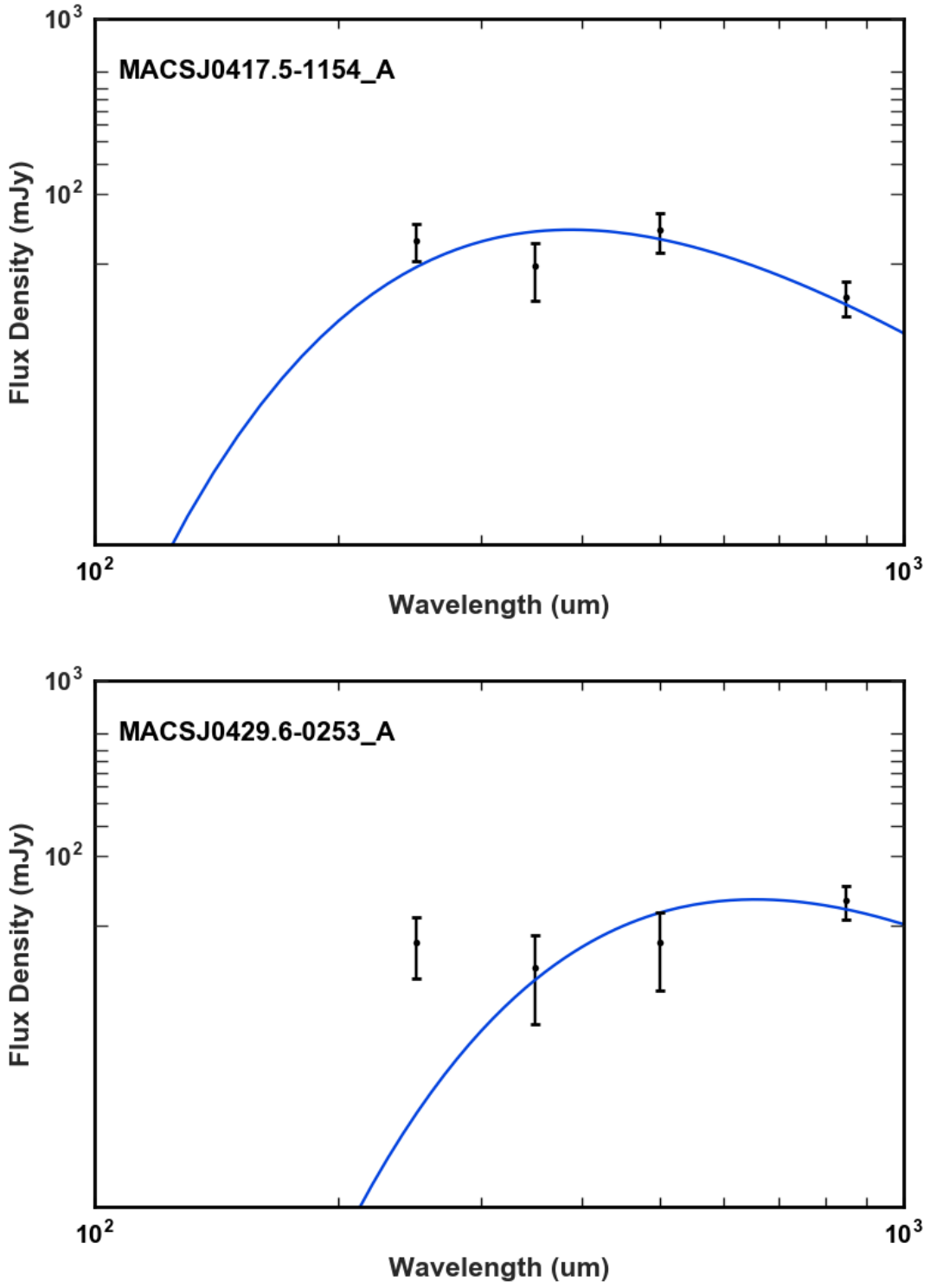

Figure B.1 Greybody fits for the SPIRE 250μm, 350μm, 500μm and SCUBA-2 850μm photometry for a fixed dust temperature of 40 K.

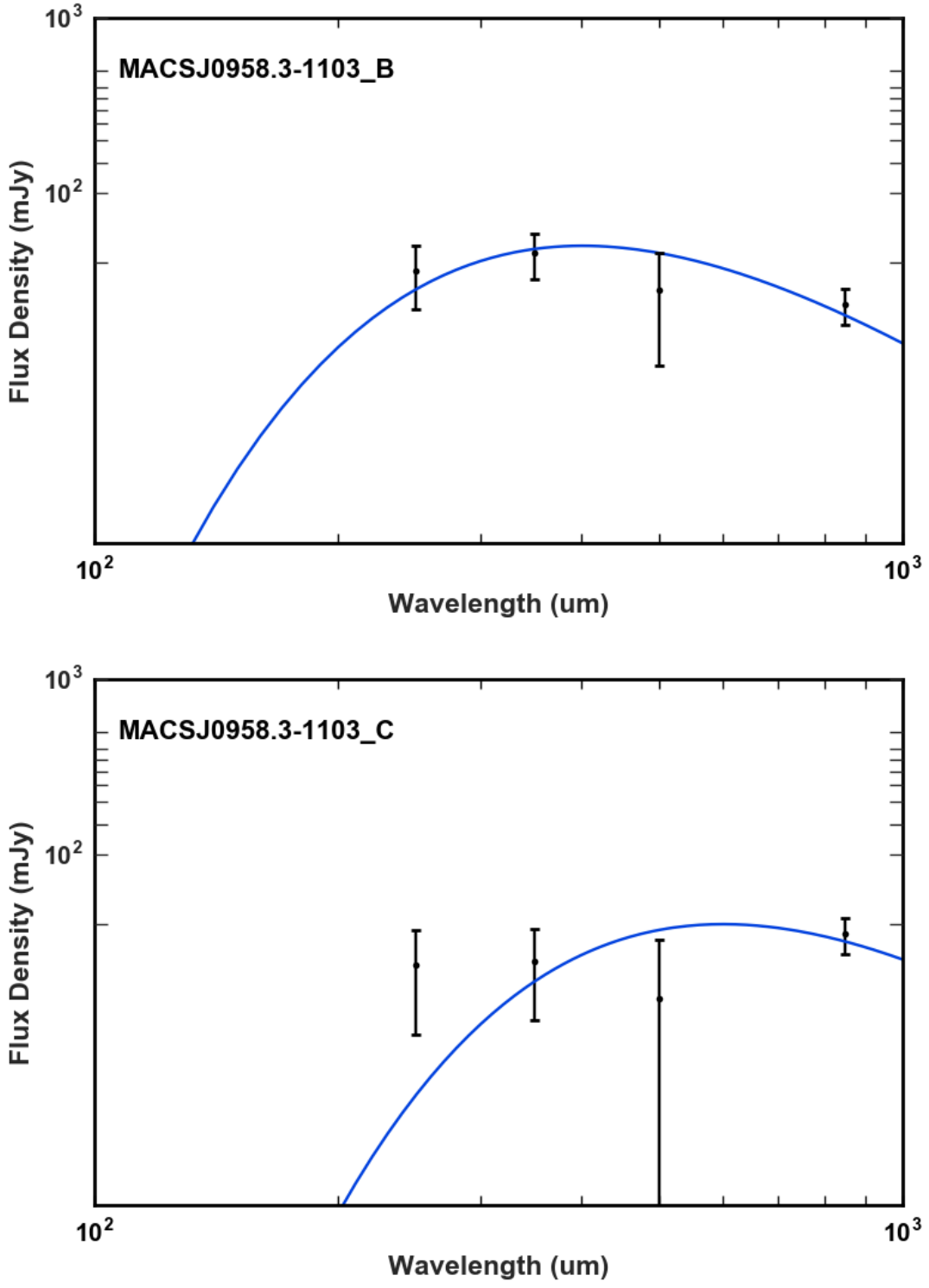

Figure B.1 cont.

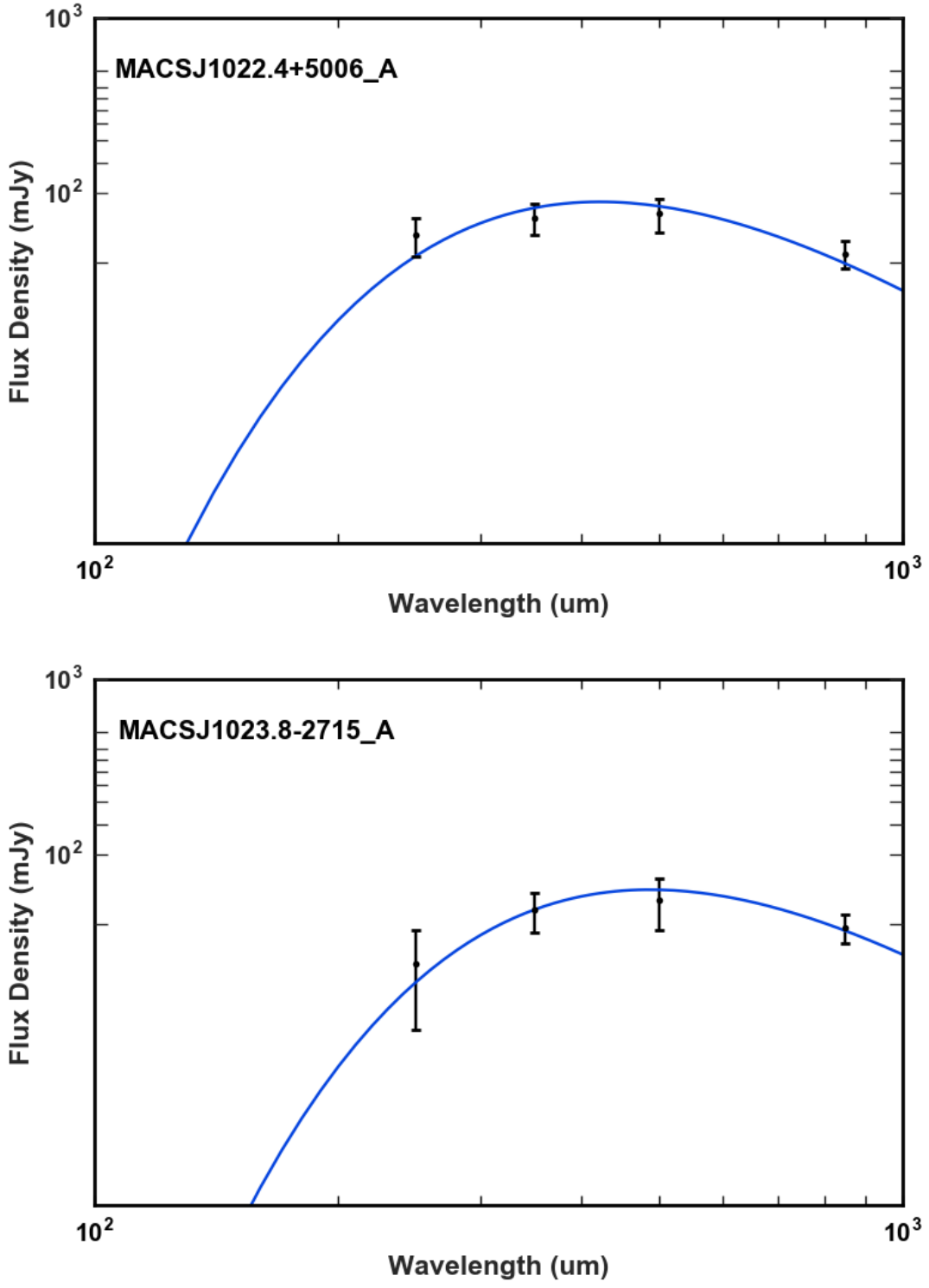

Figure B.1 cont.

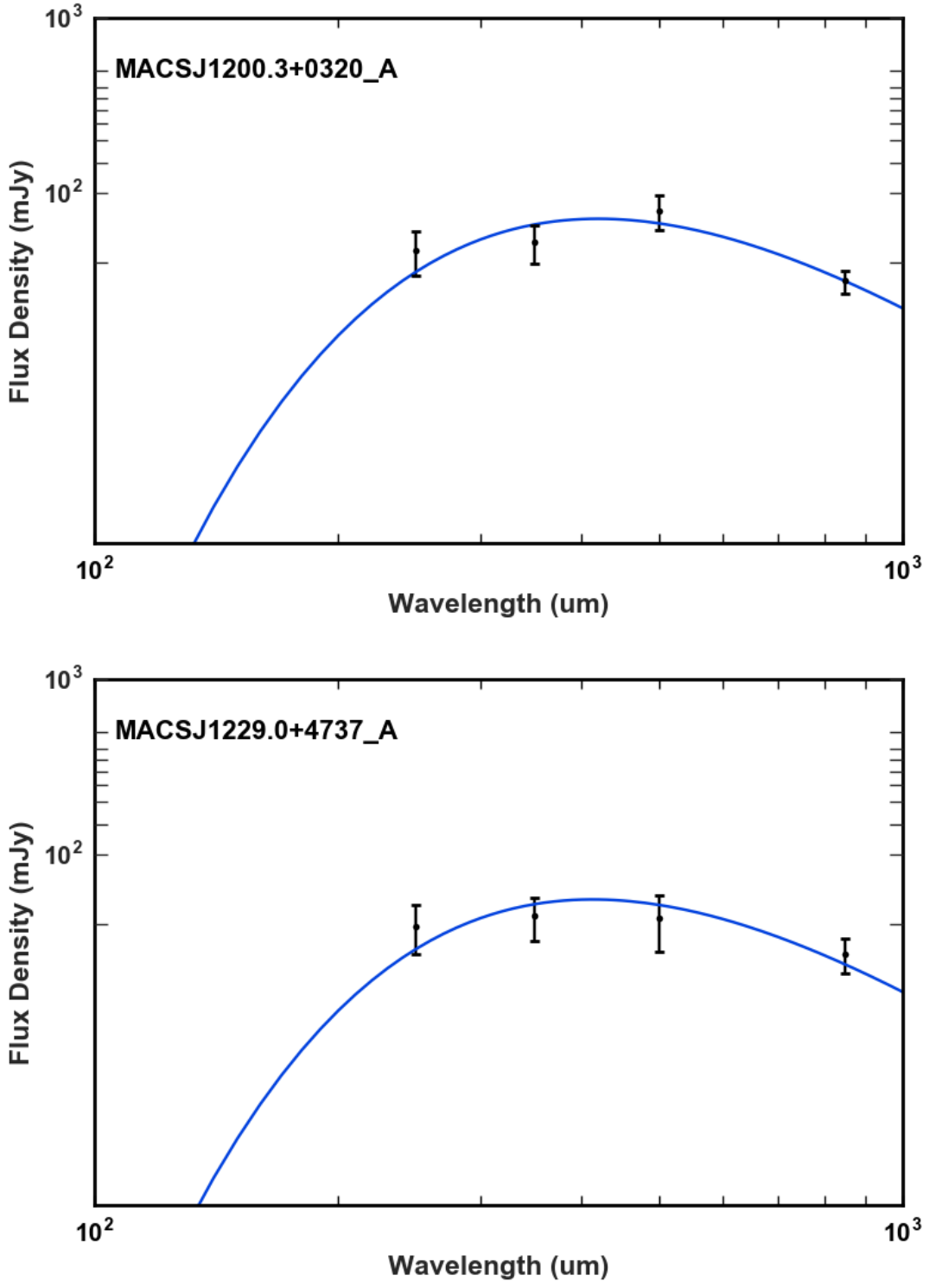

Figure B.1 cont.

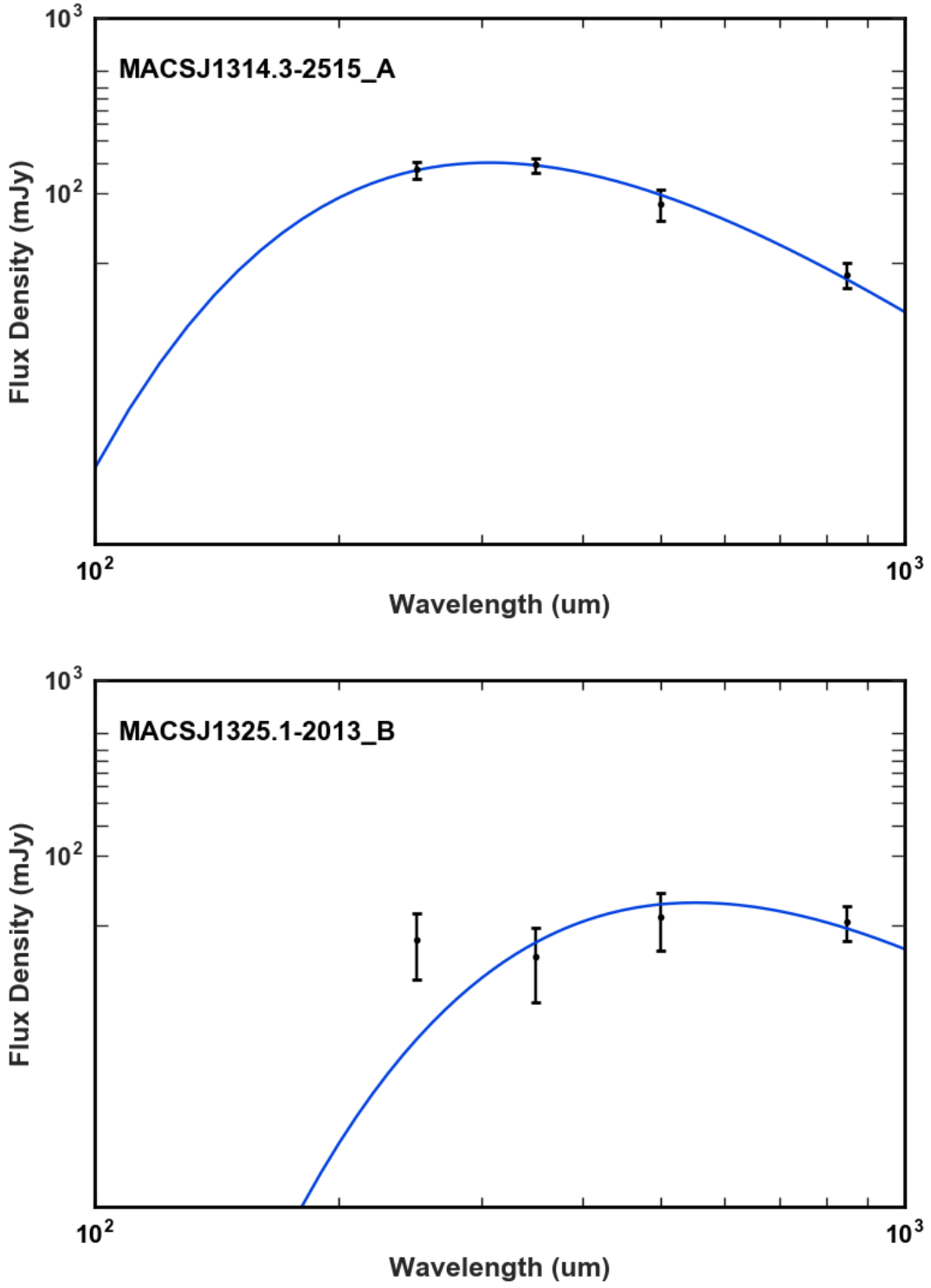

Figure B.1 cont.

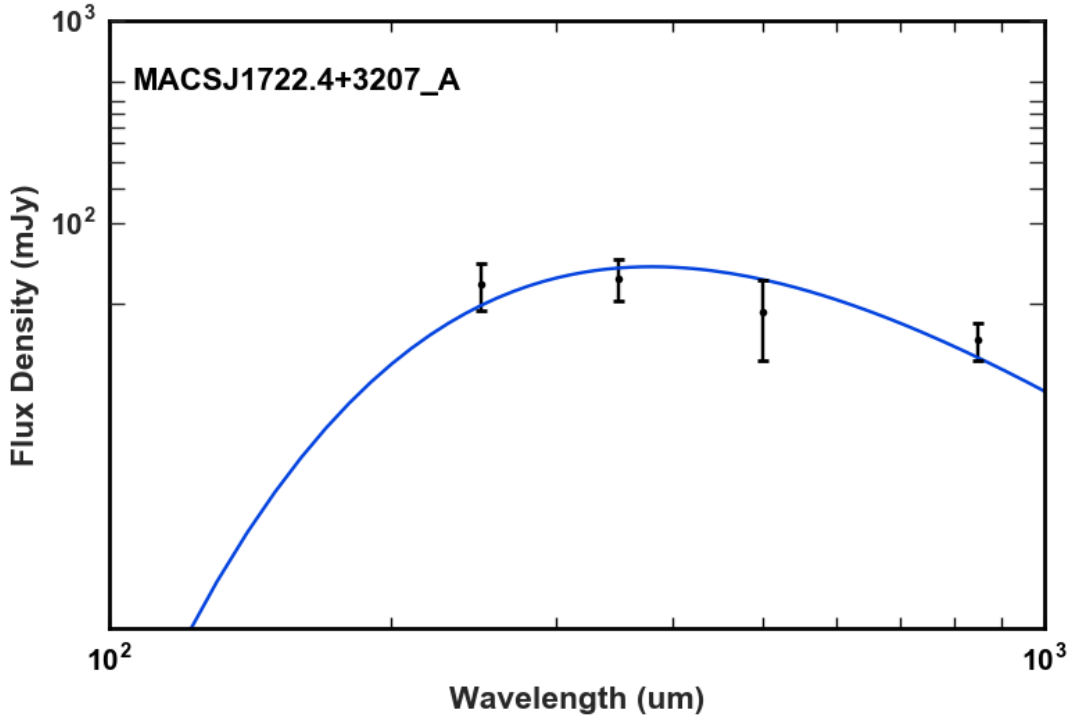

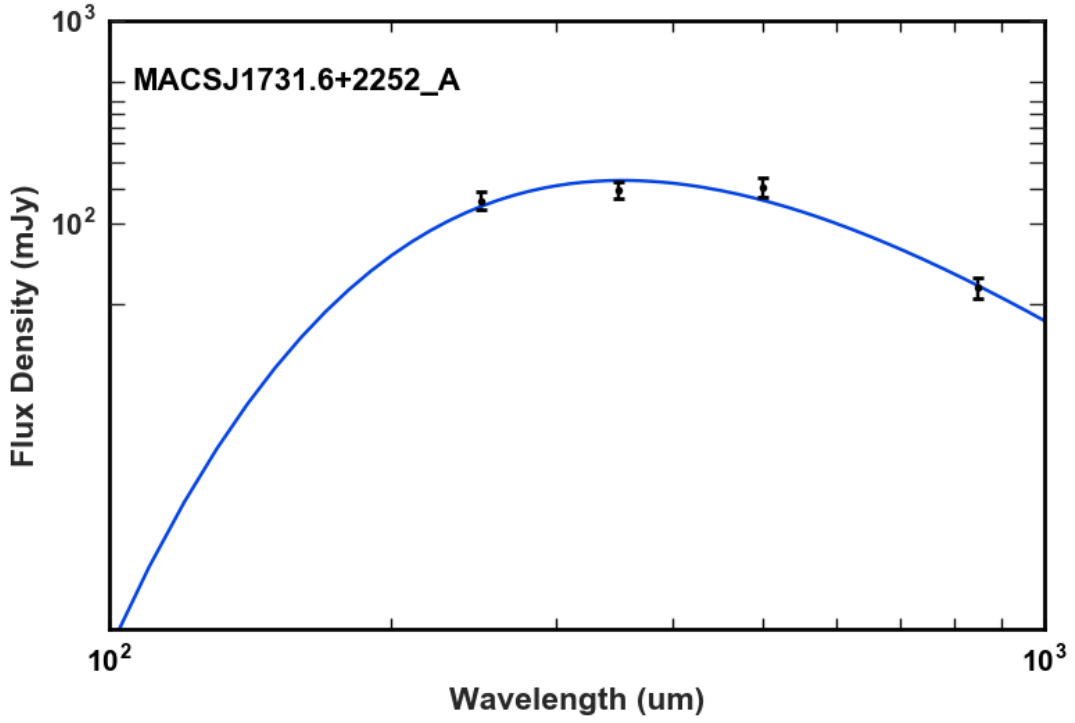

Figure B.1 cont.

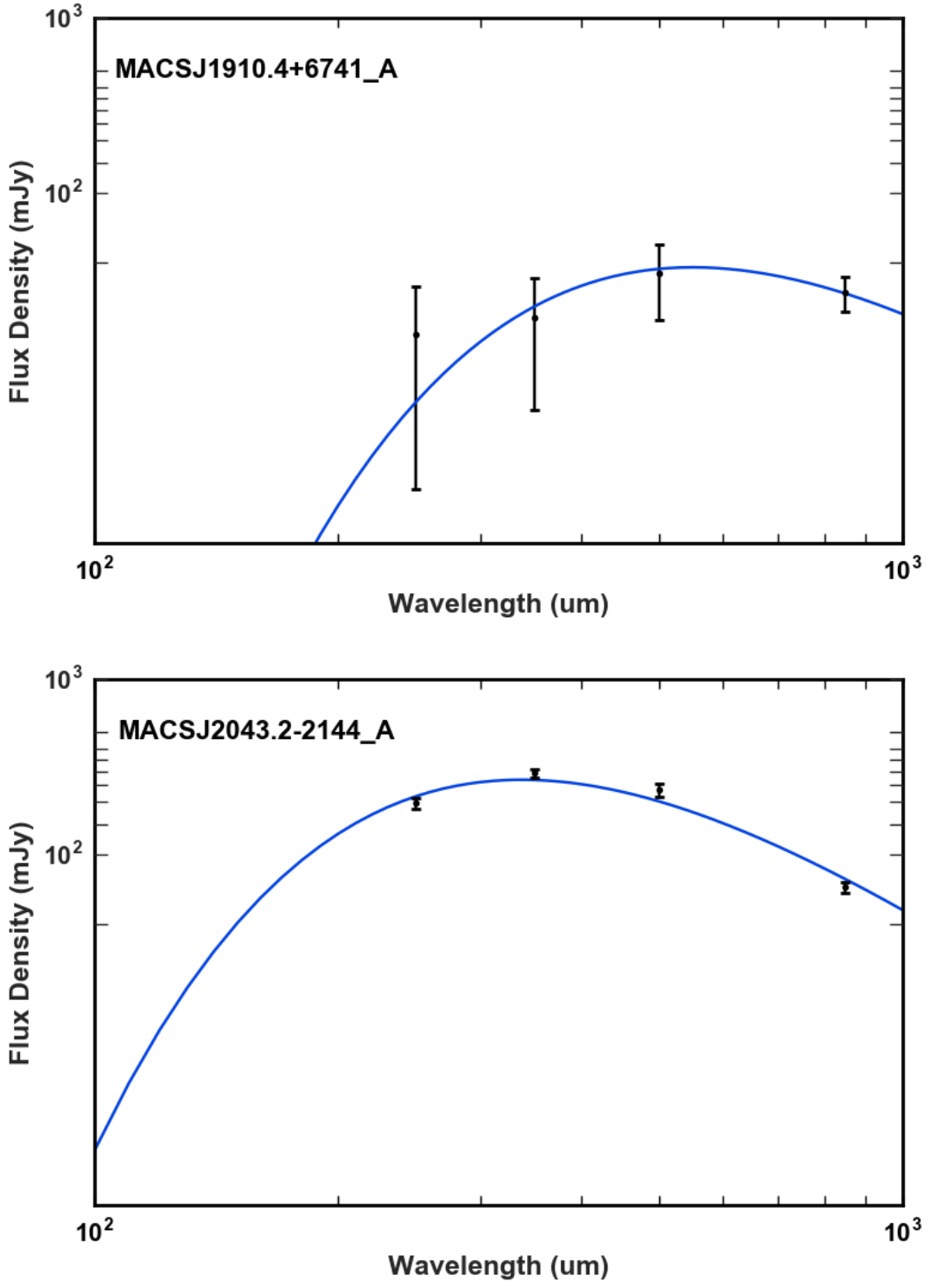

Figure B.1 cont.

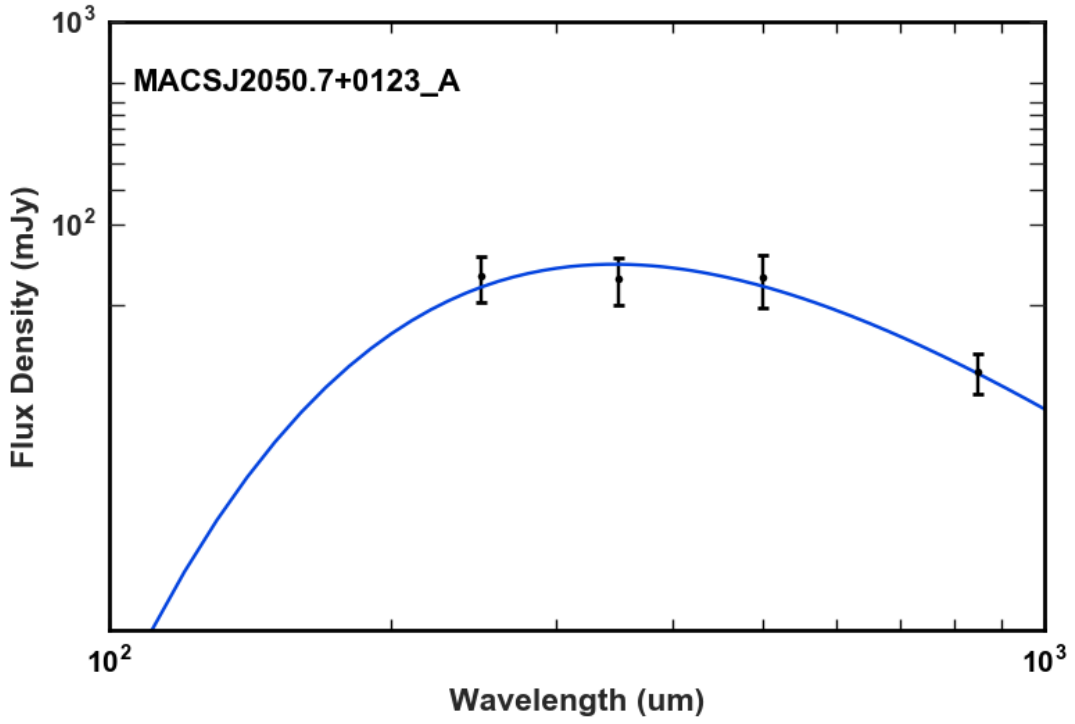
MACSJ2050.7+0123_A
Flux Density (mJy)
Wavelength (um)
10^3
10^2
10^2
10^3

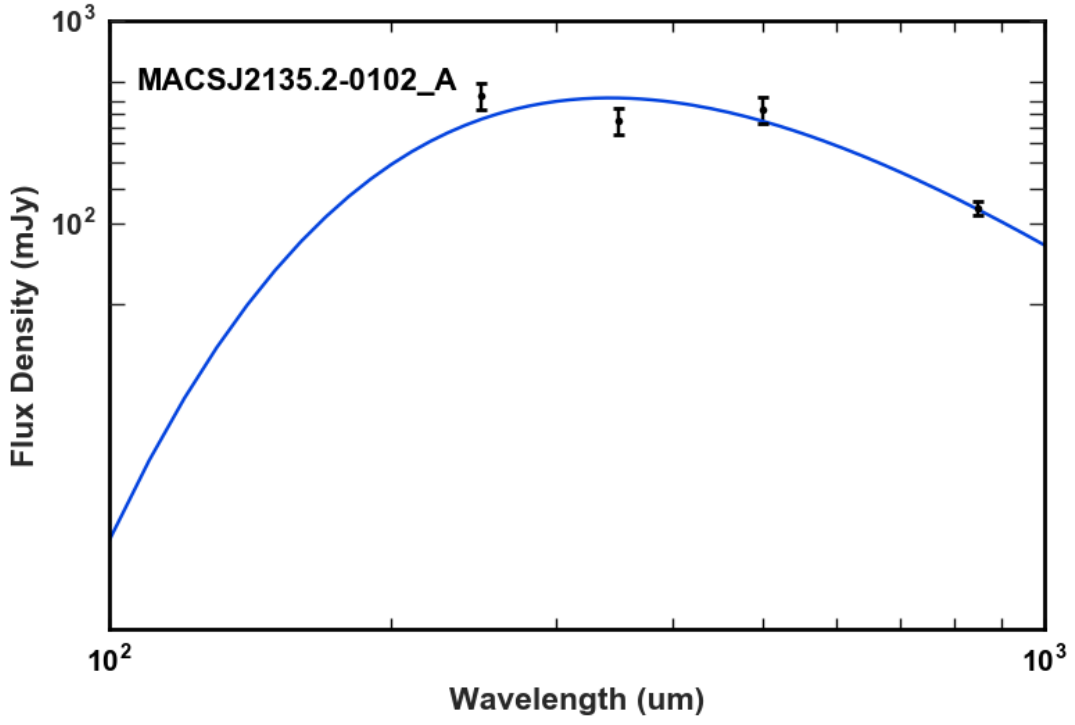
MACSJ2135.2-0102_A
Flux Density (mJy)
Wavelength (um)
10^3
10^2
10^2
10^3

Appendix C

S2CSS Pan-STARRS *I*-band Imaging

The Pan-STARRS i-band imaging for the S2CSS catalogue is shown here.

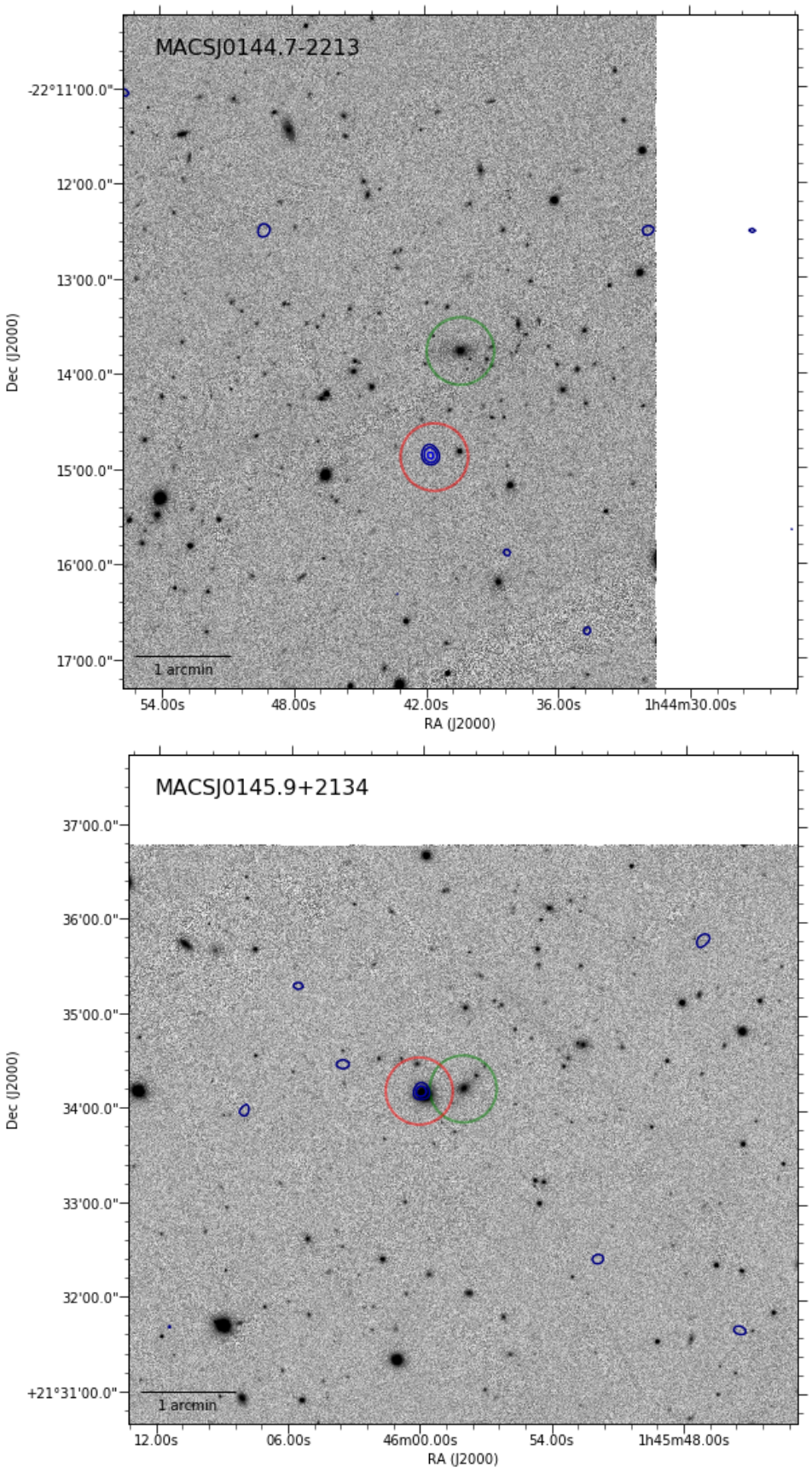

Figure C.1 Pan-STARRS i-band imaging with SCUBA-2 contours overlaid (3σ in 0.5σ increments) of sources in Table A.1. The diameter of the circles represents the FOV of SCUBA-2, red are the SCUBA-2 observation and green the host cluster BCG.

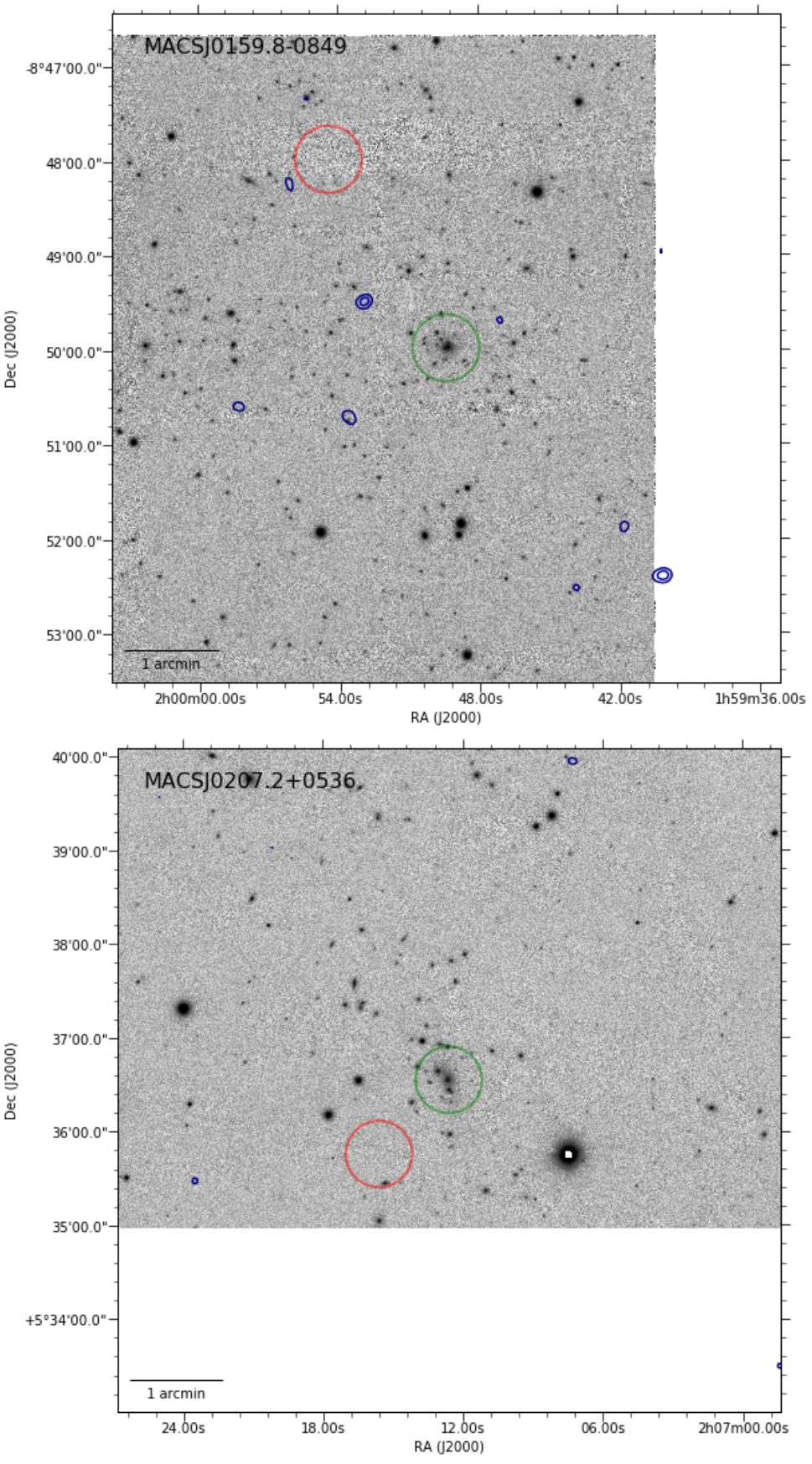

Figure C.1 cont.

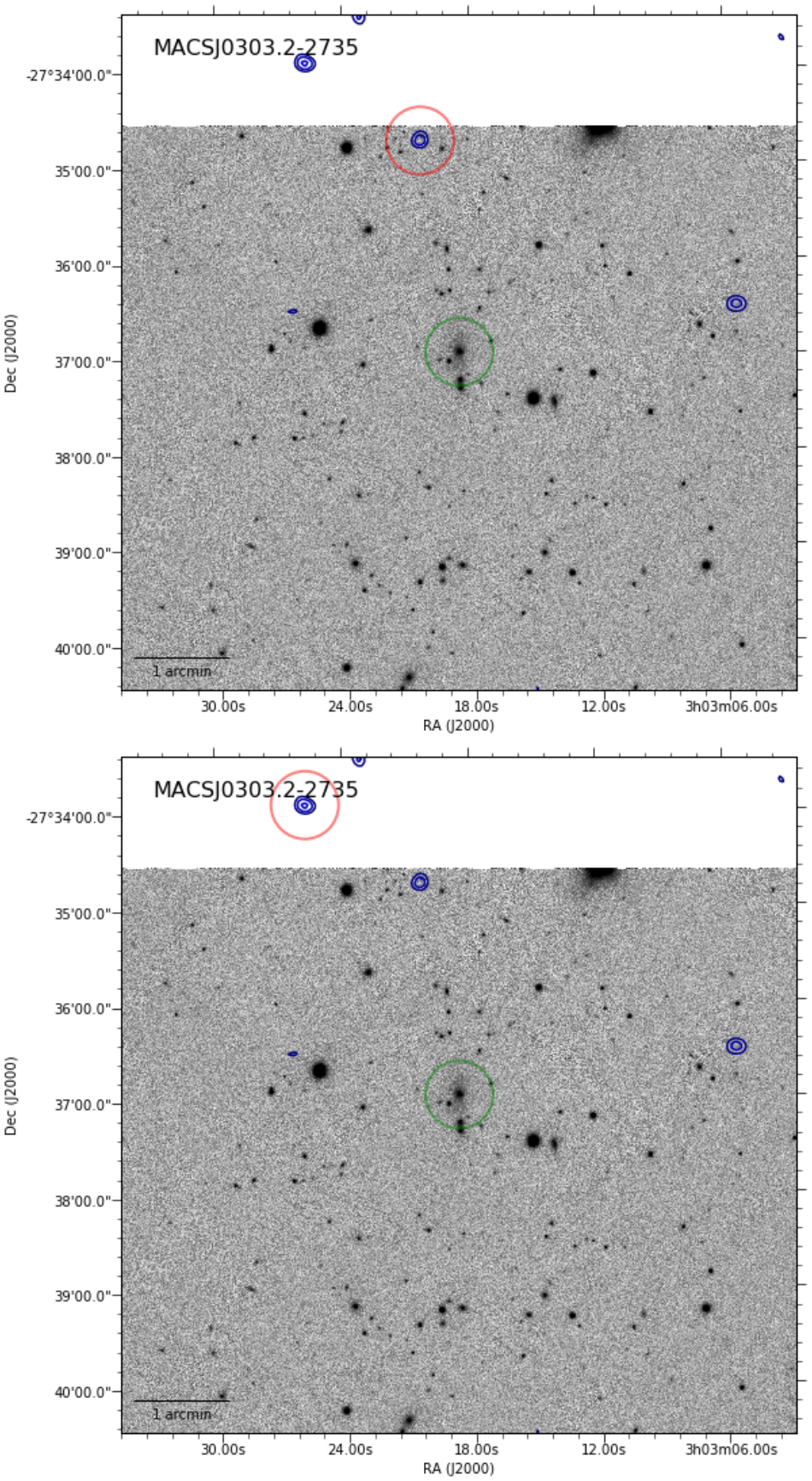

Figure C.1 cont.

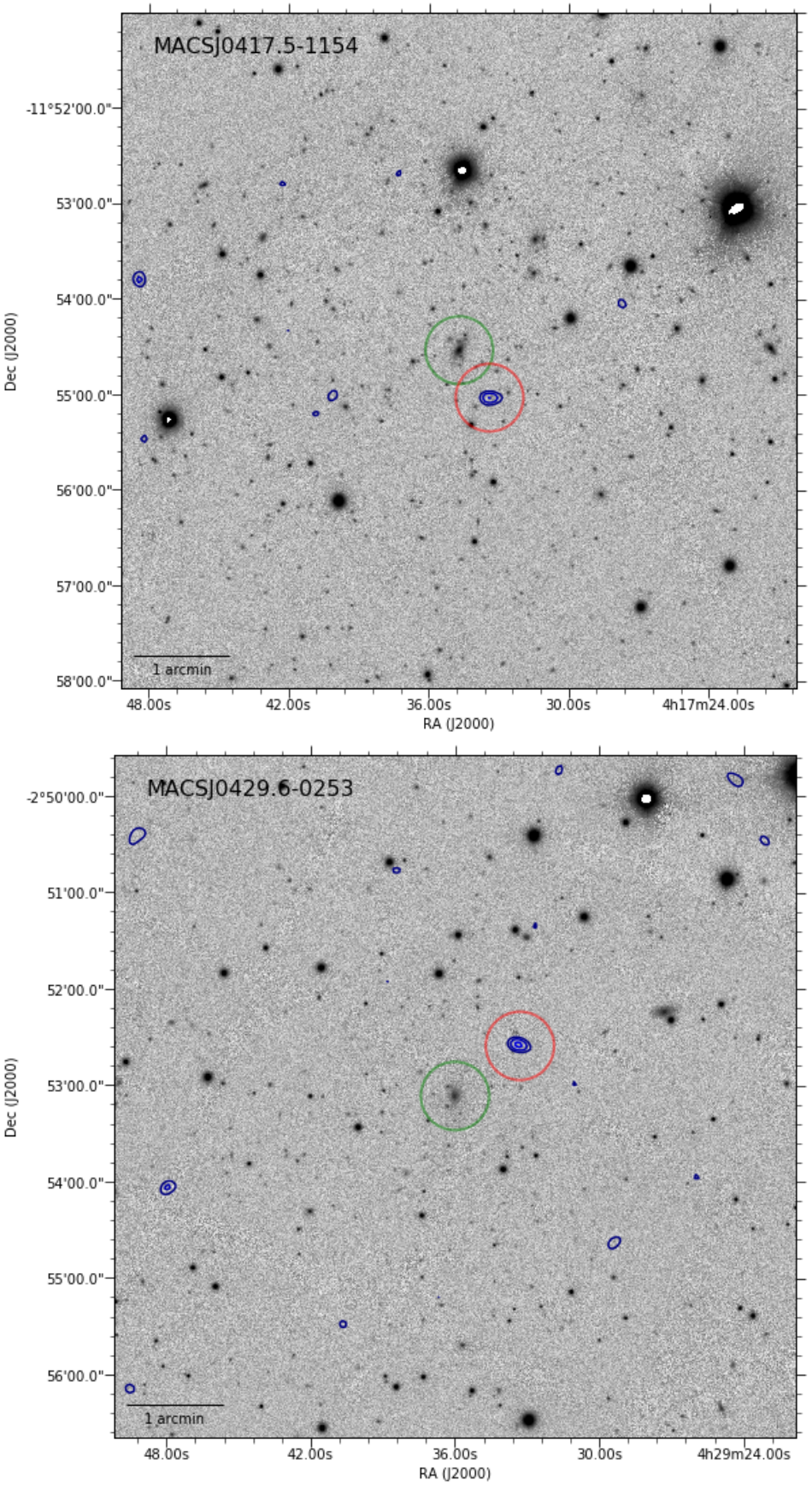

Figure C.1 cont.

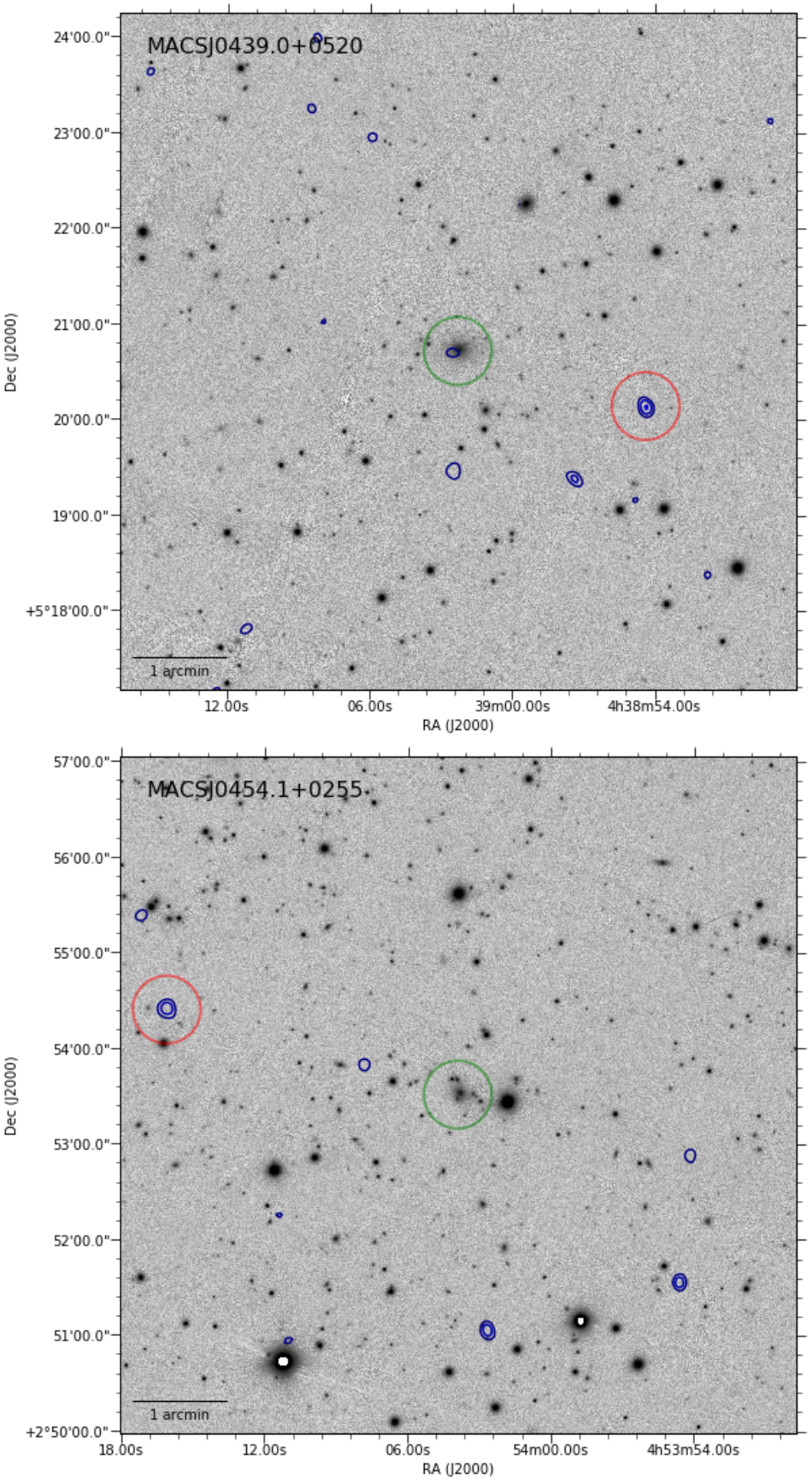

Figure C.1 cont.

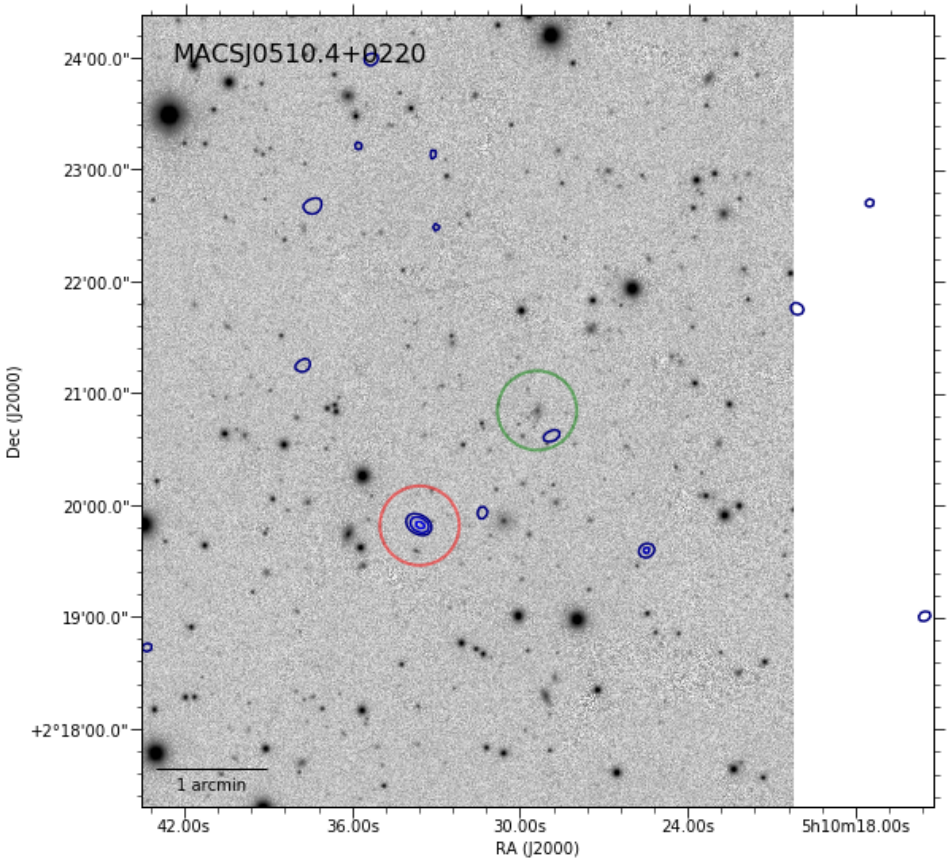

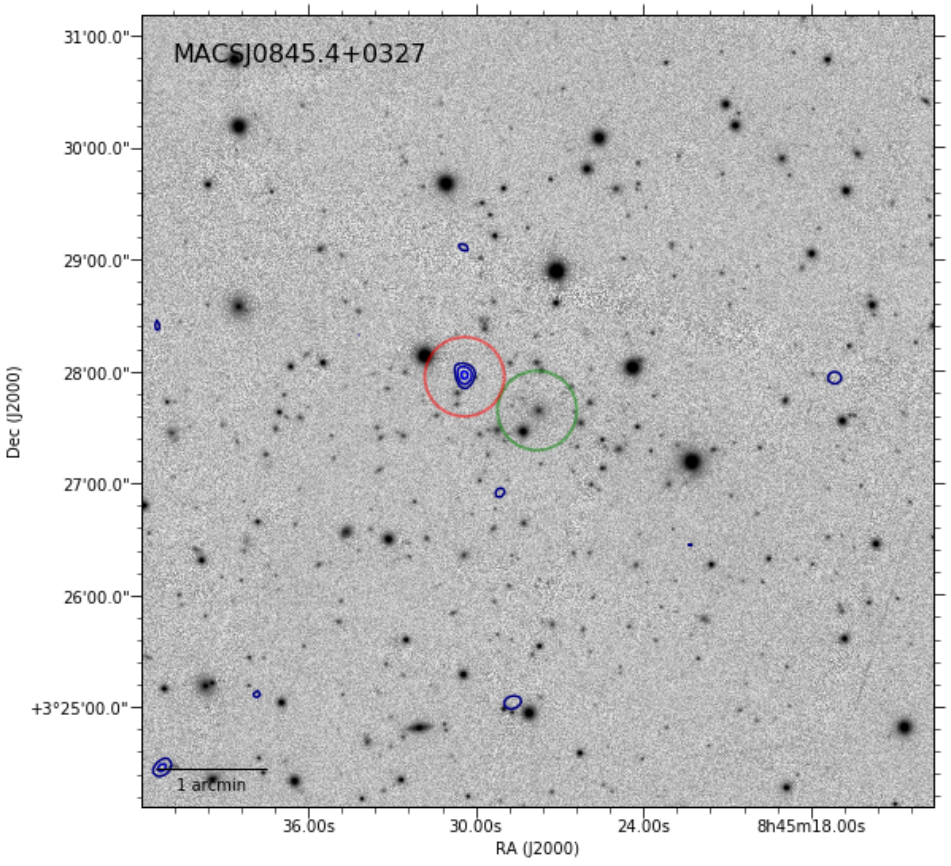

Figure C.1 cont.

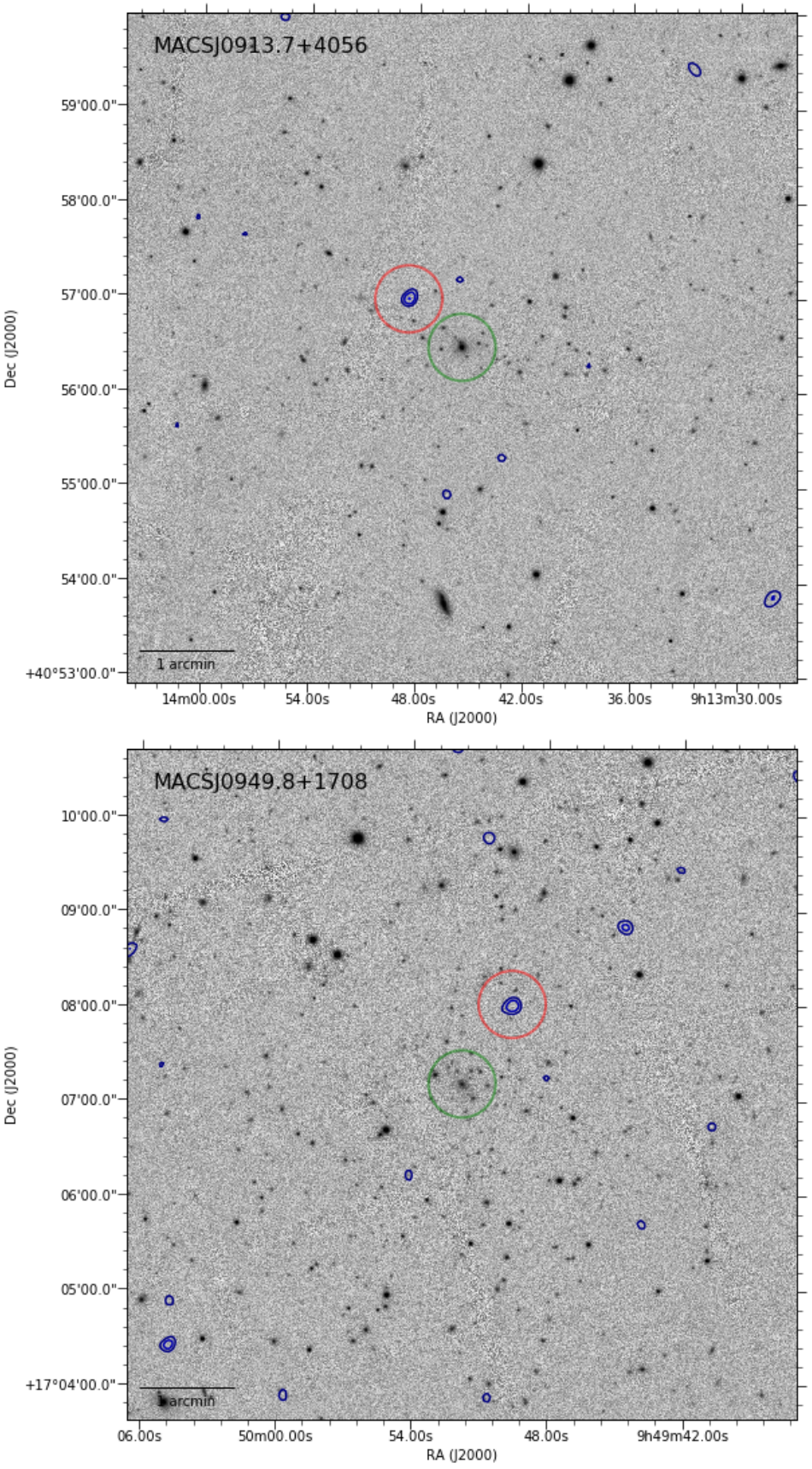

Figure C.1 cont.

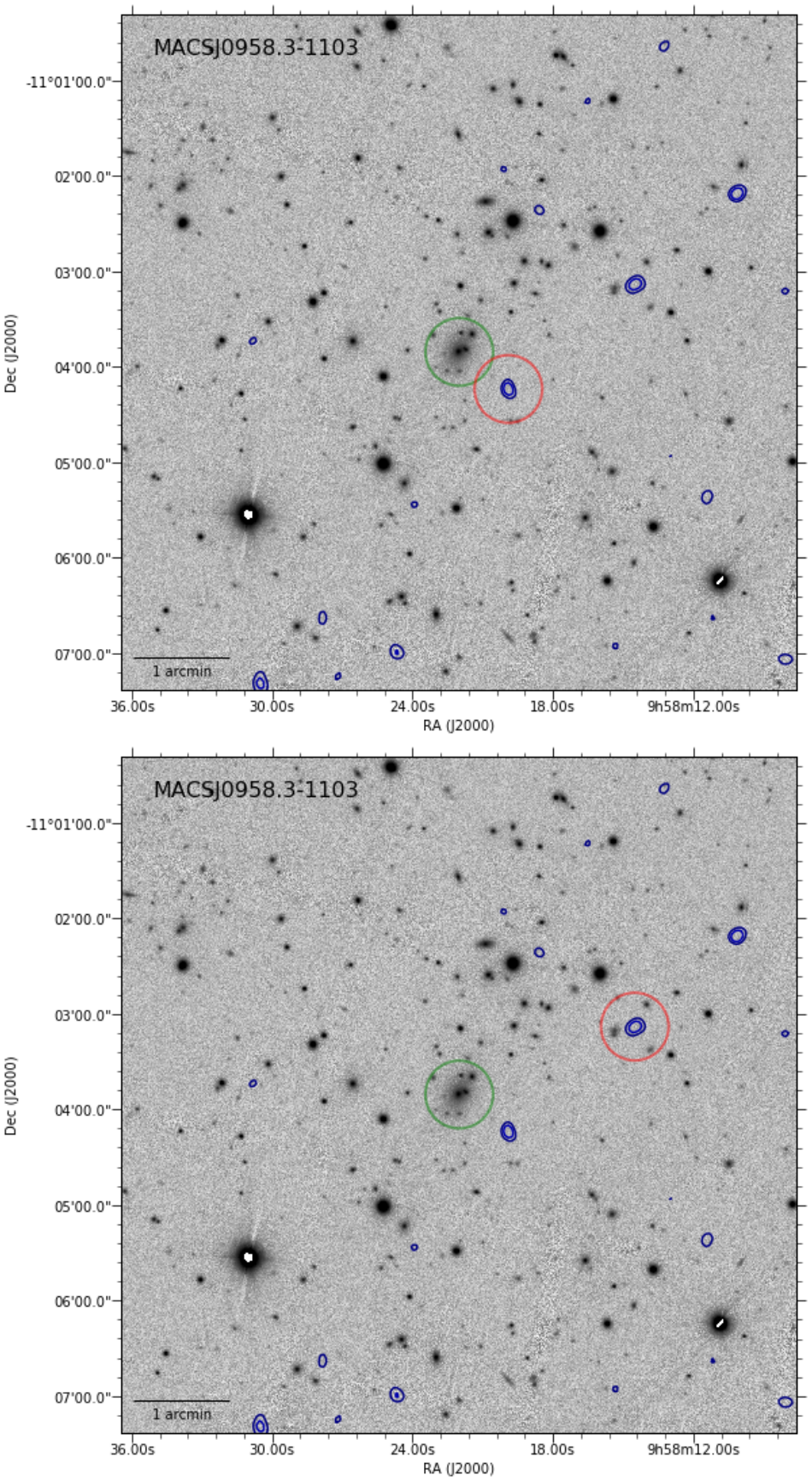

Figure C.1 cont.

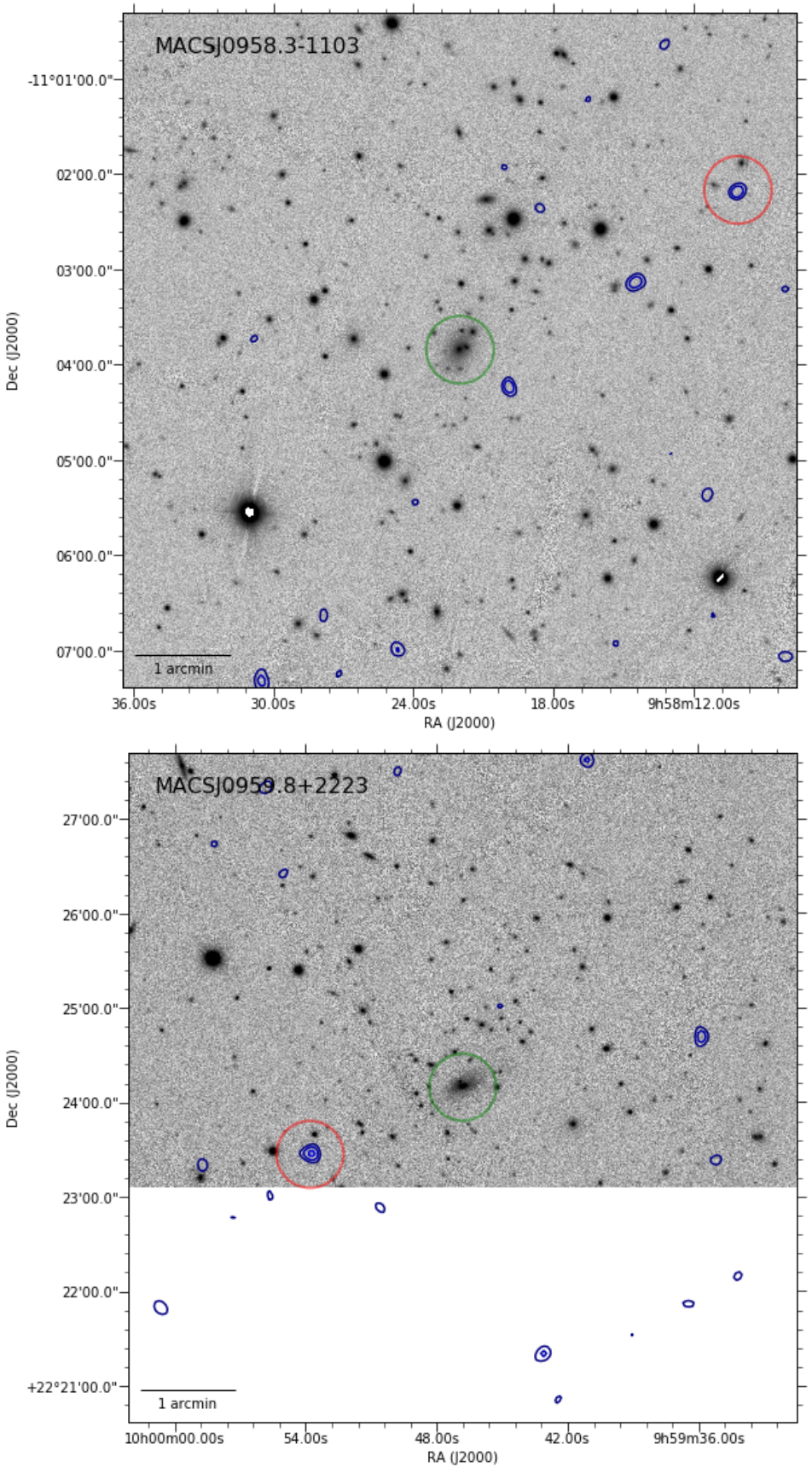

Figure C.1 cont.

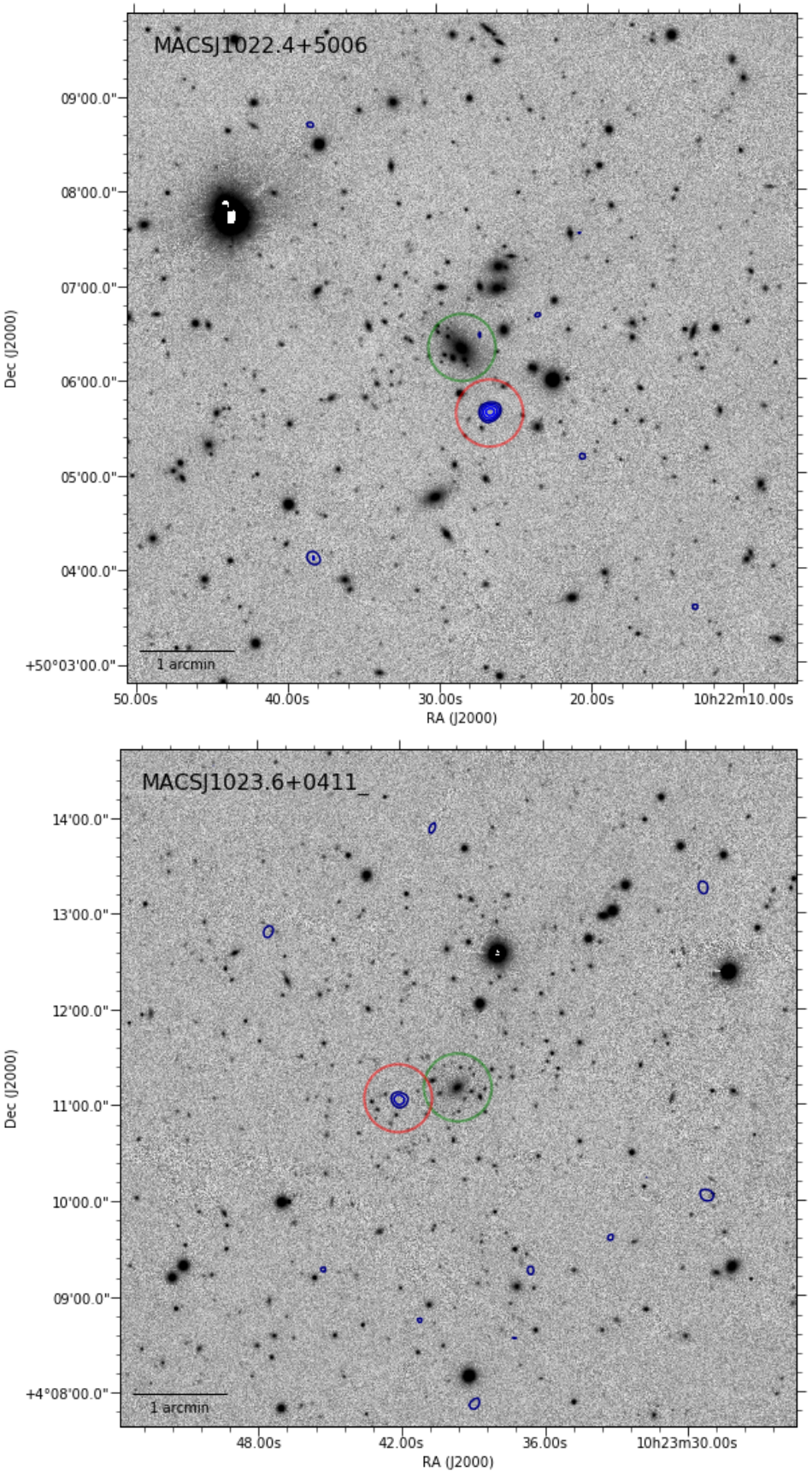

Figure C.1 cont.

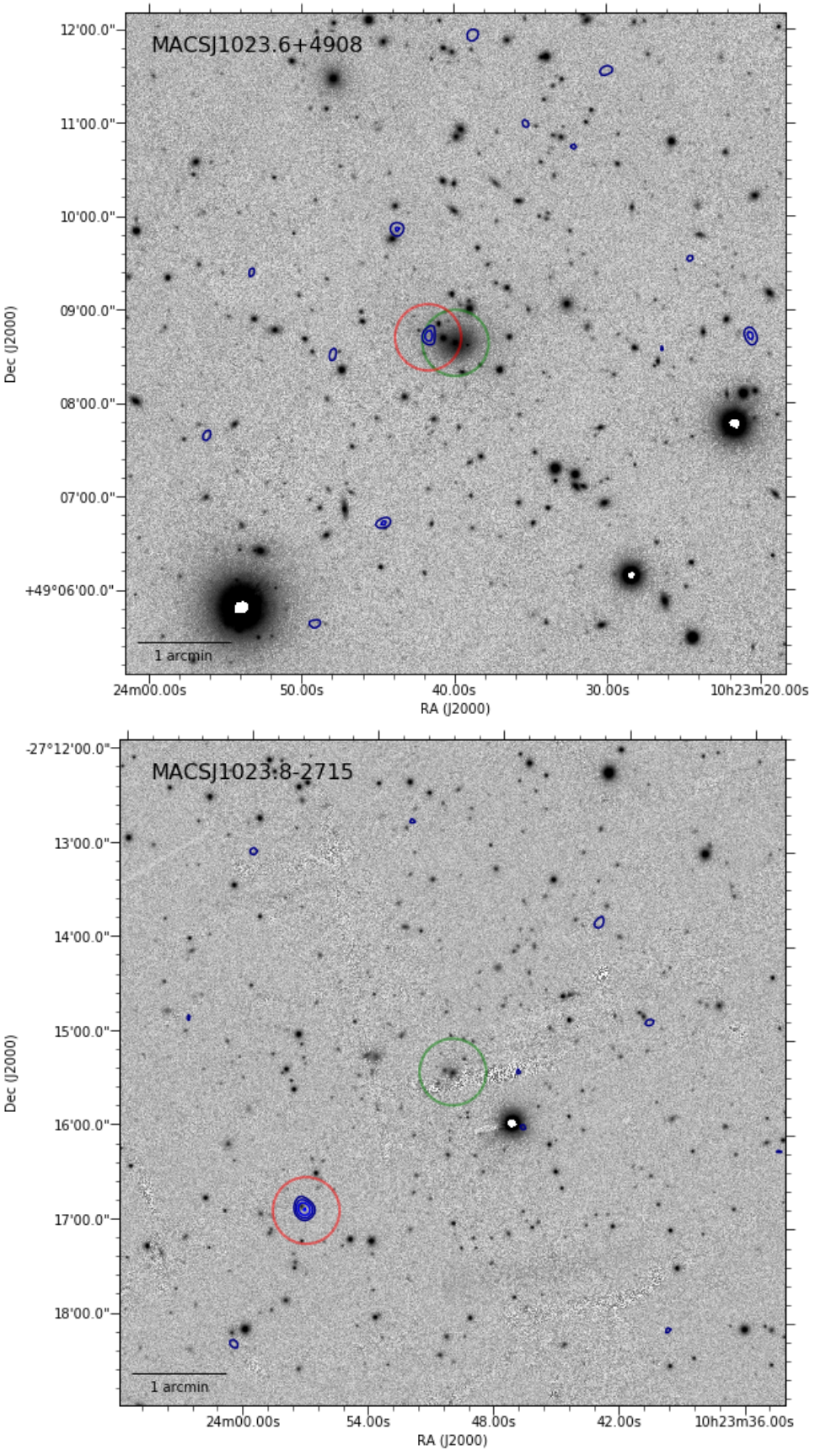

Figure C.1 cont.

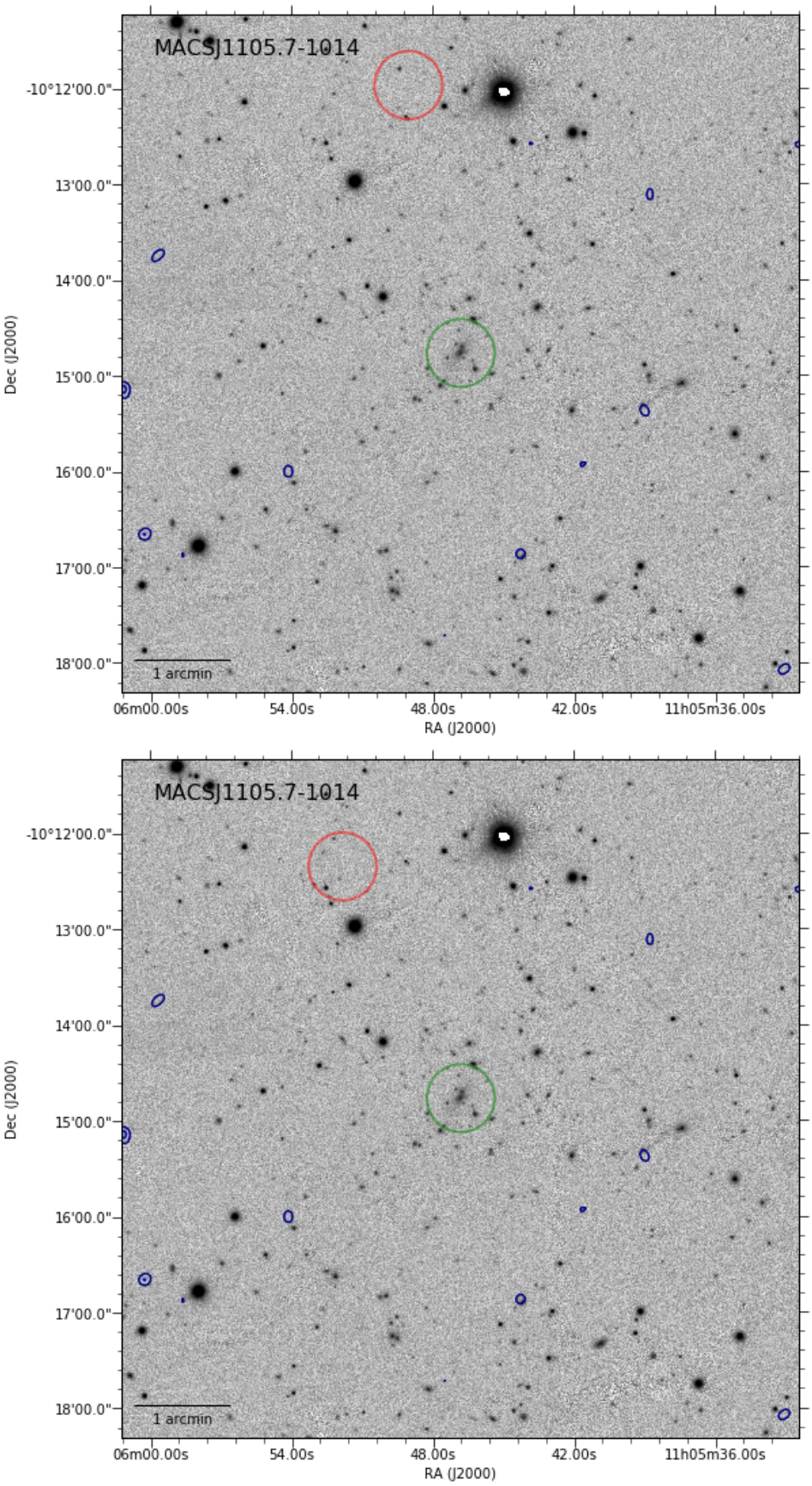

Figure C.1 cont.

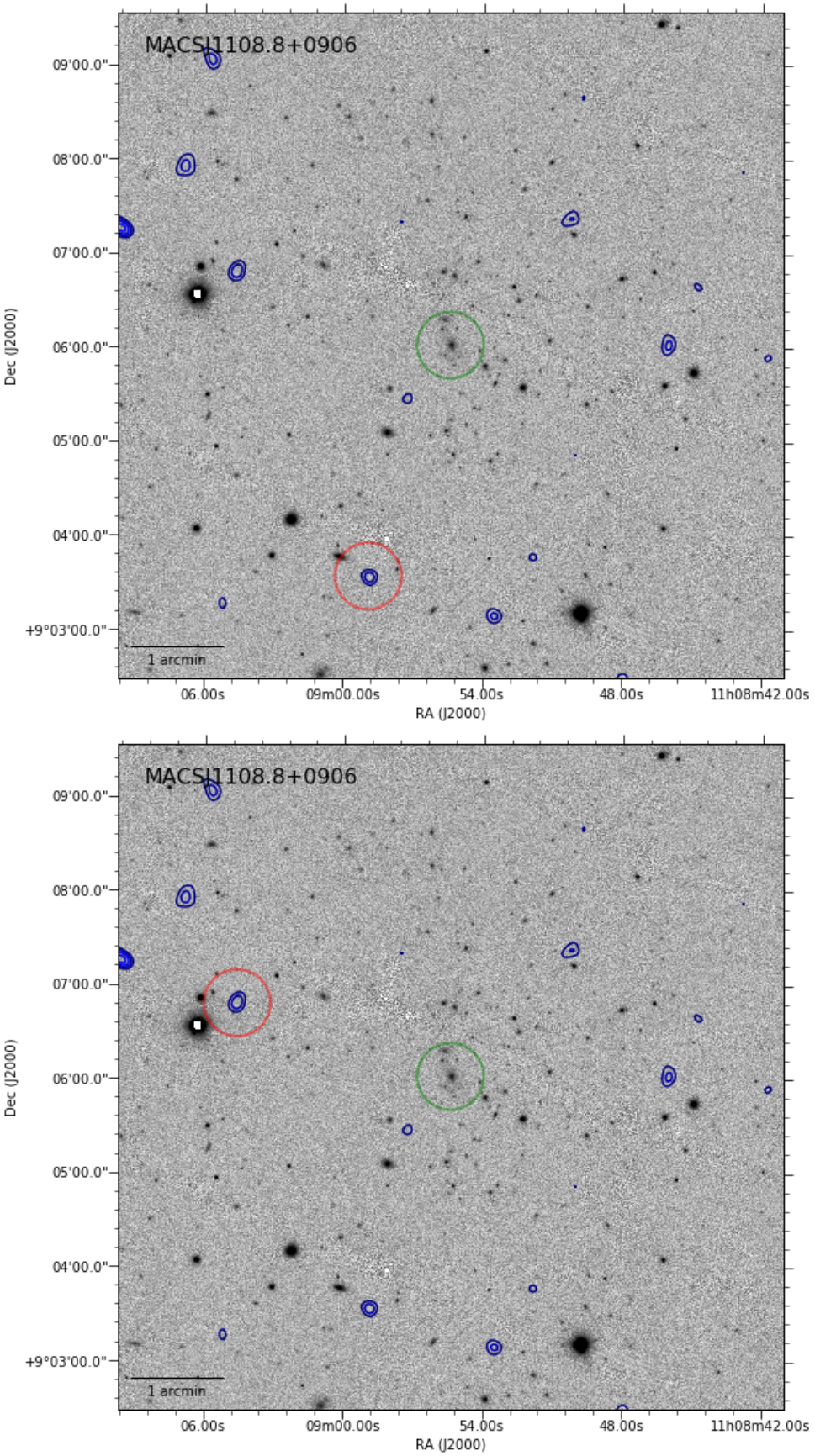

Figure C.1 cont.

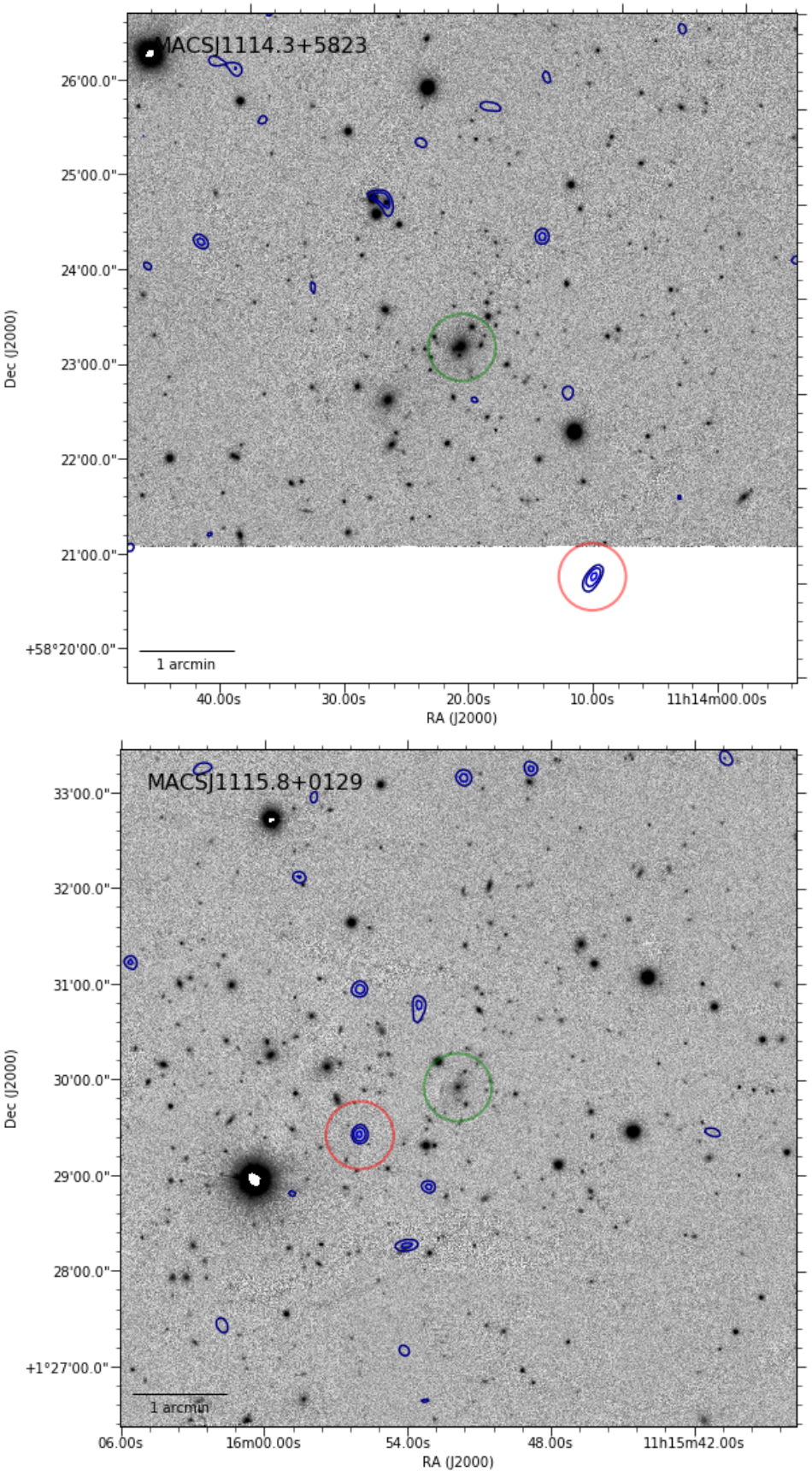

Figure C.1 cont.

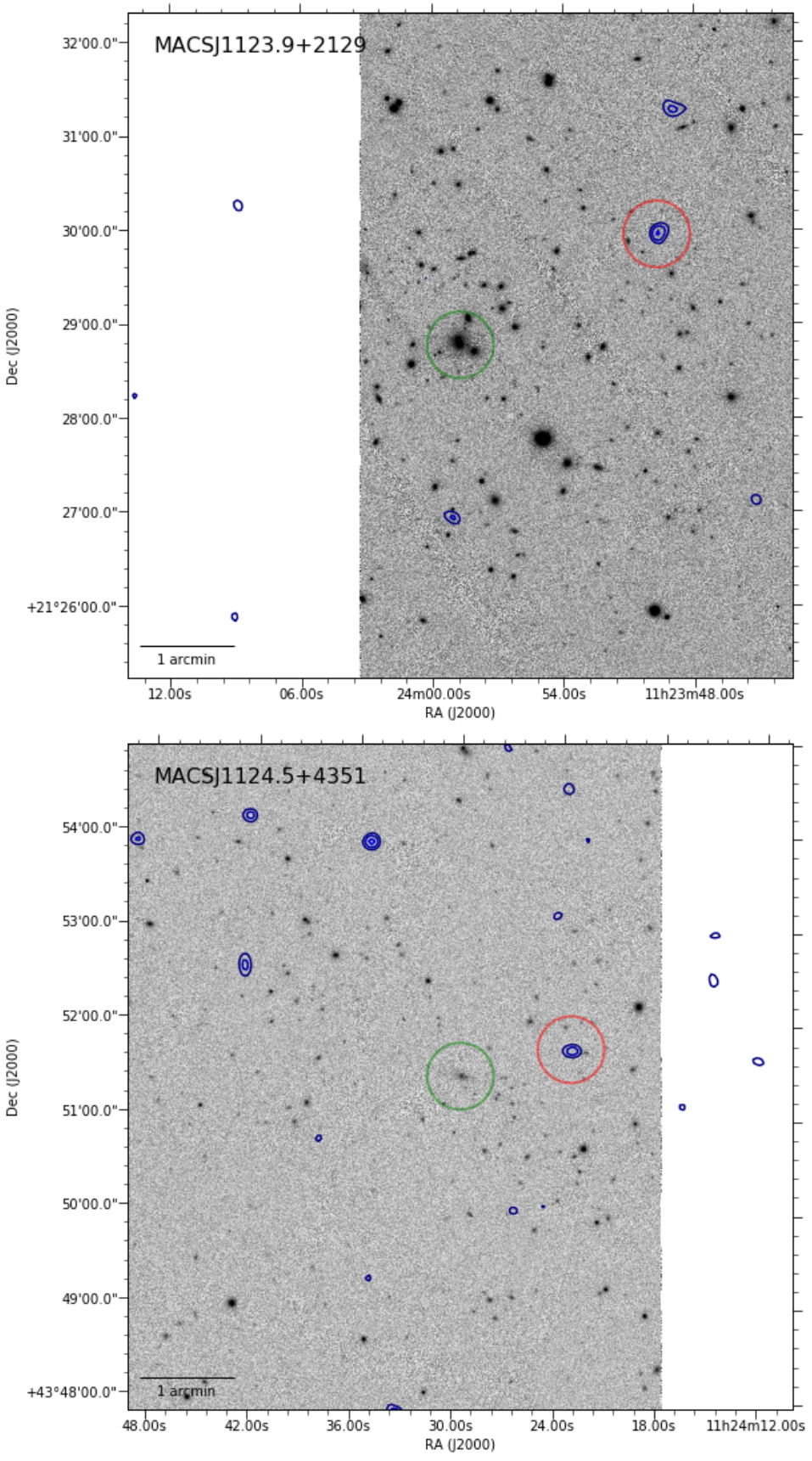

Figure C.1 cont.

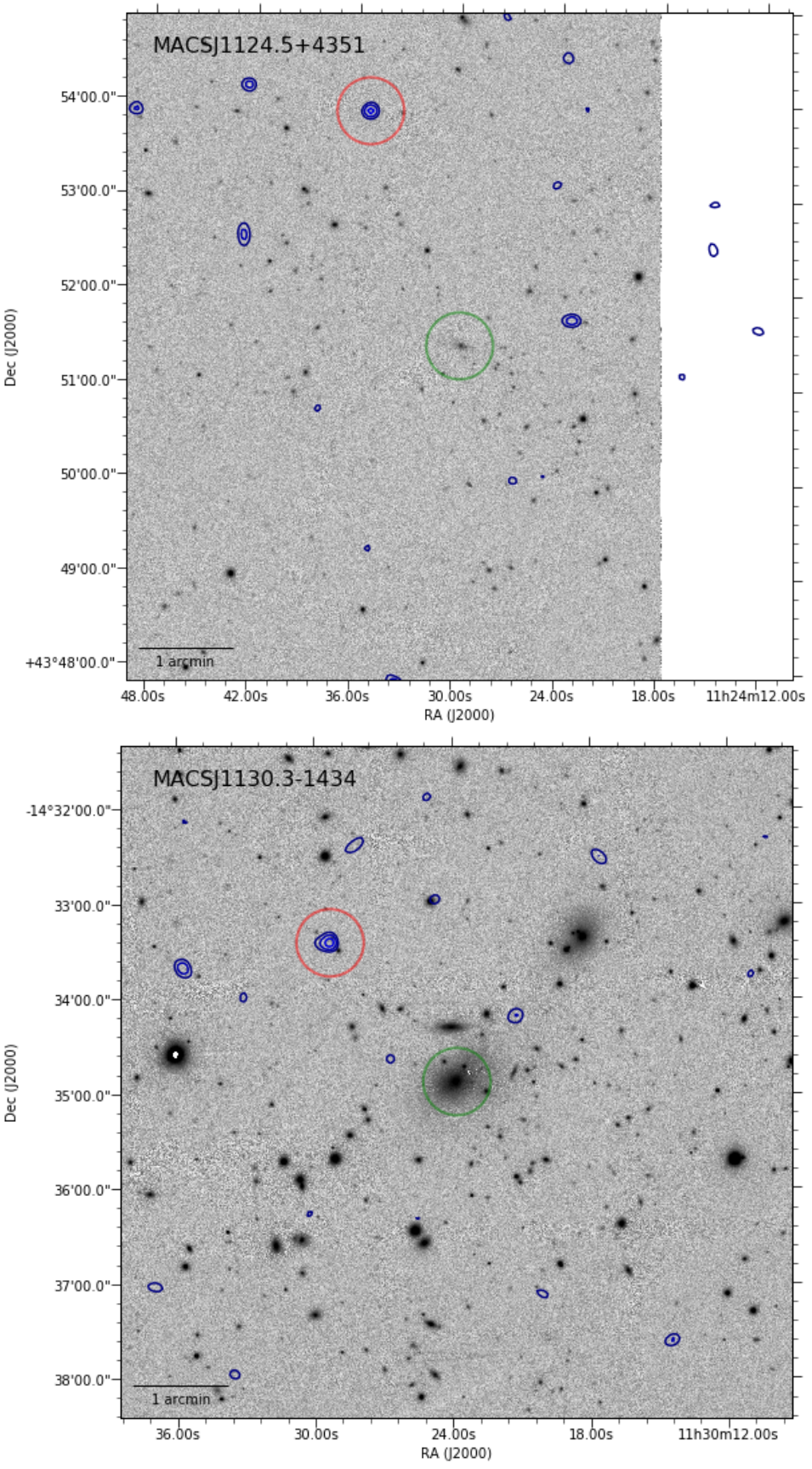

Figure C.1 cont.

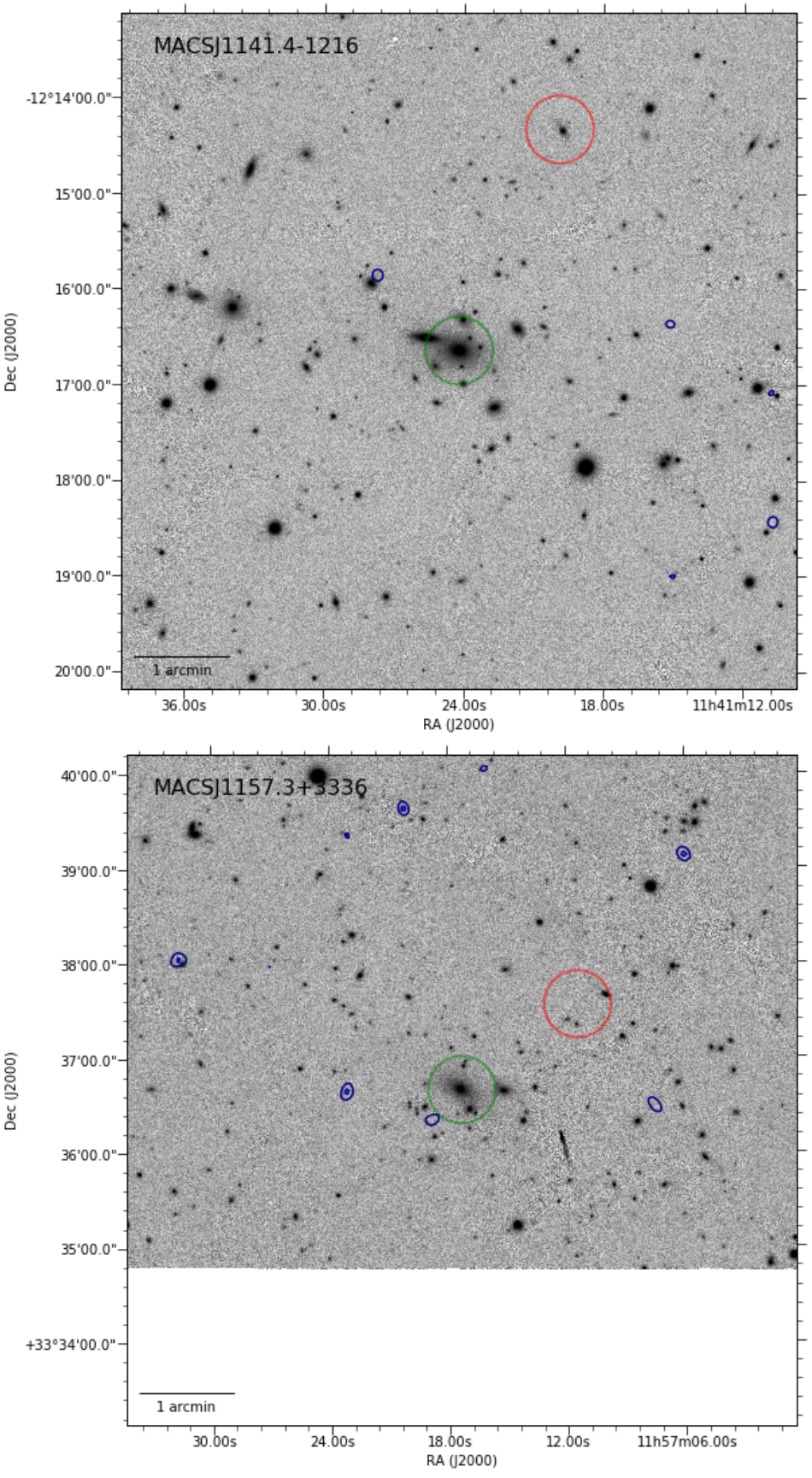

Figure C.1 cont.

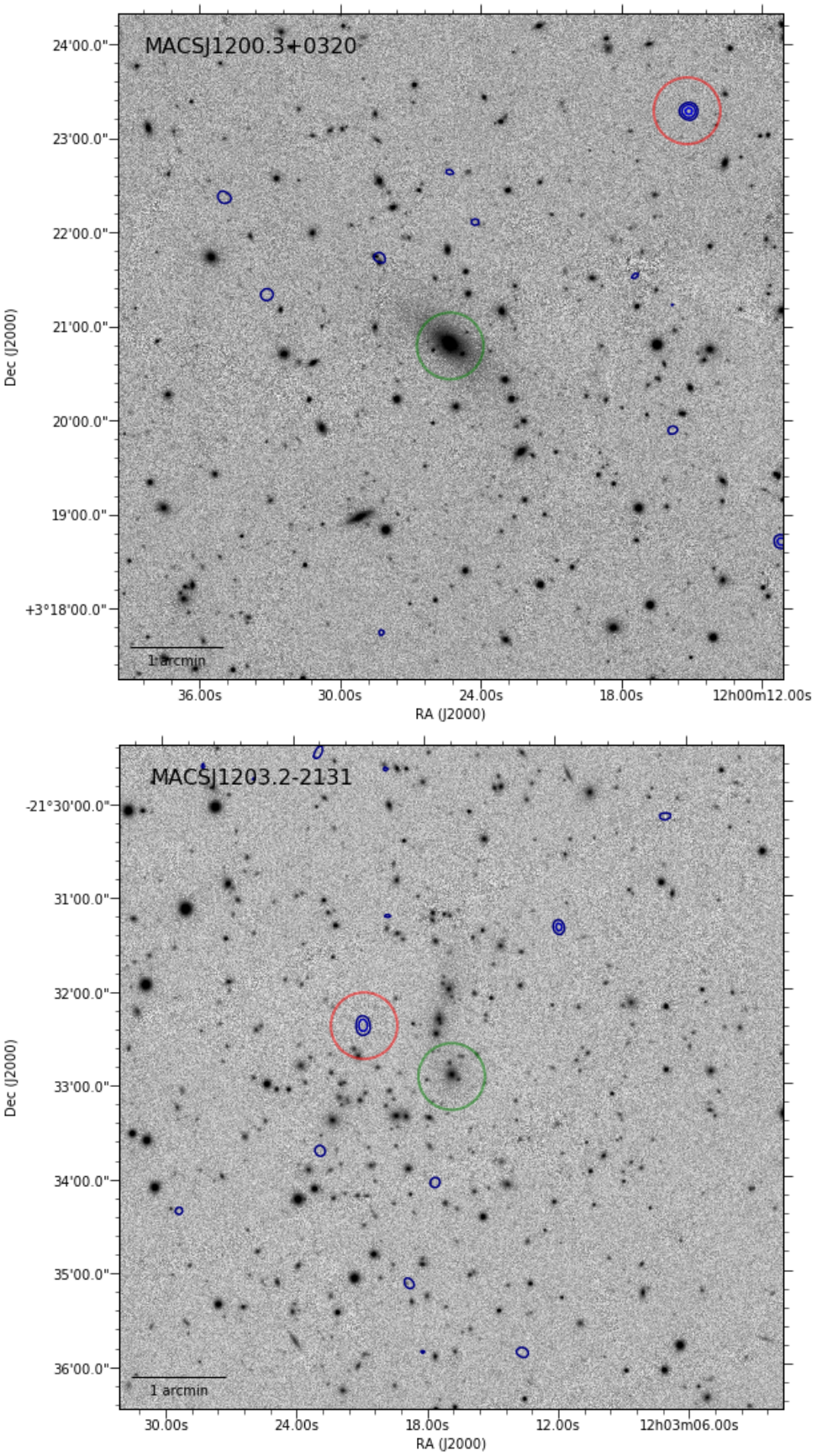

Figure C.1 cont.

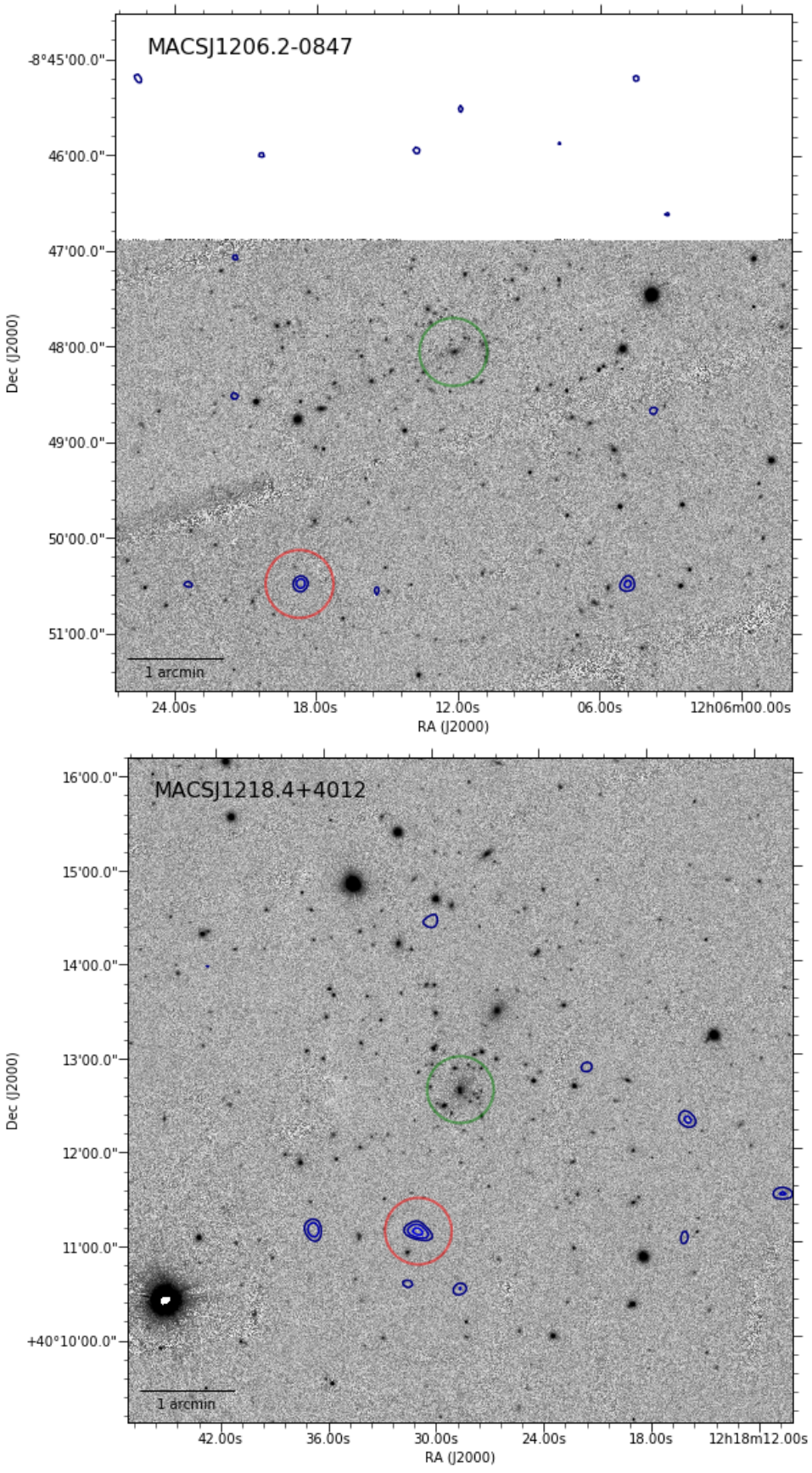

Figure C.1 cont.

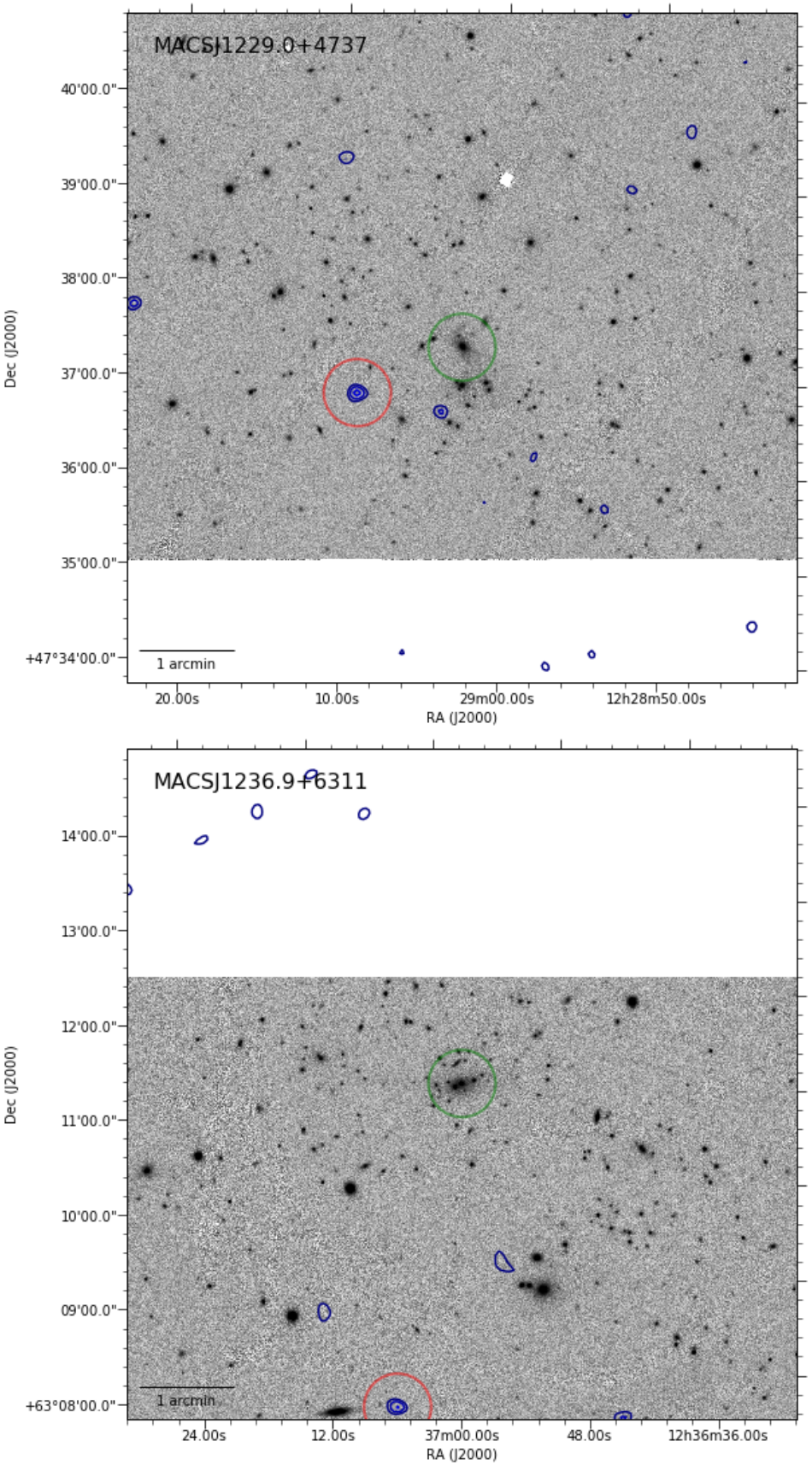

Figure C.1 cont.

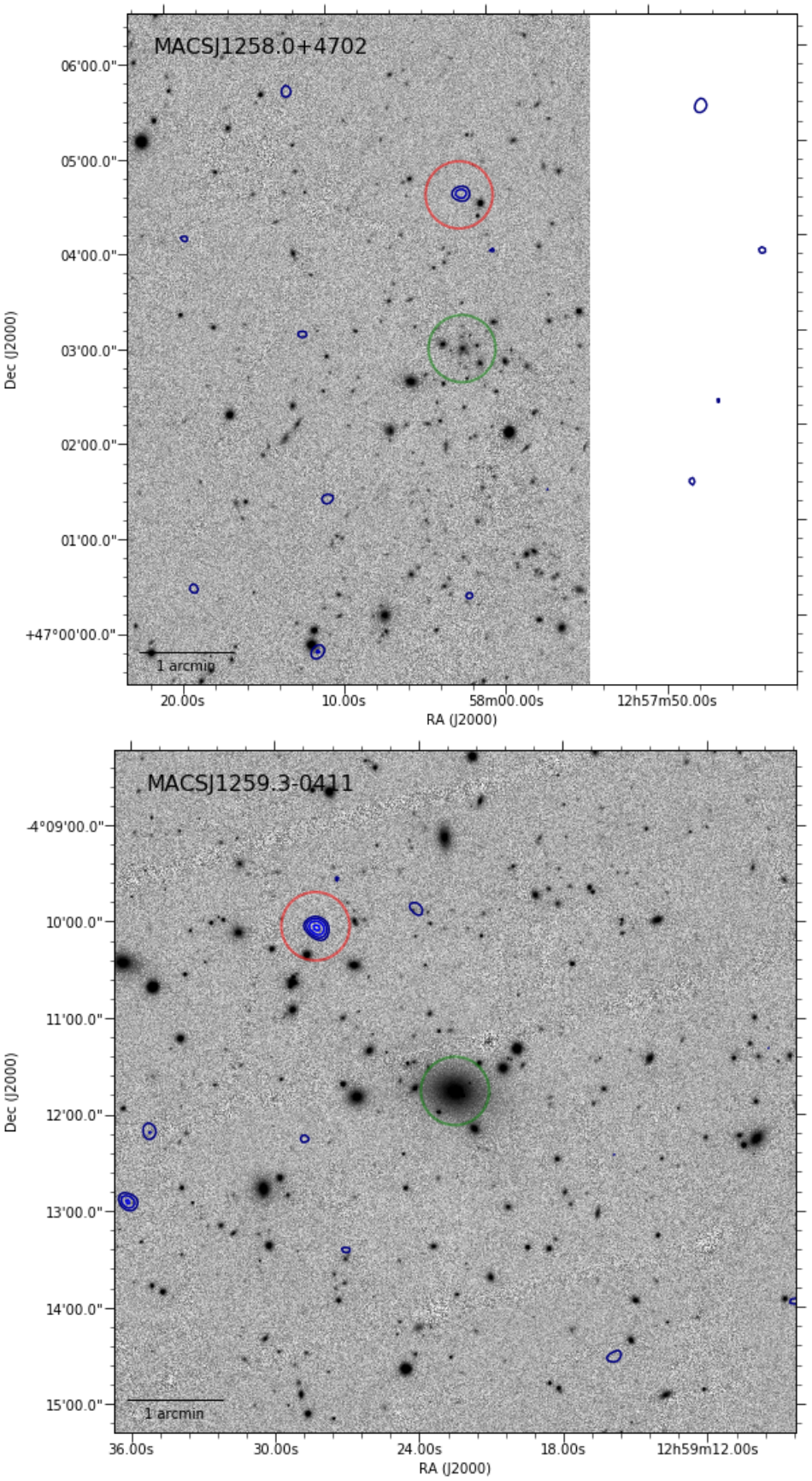

Figure C.1 cont.

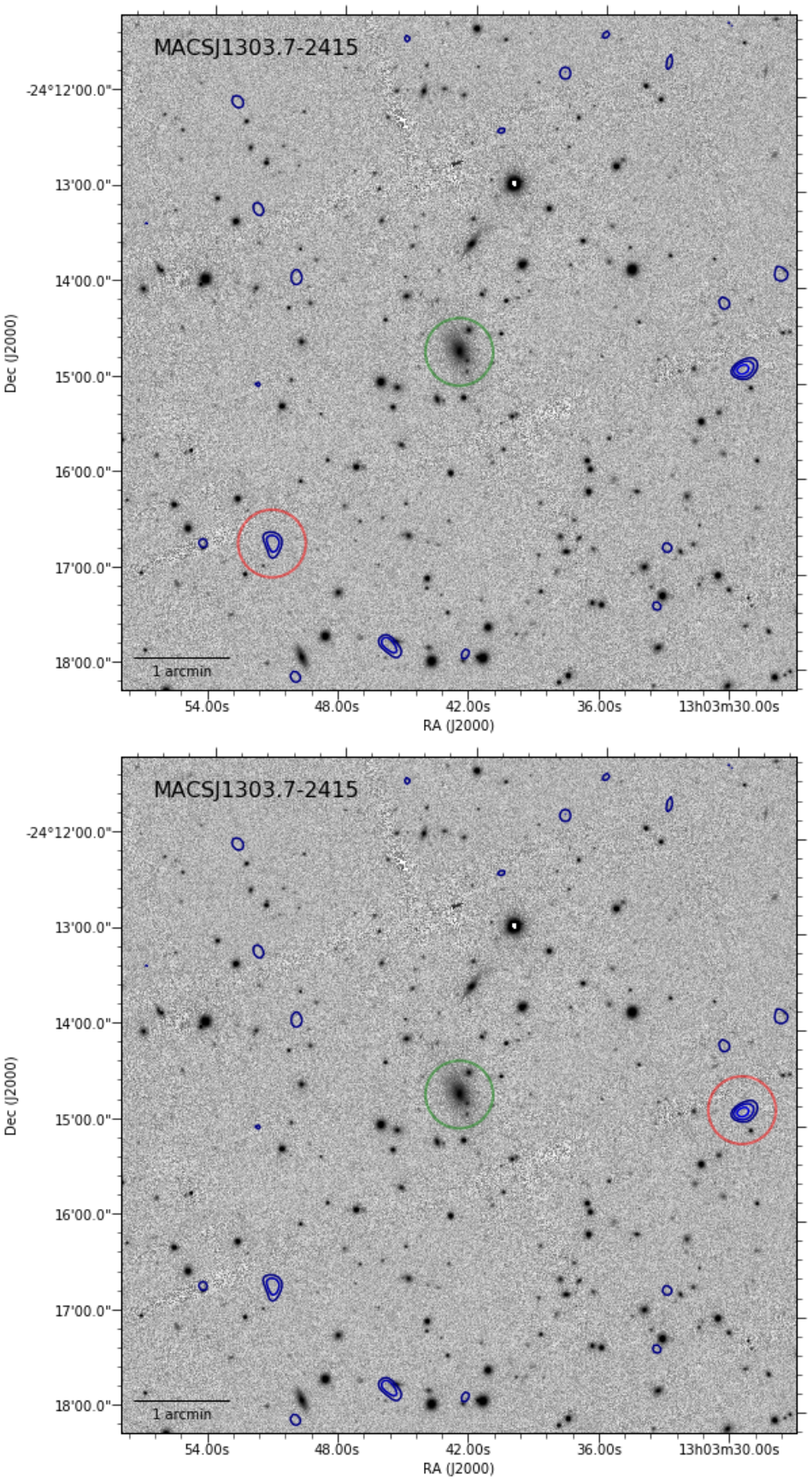

Figure C.1 cont.

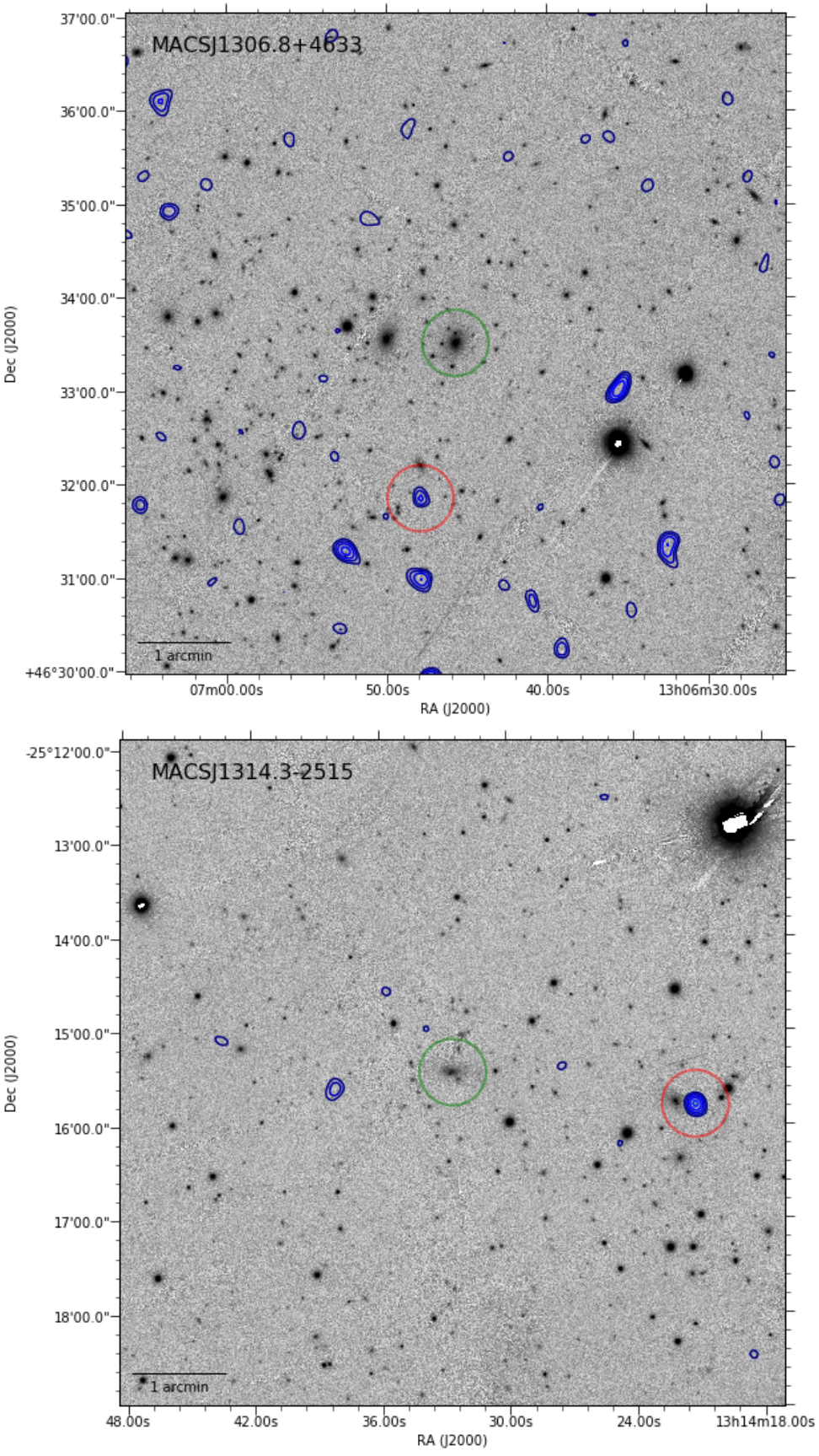

Figure C.1 cont.

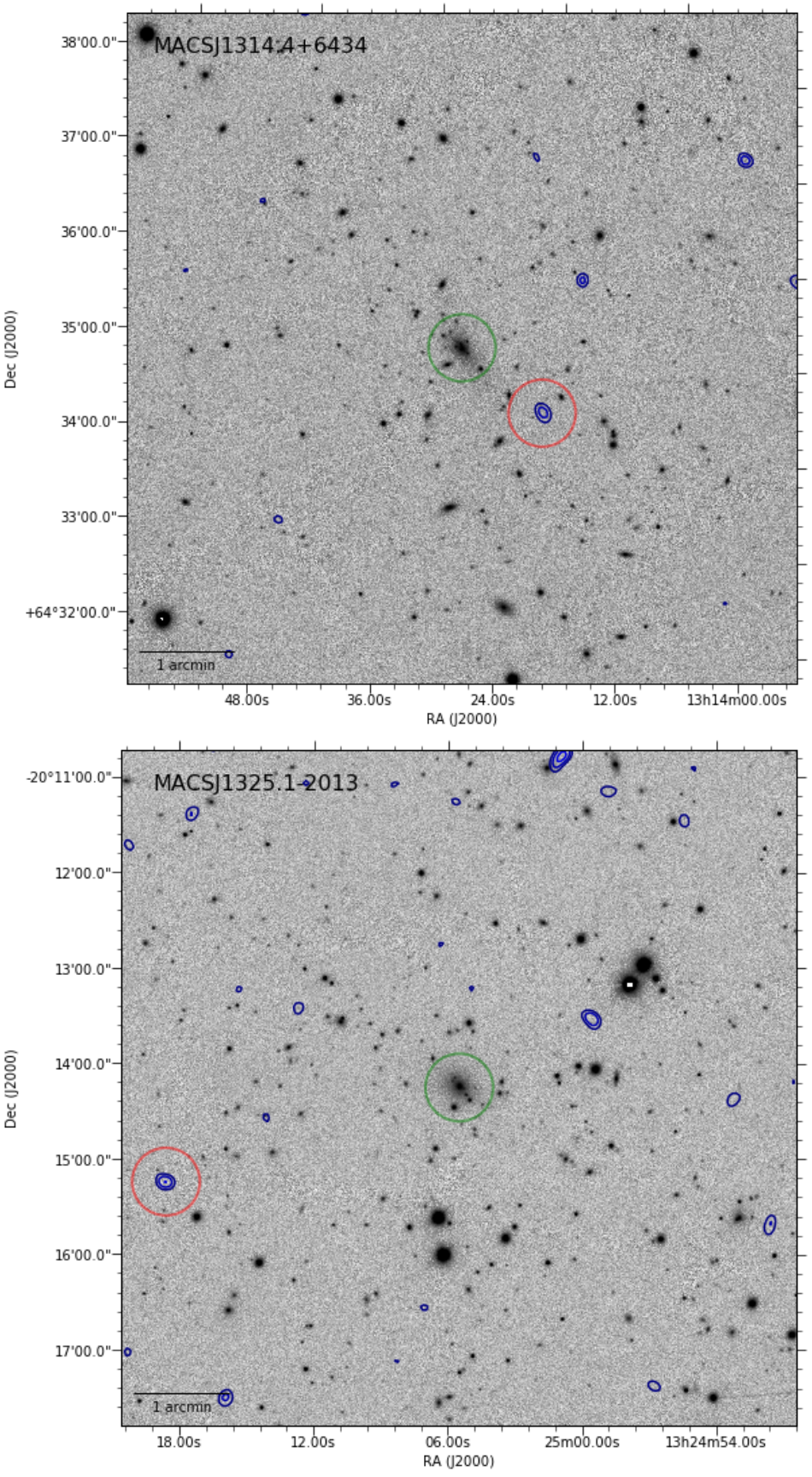

Figure C.1 cont.

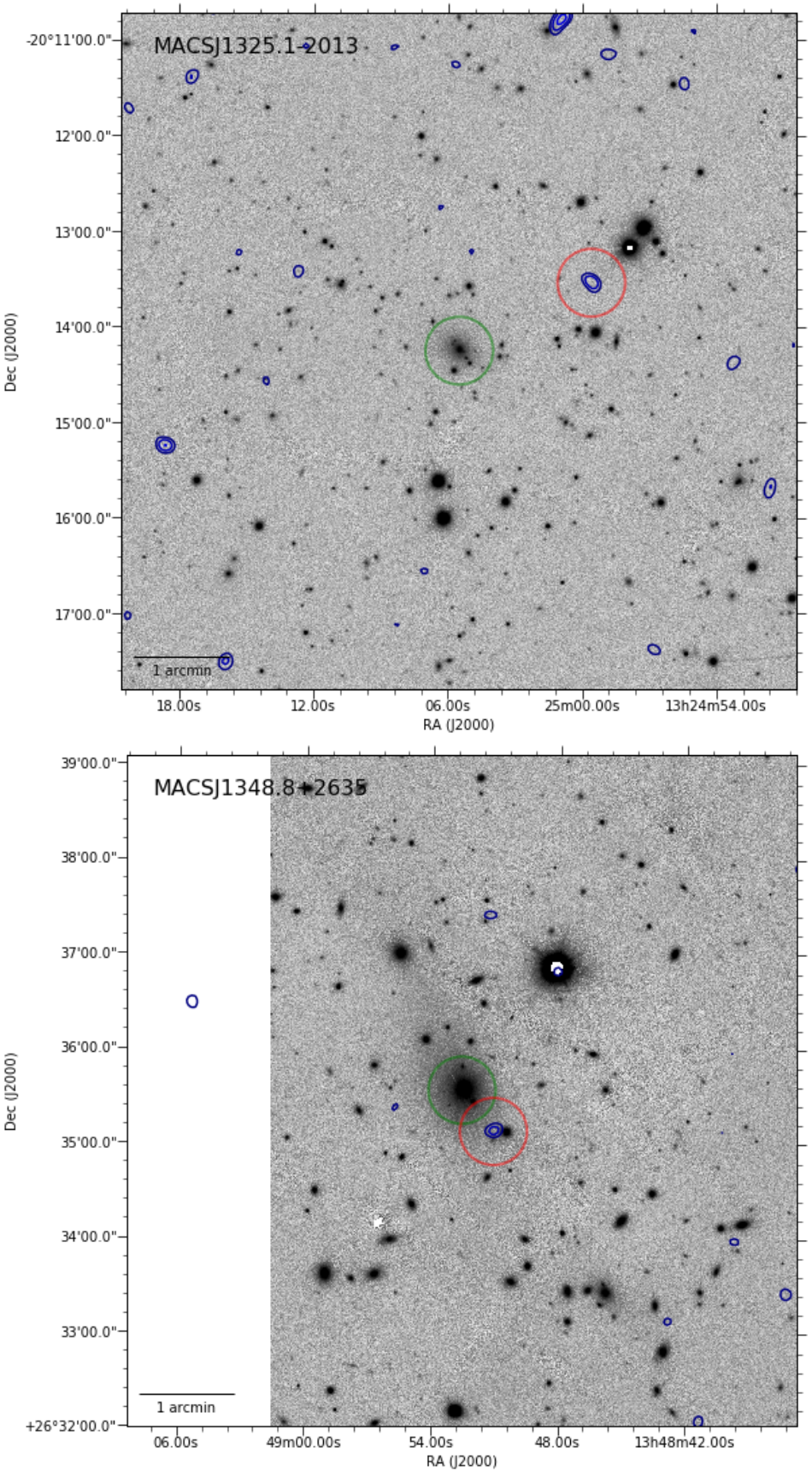

Figure C.1 cont.

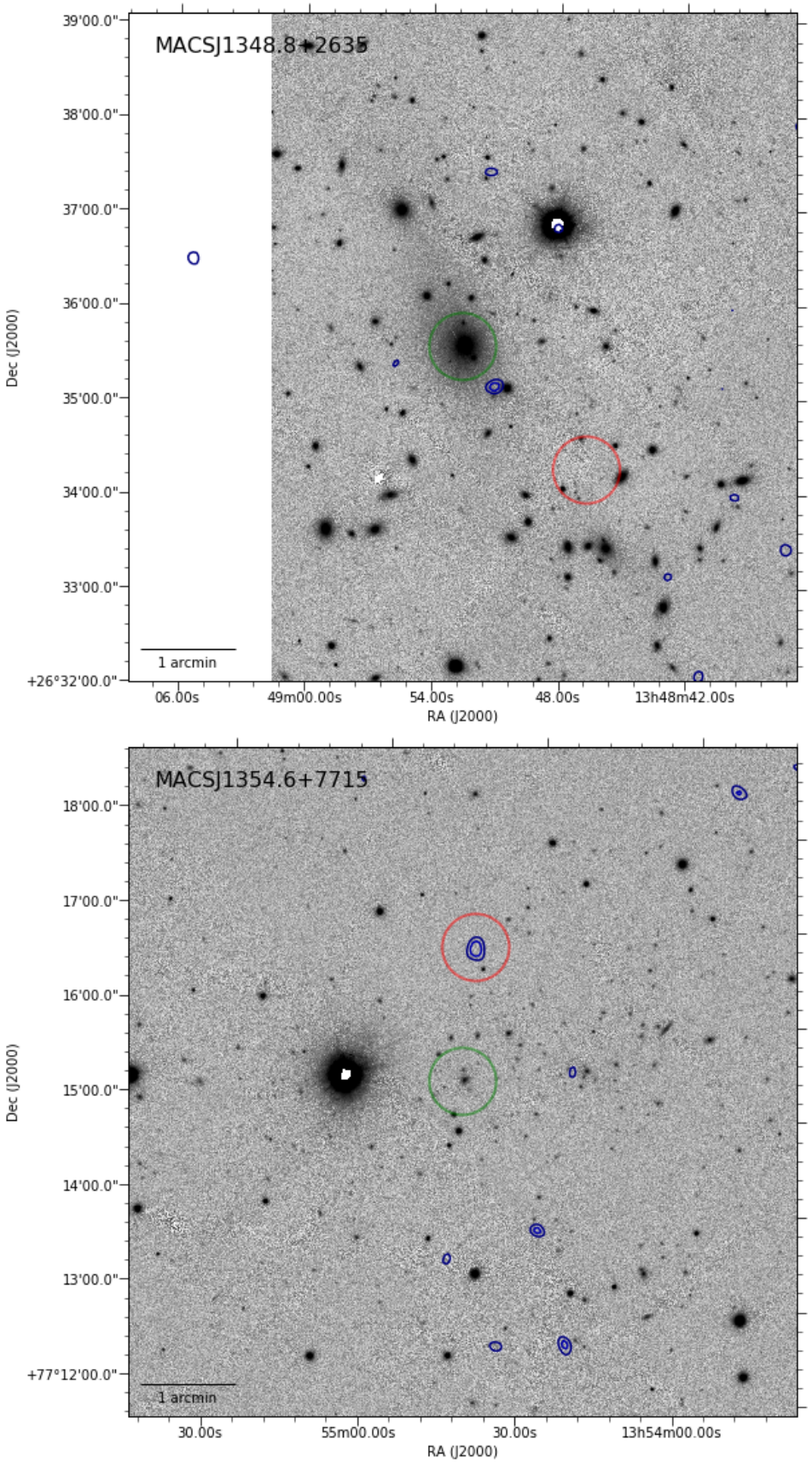

Figure C.1 cont.

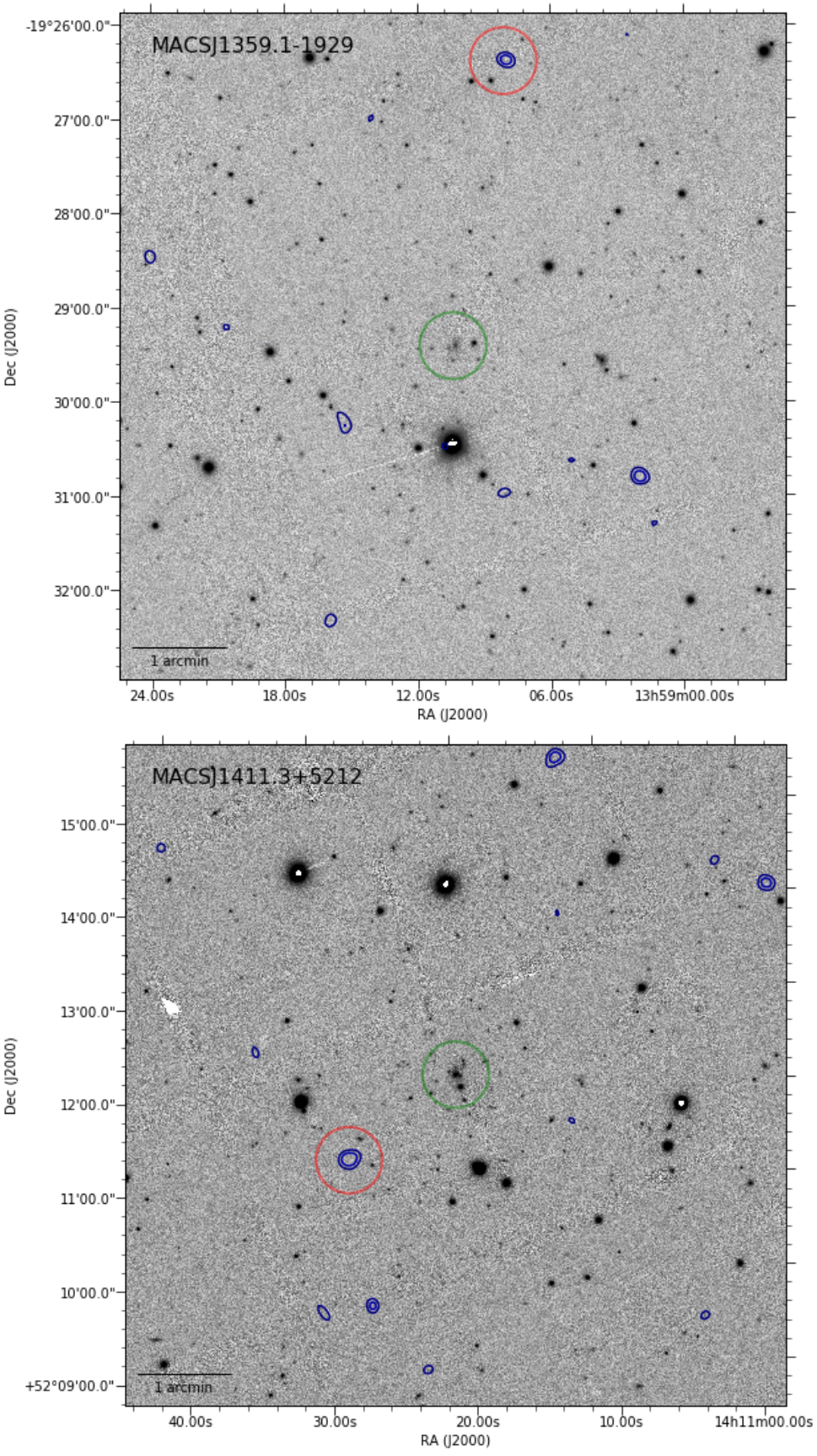

Figure C.1 cont.

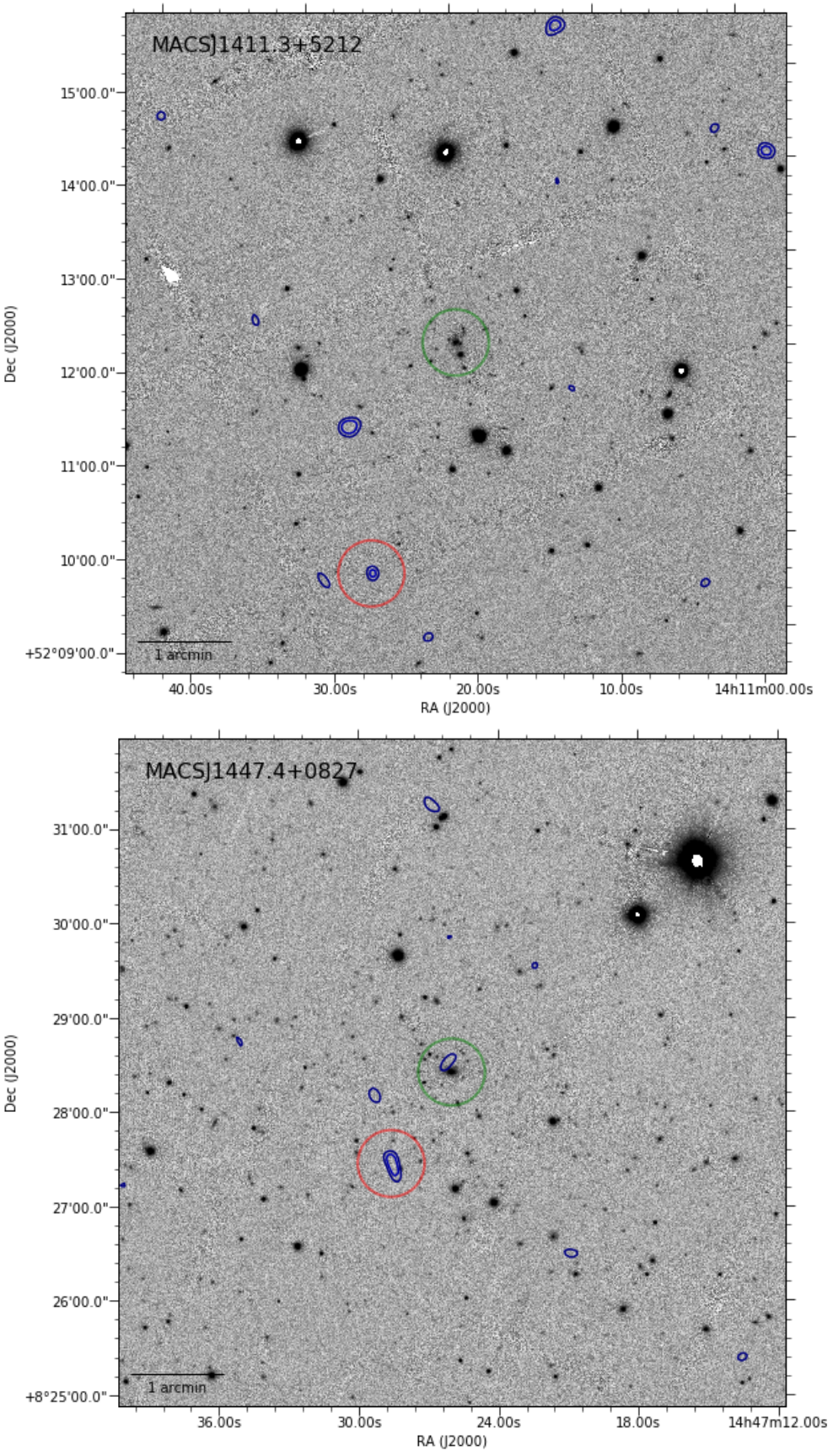

Figure C.1 cont.

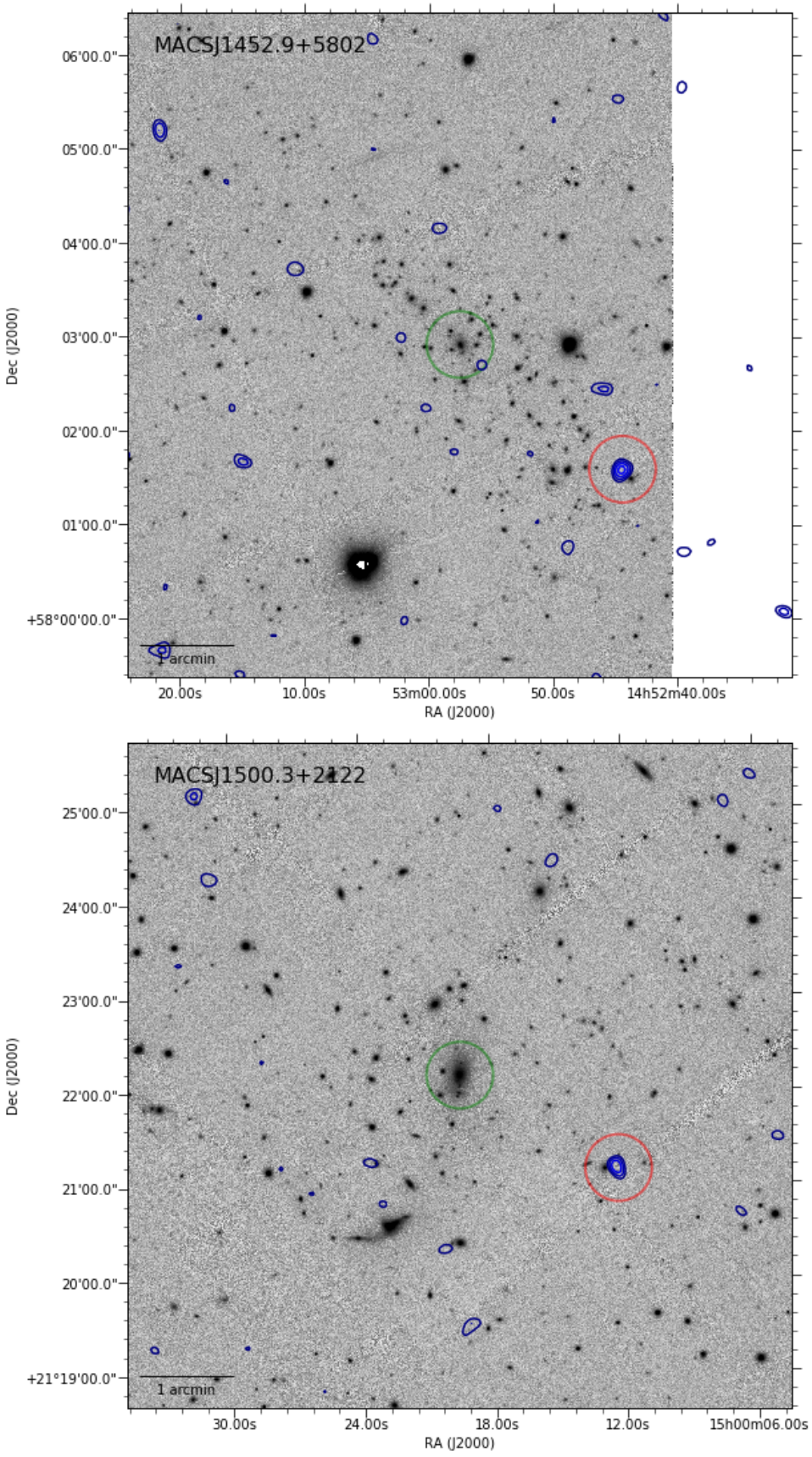

Figure C.1 cont.

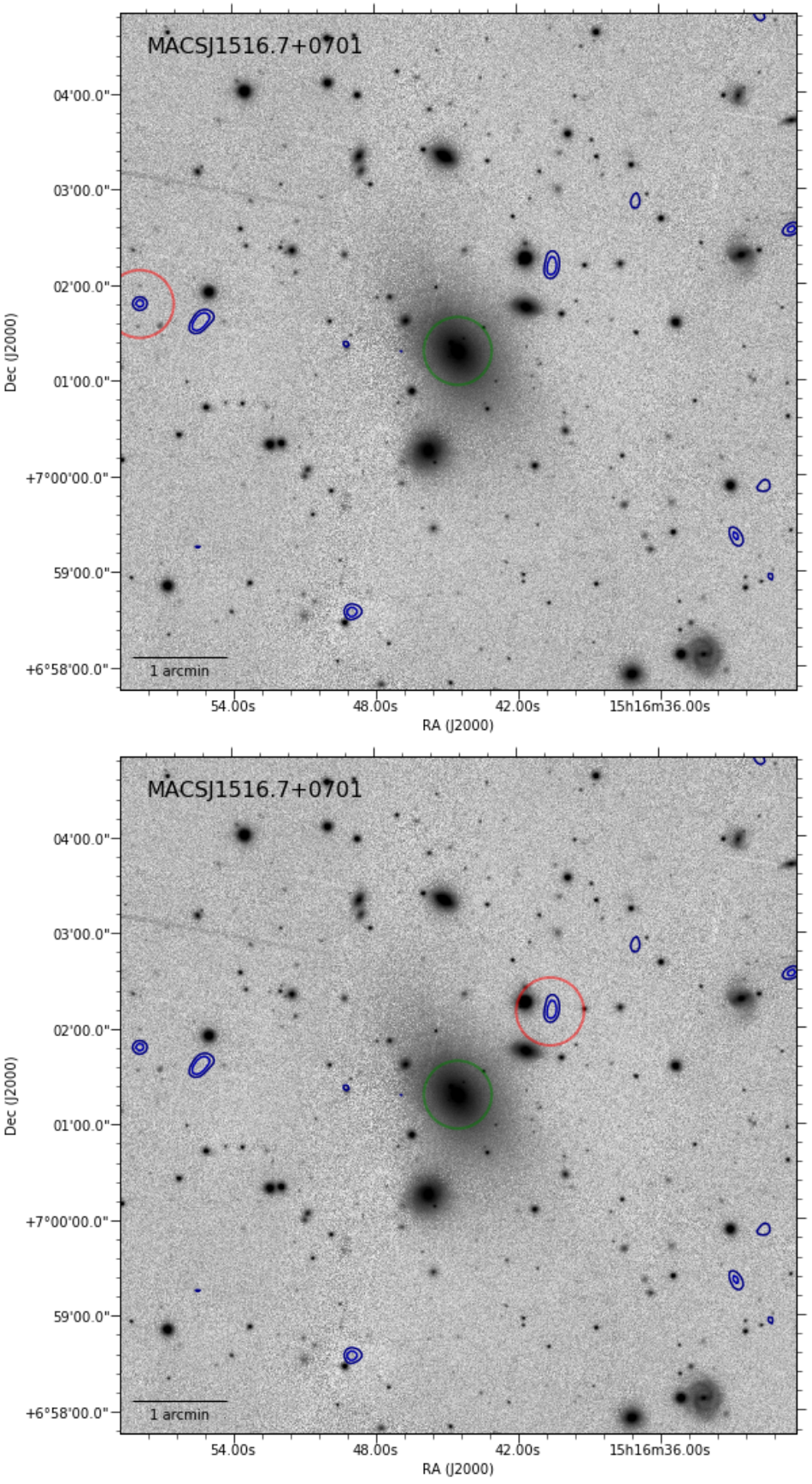

Figure C.1 cont.

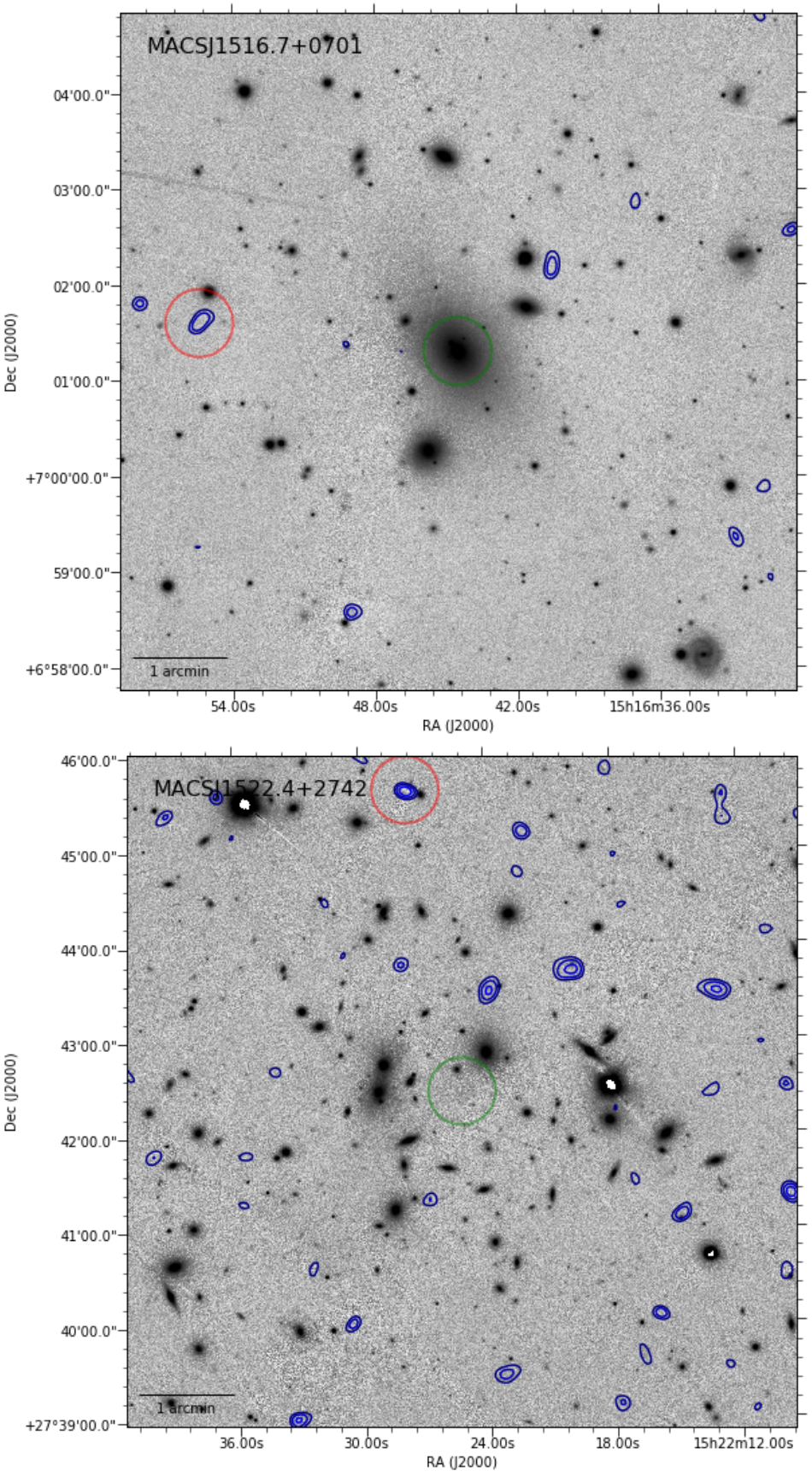

Figure C.1 cont.

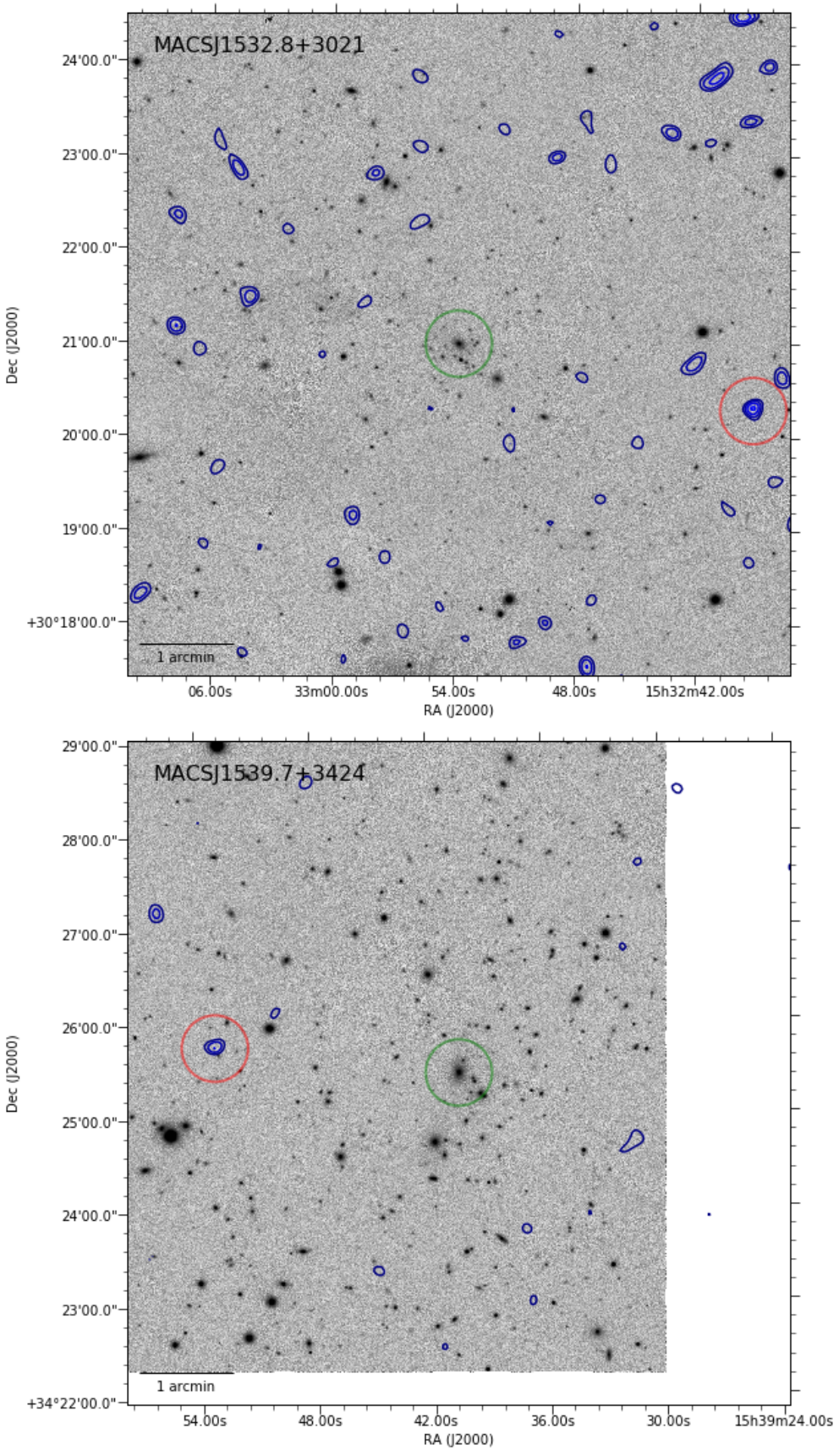

Figure C.1 cont.

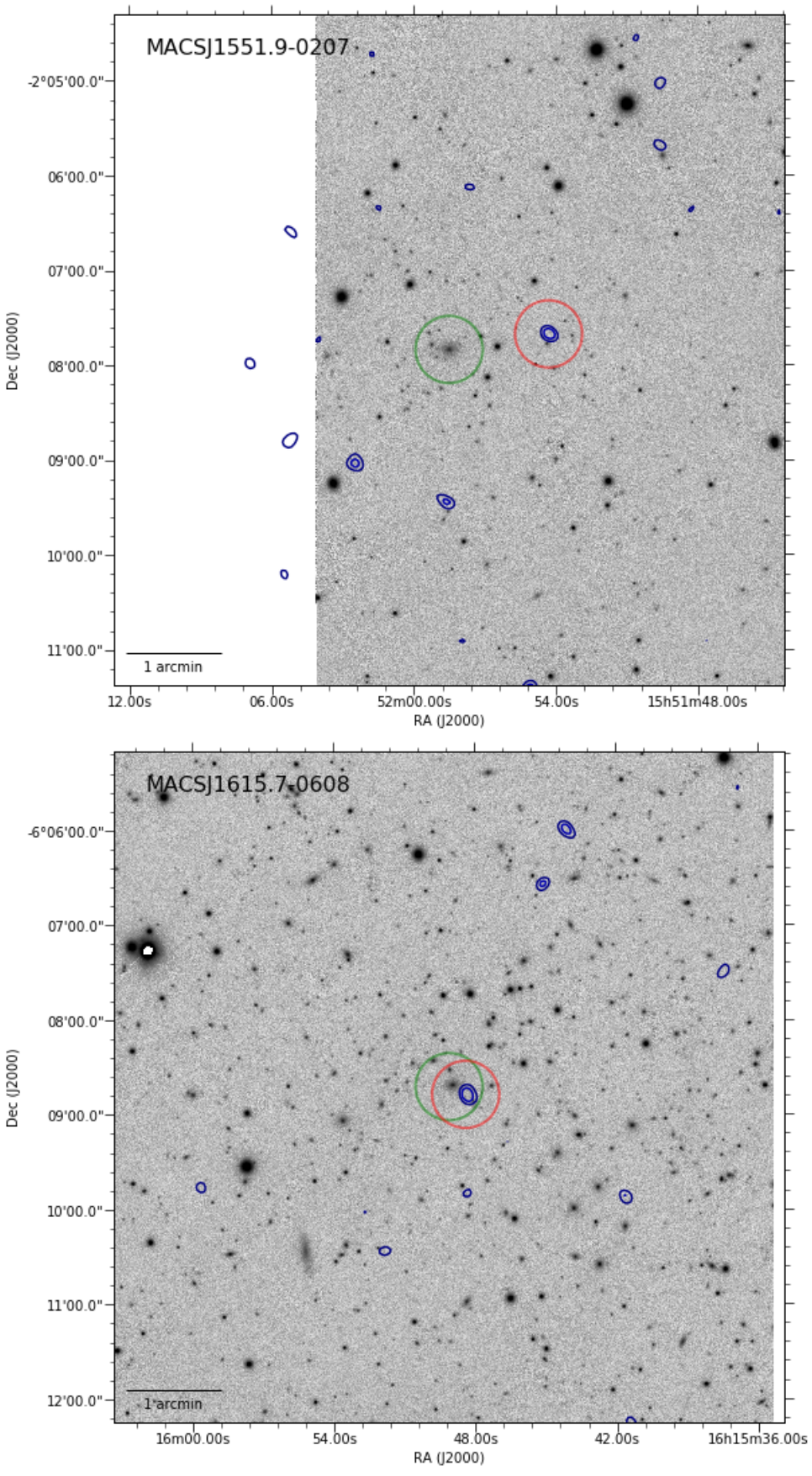

Figure C.1 cont.

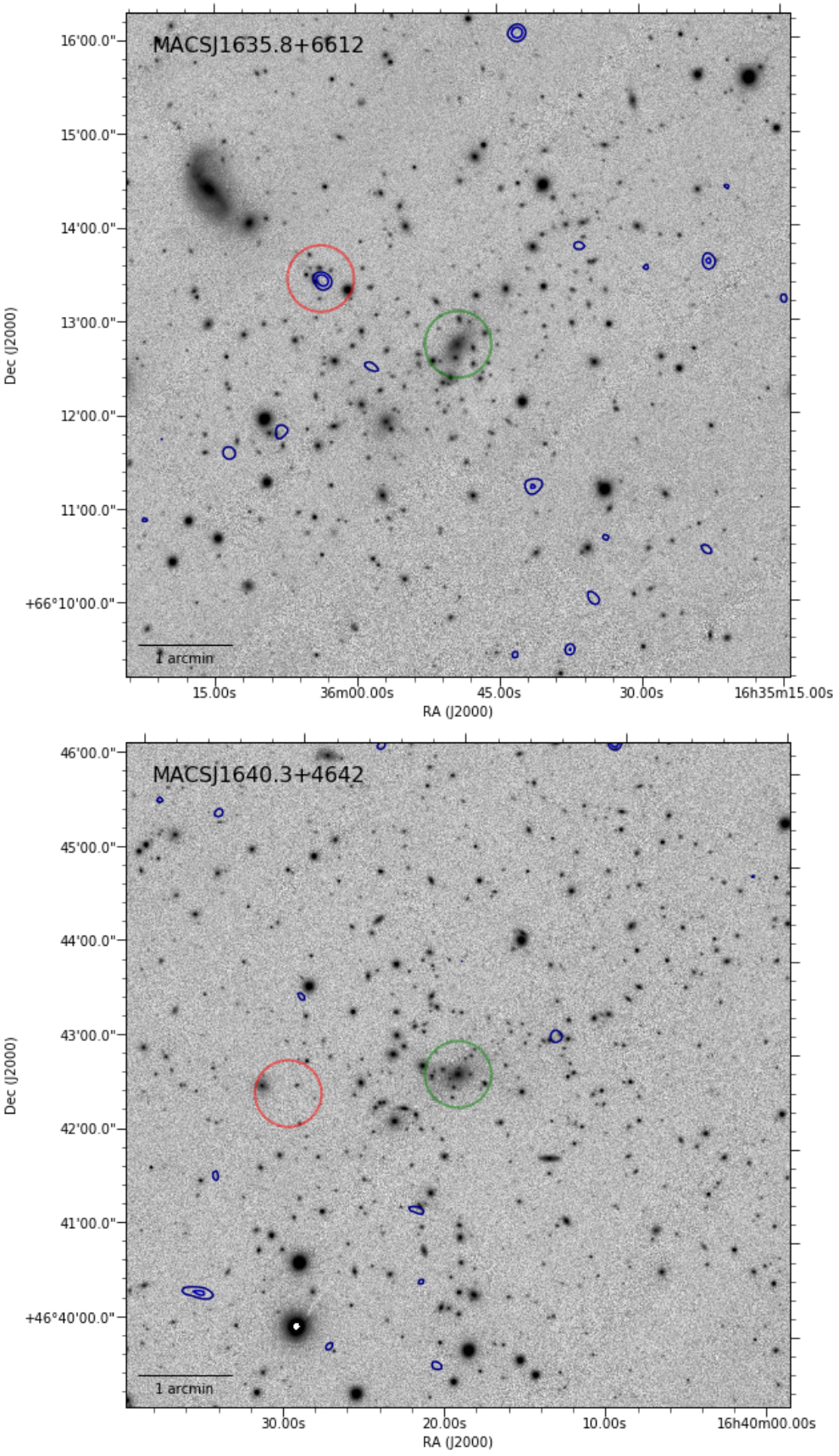

Figure C.1 cont.

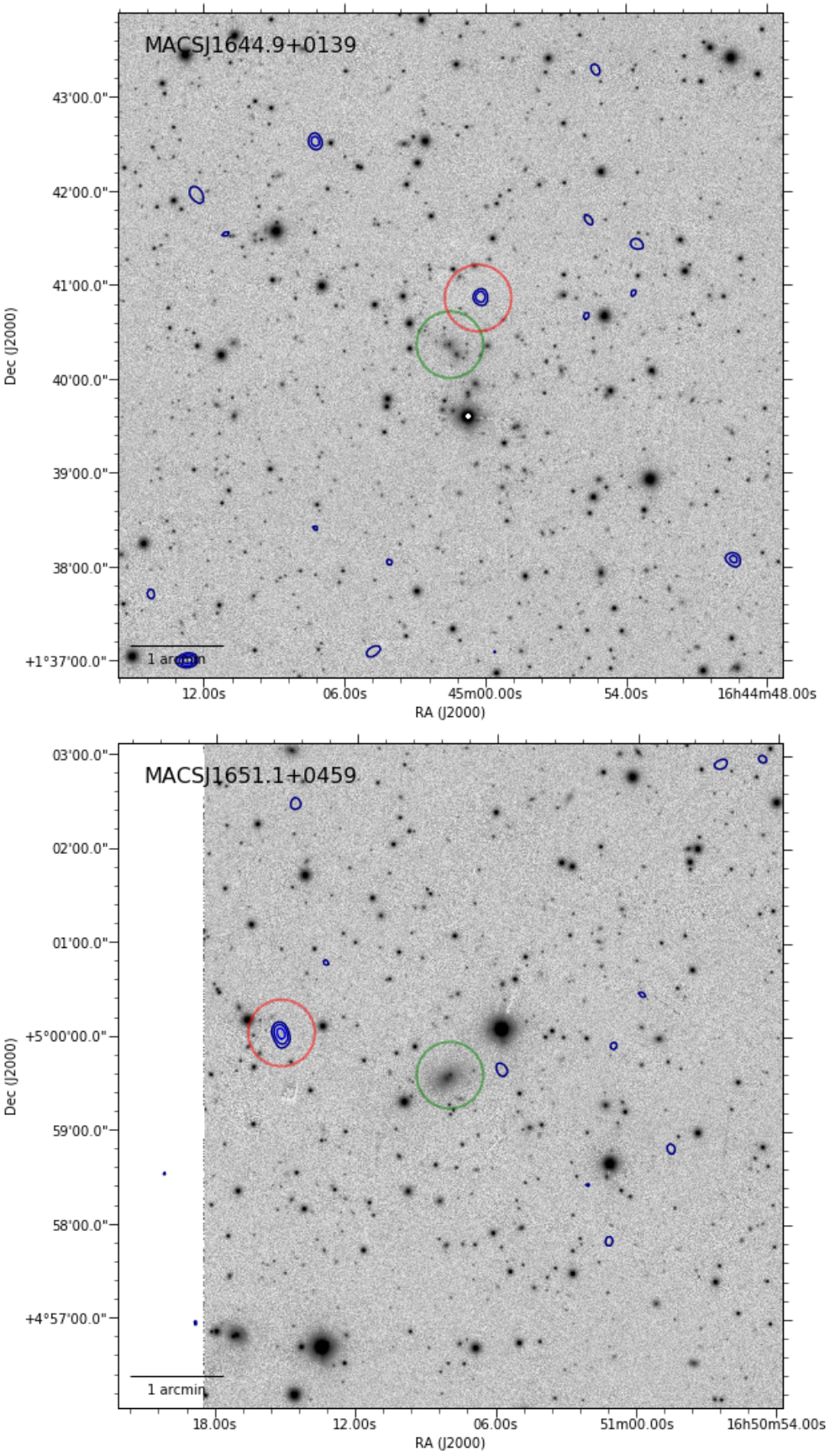

Figure C.1 cont.

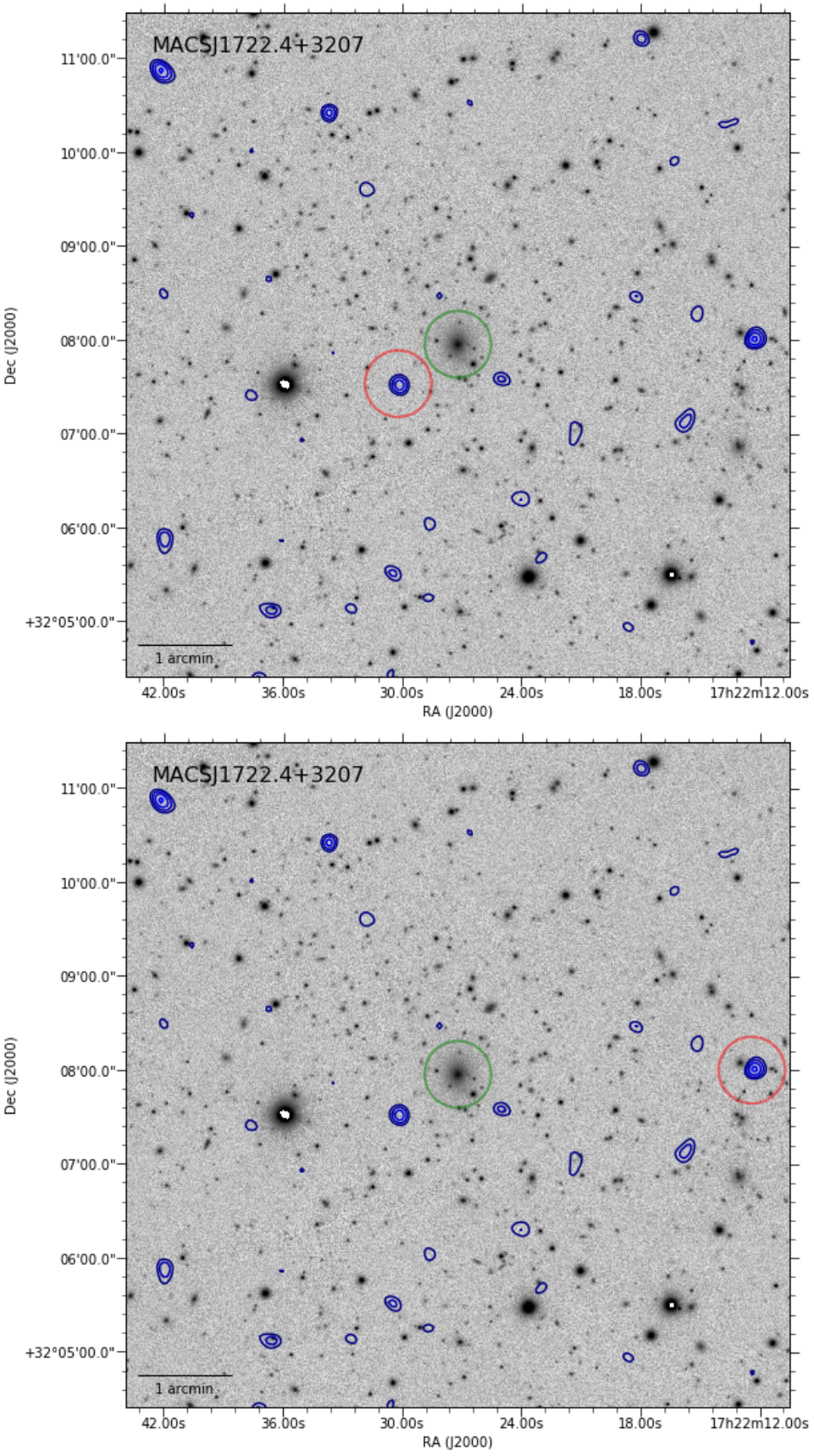

Figure C.1 cont.

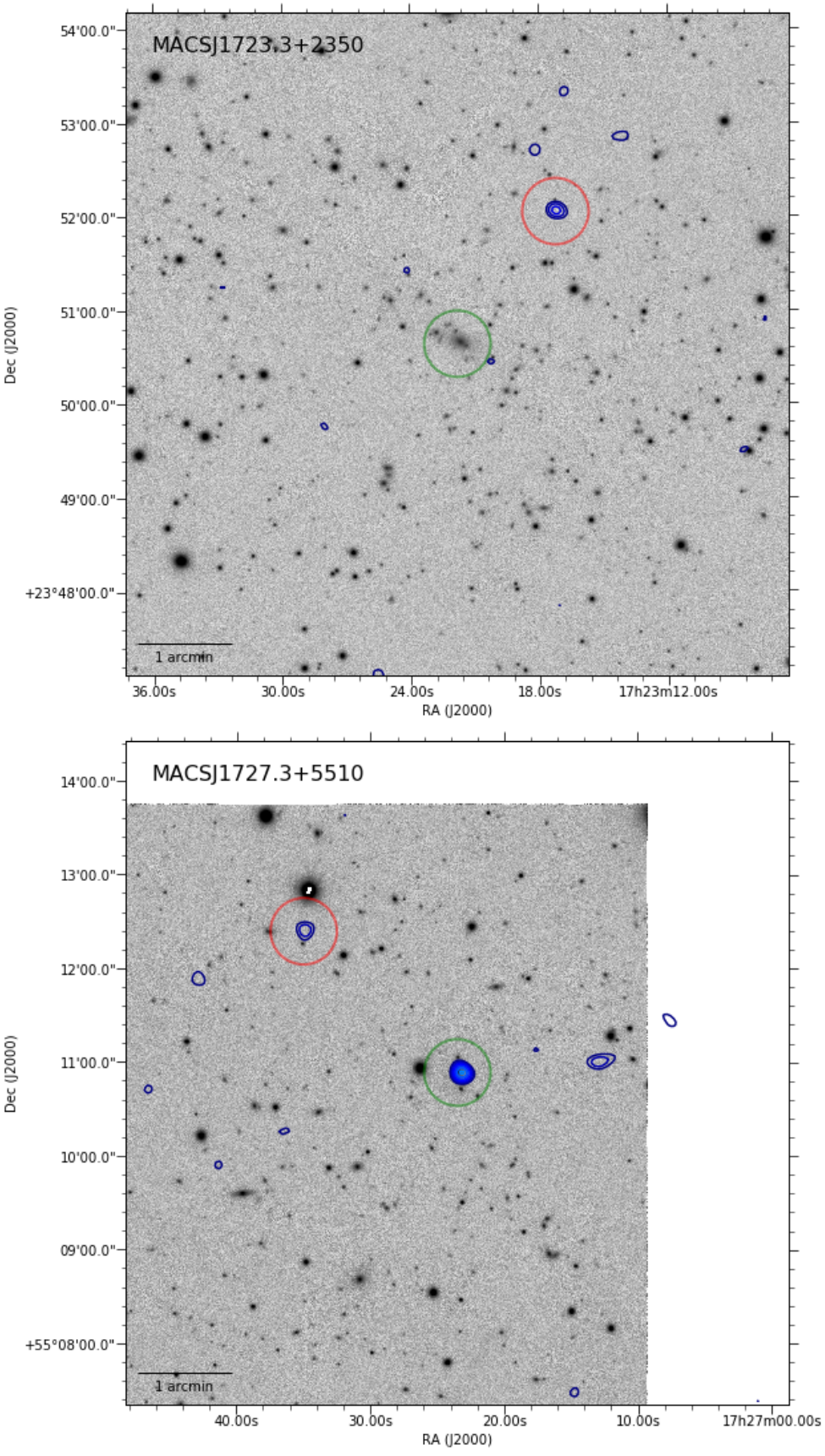

Figure C.1 cont.

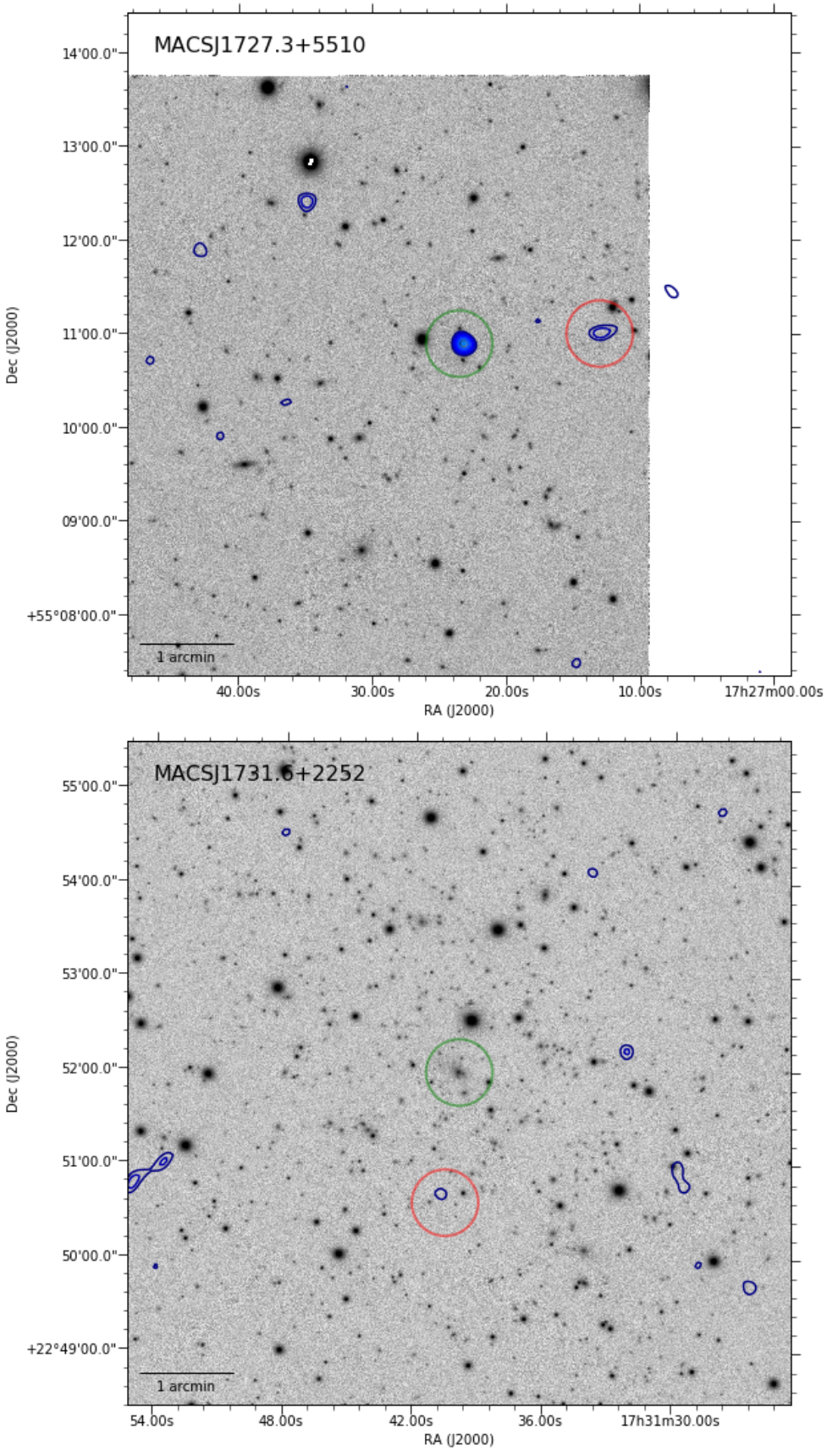

Figure C.1 cont.

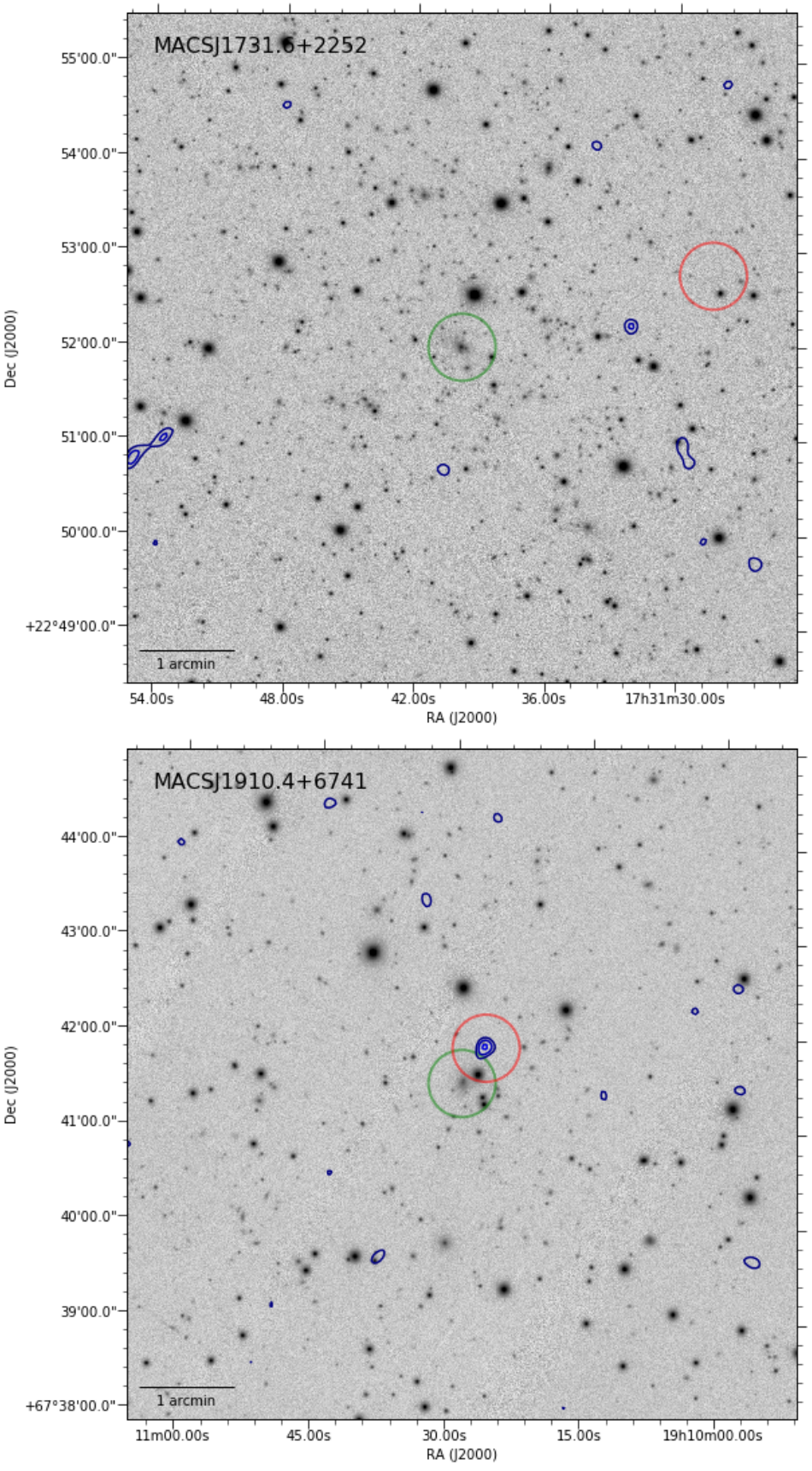

Figure C.1 cont.

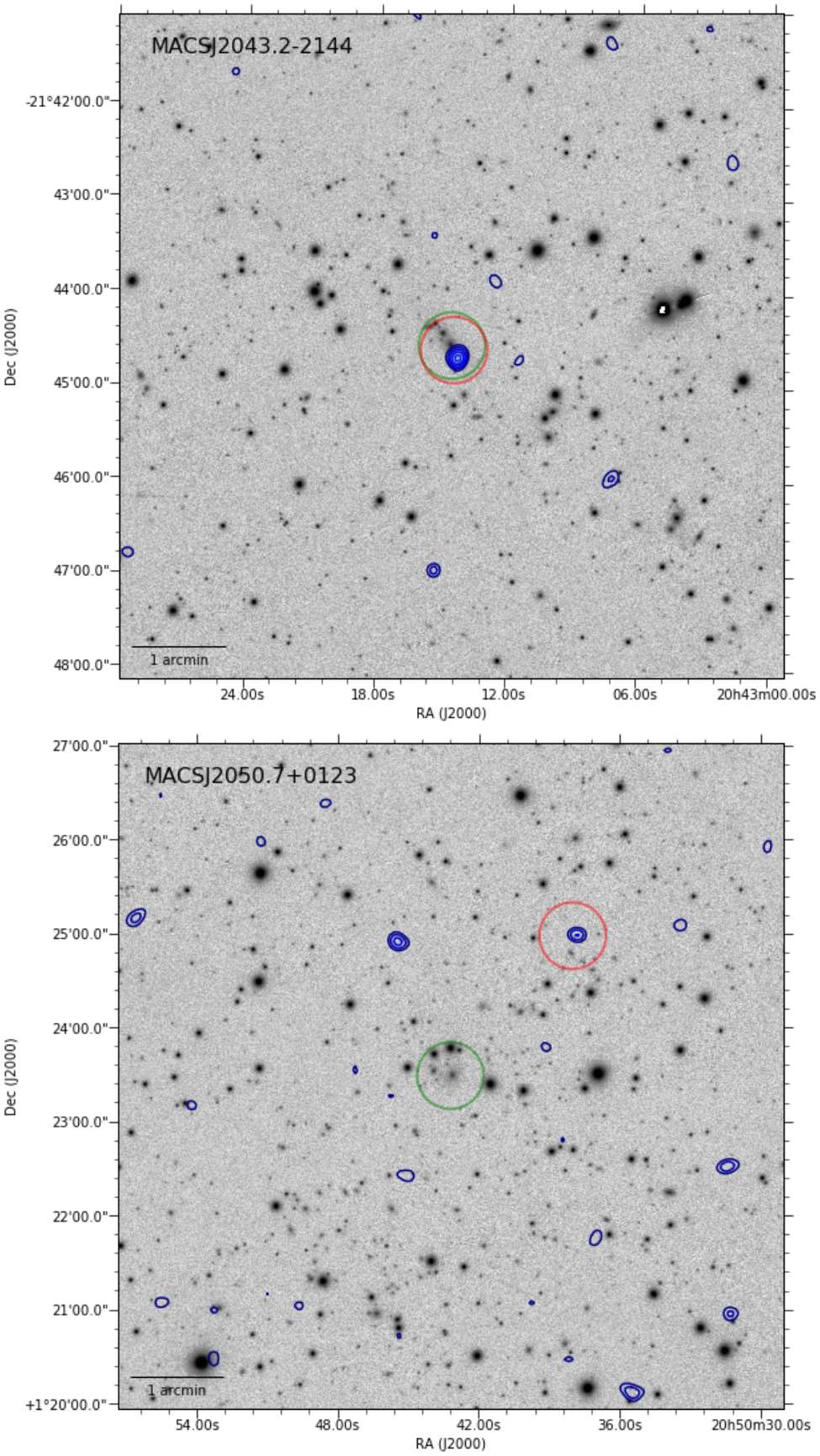

Figure C.1 cont.

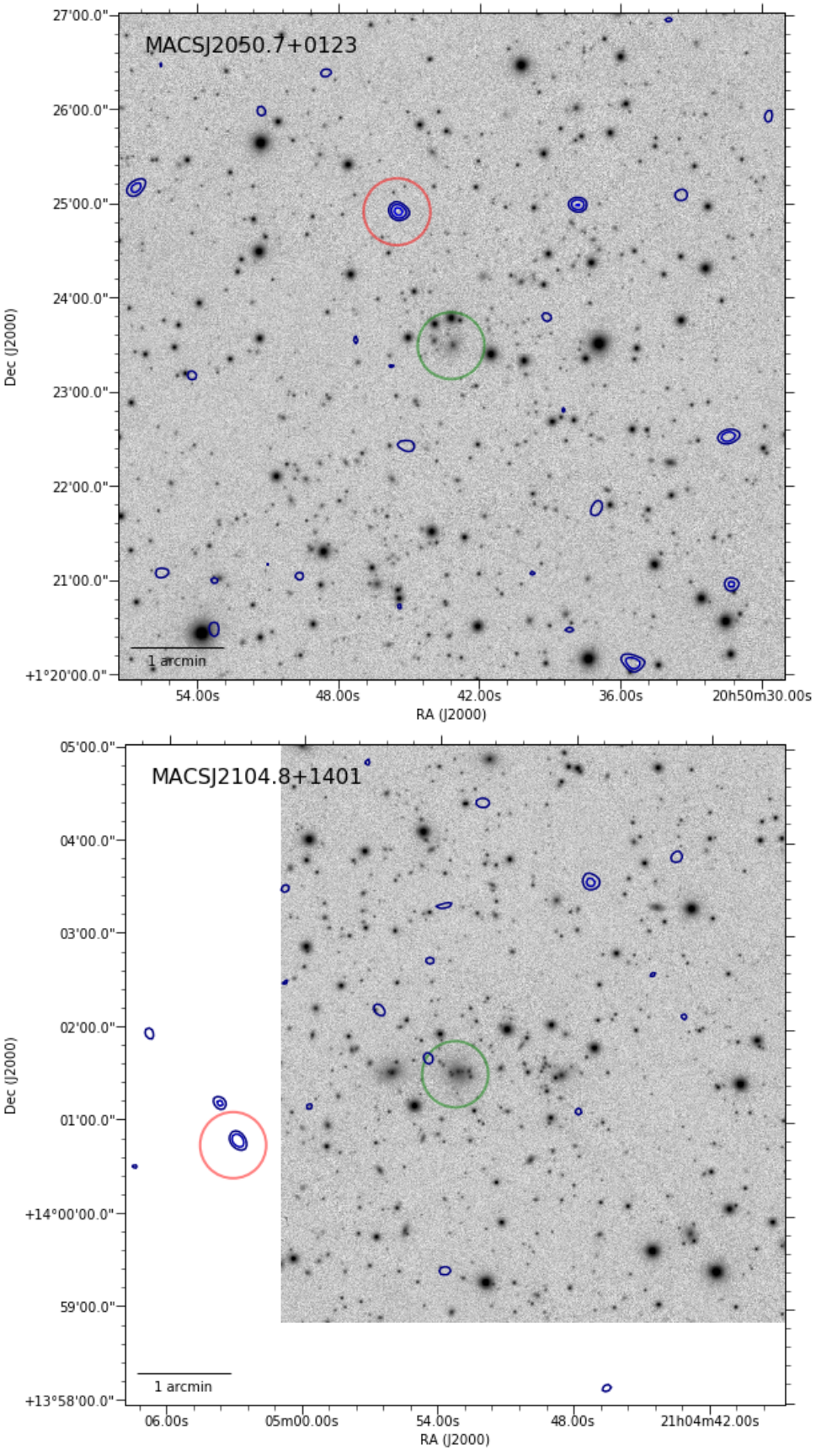

Figure C.1 cont.

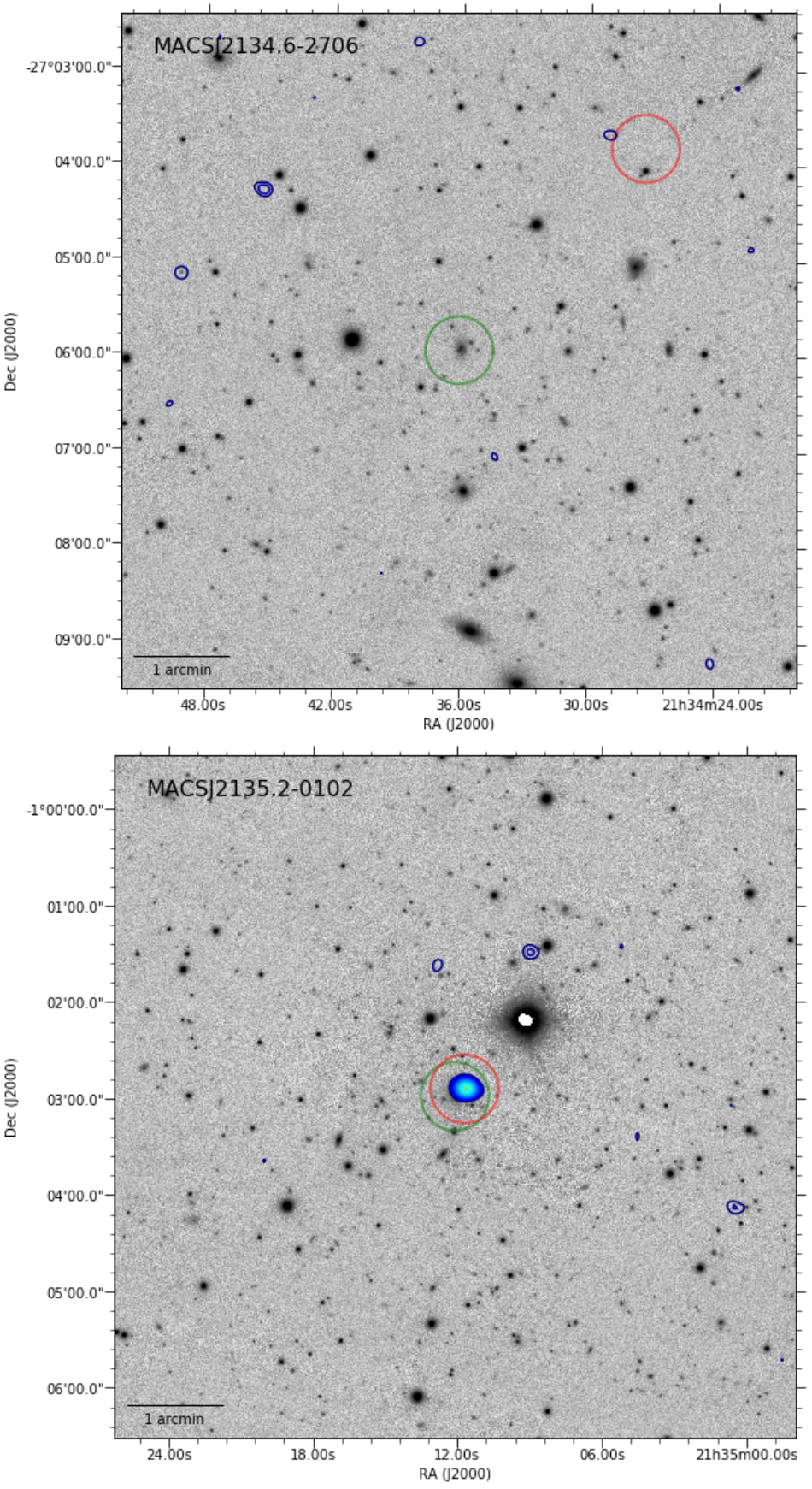

Figure C.1 cont.

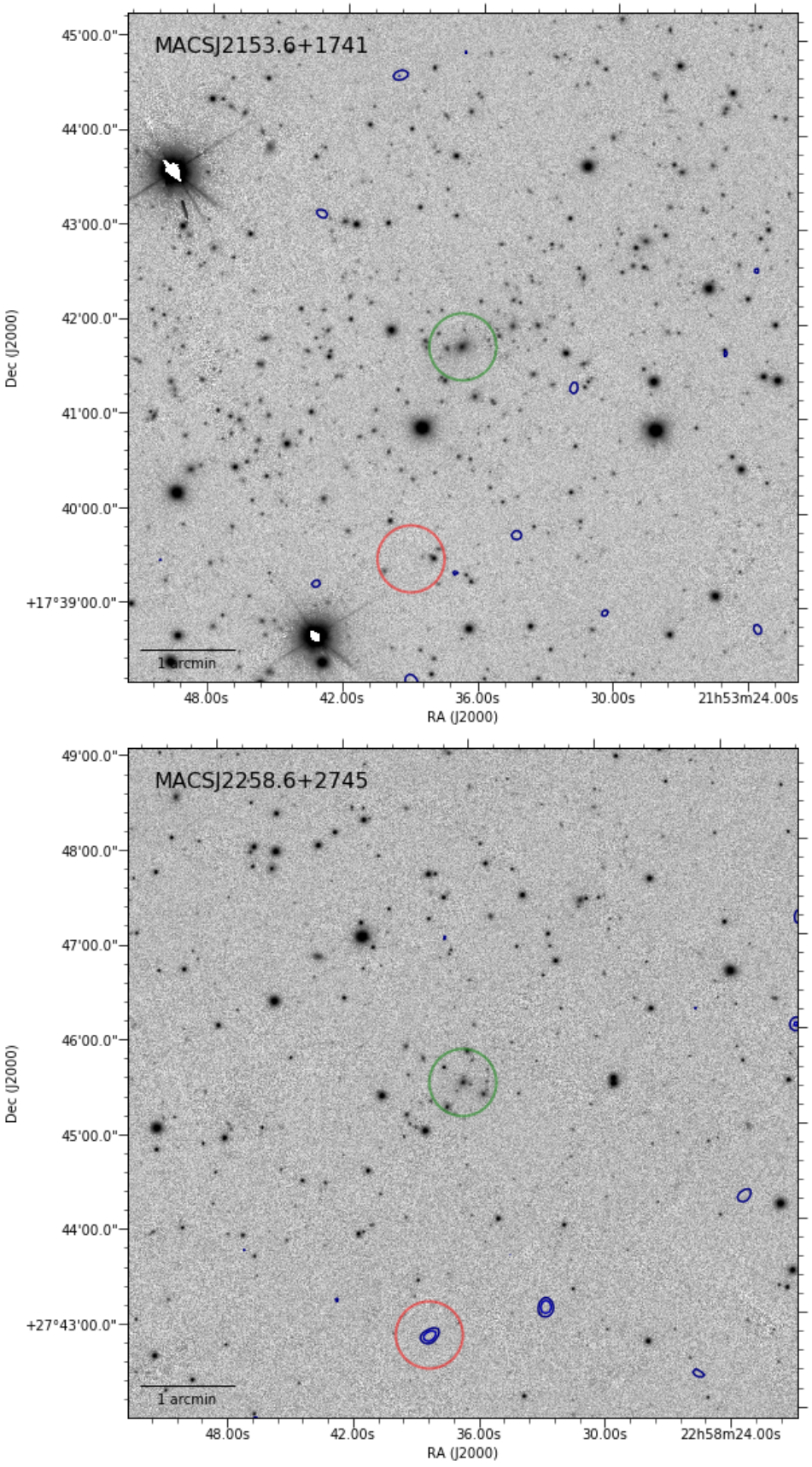

Figure C.1 cont.

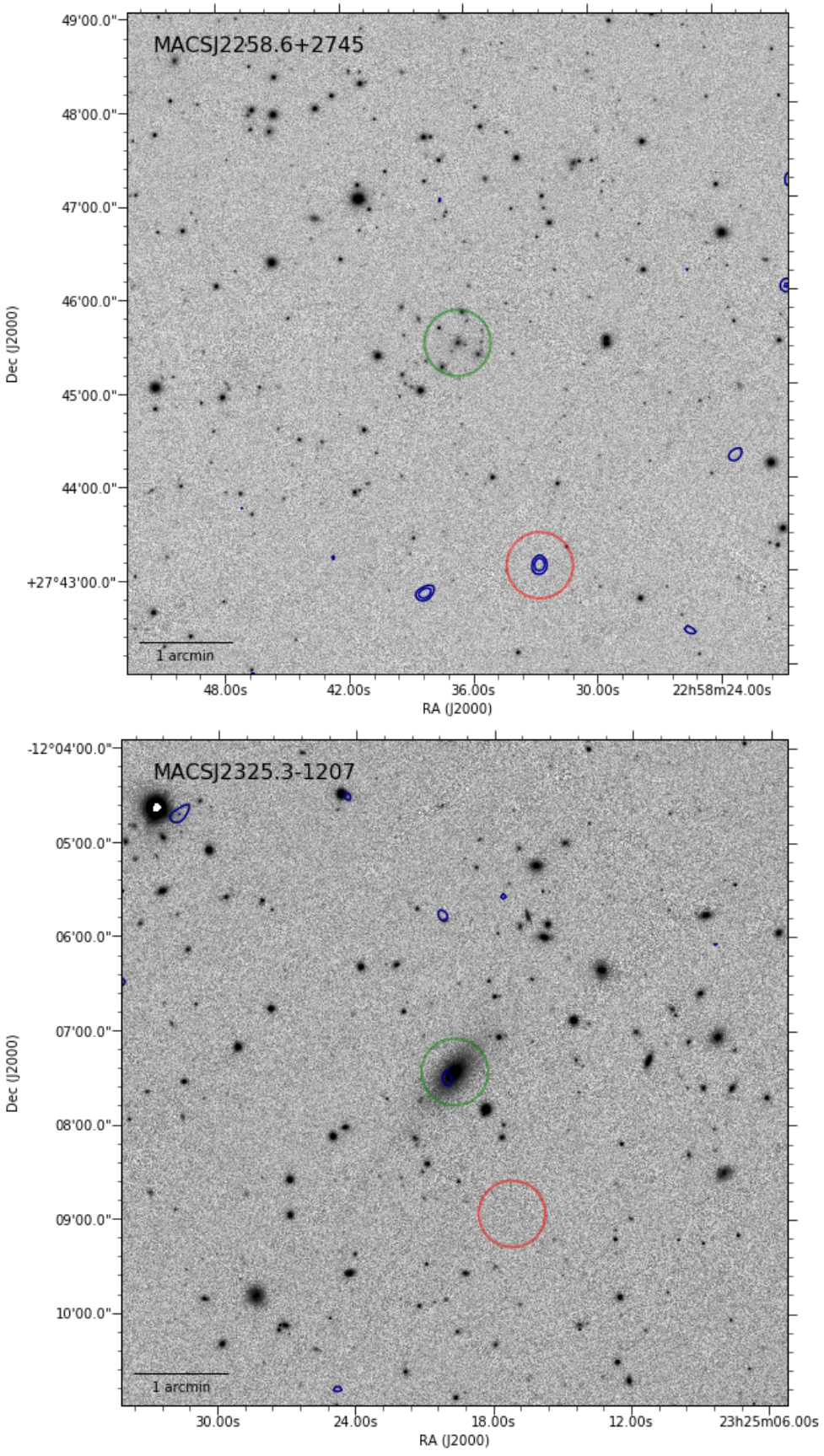

Figure C.1 cont.

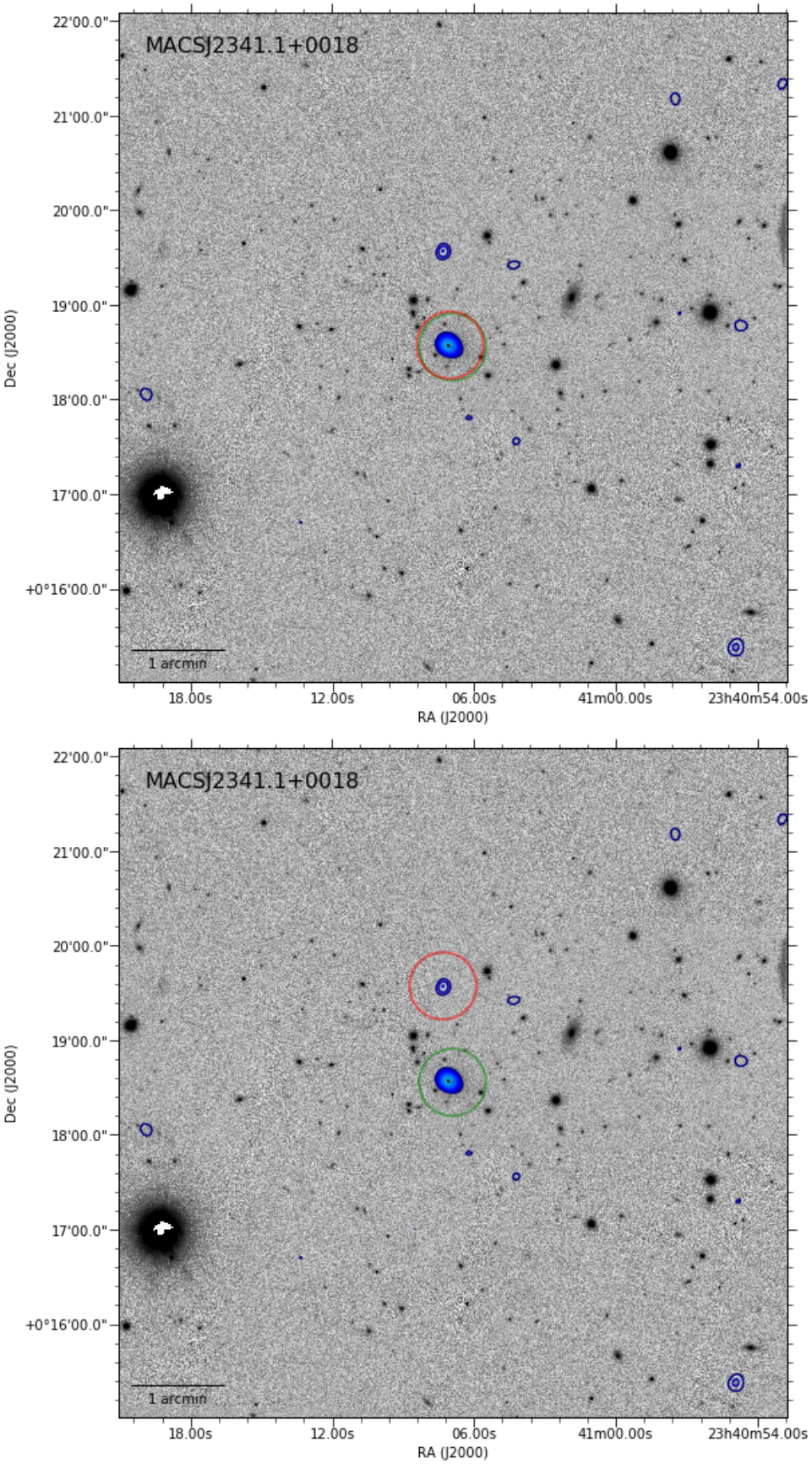

Figure C.1 cont.

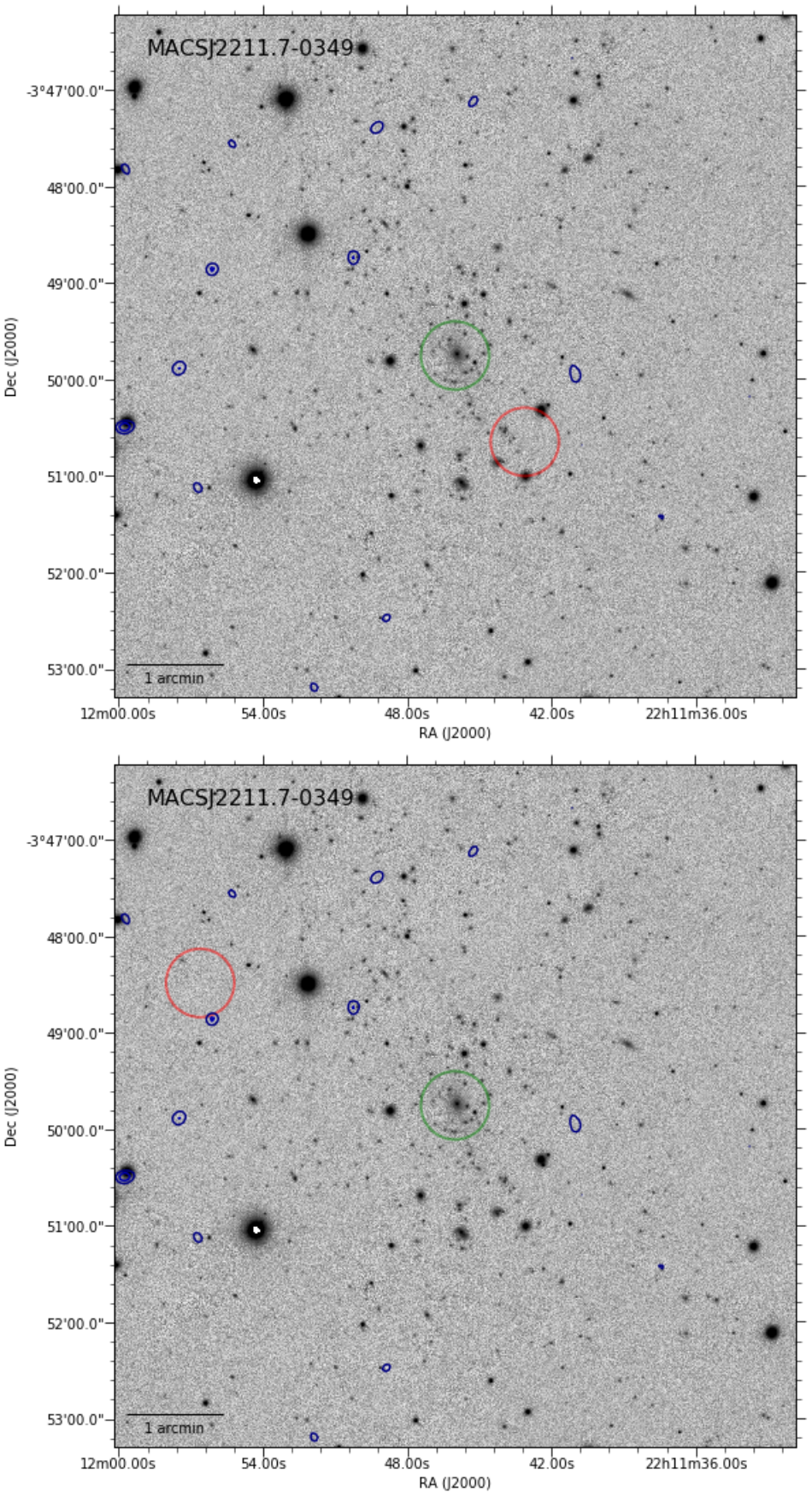

Figure C.1 cont.

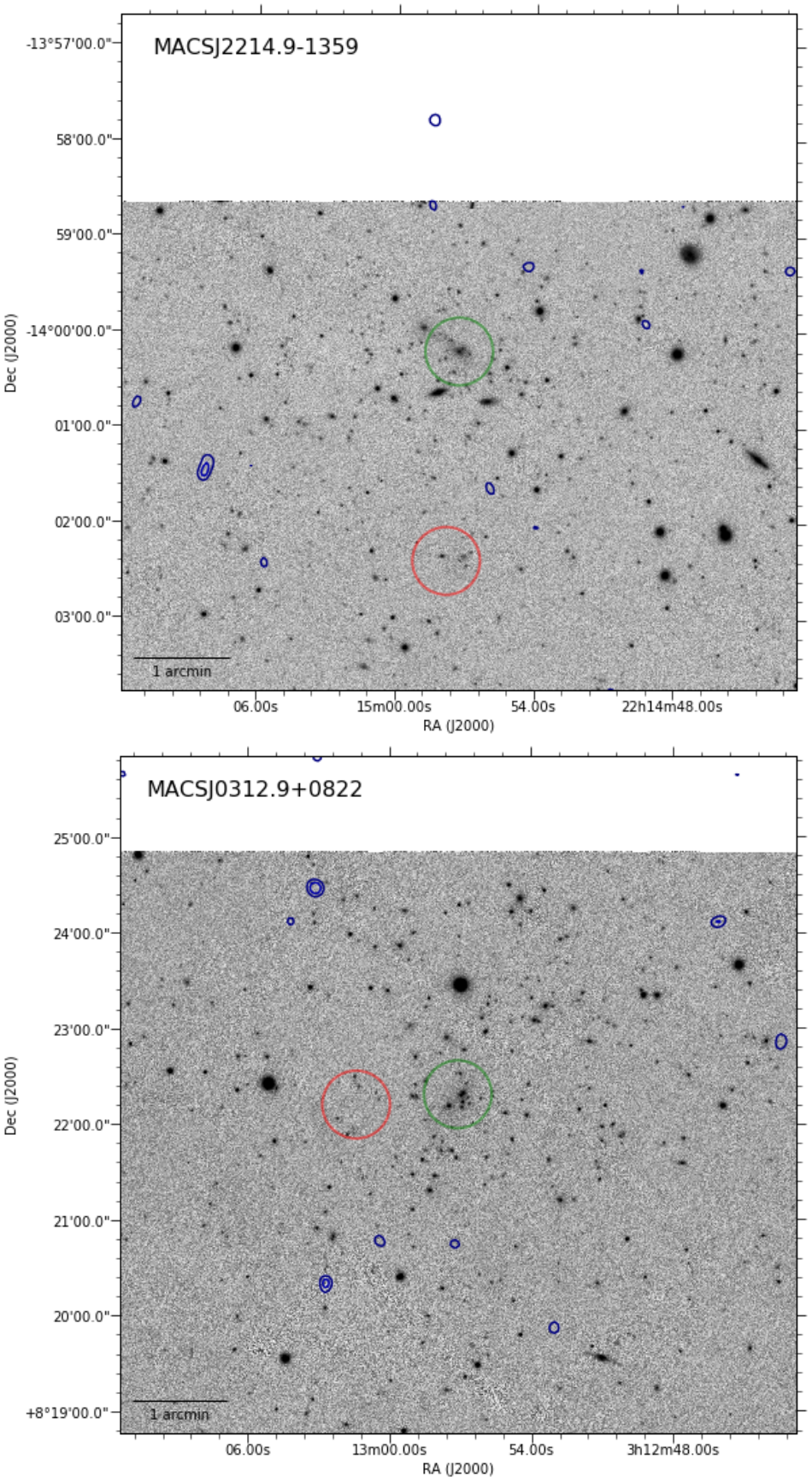

Figure C.1 cont.

Appendix D

S2CSS Target Sources

A small number of sources were specifically targeted as follow-up to existing SPIRE detections. We observed MACSJ0326.8-0043, MACSJ0455.2+0657, MACSJ0600.1-2008 as part of the survey. Figure D.1 shows the SCUBA-2 detection contours overlaid on Pan-STARRS i-band imaging. The SCUBA-2 observations were at the location of these sources, but lay $3-4'$ away from their host BCG and would have not been picked up if we targeted the cluster BCG. Their redshift estimates for the fitted SEDs (determined in the same way as Section 2.3.2) are included at the bottom of Table D.

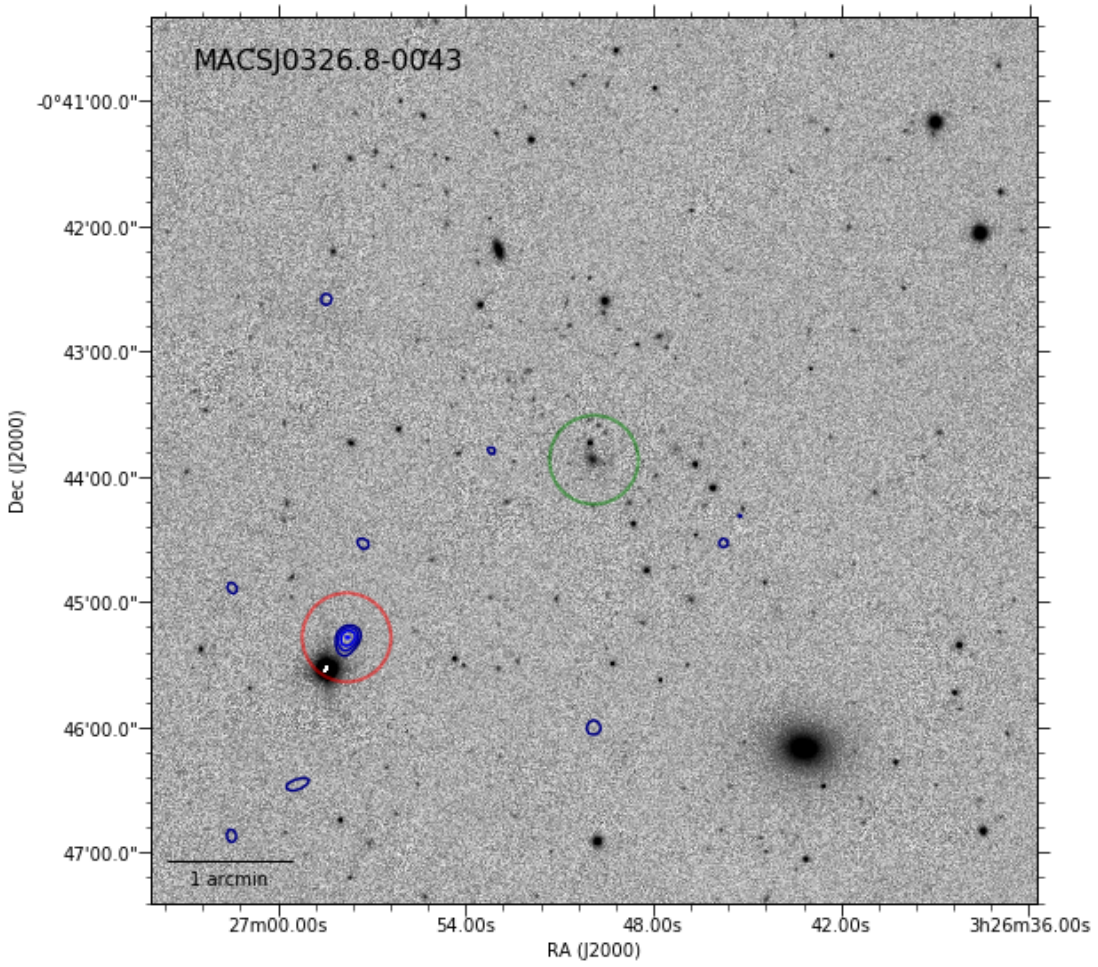

Figure D.1 Pan-STARRS i-band imaging with SCUBA-2 contours overlaid (3σ in 0.5σ increments) of the three Targeted sources from the S2CSS: MACSJ0326.8-0043, MACSJ0455.2+0657 and MACSJ0600.1-2008, red circle: BCG, green circle. MACSJ0600.1-2008 displayed field is r= $4'$ due to the location of the source.

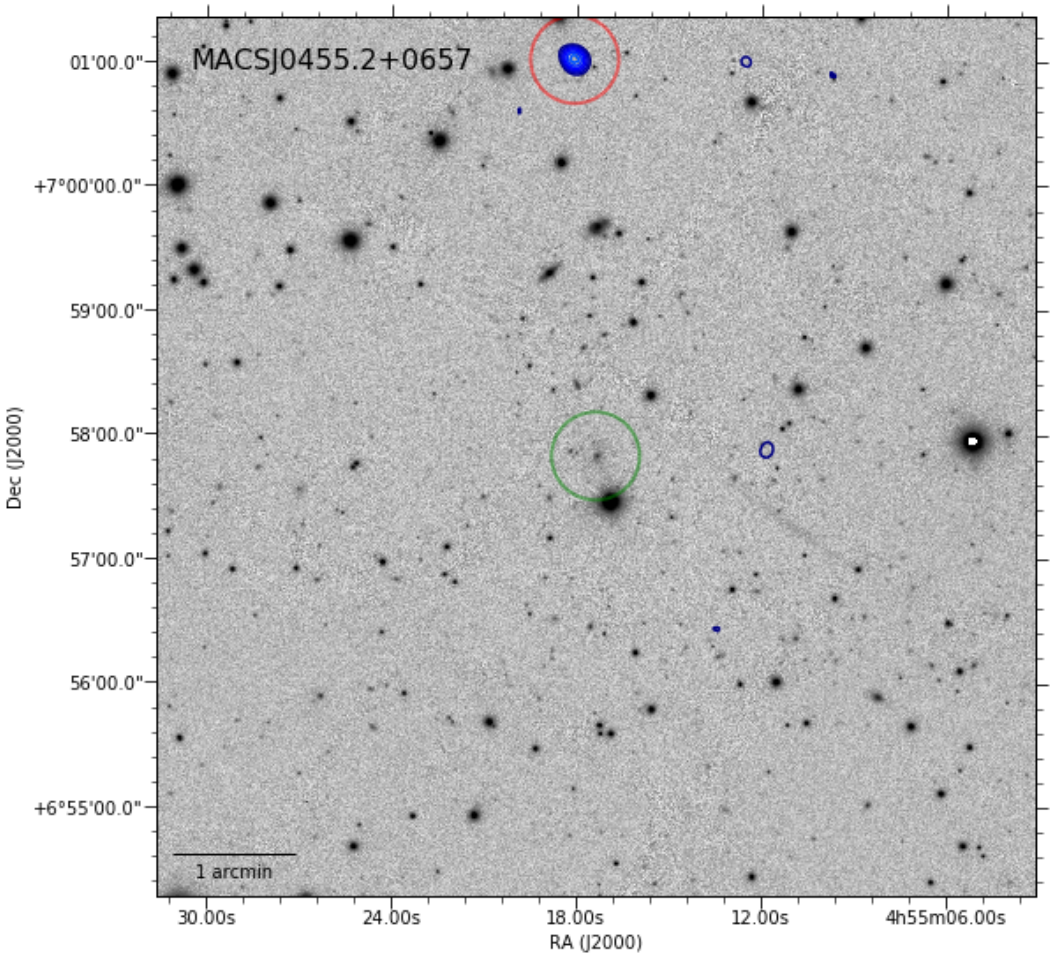

Figure D.1 cont.

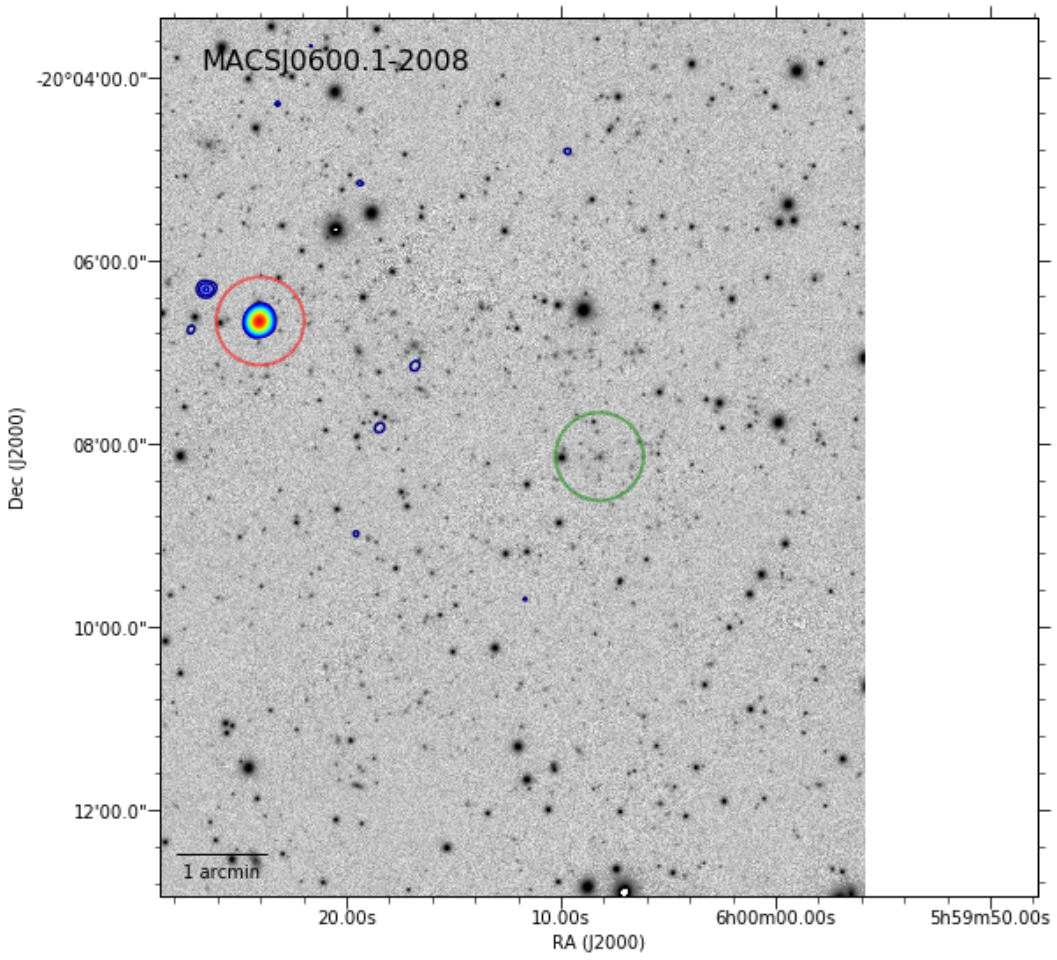

Figure D.1 cont.

Table D.1. We list the three bright HLS sources which were targeted with the SCUBA-2 instrument for an additional sub-mm band. Column 1: Cluster Field; column 2: SCUBA-2 detection position, column 3: 80% completeness sensitivity for field, column 4-7: sub-mm bands 250–850 μm.

ID	SCUBA-2 Position (J2000)	C80 (mJy)	S850 (mJy)	S250 (mJy)	S350 (mJy)	S500 (mJy)
MACSJ0326.8-0043	03:26:57.8−00:45:17	36	29 ± 6	62 ± 13	73 ± 13	73 ± 16
MACSJ0455.2+0657	04:55:18.1+07:01:01	31	37 ± 5	189 ± 14	123 ± 12	98 ± 16
MACSJ0600.1-2008	06:00:24.0 −20:06:40	44	125 ± 7	165 ± 14	290 ± 12	286 ± 16

Appendix E

Variability SED Fits

Below are examples of fits to the Variability in Abell-851 using the well known FIR/sub-mm templates described by Dale and Helou, 2002 to fit the $100 - 350\mu m$ data. In Figure E.1 normalisations are show for $160\mu m$ PACS with a power law index of $\alpha = 1.250$ (top panel), $250\mu m$ SPIRE with a power law index of $\alpha = 5.625$ (middle panel) and $250\mu m$ SPIRE with a power law index of $\alpha = 6.875$ (bottom panel)

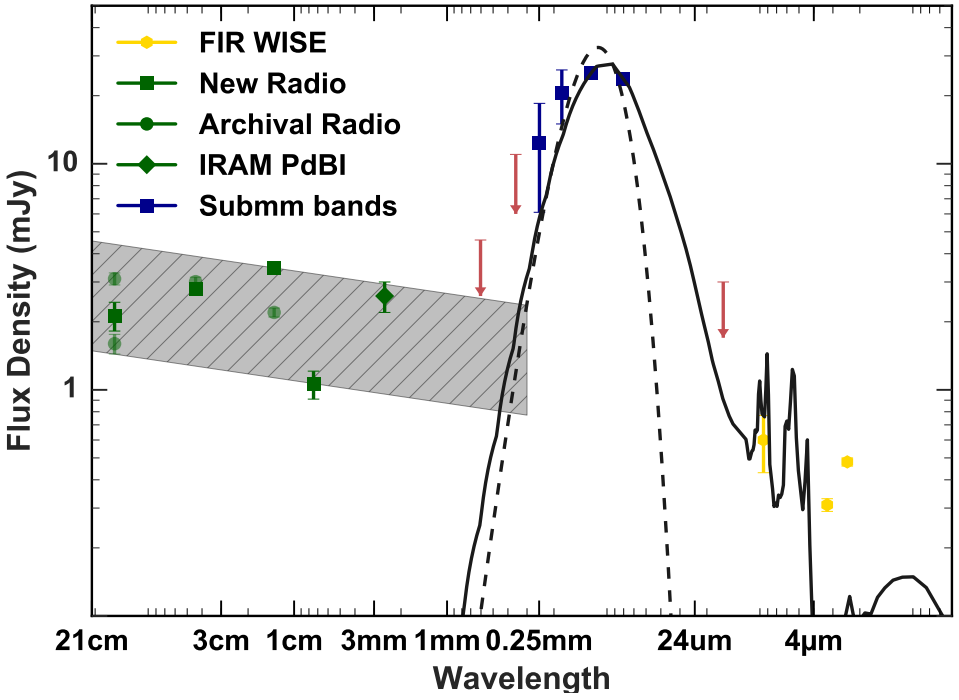

Figure E.1 The rest-frame spectral energy distribution for dg92_311. The blue squares cover the sub-mm wavebands: 100, 160, 250, 350, 500, 850μm, the green diamond is the imaged IRAM PdBI 3.6mm detection, the gold hexagons are the FIR WISE bands, green squares are the most recent radio observations whereas the fainter green circles are historic observations (listed in Table 4.1). The black solid line is a PACS 160μm normalised template from Dale and Helou, 2002

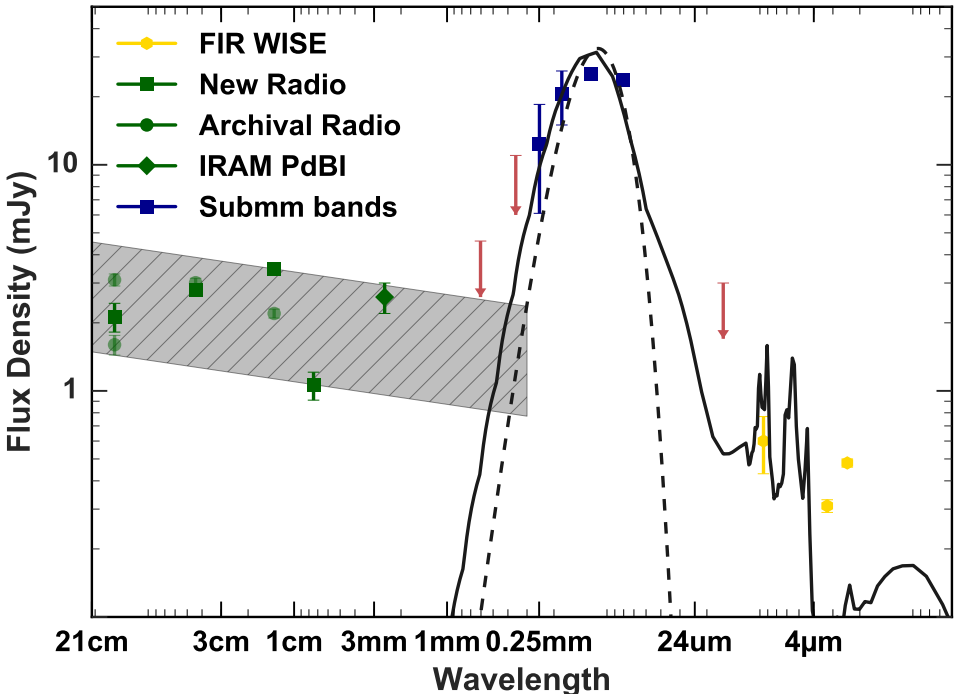

Figure E.1 cont. The black solid line is a SPIRE 250μm normalised template from Dale and Helou, 2002

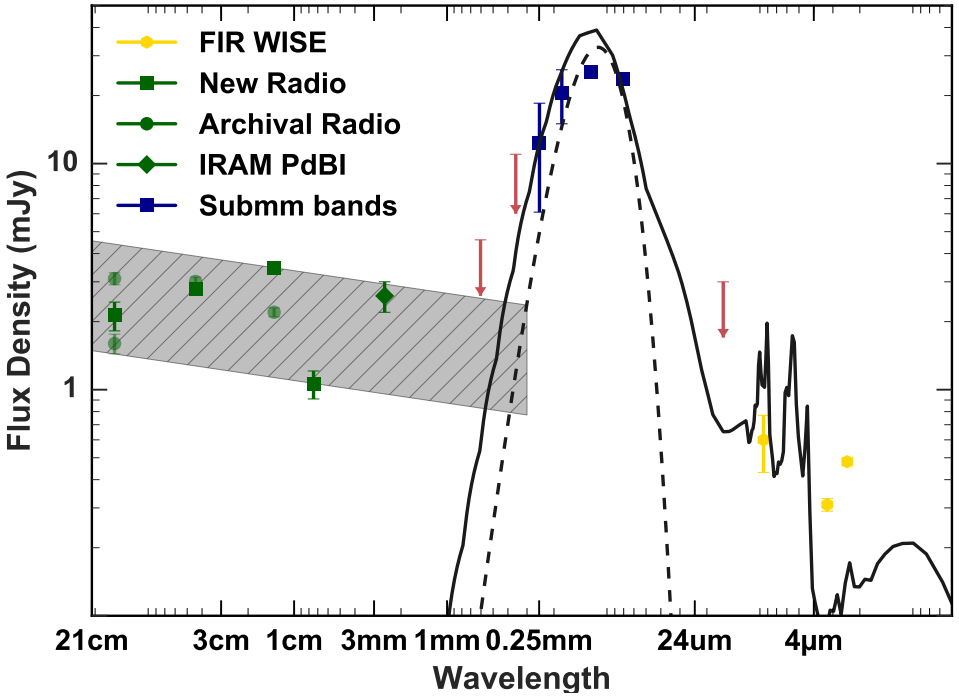

Figure E.1 cont. The black solid line is a SPIRE 350μm normalised template from Dale and Helou, 2002

Bibliography

ALMA Partnership, Vlahakis, C., Hunter, T.R., et al., 2015. The 2014 ALMA Long Baseline Campaign: Observations of the Strongly Lensed Submillimeter Galaxy HATLAS J090311.6+003906 at z = 3.042. *The Astrophysical Journal Letters*, 808:L4.

Alpher, R.A., Bethe, H., and Gamow, G., 1948. The Origin of Chemical Elements. *Physical Review*, 73:803.

Aretxaga, I., Hughes, D.H., Coppin, K., et al., 2007. The SCUBA Half Degree Extragalactic Survey - IV. Radio-mm-FIR photometric redshifts. *Monthly Notices of the Royal Astronomical Society*, 379:1571.

Arnouts, S., Schiminovich, D., Ilbert, O., et al., 2005. The GALEX VIMOS-VLT Deep Survey Measurement of the Evolution of the 1500 Å Luminosity Function. *The Astrophysical Journal Letters*, 619:L43.

Baldi, R.D., Behar, E., Laor, A., et al., 2015. Milimetre-band variability of the radio-quiet nucleus of NGC 7469. *Monthly Notices of the Royal Astronomical Society*, 454:4277.

Barger, A.J., Cowie, L.L., Sanders, D.B., et al., 1998. Submillimetre-wavelength detection of dusty star-forming galaxies at high redshift. *Nature*, 394:248.

Behar, E., Vogel, S., Baldi, R.D., et al., 2018. The mm-wave compact component of an AGN. *Monthly Notices of the Royal Astronomical Society*, 478:399.

Belloni, P., Bruzual, A.G., Thimm, G.J., et al., 1995. Detectability and incidence of E+A galaxies in the distance cluster C10930+472 (z = 0.41). *Astronomy and Astrophysics*, 297:61.

Bendo, G.J., Joseph, R.D., Wells, M., et al., 2003. Dust Temperatures in the Infrared Space Observatory Atlas of Bright Spiral Galaxies. *The Astronomical Journal*, 125(5):2361. ArXiv: astro-ph/0303576.

Benson, A.J., 2010. Galaxy Formation Theory. *Physics Reports*, 495(2-3):33. ArXiv: 1006.5394.

Bernstein, R.A., Freedman, W.L., and Madore, B.F., 2002. The First Detections of the Extragalactic Background Light at 3000, 5500, and 8000 Å. I. Results. *The Astrophysical Journal*, 571:56.

Bertin, E. and Arnouts, S., 1996. SExtractor: Software for source extraction. *Astronomy and Astrophysics Supplement Series*, 117:393.

Bisbas, T.G., Papadopoulos, P.P., and Viti, S., 2015. Effective Destruction of CO by Cosmic Rays: Implications for Tracing H2 Gas in the Universe. *The Astrophysical Journal*, 803:37.

Blain, A.W., 1997. Gravitational lensing by clusters of galaxies in the millimetre/submillimetre waveband. *Monthly Notices of the Royal Astronomical Society*, 290:553.

Blain, A.W. and Longair, M.S., 1996. Observing strategies for blank-field surveys in the submillimetre waveband. *Monthly Notices of the Royal Astronomical Society*, 279:847.

Blain, A.W., Smail, I., Ivison, R.J., et al., 1999. The history of star formation in dusty galaxies. *Monthly Notices of the Royal Astronomical Society*, 302:632.

Blain, A.W., Smail, I., Ivison, R.J., et al., 2002. Submillimeter galaxies. *Physics Reports*, 369:111.

Blumenthal, G.R., Faber, S.M., Primack, J.R., et al., 1984. Formation of galaxies and large-scale structure with cold dark matter. *Nature*, 311:517.

Bolatto, A.D., Wolfire, M., and Leroy, A.K., 2013. The CO-to-H2 Conversion Factor. *Annual Review of Astronomy and Astrophysics*, 51:207.

Booth, C.M. and Schaye, J., 2009. Cosmological simulations of the growth of supermassive black holes and feedback from active galactic nuclei: method and tests. *Monthly Notices of the Royal Astronomical Society*, 398:53.

Bothwell, M.S., Aguirre, J.E., Chapman, S.C., et al., 2013. SPT 0538-50: Physical Conditions in the Interstellar Medium of a Strongly Lensed Dusty Star-forming Galaxy at z = 2.8. *The Astrophysical Journal*, 779:67.

Bothwell, M.S., Kennicutt, R.C., Johnson, B.D., et al., 2011. The star formation rate distribution function of the local Universe. *Monthly Notices of the Royal Astronomical Society*, 415:1815.

Bower, R.G., Benson, A.J., Malbon, R., et al., 2006. Breaking the hierarchy of galaxy formation. *Monthly Notices of the Royal Astronomical Society*, 370(2):645.

Burigana, C., Danese, L., de Zotti, G., et al., 1997. Constraints on the Cosmic Star Formation History from the Far-infrared Background. *Monthly Notices of the Royal Astronomical Society*, 287:L17.

Burles, S., Nollett, K.M., and Turner, M.S., 2001. Big Bang Nucleosynthesis Predictions for Precision Cosmology. *The Astrophysical Journal Letters*, 552:L1.

Burton, M.G., Hollenbach, D.J., and Tielens, A.G.G.M., 1990. Line emission from clumpy photodissociation regions. *The Astrophysical Journal*, 365:620.

Béthermin, M., Daddi, E., Magdis, G., et al., 2015. Evolution of the dust emission of massive galaxies up to z = 4 and constraints on their dominant mode of star formation. *Astronomy and Astrophysics*, 573:A113.

Böhringer, H., Schuecker, P., Guzzo, L., et al., 2004. The ROSAT-ESO Flux Limited X-ray (REFLEX) Galaxy cluster survey. V. The cluster catalogue. *Astronomy and Astrophysics*, 425:367.

Carilli, C.L. and Walter, F., 2013. Cool Gas in High-Redshift Galaxies. *Annual Review of Astronomy and Astrophysics*, 51:105.

Carlstrom, J.E., Holder, G.P., and Reese, E.D., 2002. Cosmology with the Sunyaev-Zel'dovich Effect. *Annual Review of Astronomy and Astrophysics*, 40:643.

Casey, C.M., 2012. Far-infrared spectral energy distribution fitting for galaxies near and far. *Monthly Notices of the Royal Astronomical Society*, 425:3094.

Casey, C.M., Narayanan, D., and Cooray, A., 2014. Dusty star-forming galaxies at high redshift. *Physics Reports*, 541:45.

Chapin, E., Gibb, A.G., Jenness, T., et al., 2013. SMURF – the Sub-Millimetre User Reduction Facility. *Starlink User Note*, 258.

Chapman, S.C., Blain, A.W., Smail, I., et al., 2005. A Redshift Survey of the Submillimeter Galaxy Population. *The Astrophysical Journal*, 622:772.

Cheale, R.A., Geach, J.E., Edge, A.C., et al., 2018. The nature of the variable millimetre-selected AGN in the Brightest Cluster Galaxy of Abell 851. *Monthly Notices of the Royal Astronomical Society*.

Cheale, R.A., Geach, J.E., Edge, A.C., et al., 2019. The SCUBA-2 Cluster Snapshot Survey - I. Catalogue of lensed galaxies and submillimetre-bright central galaxies. *Monthly Notices of the Royal Astronomical Society*, 484:2757.

Chen, C.C., Cowie, L.L., Barger, A.J., et al., 2013. Resolving the Cosmic Far-infrared Background at 450 and 850 μm with SCUBA-2. *The Astrophysical Journal*, 776:131.

Chen, G.C.F., Fassnacht, C.D., Suyu, S.H., et al., 2019. A SHARP view of H0licow: H0 from three time-delay gravitational lens systems with adaptive optics imaging. *Monthly Notices of the Royal Astronomical Society*, 490(2):1743.

Cimatti, A., Cassata, P., Pozzetti, L., et al., 2008. GMASS ultradeep spectroscopy of galaxies at z ˜ 2. II. Superdense passive galaxies: how did they form and evolve? *Astronomy and Astrophysics*, 482:21.

Clements, D.L., Rigby, E., Maddox, S., et al., 2010. Herschel-ATLAS: Extragalactic number counts from 250 to 500 microns. *Astronomy and Astrophysics*, 518:L8.

Coble, K., Bonamente, M., Carlstrom, J.E., et al., 2007. Radio Sources toward Galaxy Clusters at 30 GHz. *The Astronomical Journal*, 134:897.

Collaboration, P., Ade, P.A.R., Aghanim, N., et al., 2014. Planck 2013 results. XVI. Cosmological parameters. *Astronomy & Astrophysics*, 571:A16. ArXiv: 1303.5076.

Combes, F., Rex, M., Rawle, T.D., et al., 2012. A bright z = 5.2 lensed submillimeter galaxy in the field of Abell 773. HLSJ091828.6+514223. *Astronomy and Astrophysics*, 538:L4.

Compiégne, M., 2010. Interstellar Dust. volume 438, page 55. eprint: arXiv:1104.2949.

Condon, J.J., Cotton, W.D., Greisen, E.W., et al., 1998. The NRAO VLA Sky Survey. *The Astronomical Journal*, 115:1693.

Condon, J.J., Dickey, J.M., and Salpeter, E.E., 1990. A 1.4 GHz Source Survey in an Area without Nearby Rich Galaxy Clusters. *The Astronomical Journal*, 99:1071.

Conley, A., Cooray, A., Vieira, J.D., et al., 2011. Discovery of a Multiply Lensed Submillimeter Galaxy in Early HerMES Herschel/SPIRE Data. *The Astrophysical Journal Letters*, 732:L35.

Connolly, A.J., Szalay, A.S., Dickinson, M., et al., 1997. The Evolution of the Global Star Formation History as Measured from the Hubble Deep Field. *The Astrophysical Journal Letters*, 486:L11.

Cooke, K.C., O'Dea, C.P., Baum, S.A., et al., 2016. Star Formation in Intermediate Redshift 0.2 $<$ z $<$ 0.7 Brightest Cluster Galaxies. *The Astrophysical Journal*, 833:224.

Coppin, K., Chapin, E.L., Mortier, A.M.J., et al., 2006. The SCUBA Half-Degree Extragalactic Survey - II. Submillimetre maps, catalogue and number counts. *Monthly Notices of the Royal Astronomical Society*, 372:1621.

Coppin, K.E.K., Geach, J.E., Smail, I., et al., 2011. Herschel-Astrophysical Terahertz Large Area Survey: detection of a far-infrared population around galaxy clusters. *Monthly Notices of the Royal Astronomical Society*, 416:680.

Croton, D.J., Springel, V., White, S.D.M., et al., 2006. The many lives of active galactic nuclei: cooling flows, black holes and the luminosities and colours of galaxies. *Monthly Notices of the Royal Astronomical Society*, 365(1):11.

Daddi, E., Dannerbauer, H., Krips, M., et al., 2009a. A CO Emission Line from the Optical and Near-IR Undetected Submillimeter Galaxy GN10. *The Astrophysical Journal Letters*, 695:L176.

Daddi, E., Dannerbauer, H., Stern, D., et al., 2009b. Two Bright Submillimeter Galaxies in a z = 4.05 Protocluster in Goods-North, and Accurate Radio-Infrared Photometric Redshifts. *The Astrophysical Journal*, 694:1517.

Daddi, E., Dickinson, M., Morrison, G., et al., 2007. Multiwavelength Study of Massive Galaxies at z˜2. I. Star Formation and Galaxy Growth. *The Astrophysical Journal*, 670:156.

Dale, D.A. and Helou, G., 2002. The Infrared Spectral Energy Distribution of Normal Star-forming Galaxies: Calibration at Far-Infrared and Submillimeter Wavelengths. *The Astrophysical Journal*, 576:159.

Danielson, A.L.R., Swinbank, A.M., Smail, I., et al., 2011. The properties of the interstellar medium within a star-forming galaxy at z= 2.3. *Monthly Notices of the Royal Astronomical Society*, 410:1687.

Danielson, A.L.R., Swinbank, A.M., Smail, I., et al., 2013. 13co and C18o emission from a dense gas disc at z = 2.3: abundance variations, cosmic rays and the initial conditions for star formation. *Monthly Notices of the Royal Astronomical Society*, 436:2793.

Danielson, A.L.R., Swinbank, A.M., Smail, I., et al., 2017. An ALMA Survey of Submillimeter Galaxies in the Extended Chandra Deep Field South: Spectroscopic Redshifts. *The Astrophysical Journal*, 840:78.

Datta, R., Aiola, S., Choi, S.K., et al., 2018. The Atacama Cosmology Telescope: Two-season ACTPol Extragalactic Point Sources and their Polarization properties. *Monthly Notices of the Royal Astronomical Society*.

Decarli, R., Walter, F., Neri, R., et al., 2012. Ionized Nitrogen at High Redshift. *The Astrophysical Journal*, 752:2.

Dey, A., Graham, J.R., Ivison, R.J., et al., 1999. Observations of a Z = 1.44 Dusty, Ultraluminous Galaxy and Implications for Deep Submillimeter Surveys. *The Astrophysical Journal*, 519:610.

Doi, A., Kameno, S., Kohno, K., et al., 2005. A high-frequency radio survey of low-luminosity active galactic nuclei. *Monthly Notices of the Royal Astronomical Society*, 363:692.

Doi, A., Nakanishi, K., Nagai, H., et al., 2011. Millimeter Radio Continuum Emissions as the Activity of Supermassive Black Holes in Nearby Early-type Galaxies and Low-luminosity Active Galactic Nuclei. *The Astronomical Journal*, 142(5):167.

Draine, B.T., 2006. On the Submillimeter Opacity of Protoplanetary Disks. *The Astrophysical Journal*, 636:1114.

Dressler, A. and Gunn, J.E., 1992. Spectroscopy of galaxies in distant clusters. IV - A catalog of photometry and spectroscopy for galaxies in seven clusters with Z in the range of 0.35 to 0.55. *The Astrophysical Journal Supplement Series*, 78:1.

Dressler, A., Smail, I., Poggianti, B., et al., 1999. A Spectroscopic Catalog of 10 Distant Rich Clusters of Galaxies. *The Astrophysical Journal Supplement Series*, 122(1):51. ArXiv: astro-ph/9901263.

Dubois, Y., Pichon, C., Devriendt, J., et al., 2013. Blowing cold flows away: the impact of early AGN activity on the formation of a brightest cluster galaxy progenitor. *Monthly Notices of the Royal Astronomical Society*, 428(4):2885. ArXiv: 1206.5838.

Dunn, R.J.H. and Fabian, A.C., 2008. Investigating Heating and Cooling in the BCS & B55 Cluster Samples. *Monthly Notices of the Royal Astronomical Society*, 385(2):757. ArXiv: 0801.1215.

Dutson, K.L., Edge, A.C., Hinton, J.A., et al., 2014. A non-thermal study of the brightest cluster galaxy NGC 1275 - the Gamma-Radio connection over four decades. *Monthly Notices of the Royal Astronomical Society*, 442(3):2048.

Dwek, E., 2005. Interstellar dust: what is it, how does it evolve, and what are its observational consequences? volume 761, pages 103–122. eprint: arXiv:astro-ph/0412344.

Dwek, E. and Krennrich, F., 2013. The extragalactic background light and the gamma-ray opacity of the universe. *Astroparticle Physics*, 43:112.

Dye, S., Eales, S.A., Aretxaga, I., et al., 2008. The SCUBA HAlf Degree Extragalactic Survey (SHADES) - VII. Optical/IR photometry and stellar masses of submillimetre galaxies. *Monthly Notices of the Royal Astronomical Society*, 386:1107.

Eales, S., Lilly, S., Webb, T., et al., 2000. The Canada-UK Deep Submillimeter Survey. IV. The Survey of the 14 Hour Field. *The Astronomical Journal*, 120:2244.

Ebeling, H., Edge, A.C., Allen, S.W., et al., 2000. The ROSAT Brightest Cluster Sample - IV. The extended sample. *Monthly Notices of the Royal Astronomical Society*, 318:333.

Ebeling, H., Edge, A.C., Bohringer, H., et al., 1998. The ROSAT Brightest Cluster Sample - I. The compilation of the sample and the cluster log N-log S distribution. *Monthly Notices of the Royal Astronomical Society*, 301:881.

Ebeling, H., Edge, A.C., Burgett, W.S., et al., 2013. X-ray selected galaxy clusters in the Pan-STARRS Medium Deep Survey. *Monthly Notices of the Royal Astronomical Society*, 432:62.

Ebeling, H., Edge, A.C., and Henry, J.P., 2001. MACS: A Quest for the Most Massive Galaxy Clusters in the Universe. *The Astrophysical Journal*, 553:668.

Edge, A.C., Ivison, R.J., Smail, I., et al., 1999. The detection of dust in the central galaxies of distant cooling-flow clusters. *Monthly Notices of the Royal Astronomical Society*, 306:599.

Edge, A.C., Oonk, J.B.R., Mittal, R., et al., 2010. Herschel photometry of brightest cluster galaxies in cooling flow clusters. *Astronomy and Astrophysics*, 518:L47.

Egami, E., Rex, M., Rawle, T.D., et al., 2010. The Herschel Lensing Survey (HLS): Overview. *Astronomy and Astrophysics*, 518:L12.

Elbaz, D., Daddi, E., Le Borgne, D., et al., 2007. The reversal of the star formation-density relation in the distant universe. *Astronomy and Astrophysics*, 468:33.

Fabian, A.C., 1994. Cooling Flows in Clusters of Galaxies. *Annual Review of Astronomy and Astrophysics*, 32:277.

Fabian, A.C., 2012. Observational Evidence of Active Galactic Nuclei Feedback. *Annual Review of Astronomy and Astrophysics*, 50(1):455.

Fixsen, D.J., Dwek, E., Mather, J.C., et al., 1998. The Spectrum of the Extragalactic Far Infrared Background from the COBE Firas Observations. *The Astrophysical Journal*, 508(1):123. ArXiv: astro-ph/9803021.

Flewelling, H.A., Magnier, E.A., Chambers, K.C., et al., 2016. The Pan-STARRS1 Database and Data Products. *ArXiv e-prints*, 1612:arXiv:1612.05243.

Freedman, W.L., 2017. Correction: Cosmology at a crossroads. *Nature Astronomy*, 1:0169.

Gao, Y., Carilli, C.L., Solomon, P.M., et al., 2007. HCN Observations of Submillimeter Galaxies and QSOs at High Redshift. volume 235, pages 403–403.

Gao, Y. and Solomon, P.M., 2004. The Star Formation Rate and Dense Molecular Gas in Galaxies. *The Astrophysical Journal*, 606:271.

Gaspari, M., Brighenti, F., D'Ercole, A., et al., 2011. AGN Feedback in Galaxy Groups: the Delicate Touch of Self-Regulated Outflows. *Monthly Notices of the Royal Astronomical Society*, 415(2):1549. ArXiv: 1103.5351.

Geach, J.E., Chapin, E.L., Coppin, K.E.K., et al., 2013. The SCUBA-2 Cosmology Legacy Survey: blank-field number counts of 450-μm-selected galaxies and their contribution to the cosmic infrared background. *Monthly Notices of the Royal Astronomical Society*, 432:53.

Geach, J.E., Dunlop, J.S., Halpern, M., et al., 2017. The SCUBA-2 Cosmology Legacy Survey: 850 μm maps, catalogues and number counts. *Monthly Notices of the Royal Astronomical Society*, 465:1789.

Gear, W.K. and Cunningham, C.R., 1990. SCUBA: A submillimetre camera. volume 29.

Gehrels, N., 1986. Confidence limits for small numbers of events in astrophysical data. *The Astrophysical Journal*, 303:336.

Genzel, R., Lutz, D., Sturm, E., et al., 1998. What Powers Ultraluminous IRAS Galaxies? *The Astrophysical Journal*, 498:579.

George, R.D., Ivison, R.J., Smail, I., et al., 2014. Herschel reveals a molecular outflow in a z = 2.3 ULIRG. *Monthly Notices of the Royal Astronomical Society*, 442(2):1877.

Greve, T.R., Weiβ, A., Walter, F., et al., 2010. A LABOCA Survey of the Extended Chandra Deep Field South—Submillimeter Properties of Near-infrared Selected Galaxies. *ApJ*, 719(1):483.

Guth, A.H., 1981. Inflationary universe: A possible solution to the horizon and flatness problems. *Physical Review D*, 23:347.

Hainline, L.J., Blain, A.W., Smail, I., et al., 2011. The Stellar Mass Content of Submillimeter-selected Galaxies. *The Astrophysical Journal*, 740:96.

Hardcastle, M.J., Ching, J.H.Y., Virdee, J.S., et al., 2013. Herschel-ATLAS/GAMA: a difference between star formation rates in strong-line and weak-line radio galaxies. *Monthly Notices of the Royal Astronomical Society*, 429:2407.

Heger, A., Fryer, C.L., Woosley, S.E., et al., 2003. How Massive Single Stars End Their Life. *The Astrophysical Journal*, 591(1):288.

Hickish, J., Razavi-Ghods, N., Perrott, Y.C., et al., 2018. A digital correlator upgrade for the Arcminute MicroKelvin Imager. *Monthly Notices of the Royal Astronomical Society*, 475(4):5677.

Hildebrand, R.H., 1983. The Determination of Cloud Masses and Dust Characteristics from Submillimetre Thermal Emission. *Quarterly Journal of the Royal Astronomical Society*, 24:267.

Hogan, M.T., Edge, A.C., Geach, J.E., et al., 2015a. High Radio Frequency Properties and Variability of Brightest Cluster Galaxies. *Monthly Notices of the Royal Astronomical Society*, 453(2):1223. ArXiv: 1507.03022.

Hogan, M.T., Edge, A.C., Hlavacek-Larrondo, J., et al., 2015b. A Comprehensive Study of the Radio Properties of Brightest Cluster Galaxies. *Monthly Notices of the Royal Astronomical Society*, 453(2):1201. ArXiv: 1507.03019.

Holland, W.S., Bintley, D., Chapin, E.L., et al., 2013. SCUBA-2: the 10 000 pixel bolometer camera on the James Clerk Maxwell Telescope. *Monthly Notices of the Royal Astronomical Society*, 430:2513.

Holland, W.S., Robson, E.I., Gear, W.K., et al., 1999. SCUBA: a common-user submillimetre camera operating on the James Clerk Maxwell Telescope. *Monthly Notices of the Royal Astronomical Society*, 303:659.

Hollenbach, D.J. and Tielens, a.A.G.G.M., 1997. DENSE PHOTODISSOCIATION REGIONS (PDRs). *Annual Review of Astronomy and Astrophysics*, 35(1):179.

Hopkins, A.M. and Beacom, J.F., 2006. On the Normalization of the Cosmic Star Formation History. *The Astrophysical Journal*, 651:142.

Houck, J.R., Schneider, D.P., Danielson, G.E., et al., 1985. Unidentified IRAS sources - Ultrahigh-luminosity galaxies. *The Astrophysical Journal Letters*, 290:L5.

Hubble, E., 1929. A Relation between Distance and Radial Velocity among Extra-Galactic Nebulae. *Proceedings of the National Academy of Science*, 15:168.

Hughes, D. and Dunlop, J., 1998. Using New Submillimetre Surveys to Identify the Evolutionary Status of High-Z Galaxies. volume 226, page 259. eprint: arXiv:astro-ph/9707255.

Hughes, D.H., Serjeant, S., Dunlop, J., et al., 1998. High-redshift star formation in the Hubble Deep Field revealed by a submillimetre-wavelength survey. *Nature*, 394:241.

Hurley-Walker, N., Bridle, S., Cypriano, E.S., et al., 2012. Bayesian analysis of weak gravitational lensing and Sunyaev-Zel'dovich data for six galaxy clusters. *Monthly Notices of the Royal Astronomical Society*, 419:2921.

Intema, H.T., Jagannathan, P., Mooley, K.P., et al., 2017. The GMRT 150 MHz all-sky radio survey. First alternative data release TGSS ADR1. *Astronomy and Astrophysics*, 598:A78.

Irwin, K.D., 1995. An application of electrothermal feedback for high resolution cryogenic particle detection. *Applied Physics Letters*, 66:1998.

Ishibashi, W. and Fabian, A.C., 2012. Active galactic nucleus feedback and triggering of star formation in galaxies. *Monthly Notices of the Royal Astronomical Society*, 427:2998.

Israel, F.P., Raban, D., Booth, R.S., et al., 2008. The millimeter-wave continuum spectrum of Centaurus A and its nucleus. *Astronomy and Astrophysics*, 483:741.

Ivison, R.J., Greve, T.R., Dunlop, J.S., et al., 2007. The SCUBA HAlf Degree Extragalactic Survey - III. Identification of radio and mid-infrared counterparts to submillimetre galaxies. *Monthly Notices of the Royal Astronomical Society*, 380:199.

Ivison, R.J., Smail, I., Le Borgne, J.F., et al., 1998. A hyperluminous galaxy at z=2.8 found in a deep submillimetre survey. *Monthly Notices of the Royal Astronomical Society*, 298(2):583.

Ivison, R.J., Swinbank, A.M., Swinyard, B., et al., 2010. Herschel and SCUBA-2 imaging and spectroscopy of a bright, lensed submillimetre galaxy at z = 2.3. *Astronomy and Astrophysics*, 518:L35.

Jenness, T., Lightfoot, J.F., Holland, W.S., et al., 2000. SCUBA Observing Techniques and Data Reduction Pipeline, SCUBA Observing Techniques and Data Reduction Pipeline. *Imaging at Radio through Submillimeter Wavelengths*, 217:205.

Jones, A.P., 2004. Dust Destruction Processes. volume 309, page 347.

Jones, S.F., Blain, A.W., Lonsdale, C., et al., 2015. Submillimetre observations of WISE/radio-selected AGN and their environments. *Monthly Notices of the Royal Astronomical Society*, 448:3325.

Karim, A., Swinbank, A.M., Hodge, J.A., et al., 2013. An ALMA survey of submillimetre galaxies in the Extended Chandra Deep Field South: high-resolution 870 μm source counts. *Monthly Notices of the Royal Astronomical Society*, 432:2.

Kaufman, M.J., Wolfire, M.G., Hollenbach, D.J., et al., 1999. Far-Infrared and Submillimeter Emission from Galactic and Extragalactic Photodissociation Regions. *The Astrophysical Journal*, 527:795.

Knudsen, K.K., Watson, D., Frayer, D., et al., 2017. A merger in the dusty, z = 7.5 galaxy A1689-zD1? *Monthly Notices of the Royal Astronomical Society*, 466:138.

Koprowski, M.P., Dunlop, J.S., Michałowski, M.J., et al., 2016. The SCUBA-2 Cosmology Legacy Survey: galaxies in the deep 850 μm survey, and the star-forming 'main sequence'. *Monthly Notices of the Royal Astronomical Society*, 458:4321.

Koyama, Y., Kodama, T., Nakata, F., et al., 2011. Red Star-forming Galaxies and Their Environment at z = 0.4 Revealed by Panoramic Hα Imaging. *The Astrophysical Journal*, 734(1):66.

Krumholz, M.R., 2014. DESPOTIC – A New Software Library to Derive the Energetics and SPectra of Optically Thick Interstellar Clouds. *Monthly Notices of the Royal Astronomical Society*, 437(2):1662. ArXiv: 1304.2404.

Leavitt, H.S., 1908. 1777 variables in the Magellanic Clouds. *Annals of Harvard College Observatory*, 60:87.

Leavitt, H.S. and Pickering, E.C., 1912. Periods of 25 Variable Stars in the Small Magellanic Cloud. *Harvard College Observatory Circular*, 173:1.

Lilly, S.J., Eales, S.A., Gear, W.K.P., et al., 1999. The Canada-United Kingdom Deep Submillimeter Survey. II. First Identifications, Redshifts, and Implications for Galaxy Evolution. *The Astrophysical Journal*, 518:641.

Lin, Y.T. and Mohr, J.J., 2004. K-band Properties of Galaxy Clusters and Groups: Brightest Cluster Galaxies and Intracluster Light. *The Astrophysical Journal*, 617:879.

Lonsdale, C.J., Persson, S.E., and Matthews, K., 1984. Infrared observations of interacting/merging galaxies. *The Astrophysical Journal*, 287:95.

Madau, P. and Dickinson, M., 2014. Cosmic Star-Formation History. *Annual Review of Astronomy and Astrophysics*, 52:415.

Madau, P., Pozzetti, L., and Dickinson, M., 1998. The Star Formation History of Field Galaxies. *The Astrophysical Journal*, 498:106.

Magnelli, B., Lutz, D., Santini, P., et al., 2012. A Herschel view of the far-infrared properties of submillimetre galaxies. *Astronomy and Astrophysics*, 539:A155.

Magorrian, J., Tremaine, S., Richstone, D., et al., 1998. The Demography of Massive Dark Objects in Galaxy Centres. *The Astronomical Journal*, 115(6):2285. ArXiv: astro-ph/9708072.

Mahadevan, R., 1997. Scaling Laws for Advection-dominated Flows: Applications to Low-Luminosity Galactic Nuclei. *The Astrophysical Journal*, 477:585.

Marrone, D.P., Spilker, J.S., Hayward, C.C., et al., 2018. Galaxy growth in a massive halo in the first billion years of cosmic history. *Nature*, 553:51.

Martin, D.C., Seibert, M., Buat, V., et al., 2005. The Star Formation Rate Function of the Local Universe. *The Astrophysical Journal Letters*, 619:L59.

McDonald, M., Stalder, B., Bayliss, M., et al., 2016. Star-forming Brightest Cluster Galaxies at $0.25 < z < 1.25$: A Transitioning Fuel Supply. *The Astrophysical Journal*, 817:86.

McHardy, I.M., Koerding, E., Knigge, C., et al., 2006. Active galactic nuclei as scaled-up Galactic black holes. *Nature*, 444(7120):730.

McMullin, J.P., Waters, B., Schiebel, D., et al., 2007. CASA Architecture and Applications, CASA Architecture and Applications. *Astronomical Data Analysis Software and Systems XVI*, 376:127.

Moorwood, A.F.M., 1996. Starburst Galaxies. *Space Science Reviews*, 77:303.

Morrison, G.E., 1999. The radio Butcher-Oemler effect. *Ph.D. Thesis*, page 314.

Nagao, T., Maiolino, R., De Breuck, C., et al., 2012. ALMA reveals a chemically evolved submillimeter galaxy at z = 4.76. *Astronomy and Astrophysics*, 542:L34.

Narayanan, D., Dey, A., Hayward, C.C., et al., 2010. A physical model for z ˜ 2 dust-obscured galaxies. *Monthly Notices of the Royal Astronomical Society*, 407:1701.

Narayanan, D. and Krumholz, M.R., 2014. A theory for the excitation of CO in star-forming galaxies. *Monthly Notices of the Royal Astronomical Society*, 442(2):1411.

Narayanan, D., Turk, M., Feldmann, R., et al., 2015. The formation of submillimetre-bright galaxies from gas infall over a billion years. *Nature*, 525:496.

Neugebauer, G., Habing, H.J., van Duinen, R., et al., 1984. The Infrared Astronomical Satellite (IRAS) mission., The Infrared Astronomical Satellite (IRAS) mission. *The Astrophysical Journal, The Astrophysical Journal*, 278, 278:L1, L1.

Nguyen, H.T., Schulz, B., Levenson, L., et al., 2010. HerMES: The SPIRE confusion limit. *Astronomy and Astrophysics*, 518:L5.

Oemler Jr, A., Dressler, A., Kelson, D., et al., 2009. Abell 851 and the Role of Starbursts in Cluster Galaxy Evolution. *The Astrophysical Journal*, 696(1):1063. ArXiv: 0812.4405.

Omont, A., Yang, C., Cox, P., et al., 2013. H₂O emission in high-z ultra-luminous infrared galaxies. *Astronomy and Astrophysics*, 551:A115.

Ostriker, E.C. and Shetty, R., 2011. Maximally Star-forming Galactic Disks. I. Starburst Regulation Via Feedback-driven Turbulence. *ApJ*, 731(1):41.

Ott, S., 2010. The Herschel Data Processing System — HIPE and Pipelines — Up and Running Since the Start of the Mission. volume 434, page 139. eprint: arXiv:1011.1209.

Papadopoulos, P.P., 2007. HCN versus HCO+ as Dense Molecular Gas Mass Tracers in Luminous Infrared Galaxies. *The Astrophysical Journal*, 656:792.

Penzias, A.A. and Wilson, R.W., 1965. A Measurement of Excess Antenna Temperature at 4080 Mc/s. *The Astrophysical Journal*, 142:419.

Perley, R.A. and Butler, B.J., 2013a. An Accurate Flux Density Scale from 1 to 50 GHz. *The Astrophysical Journal Supplement Series*, 204(2):19.

Perley, R.A. and Butler, B.J., 2013b. Integrated Polarization Properties of 3c48, 3c138, 3c147, and 3c286. *The Astrophysical Journal Supplement Series*, 206(2):16.

Planck Collaboration, Adam, R., Ade, P.A.R., et al., 2016. Planck 2015 results. I. Overview of products and scientific results. *Astronomy and Astrophysics*, 594:A1.

Planck Collaboration, Aghanim, N., Akrami, Y., et al., 2018. Planck 2018 results. VI. Cosmological parameters. *ArXiv e-prints*, 1807:arXiv:1807.06209.

Puget, J.L., Abergel, A., Bernard, J.P., et al., 1996. Tentative detection of a cosmic far-infrared background with COBE., Tentative detection of a cosmic far-infrared background with COBE. *Astronomy and Astrophysics, Astronomy and Astrophysics*, 308, 308:L5, L5.

Rawle, T.D., Edge, A.C., Egami, E., et al., 2012. The Relation Between Cool Cluster Cores and Herschel-Detected Star Formation in Brightest Cluster Galaxies. *The Astrophysical Journal*, 747(1):29. ArXiv: 1201.1294.

Riechers, D.A., Capak, P.L., and Carilli, C.L., 2016. The Intricate Role of Cold Gas and Dust in Galaxy Evolution at Early Cosmic Epochs. volume 319, pages 105–108.

Saha, P., 1995. On Magnitude Limits for Point Source Detections. *The Astronomical Journal*, 110:916.

Sakamoto, K., Fukuda, H., Wada, K., et al., 2001. Millimetric Observations of the Center of M81: A Starved Nucleus with Intraday Variability. *The Astronomical Journal*, 122:1319.

Sanders, D.B. and Mirabel, I.F., 1996. Luminous Infrared Galaxies. *Annual Review of Astronomy and Astrophysics*, 34(1):749.

Sanders, D.B., Soifer, B.T., Elias, J.H., et al., 1988. Ultraluminous infrared galaxies and the origin of quasars. *The Astrophysical Journal*, 325:74.

Sanderson, A.J.R., Edge, A.C., and Smith, G.P., 2009. LoCuSS: the connection between brightest cluster galaxy activity, gas cooling and dynamical disturbance of X-ray cluster cores. *Monthly Notices of the Royal Astronomical Society*, 398:1698.

Schaye, J., Crain, R.A., Bower, R.G., et al., 2015. The EAGLE project: simulating the evolution and assembly of galaxies and their environments. *Monthly Notices of the Royal Astronomical Society*, 446:521.

Schindler, S., Belloni, P., Ikebe, Y., et al., 1998. X-ray observations of the rich cluster CL 0939+4713 and discovery of the strongly variable source RXJ0943.0+4701. *Astronomy and Astrophysics*, 338:843.

Schinnerer, E., Groves, B., Sargent, M.T., et al., 2016. Gas Fraction and Depletion Time of Massive Star-forming Galaxies at z ˜ 3.2: No Change in Global Star Formation Process out to z $>$ 3. *The Astrophysical Journal*, 833:112.

Schneider, P., Ehlers, J., and Falco, E.E., 1992. *Gravitational Lenses*.

Schodel, R., Krips, M., Markoff, S., et al., 2007. The millimetre variability of M 81*. Multi-epoch dual frequency mm-observations of the nucleus of M 81. *Astronomy and Astrophysics*, 463:551.

Schramm, D.N. and Turner, M.S., 1998. Big-bang nucleosynthesis enters the precision era. *Reviews of Modern Physics*, 70:303.

Seitz, C., Kneib, J.P., Schneider, P., et al., 1996. The mass distribution of CL0939+4713 obtained from a 'weak' lensing analysis of a WFPC2 image. *Astronomy and Astrophysics*, 314:L707.

Serjeant, S., 2012. Strong biases in infrared-selected gravitational lenses. *Monthly Notices of the Royal Astronomical Society*, 424:2429.

Serjeant, S., Dye, S., Mortier, A., et al., 2008. The SCUBA Half Degree Extragalactic Survey (SHADES) - IX. The environment, mass and redshift dependence of star formation. *Monthly Notices of the Royal Astronomical Society*, 386:1907.

Seymour, N., Dwelly, T., Moss, D., et al., 2008. The star formation history of the Universe as revealed by deep radio observations. *Monthly Notices of the Royal Astronomical Society*, 386:1695.

Shim, H., Colbert, J., Teplitz, H., et al., 2009. Global Star Formation Rate Density over $0.7 < z < 1.9$. *The Astrophysical Journal*, 696:785.

Sijacki, D., Springel, V., Di Matteo, T., et al., 2007. A unified model for AGN feedback in cosmological simulations of structure formation. *Monthly Notices of the Royal Astronomical Society*, 380:877.

Silk, J. and Rees, M.J., 1998. Quasars and galaxy formation. *Astronomy and Astrophysics*, 331:L1.

Simpson, J.M., Smail, I., Swinbank, A.M., et al., 2015. The SCUBA-2 Cosmology Legacy Survey: ALMA Resolves the Bright-end of the Sub-millimeter Number Counts. *The Astrophysical Journal*, 807:128.

Simpson, J.M., Swinbank, A.M., Smail, I., et al., 2014. An ALMA Survey of Submillimeter Galaxies in the Extended Chandra Deep Field South: The Redshift Distribution and Evolution of Submillimeter Galaxies. *The Astrophysical Journal*, 788:125.

Slipher, V.M., 1915. Spectrographic Observations of Nebulae. *Popular Astronomy*, 23:21.

Smail, I., Ivison, R., Blain, A., et al., 1999. Deep sub-mm surveys with SCUBA. volume 470, pages 312–321. eprint: arXiv:astro-ph/9810281.

Smail, I., Ivison, R.J., and Blain, A.W., 1997. A Deep Sub-millimeter Survey of Lensing Clusters: A New Window on Galaxy Formation and Evolution. *The Astrophysical Journal Letters*, 490:L5.

Smail, I., Ivison, R.J., Blain, A.W., et al., 2002. The nature of faint submillimetre-selected galaxies. *Monthly Notices of the Royal Astronomical Society*, 331(2):495.

Smith, G.P., Khosroshahi, H.G., Dariush, A., et al., 2010. LoCuSS: connecting the dominance and shape of brightest cluster galaxies with the assembly history of massive clusters. *Monthly Notices of the Royal Astronomical Society*, 409:169.

Soifer, B.T., Boehmer, L., Neugebauer, G., et al., 1989. The IRAS Bright Galaxy Sample. IV. Complete IRAS Observations, The IRAS Bright Galaxy Sample. IV. Complete IRAS Observations. *The Astronomical Journal, The Astronomical Journal*, 98, 98:766, 766.

Soifer, B.T., Houck, J.R., and Neugebauer, G., 1987. The IRAS View of the Extragalactic Sky. *Annual Review of Astronomy and Astrophysics*, 25(1):187.

Soifer, B.T., Neugebauer, G., Soifer, B.T., et al., 1991. The Properties of Infrared Galaxies in the Local Universe, The Properties of Infrared Galaxies in the Local Universe. *The Astronomical Journal, The Astronomical Journal*, 101, 101:354, 354.

Soifer, B.T., Rowan-Robinson, M., Houck, J.R., et al., 1984. Infrared galaxies in the IRAS minisurvey. *The Astrophysical Journal Letters*, 278:L71.

Spilker, J.S., Marrone, D.P., Aravena, M., et al., 2016. ALMA Imaging and Gravitational Lens Models of South Pole Telescope—Selected Dusty, Star-Forming Galaxies at High Redshifts. *The Astrophysical Journal*, 826:112.

Springel, V., Di Matteo, T., and Hernquist, L., 2005. Modeling feedback from stars and black holes in galaxy mergers. *Monthly Notices of the Royal Astronomical Society*, 361(3):776. ArXiv: astro-ph/0411108.

Stevens, J.A., Ivison, R.J., Dunlop, J.S., et al., 2003. The formation of cluster elliptical galaxies as revealed by extensive star formation. *Nature*, 425:264.

Sunyaev, R.A. and Zeldovich, I.B., 1980. Microwave background radiation as a probe of the contemporary structure and history of the universe. *Annual Review of Astronomy and Astrophysics*, 18:537.

Sunyaev, R.A. and Zeldovich, Y.B., 1972. The Observations of Relic Radiation as a Test of the Nature of X-Ray Radiation from the Clusters of Galaxies. *Comments on Astrophysics and Space Physics*, 4:173.

Swinbank, A.M., Smail, I., Chapman, S.C., et al., 2004. The Rest-Frame Optical Spectra of SCUBA Galaxies. *The Astrophysical Journal*, 617:64.

Swinbank, A.M., Smail, I., Longmore, S., et al., 2010. Intense star formation within resolved compact regions in a galaxy at z = 2.3. *Nature*, 464:733.

Swinbank, M., Smail, I., Karim, A., et al., 2012. An ALMA Survey of Submillimetre Galaxies in the Extended Chandra Deep Field South: First Results. *The Messenger*, 149:40.

Tacconi, L.J., Genzel, R., Neri, R., et al., 2010. High molecular gas fractions in normal massive star-forming galaxies in the young Universe. *Nature*, 463:781.

Tanvir, N.R., Levan, A.J., Fruchter, A.S., et al., 2012. Star Formation in the Early Universe: Beyond the Tip of the Iceberg. *The Astrophysical Journal*, 754:46.

Tauber, J.A., ESA Scientific Collaboration, and Planck Scientific Collaboration, 2004. The Planck mission. *Advances in Space Research*, 34:491.

Thomas, H.S. and Currie, M.J., 2014. The SCUBA-2 Data Reduction Cookbook. *Starlink Cookbook*, 21.

Thompson, M.A., Serjeant, S., Jenness, T., et al., 2007. The SCUBA-2 "All-Sky" Survey. *arXiv e-prints*, 0704:arXiv:0704.3202.

Thomson, A.P., Ivison, R.J., Owen, F.N., et al., 2015. Tracing cool molecular gas and star formation on $\sim$100 pc scales within a z $\sim$ 2.3 galaxy. *Monthly Notices of the Royal Astronomical Society*, 448(2):1874.

Tody, D., 1993. IRAF in the Nineties. In *IRAF in the Nineties*, volume 52, page 173. Astronomical Data Analysis Software and Systems II.

Toft, S., Smolčić, V., Magnelli, B., et al., 2014. Submillimeter Galaxies as Progenitors of Compact Quiescent Galaxies. *The Astrophysical Journal*, 782:68.

Torniainen, I., Tornikoski, M., Teräsranta, H., et al., 2005. Long term variability of gigahertz-peaked spectrum sources and candidates. *Astronomy and Astrophysics*, 435(3):839.

Trumpler, R.J., 1930. Absorption of Light in the Galactic System. *Publications of the Astronomical Society of the Pacific*, 42:214.

Valtchanov, I., Virdee, J., Ivison, R.J., et al., 2011. Physical conditions of the interstellar medium of high-redshift, strongly lensed submillimetre galaxies from the Herschel-ATLAS. *Monthly Notices of the Royal Astronomical Society*, 415:3473.

Vantyghem, A.N., McNamara, B.R., Russell, H.R., et al., 2016. Molecular Gas Along a Bright Hα Filament in 2a 0335+096 Revealed by ALMA. *The Astrophysical Journal*, 832:148.

Voges, W., Aschenbach, B., Boller, T., et al., 1999. The ROSAT all-sky survey bright source catalogue. *Astronomy and Astrophysics*, 349:389.

Wang, B. and Heckman, T.M., 1996. Internal Absorption and the Luminosity of Disk Galaxies. *The Astrophysical Journal*, 457:645.

Whitaker, K.E., Franx, M., Leja, J., et al., 2014. Constraining the Low-mass Slope of the Star Formation Sequence at $0.5 < z < 2.5$. *The Astrophysical Journal*, 795:104.

White, R.L., Becker, R.H., Helfand, D.J., et al., 1997. A Catalog of 1.4 GHz Radio Sources from the FIRST Survey. *The Astrophysical Journal*, 475(2):479.

Wright, E.L., Eisenhardt, P.R.M., Mainzer, A.K., et al., 2010. The Wide-field Infrared Survey Explorer (WISE): Mission Description and Initial On-orbit Performance. *The Astronomical Journal*, 140(6):1868.

Zavala, J.A., Yun, M.S., Aretxaga, I., et al., 2015. Early Science with the Large Millimeter Telescope: observations of dust continuum and CO emission lines of cluster-lensed submillimetre galaxies at z=2.0-4.7. *Monthly Notices of the Royal Astronomical Society*, 452:1140.

Zemcov, M., Rex, M., Rawle, T.D., et al., 2010. First detection of the Sunyaev Zel'dovich effect increment at $\mathrm{l} < 650$ um. *Astronomy and Astrophysics*, 518:L16.

Zwart, J.T.L., Barker, R.W., Biddulph, P., et al., 2008. The Arcminute Microkelvin Imager. *Monthly Notices of the Royal Astronomical Society*, 391:1545.

Zwicky, F., 1937. On the Masses of Nebulae and of Clusters of Nebulae. *The Astrophysical Journal*, 86:217.